AD-A037184

FUNDAMENTAL INVESTIGATION OF FATIGUE CRACK GROWTH RETARDATION IN ALUMINUM ALLOYS

Northrop Corporation
Aircraft Division
3901 West Broadway
Hawthorne, California 90250

2007092 1545

AIR FORCE MATERIALS LABORATORY
AIR FORCE WRIGHT AERONAUTICAL LABORATORIES
AIR FORCE SYSTEMS COMMAND
UNITED STATES AIR FORCE

WRIGHT-PATTERSON AIR FORCE BASE, OHIO 45433

NOTICE

When Government drawings, specifications, or other data are used for any purpose other than in connection with a definitely related Government procurement operation, the United States Government thereby incurs no responsibility nor any obligation whatsoever; and the fact that the Government may have formulated, furnished, or in any way supplied the said drawings, specifications, or other data, is not to be regarded by implication or otherwise as in any manner licensing the holder or any other person or corporation, or conveying any rights or permission to manufacture, use, or sell any patented invention that may in any way be related thereto.

This technical report has been reviewed and is approved for publication.

DENNIS M. CORBLY,
Project Engineer

FOR THE COMMANDER

VINCENT J. RUSSO
Chief, Metals Behavior Branch
Metals and Ceramics Division
Air Force Materials Laboratory

Copies of this report should not be returned unless return is required by security considerations, contractual obligations, or notice on a specific document.

REPORT DOCUMENTATION PAGE		READ INSTRUCTIONS BEFORE COMPLETING FORM
1. REPORT NUMBER AFML-TR-76-156	2. GOVT ACCESSION NO.	3. RECIPIENT'S CATALOG NUMBER
4. TITLE (and Subtitle) FUNDAMENTAL INVESTIGATION OF FATIGUE CRACK GROWTH RETARDATION IN ALUMINUM ALLOYS		5. TYPE OF REPORT & PERIOD COVERED FINAL TECHNICAL REPORT JUNE 1974—JUNE 1976
		6. PERFORMING ORG. REPORT NUMBER NOR 76-110
7. AUTHOR(s) G. R. CHANANI		8. CONTRACT OR GRANT NUMBER(s) F33615-74-C-5126
9. PERFORMING ORGANIZATION NAME AND ADDRESS Northrop Corporation 3901 W. Broadway Hawthorne, California 90250		10. PROGRAM ELEMENT, PROJECT, TASK AREA & WORK UNIT NUMBERS 7351
11. CONTROLLING OFFICE NAME AND ADDRESS Air Force Materials Laboratory (AFML/LLN) Air Force Wright Aeronautical Laboratories Wright-Patterson Air Force Base, OHIO 45433		12. REPORT DATE September 1976
		13. NUMBER OF PAGES 234
14. MONITORING AGENCY NAME & ADDRESS(if different from Controlling Office)		15. SECURITY CLASS. (of this report) UNCLASSIFIED
		15a. DECLASSIFICATION/DOWNGRADING SCHEDULE NA

16. DISTRIBUTION STATEMENT (of this Report)

APPROVED FOR PUBLIC RELEASE,   DISTRIBUTION UNLIMITED

17. DISTRIBUTION STATEMENT (of the abstract entered in Block 20, if different from Report)

18. SUPPLEMENTARY NOTES

19. KEY WORDS (Continue on reverse side if necessary and identify by block number)

Fatigue-Crack Growth, Retardation, Fractography, Interferometry, Microstructure, Plastic-Zone, Corrosion Fatigue, and Aluminum Alloys

20. ABSTRACT (Continue on reverse side if necessary and identify by block number)

A fundamental investigation was performed to determine the important metallurgical and environmental factors that influence retardation behavior in aluminum alloys. The retardation phenomenon was found to be very complex and dependent on loading variables as well as material parameters. The results suggest that a phenomenological model for prediction of fatigue-crack growth under variable amplitude loading can be developed by taking the various important parameters into account. Of the four alloys investigated (2024-T3, 2024-T8, 7075-T6 and 7075-T73), the alloy with the lowest yield strength,

DD FORM 1473   EDITION OF 1 NOV 65 IS OBSOLETE
1 JAN 73

ABSTRACT (Continued)

2024-T3, was found to give maximum delay. The important material parameters were yield strength, cyclic-hardening exponent, and microstructure. Overload ratio (OLR) was the most important test-parameter. An increase in OLR always produced an increased retardation. Crack-arrest occurred at either 2.5 or 3.0 OLR depending on the alloy and the baseline stress-intensity (K_{max}). For the 7075-T6 SEN specimens, no significant changes in crack-closure were detected as the cycling progressed after the overload cycle. The overload cycle manifests itself as a stretch band on the fracture surfaces of retardation specimens. The width of the stretch zone increases with increase in K_{max} and decrease in thickness. For specimens with discernible striations, correlation between measured da/dN and changes in striation spacing was good. The optical interference technique was found to give a good agreement between measured plastic-zone and that calculated under plane-stress conditions. Test frequency changes and hold-time at low stress levels were found to have no significant effects on retardation behavior. Exposure to 176F or 248F and compressive load after the overload cycle were found to cause a decrease in retardation. Multiple overload cycles increase retardation up to a certain number of overload cycles, after which the delay reached a saturation maximum. The effect of saltwater on retardation behavior was much greater in the 7075-T6 than in the 2024-T8 and 7075-T73. The 2024-T8 and 7075-T6 showed similar retardation behavior in air, while in saltwater the 2024-T8 was distinctly superior. The number of delay cycles was found to decrease with increase in thickness. However, only a minor effect of thickness was seen on the retardation behavior of the 2024-T8. TEM investigation of thin foils obtained from the overload plastic-zone and area below the fracture surfaces of all four alloys showed that the dislocation interactions as observed in 2024-T3 were much more beneficial in inhibiting fatigue-crack growth than the precipitation changes observed in 2024-T8.

PREFACE

TABLE OF CONTENTS

LIST OF ILLUSTRATIONS

LIST OF TABLES

LIST OF SYMBOLS

a	Crack-Length
a_i	Crack-Length at which an overload(s) was applied
a_o	Initial crack-length
a*	Affected crack-length
B	Thickness
B_O	Plane-strain thickness
da/dN	Crack-growth rate
FIP	Foils obtained from the overload plastic-zone area of specially designed tests after the application of overload cycle
HTP	Foils obtained when the crack was halfway through the overload plastic-zone
K	Stress-intensity factor
$K_{critical}$	K based on the maximum load and instantaneous crack-length
K_{C5}	K based on P_5 and the initial crack-length
$K_{effective}$	(K_{eff}) $2K_{next}$ - K required
K_{max}	K based on the maximum load and the initial crack-length
K_{next}	K applied after the overload cycle
K_O	Overload stress intensity factor
$K_{required}$	(K_{reqd}) K needed to reach the previous plastic-zone boundary
ΔK	Constant-amplitude stress-intensity range
K'	Cyclic strength coefficient
K_{Ic}	Plane-strain fracture toughness
ΔK_o	Overload stress-intensity range
N	Cycles of load
n'	Cyclic strain hardening exponent
N_c	Number of constant-amplitude cycles
N_o	Number of overload cycles

N^*	Number of cycles during growth of a^* (number of delay cycles)
N_R	Empirical parameter used to define stress-condition at crack-tip; varies from 2 for plane stress to 6 for plane strain
n	Strain-hardening exponent
Net Stress Ratio	σ_{net}/σ_{ys}
OLR	Overload ratio
P	Load
P_{max}	Maximum applied baseline load
P_{min}	Minimum applied baseline load
P_o	Overload, maximum applied load
P_5	Load at 5% offset
R	Constant-amplitude stress ratio
R_{C5}	Net stress ratio at P_5 and a_o
R_{max}	Net stress ratio based on maximum load and a_o
$R_{critical}$	Net stress ratio based on maximum load and instantaneous crack-length
RE	Distance remaining to be crossed in plastic-zone after a period of cyclic crack-growth
R_o	Peak stress ratio
R_p	Plastic-zone size due to overload cycle
R_y	Calculated plastic-zone size for the next load being investigated
R^*	Normalized crack-growth rate $\left(\frac{da}{dN}/\frac{a^*}{N^*}\right)$
r_1	Steady-state crack-growth rate before overload
r_2	Steady-state crack-growth rate after overload
S	Strength coefficient
SEM	Scanning electron microscope
SEN	Single edge notched specimen

TEM   Transmission electron microscope

W   Width

σ True stress

σ_{net} $\sigma/(1-a/W)$

ϵ True strain

σ_a Stable stress amplitude

$\epsilon_p/2$ Stable plastic strain amplitude

I. INTRODUCTION

During its lifetime, an aircraft structure is subjected to both an aggressive environment and cyclic stresses that are variable in amplitude and generally random in nature. The initial crack-like flaws that may exist in critical structural components can grow subcritically under these conditions, eventually becoming large enough to cause catastrophic failure at a given operating stress level. These flaws may be introduced during fabrication or may be present in the basic material. The life of these structures can be predicted reliably only in a constant-amplitude loading situation. Frequently-occurring overloads resulting from severe gusts or aircraft maneuvers can affect crack growth and life predictions considerably.

Research in the last decade or so[1-11] has shown that load sequences have a considerable effect on fatigue-crack propagation (FCP). In particular, the application of a single overload or a few cycles at high tensile loads may cause retardation; that is, a decrease in fatigue-crack growth rate. In general, there is no observable effect when a low-amplitude load precedes a high-amplitude load [1, 12], although an initial acceleration has occasionally been reported[13, 14]. Hence, it is primarily the retardation behavior which makes it difficult to predict fatigue-life under a given spectrum.

At present, various aspects of load interaction phenomena lack satisfactory explanations. From all the work so far, it is clear that retardation phenomena are complex and must be systematically investigated before a reliable procedure for predicting fatigue lives of aircraft structures can be developed. The influence of service conditions such as environments and temperatures must also be determined.

Several mechanisms which have been proposed to explain the observed crack-growth behavior following single or multiple overloads include residual compressive stresses at the crack-tip[1, 4], crack closure [15] (crack closure here implies that fatigue cracks may be closed during a significant portion of the tensile load cycles), changes in the crack-tip plastic-zone size, crack-blunting, strain hardening, or combinations of these. However, Jones[16] found that strain hardening was not a major controlling factor in retardation in Ti-6Al-4V sheet after single overload cycles.

Empirical models that quantitatively take retardation into account in predicting FCP behavior have been proposed using changes in plastic-zone size and an effective stress-intensity factor, ΔK_{eff}[12, 17]. All the models have their basis in the relatively simple Paris equation: $da/dN = C(\Delta K)^n$.

In each model, crack growth rates are reduced by modifying one of the parameters in the above equation. In the Wheeler model[12] for example, a retardation parameter reduces the C term. This parameter takes on values between zero and unity as the crack grows through the plastic zone produced by the overload cycle, thereby reducing the crack-growth rate. In the Willenborg model[17], ΔK is modified to ΔK_{eff}, which is less than the applied stress intensity range, thus reducing the crack-growth rate.

However, the existing empirical models neither explain the observed results satisfactorily nor give satisfactory predictions. These models do not take into account metallurgical factors that affect FCP. The Wheeler and Willenborg models do not differentiate between the effects of multiple and single overloads, nor do they take into account any compressive-load effects or predict delayed retardation. Furthermore, effects of actual service conditions, such as hold-time and environment, are not well understood and accounted for.

The objective of this program was to develop an understanding of the retardation phenomenon and provide information about the influence of material parameters as well as compositional, metallurgical, and environmental factors on the retardation behavior of aluminum alloys. The results from this program provide a basis for obtaining improved prediction of fatigue behavior and fatigue-life under multistress-level loading in different environments.

During this program, fatigue-crack growth behavior after single overload cycles at different overload ratios was determined in four microstructures with three different yield strengths, and the observed retardation behavior was correlated with metallurgical, fractographic, and plastic-zone size changes at the crack-tip. In order to study the effects of microstructure and plastic-zone size changes, which primarily depend upon the yield strength and applied stress intensity factor, two aluminum alloys (2024 and 7075), strengthened by different hardening mechanisms and having different stress-strain characteristics, were used. The use of two heat treatments for each alloy (T6 and T73 for 7075, T3 and T8 for 2024) permitted determination of the effect of strength level alone on retardation in these alloys. The 7075-T73 and 2024-T8 had the same yield strength so that differences in retardation behavior due to metallurgical factors alone could be evaluated.

2

To determine the effect of an aggressive environment on retardation behavior, selected tests were also conducted in 3-1/2% saltwater and the results were compared with the retardation results in air. The influence of frequency was also established by tests conducted at three frequencies in both air and saltwater.

To make the results more applicable to service conditions, experiments were also performed to determine the effects of hold-time at low stress levels and compressive-load cycles on the retardation behavior. For this purpose, three hold-times at low stress levels and two levels of compressive loads were used.

As a further aid to the understanding and application of retardation, tests were also performed to determine the effects of thickness, multiple overload cycles, peening, and exposure to slightly elevated temperatures on the retardation behavior.

II. EXPERIMENTAL PROCEDURE

A. MATERIAL SELECTION AND PREPARATION

The 0.063-inch thick 2024 and 7075 alloys were procured in the T3 and T6 conditions, respectively. These alloys were verified with regard to their acceptability by means of tensile, conductivity, and hardness measurements. Part of the as-received 7075-T6 and 2024-T3 materials were then heat treated to the T73 and T8 conditions, respectively, to avoid compositional variables, which could otherwise obscure the effects of different heat treatments on retardation behavior.

The conversion of a portion of the 0.063-inch 7075-T6 to T73 was performed by heat treating the as-received T6 material for 24 hours at 325F. The T73 condition was also confirmed by tensile, conductivity, and hardness measurements. The conversion of a portion of the 0.063-inch 2024-T3 to the 2024-T8 condition was done in such a way that the 2024-T8 alloy produced had the same yield as that of the 7075-T73 alloy so that the differences in the retardation behavior due to metallurgical factors alone could be investigated. For this purpose, sample blanks of 2024-T3 were heat treated using different times at a temperature of 375F to produce variations in tensile properties within the T8 specification. From the various times and temperatures investigated, an aging treatment of 96 hours at 375F was selected as the best treatment because it produced an average yield strength of 61.2 ksi, which was essentially equal to that of the 7075-T73 alloy (60.8 ksi).

Thus, the two different strength levels for each of the two alloys obtained by using the T6 and T73 conditions in 7075 alloy and the T3 and T8 conditions in the 2024 alloy produced four different microstructures with three strength levels and two chemical compositions.

To determine the effects of thickness on retardation behavior, 0.5-inch thick 2024-T351, 2024-T851, 7075-T651, and 7075-T7351 plates were also procured. Specimen blanks of 0.25-inch thickness were obtained from the center of the as-received 0.5-inch thick plates.

5

Single-edge notched (SEN) specimens (Figure 1) in the LT orientation with three different thicknesses, 0.063-inch, 0.25-inch, and 0.50-inch, were then machined for use in this investigation.

B. MECHANICAL TESTING

1. TENSION TESTS

The tension tests were performed according to the ASTM E8 standards on a 20,000 lb. Instron machine. For 0.063-inch thick sheet, flat specimens of 2-inch gage length were used, while cylindrical specimens of 1-inch gage length and 0.25-inch diameter were used for the 0.50-inch thick plates. A minimum of three specimens were tested for each condition.

2. CYCLIC STRESS-STRAIN TESTS

The incremental step method proposed by Landgraf, Morrow, and Endo[18] was used to determine the cyclic stress-strain curves. With this method, a specimen is subjected to blocks of gradually increasing and then decreasing strain amplitudes to determine the cyclic stress-strain curve. In this manner, the cyclic stress-strain curve is obtained by the use of one specimen instead of several. After a few strain blocks, the material cyclically stabilizes. A continuous plot of the hysteresis loops results in a series of superimposed loops and the cyclic stress-strain curve can then be obtained by joining the tips of the loops.

The tests were performed on an MTS machine using 0.25-inch diameter speci-mens with an effective gage length of 0.57-inch and at a test frequency of 0.1 Hz. These specimens were obtained from the 0.50-inch thick plates. The strain was applied in a programmed manner using an EMR profiler and was recorded with a clip-on gage. Duplicate specimens for each of the four alloy-conditions were used.

3. FRACTURE TESTS

Fracture tests were performed on all four alloys using the 0.063-inch thick SEN specimens because this spectrum geometry was used for the majority of FCP tests in this investigation. These tests were performed in a manner similar to the ASTM-E399 test method for compact tension (CT) specimens. With the SEN specimens, fatigue pre-cracking was performed at loads such that $K_{f(max)}/E$ was less than $0.002\text{-inch}^{1/2}$, and

cracks were grown to an a/W of 0.33 instead of an a/W of 0.5, as is done for CT specimens. Loading rates and all other testing features were similar to those used for K_{IC} testing.

4. CONSTANT-AMPLITUDE FCP TESTS

Constant-amplitude fatigue-crack growth tests were conducted in both air and saltwater with the 0.063-inch thick SEN specimens obtained from the same heat and the same lot of material that were used for the retardation studies. In these tests, the crack-lengths were measured by printing photogrids on the surface with an inter-grid spacing of 0.0228-inch. Crack lengths were then measured to an accuracy of ± 0.003-inch by use of a filar eyepiece in a high-magnification traveling microscope. All of these tests were conducted on an MTS machine under load control at an R ratio ($\sigma_{min}/\sigma_{max}$) of 0.1 and a frequency of 5 Hz in a laboratory environment controlled to a temperature of 72F ± 5F and a relative humidity of 50% ± 5%. However, at the higher crack-growth rates (8×10^{-5} in/cycle or higher), the frequency had to be lowered to 2 Hz to facilitate accurate crack-growth measurements.

5. RETARDATION TESTS

The effects of a single overload on the fatigue-crack growth for all four conditions were determined using 0.063-inch thick SEN specimens. These specimens were used for the present program because of the ease with which they can be tested and their lower bending stresses compared to compact tension and DCB specimens. In the dimensions tested, these specimens contained large plane-stress plastic zones that were easily measured by optical interferometry. The measured plastic-zones were in agreement with the Irwin-type plastic zones[19].

To avoid the problems associated with mixed-mode crack-propagation, which can make a fundamental investigation of retardation difficult, either a thick specimen (plane strain) or thin specimen (plane stress) could be used. A thin specimen was used in this work because it meant a uniform microstructure, lower load requirements, ease of testing, and accuracy of surface-crack measurements due to the reduced likelihood of tunneling. However, very thin specimens would have presented gripping and buckling problems. Considering all of these factors and calculating the plane-stress and plane-strain plastic-zone sizes expected for the K_{max} levels to be tested assuming an Irwin-type plastic-zone, we chose a thickness of 0.063-inch for this program. All of these tests were performed on MTS machines under load control at an R ratio ($\sigma_{min}/\sigma_{max}$) of 0.1 in the controlled laboratory environment. For each alloy, three different P_{max}

values (500, 800, and 1000 lbs.) were used so that a wide range of K_{max} was obtained. Figure 2 shows K range for the test specimens used at the three P_{max} values. The test spectrum and the terms used to describe the single-peak overload test parameters in this program are illustrated in Figure 3. In all of the tests, the number of constant-amplitude cycles after the single overload cycle was sufficient for complete recovery of the unretarded crack-growth rate.

Several overload ratios, as shown in Table I, were used to determine the effect of overload ratio on retardation. Most of the constant-amplitude load cycles were run at 5 Hz, while the overload cycles were run at 0.1 Hz. In a few cases where the number of delay cycles was large, the frequency for constant-amplitude cycling was increased to a maximum of 10 Hz. Typical of these cases were tests at high overload ratios where crack-arrest occurred. The crack was considered arrested if no significant measurable crack-growth took place in 500,000 constant-amplitude cycles after the overload cycle. The R ratio was maintained at 0.1 for all the constant-amplitude load cycles. Table II shows the specimen coding system used for this program.

The crack-lengths were measured with an accuracy which ranged from ±0.0002 to ±0.002-inch, depending on the test by a combination of photogrids printed on the specimen surfaces and a high magnification traveling microscope. Thus, fatigue crack-growth rates as low as 10^{-9} in./cycle would have been measured in crack-arrest tests. The photogrids were printed with intergrid spacings of the order of 0.02-inch. The recording of the data during testing was standardized to provide maximum information.

C. METALLOGRAPHY

1. OPTICAL MICROSCOPY

The optical microstructures of all the four conditions were obtained in both the longitudinal and transverse orientations. For this purpose, polished specimens were etched with Keller's reagent and observed in a Leitz MM5 metallograph.

2. TRANSMISSION ELECTRON MICROSCOPY

Specimens were removed from test coupons by sectioning with a 0.010-inch thick water-cooled abrasive wheel. For baseline substructure characterization, a 0.005-inch thick section was removed from the test specimen. This was then electropolished in a
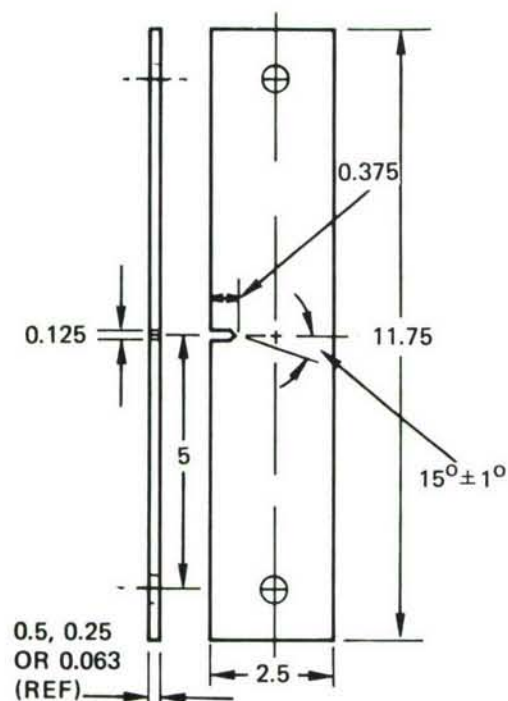
FIGURE 1. SEN ALUMINUM SPECIMEN, LT (RW) ORIENTATION
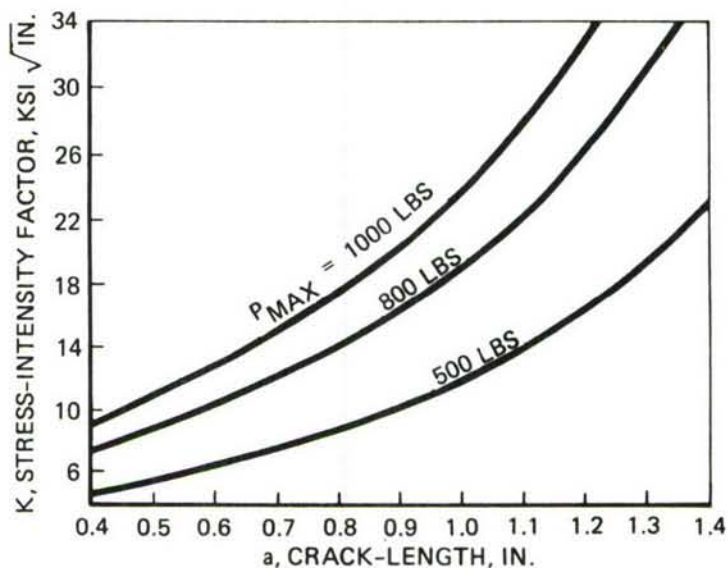
FIGURE 2. K RANGE FOR THE 0.063-IN. THICK SEN SPECIMENS AT THE THREE P_{MAX} VALUES TESTED

$$\text{OVERLOAD RATIO} = \frac{K_o}{K_{max}}$$

$$\% \text{ OVERLOAD} = \left(\frac{K_o - K_{max}}{K_{max}}\right) \times 100$$

K_o = Overload stress–intensity factor

K_{max} = Maximum stress–intensity during constant-amplitude cycling

ΔK = Constant-amplitude stress–intensity range

ΔK_o = Overload stress–intensity range

R = Constant-amplitude stress ratio

R_o = Peak stress ratio

N_c = Number of constant-amplitude cycles

N_o = Number of overload cycles
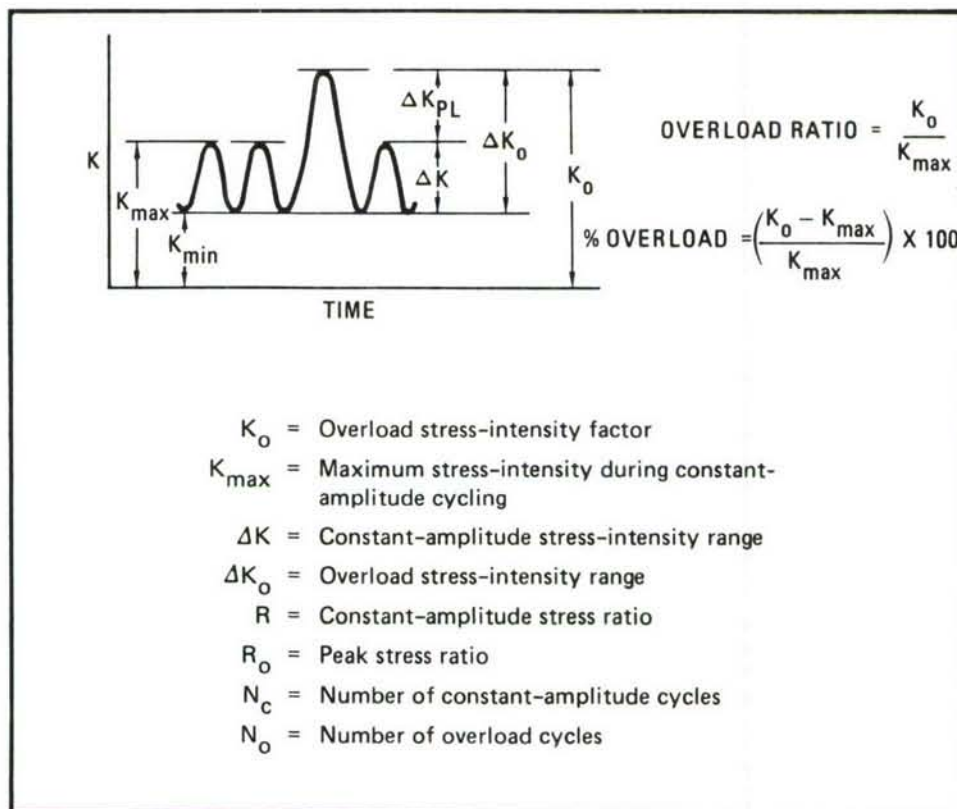
FIGURE 3. DEFINITION OF TERMS IN SINGLE PEAK OVERLOADING

TABLE I. MATRIX FOR RETARDATION TESTS
IN AIR AND 3-1/2% SALTWATER (SW)

OVERLOAD RATIO (K_O/K_{MAX})	P_{MAX} (LBS)	APPROX. K_{MAX} AT LOAD SPIKE (KSI $\sqrt{IN}$)			ENVIRONMENT
1.5	500	6	8	11	AIR, SW*
	800	10	14	20	AIR
	1000	12	17	24	AIR
2.0	500	6	8	11	AIR, SW*
	800	10	14	20	AIR
	1000		12	17	AIR
2.5	500	6	8	11	AIR, SW*
	800	10	14	20	AIR
3.0**	500	6	8	11	AIR

* SW TESTS AT 1 Hz; 2024-T8, 7075-T6, AND 7075-T73 ALLOYS ONLY.
** IF NO CRACK-ARREST AT 2.5.

TABLE II
SPECIMEN CODING SYSTEM

SPECIMEN NO. XT6ØL21

(X)	(T6)	(ØL)	(21)
TASK NO.	MATERIAL	TYPE OF TEST	SPECIMEN NO. 21 IN THIS SERIES

EXAMPLES:

SPECIMEN NO. DT6ØL11

(D)	(T6)	(ØL)	(11)
TASK D	7075-T6	OVERLOAD TESTS	SPECIMEN NO. 11 IN THIS SERIES

SPECIMEN NO. CT73CASW12

(C)	(T73)	(CASW)	(12)
TASK C	7075-T73	CONSTANT-AMPLITUDE SALTWATER	SPECIMEN NO. 12 IN THIS SERIES

simple electrolytic cell using the A2 (Disa-Electropol) solution as the electrolyte. The edges of the specimen were coated with a masking lacquer and the sample was electro-polished to a thickness of approximately 0.002-inch. Then, a section approximately 1/4-inch square was thinned by ion-milling. A stage cooled by liquid nitrogen was used to prevent overheating of the foil and the subsequent annealing out of the substructure. Milling was performed at a current density of 70 to 100 $\mu a/mm^2$ until a hole appeared in the foil. The foil was then observed in a Hitachi, HU-11A transmission electron microscope at 100 Kvp. Selected area diffraction (SAD) patterns were also obtained to determine the orientation of the foils and the precipitate morphology.

In specimens where a specific area was to be examined, such as an overload plastic-zone, as shown in Figure 4(a), electrical discharge machining (EDM) was used to obtain a 0.005-inch section from the area of interest. The remainder of the electro-polishing/ion-milling process was then followed.

For failed constant-amplitude, FCP, and retardation specimens, thin foils from the area immediately below the fracture surface of the failed specimens were obtained to determine the microstructural changes due to the overload cycles. For this purpose, thin foil specimens, as shown in Figure 4(b), were removed perpendicular and parallel to the fracture surface of a failed 7075-T6 specimen to determine directionality effects. Repetitive examination of foils prepared from the positions 1 and 2 for the 7075-T6 alloy did not reveal differences which would warrant preparing both areas. Hence, the position 2 foils were used for all the alloys and analyses because of the ease of prepa-ration and greater likelihood of obtaining a foil close to the fracture surface.

Figure 5 shows a flow chart summarizing specimen preparation from the original test coupons through sectioning (mechanical or EDM), electropolishing, final thinning by ion milling, and examination.

Szirmae and Fisher[20] have shown that EDM does result in a damage zone which is 7 to 15 μ deep (0.0003-inch to 0.0006-inch). Hence, a control evaluation was per-formed. A 7075-T6 S-N fatigue specimen ($K_t = 3$) was used to determine if EDM had caused changes in microstructure over and above any of those due to actual testing. A coupon approximately 0.375-inch by 0.006-inch by 0.060-inch was removed by EDM from a failed fatigue test (S-N) specimen. The sample was edge masked and electro-polished in the A2 solution until 0.0015-inch to 0.002-inch had been removed from both sides (a total removal of 0.003-inch to 0.004-inch). The remaining foil was then
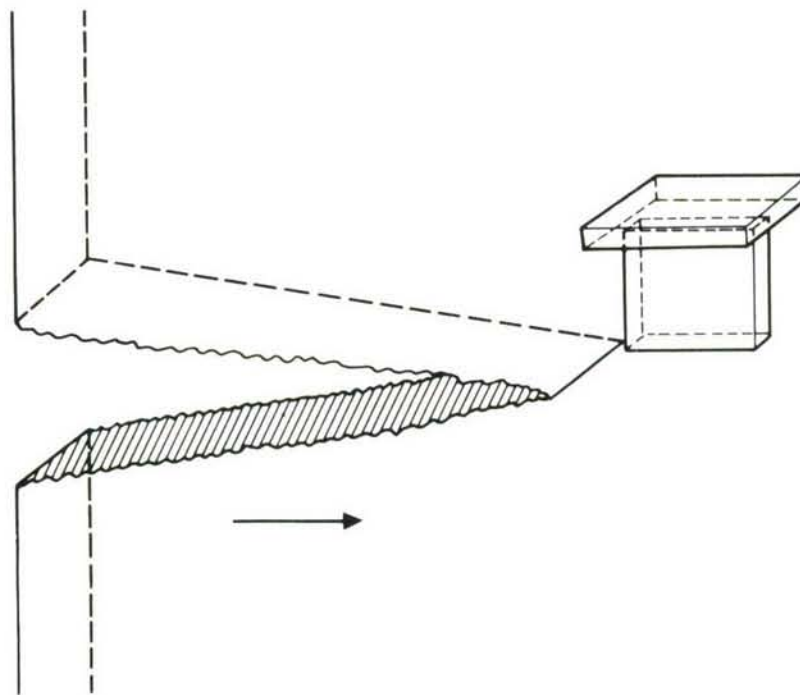
(a) FOR CHARACTERIZATION OF PLASTIC ZONE

POSITION 1, PERPENDICULAR
TO FRACTURE SURFACE

POSITION 2, PARALLEL TO
FRACTURE SURFACE
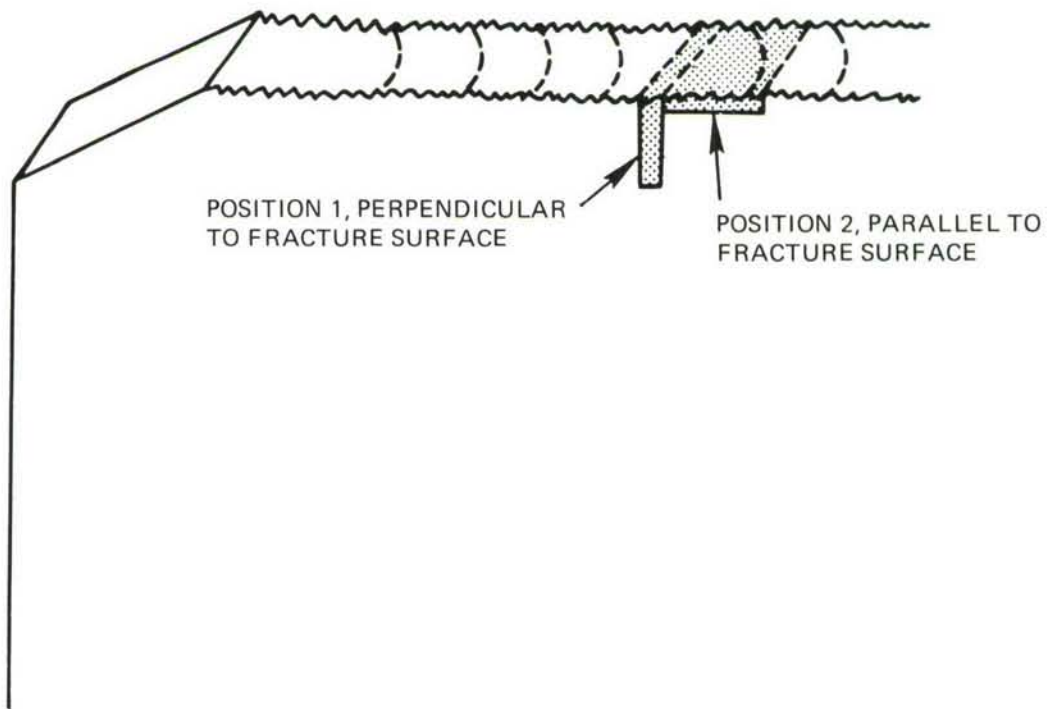
(b) FOR FAILED FCP AND RETARDATION SPECIMENS

FIGURE 4. POSITIONS FOR THIN FOIL REMOVAL FROM TEST SPECIMENS

EDM — ELECTRICAL
DISCHARGE
MACHINING

MECHANICAL SECTIONING

ELECTROPOLISHING

ION MILLING

ELECTRON DIFFRACTION

SUBSTRUCTURE
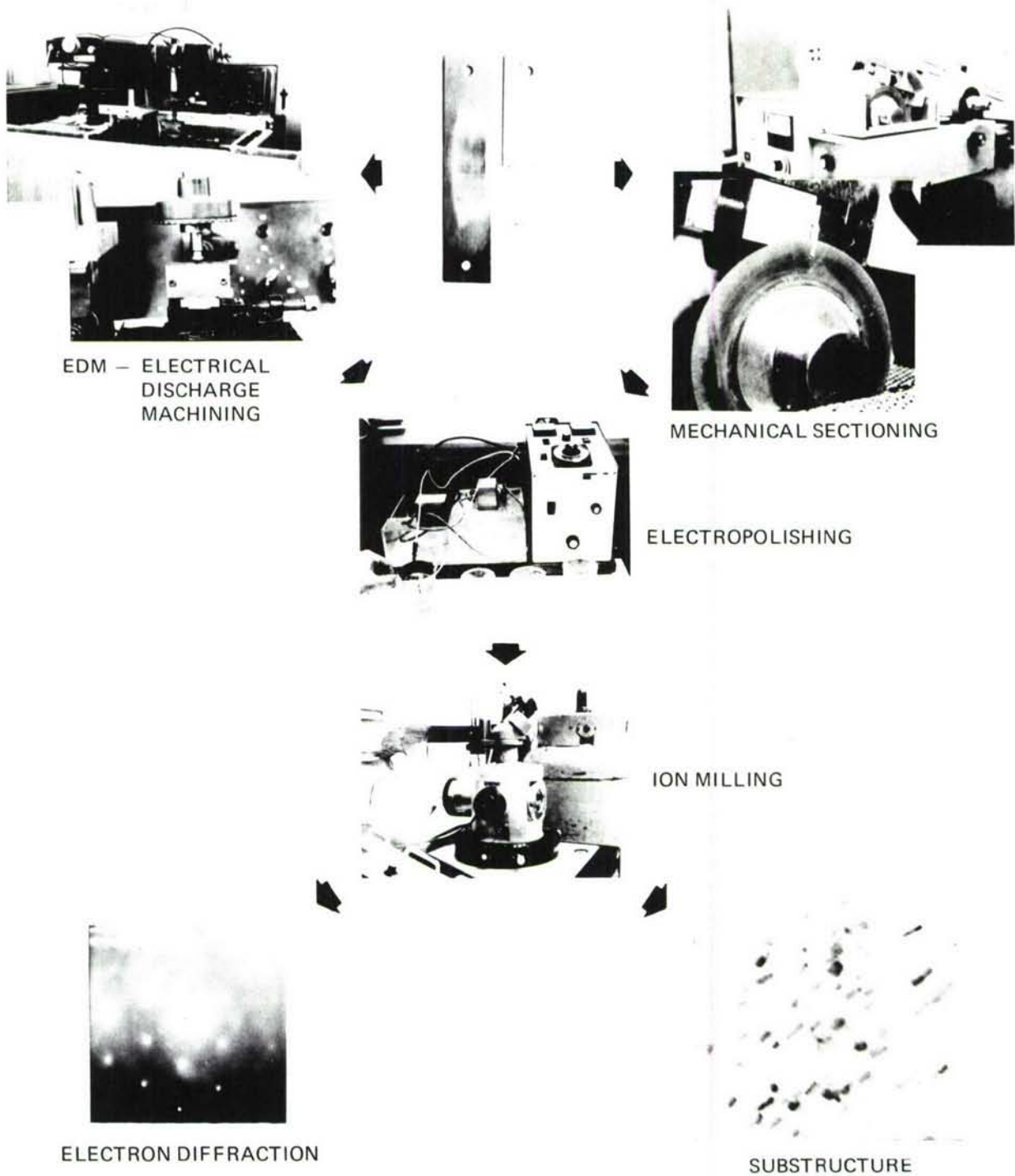
FIGURE 5. PREPARATION PROCEDURE FOR TEM FOILS

ion-milled until a hole was observed in the foil. Examination of foils with and without EDM processing showed similar microstructural characteristics. It was concluded from this series of examinations that any possible damage due to EDM was removed during electropolishing before final thinning by ion milling.

3. INTERFERENCE MICROSCOPY

A Zeiss interference microscope with a thallium spectrum lamp was used to observe the surface plastic-zone size and strain distribution at the crack-tip for all three thicknesses of the four alloys. With this procedure, one can measure thickness or flatness changes as small as 0.03μ (300Å). Interference patterns were obtained from selected specimens (1) immediately after the overload cycle, (2) when the crack was halfway through the plastic-zone, and (3) when the crack was beyond the plastic-zone. The final polishing of the SEN specimens after grinding with 600 grit paper, particularly for the relatively soft 2024-T3 alloy, is critical in obtaining interference fringes satisfactory for this work. Electropolishing was found to be unsuitable for this purpose. A 2-stage final polishing with 0.3μ and 0.5μ alumina slurry on the polishing wheels was found to produce a satisfactory mirror-like surface finish with no undesirable surface distortion.

D. FRACTOGRAPHY

The fracture surfaces were examined with an optical microscope at magnifications up to 200X and with a Cambridge S4-10 Scanning Electron Microscope at magnifications up to 10,000X. The fracture surfaces were cleaned by placing and stripping off replicating tapes, and then gold-shadowed before SEM investigation.

14

III. RESULTS AND DISCUSSION

A. BASELINE CHARACTERIZATION

1. TENSILE BEHAVIOR

Table III lists the tensile properties of the four alloys obtained from both 0.063-inch thick sheets and 0.5-inch thick plates. All of the retardation work except for the investigation to determine the effect of thickness as well as compressive load on retardation behavior was performed on the 0.063-inch thick material. Hence, unless otherwise stated, all of the results and discussions in this report refer to the 0.063-inch thick specimens.

TABLE III. TENSILE PROPERTIES OF THE ALUMINUM ALLOYS

ALLOY AND HEAT TREATMENT	THICKNESS (IN.)	0.2% Y.S. KSI	U.T.S. KSI	% ELONGA-TION	MONOTONIC STRAIN HARDENING EXPONENT	CYCLIC HARDENING EXPONENT
7075-T6	0.063	73.1	80.2	12.5	0.071	- -
7075-T651	0.50	72.8	78.5	12.6	- - -	0.07
7075-T73	0.063	60.8	71.2	12.3	0.133	- -
7075-T7351	0.50	64.6	74.3	15.0	- - -	0.09
2024-T3	0.063	51.7	68.3	18.6	0.163	- -
2024-T351	0.50	52.4	66.3	18.8	- - -	0.06
2024-T8	0.063	61.2	68.3	10.0	0.083	- -
2024-T851	0.50	70.4	75.3	10.3	- - -	0.13

Note 1: For 0.063-inch thick sheet, flat specimens of 2-inch gage-length were used, while for 0.50-inch thick plate, cylindrical specimens of 1-inch gage-length were used.

Note 2: The reported values are average of three tests.

The monotonic strain hardening exponents for all four conditions listed in Table III were determined by obtaining true stress-strain curves and using the following relationship:

$$\sigma = S\epsilon^n \tag{1}$$

where

σ = true stress,

ϵ = true strain,

S = strength coefficient, and

n = strain-hardening exponent.

15

Since the 0.25-inch thick specimens were obtained by machining the 0.5-inch thick plates, their tensile properties are essentially the same as those for the 0.5-inch thick specimens. The yield and tensile strengths of both the thick (0.25-inch and 0.5-inch) and thin (0.063-inch) material were generally within 5% of each other for three of the four alloys investigated. A significant difference (13%) in the yield strength was found between the thick and thin sections of the 2024-T8 alloy. The implications of this difference in yield strength on the retardation behavior of different thicknesses of 2024-T8 alloy are discussed later on.

2. CYCLIC STRESS-STRAIN BEHAVIOR

Figure 6 shows the cyclic stress-strain curves for all four alloys obtained by the use of the incremental step method. This method has been shown to be in excellent agreement with the conventional method in which the cyclic stress-strain curve is obtained by joining the tips of stable hysteresis loops for several comparison tests at different constant strain amplitudes[18]. The cyclic hardening exponents are listed in Table III.

The cyclic hardening exponent, n', is defined by the following power relationship between cyclic stress and plastic strain range:

$$\sigma_a = K' \left(\frac{\epsilon_p}{2} \right)^{n'} \tag{2}$$

where

σ_a = stable stress amplitude,

$\epsilon_p/2$ = stable plastic strain amplitude,

n' = cyclic strain hardening exponent, and

K' = cyclic strength coefficient

As seen in Table III, the 2024-T8 alloy has a completely different cyclic hardening exponent from the other materials. The cyclic hardening exponent apparently influences the plastic-zone size because, as described later, the plastic-zone measured by interferometry for the 0.063-inch 2024-T8 specimen was smaller than that for the 0.063-inch thick 7075-T73, even though they both had the same yield strength. The

16
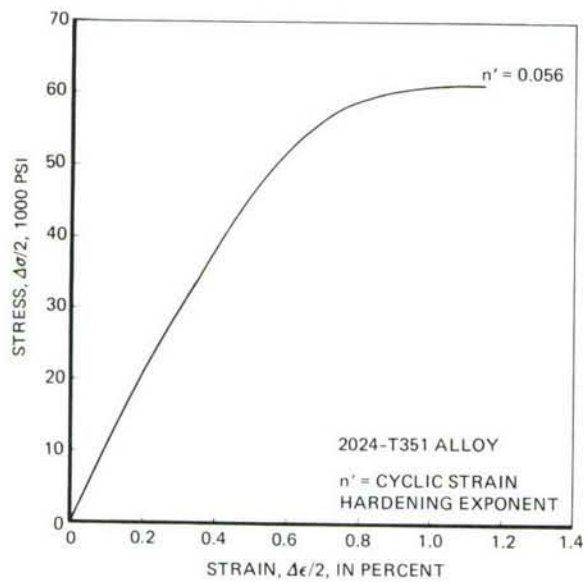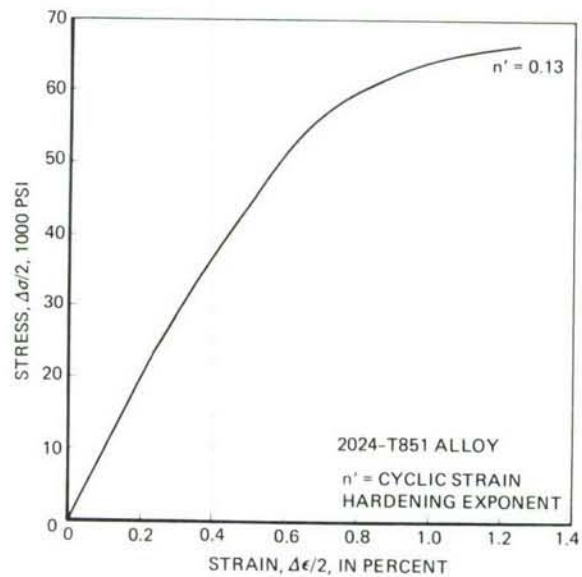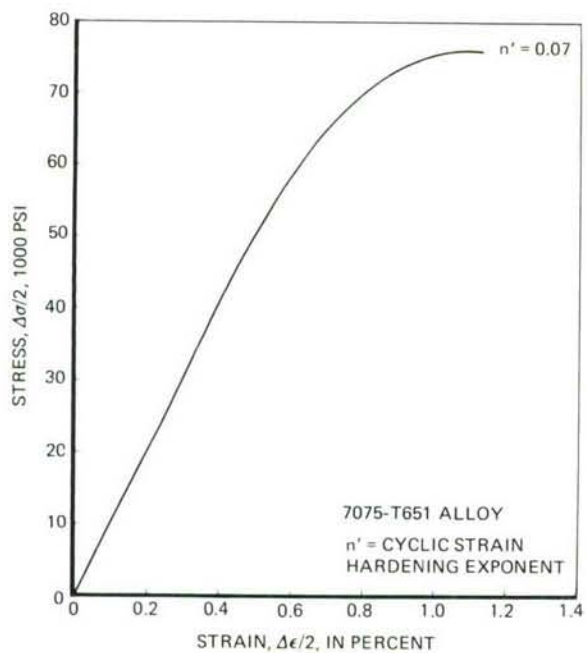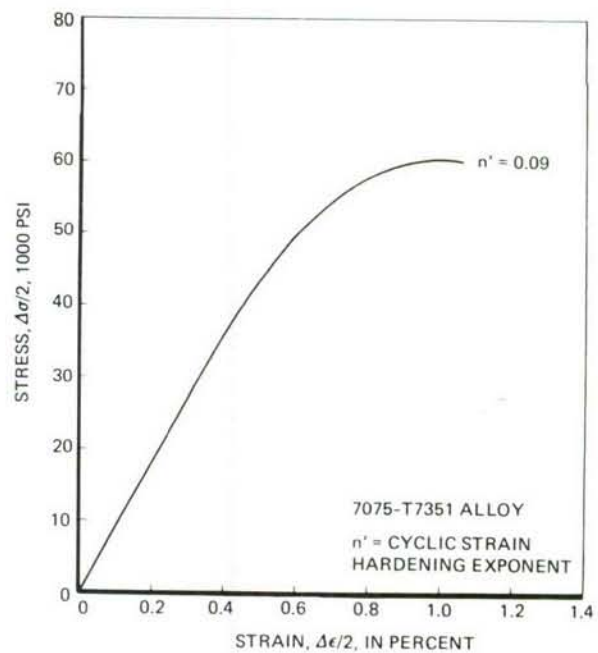
FIGURE 6. CYCLIC STRESS-STRAIN CURVES FOR THE 2024 AND 7075 ALLOYS

reason for the different value of the cyclic hardening exponent is probably due to the nature of the precipitates in the 2024-T8 alloy. The 2024-T8 has an extensive amount of S' precipitates on crystallographic planes rather than GP zones as in 2024-T3 or η' as in the 7075-T6 and T73 alloys. The resultant difference in precipitate-dislocation interaction is probably responsible for the difference in cyclic hardening exponents.

3. FRACTURE BEHAVIOR

The fracture behavior of all four alloys was determined using 0.063-inch SEN specimens. In these tests, the load-displacement curves showed a large amount of plasticity due to the thinness of the specimens. The problem in characterizing fracture behavior of a specimen showing curves with large plasticity is of theoretical as well as practical interest. The nature and extent of plasticity, crack extensions, and instability increase the complexity of the problem. A large amount of stable crack-growth can occur for a given material under these conditions. The behavior of a typical crack-growth curve is shown schematically in Figure 7. The calculations of stress-intensity factors for this geometry are performed as follows[21].

$$K = \frac{Pa^{1/2}}{BW} f(a/W) \tag{3}$$

where

$$
\begin{aligned}
P &= \text{load,} \\
B &= \text{thickness,} \\
W &= \text{width, and} \\
f(a/W) &= 1.99 - 0.4124 \ (a/W) \\
&\quad + 18.70 \ (a/W)^2 - 38.48 \ (a/W)^3 \\
&\quad + 53.85 \ (a/W)^4
\end{aligned}
$$

A typical load versus displacement record obtained for the 2024-T8 alloy is shown in Figure 8. We can see from Figures 7 and 8 that there are at least three significant points that can be used to characterize the crack-growth process in these materials:

1. The K_{C5} based on 5% offset according to ASTM recommendations:

$$K_{C5} = \frac{P_5 \ a_o^{1/2}}{BW} f(a/W)$$
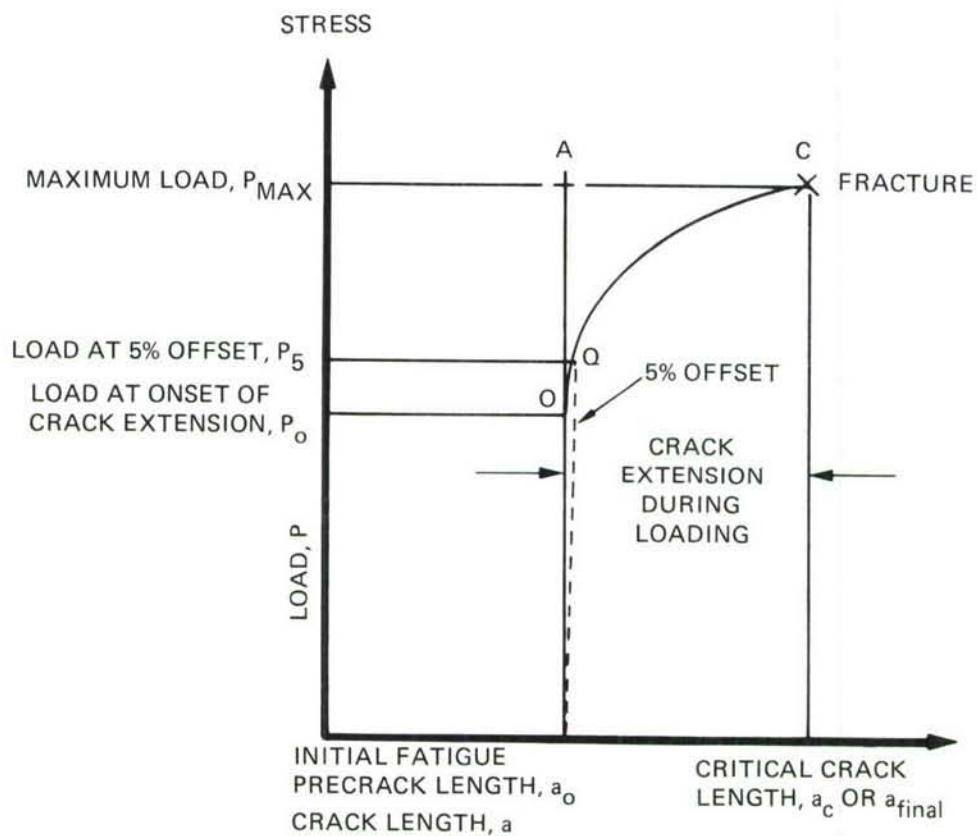
FIGURE 7. SCHEMATIC OF CRACK-GROWTH BEHAVIOR IN PLANE STRESS CONDITION
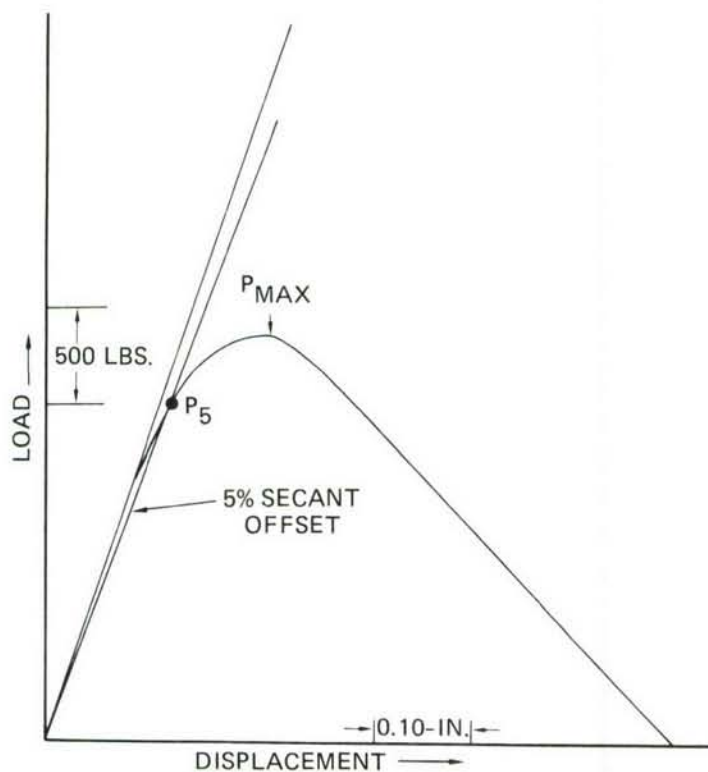
FIGURE 8. LOAD-DISPLACEMENT RECORD USING CLIP-ON GAGE
FOR A 0.063-IN. SEN SPECIMEN OF 2024-T8 ALLOY

19

where

$$a_o = \text{initial crack-length}$$

$$P_5 = \text{load at 5\% offset.}$$

2. The K_{max} based on maximum load (point C in Figure 7) and initial crack length:

$$K_{max} = \frac{P_{max} \, a_o^{1/2}}{BW} \, f(a/W)$$

3. The $K_{critical}$ based on the maximum load and instantaneous crack-length (a_{final} or a_c):

$$K_{critical} = \frac{P_{max} \, a_{final}^{1/2}}{BW} \, f(a/W)$$

Table IV summarizes all of the fracture results. These results were utilized to establish the stress-intensity factor range used during the retardation tests. The plane-stress fracture toughness values measured this way are representative only for the geometry and thickness used in this investigation.

TABLE IV. PLANE-STRESS FRACTURE TOUGHNESS PARAMETERS FOR 0.063-IN. THICK SEN ALUMINUM SPECIMENS (2.5-INCH WIDE, 11.75-INCH LONG)

ALLOY & HEAT TREATMENT	SPEC. IDENT. NO.	CRACK LENGTH INCH		LOAD, LBS.		MATL. TOUGHNESS, KSI $\sqrt{\text{IN.}}$			NET STRESS RATIO		
		INITIAL	FINAL	5% OFF-SET, P_5	MAX., P_{MAX}	K_{C5}	K_{MAX}	$K_{CRITICAL}$	R_{C5}	R_{MAX}	$R_{CRITICAL}$
7075-T6	BT6KCQ3	0.84	0.998	2375	2750	42.9	51.9	64.9	0.31	0.25	0.40
	BT6KCQ4	0.84	0.998	2175	2725	41.0	51.4	64.4	0.28	0.36	0.40
					Avg.	41.9	51.7	64.7			
7075-T73	BT73KCQ3	0.84	1.077	2250	2825	42.4	53.2	75.7	0.35	0.44	0.52
	BT73KCQ4	0.84	1.1025	1950	2925	36.8	55.1	81.6	0.31	0.45	0.55
					Avg.	38.4	54.2	78.7			
2024-T3	BT3KCQ1	0.84	1.078	1850	2750	34.8	51.7	73.7	0.34	0.51	0.59
	BT3KCQ2	0.84	1.14	1750	2650	33.0	49.9	78.5	0.32	0.49	0.60
					Avg.	33.9	50.8	76.1			
2024-T8	BT8KCQ2	0.84	1.003	1625	1925	30.5	36.3	45.8	0.21	0.30	0.33
	BT8KCQ3	0.84	1.033	1750	2125	33.0	40.1	53.0	0.27	0.33	0.38
					Avg.	31.8	38.2	49.4			

P_{MAX} = Maximum load from the load-displacement record

P_5 = Load at 5% offset

K_{C5}, R_{C5} = Based on P_5 and the initial crack-length

K_{MAX}, R_{MAX} = Based on the maximum load and the initial crack-length.

$K_{CRITICAL}$, $R_{CRITICAL}$ = Based on the maximum load and instantaneous crack length

4. CONSTANT AMPLITUDE FCP BEHAVIOR

Constant-amplitude fatigue-crack propagation tests were performed in both air and saltwater to serve as a reference state from which to evaluate the effect of overload cycles on fatigue-crack propagation. Furthermore, these tests provide constant-amplitude FCP data needed to predict fatigue-crack growth behavior under spectrum loading using analytical models. Figure 9 shows the FCP results for all four micro-structures in both air and saltwater environments. As expected, the FCP rates in saltwater were much faster than those in the air. Figure 10 shows the trend of the FCP curves for all four cases, both in air and saltwater. The 2024 alloy showed a somewhat higher fatigue-crack growth resistance compared to the 7075 alloy. In air, the 7075-T73 and 2024-T3 alloys exhibited FCP properties better than those for the 7075-T6 and 2024-T8, respectively. In saltwater, the difference in the FCP behavior of the four conditions was maximum at the intermediate and low crack-growth rates. The 2024-T3 alloy was the superior alloy in the saltwater environment.

5. MICROSTRUCTURAL CHARACTERIZATION

As-Received Material

Both optical and transmission electron microscopy (TEM) techniques were used for this purpose. The optical microstructures for all four conditions in both the longitudinal and transverse orientations are shown in Figures 11 and 12. Thin foils of all four alloys were also investigated by TEM. The results are described below.

2024 Alloy:

The 2024 alloy is an aluminum-copper-magnesium based age hardening alloy. The basic hardening mechanisms are associated with those occurring in the Al-Cu binary system. The magnesium addition accelerates and intensifies the natural aging. Because of this, one less intermediate transition structure is observed. The sequence of precipitation in the 2024 alloy in a simplified form is as follows: G.P. zones rich in Mg and Cu atoms on the (100) Al planes $\longrightarrow$ S' platelets on (021) Al planes $\longrightarrow$ equilibrium S phase. The S phase is Al_2CuMg, while S' is its transition phase.

Figure 13 (a) shows an area of G.P. zones with isolated large precipitates of Al_2O_3 and S in the 2024-T3 alloy. The "black dots" are the G.P. zones. Small areas of pinned dislocations are evident. The selected area diffraction (SAD) pattern showed the Al matrix and scattered diffraction effects from the G.P. zones. Figure 13 (b) shows fine substructure cell development and precipitates of S' and S. A few dislocations are pinned in the fine cellular structure. The material is considered representative of commercially available 2024-T3 sheet.
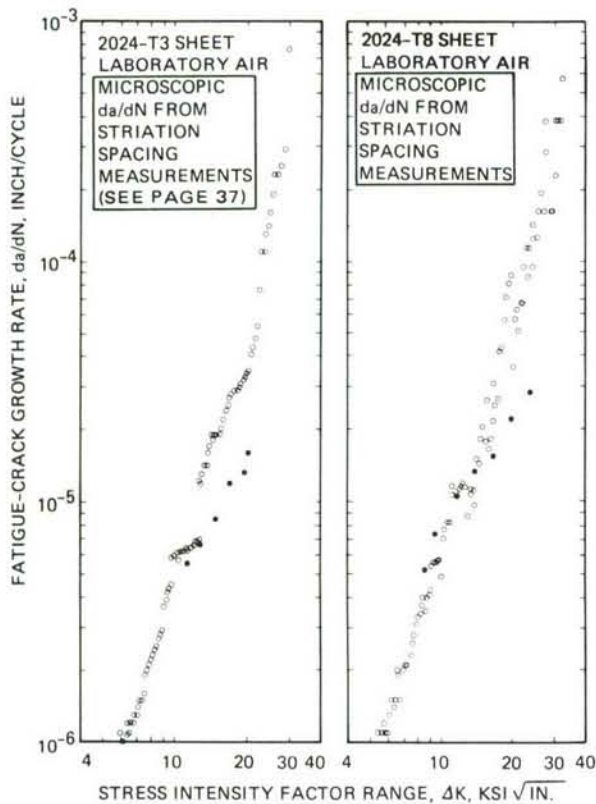
(a) 2024 ALLOY IN AIR
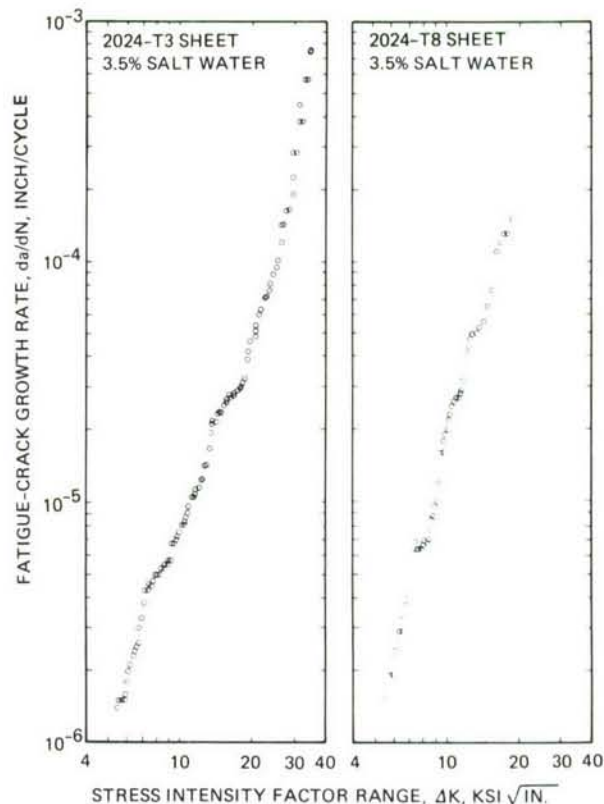
(b) 2024 ALLOY IN SALT WATER
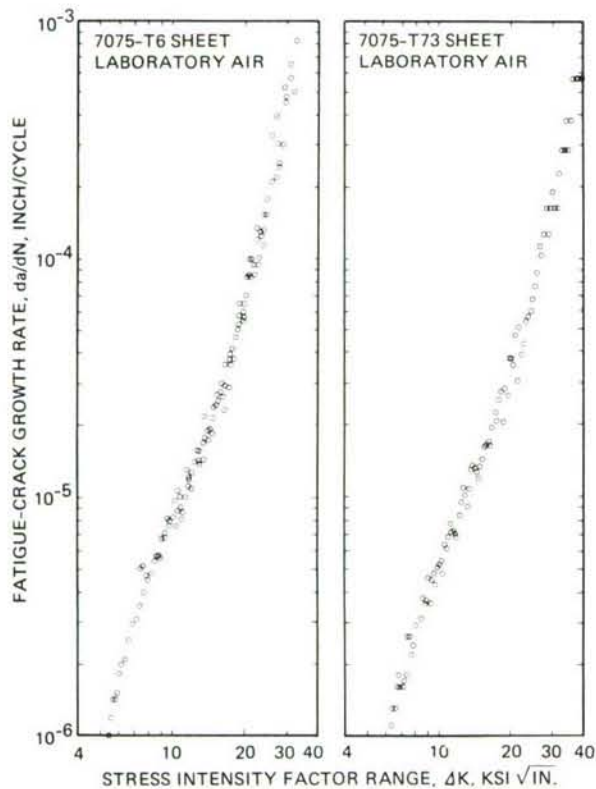
(c) 7075 ALLOY IN AIR
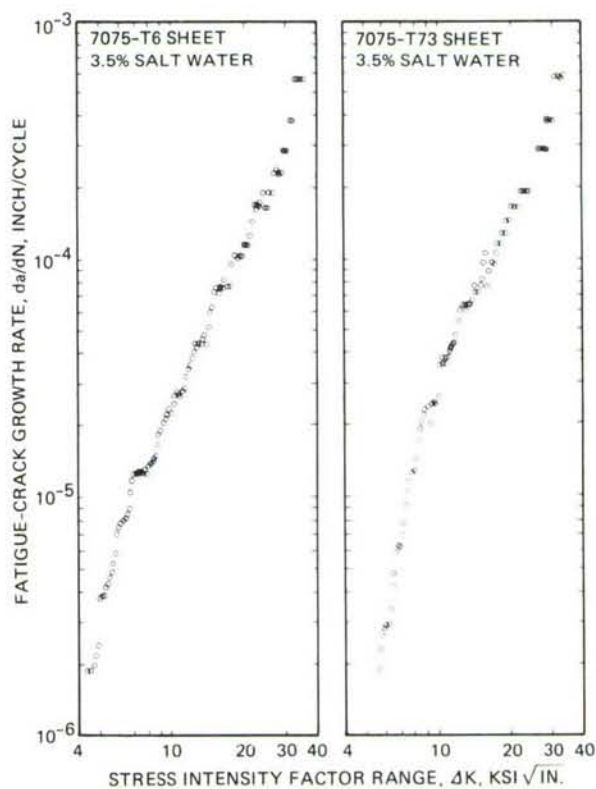
(d) 7075 ALLOY IN SALT WATER

FIGURE 9. FCP BEHAVIOR OF 2024 AND 7075 ALLOYS IN AIR AND SALT WATER AT R = 0.1 USING 0.063-IN. THICK SEN SPECIMEN IN LT ORIENTATION

22

FATIGUE-CRACK GROWTH RATE, da/dN, INCH/CYCLE

10⁻³

2024-T3 —·—·—
2024-T8 ··········
7075-T6 ————
7075-T73 — — —

LAB AIR
ENVIRONMENT

R = 0.1

2024-T3 —·—·—
2024-T8 ··········
7075-T6 ————
7075-T73 — — —

3.5% SALT
WATER
ENVIRON-
MENT

R = 0.1

10⁻⁴

10⁻⁵

10⁻⁶

4   10   20   30 40   4   10   20   30 40

STRESS INTENSITY FACTOR RANGE, ΔK, KSI √IN
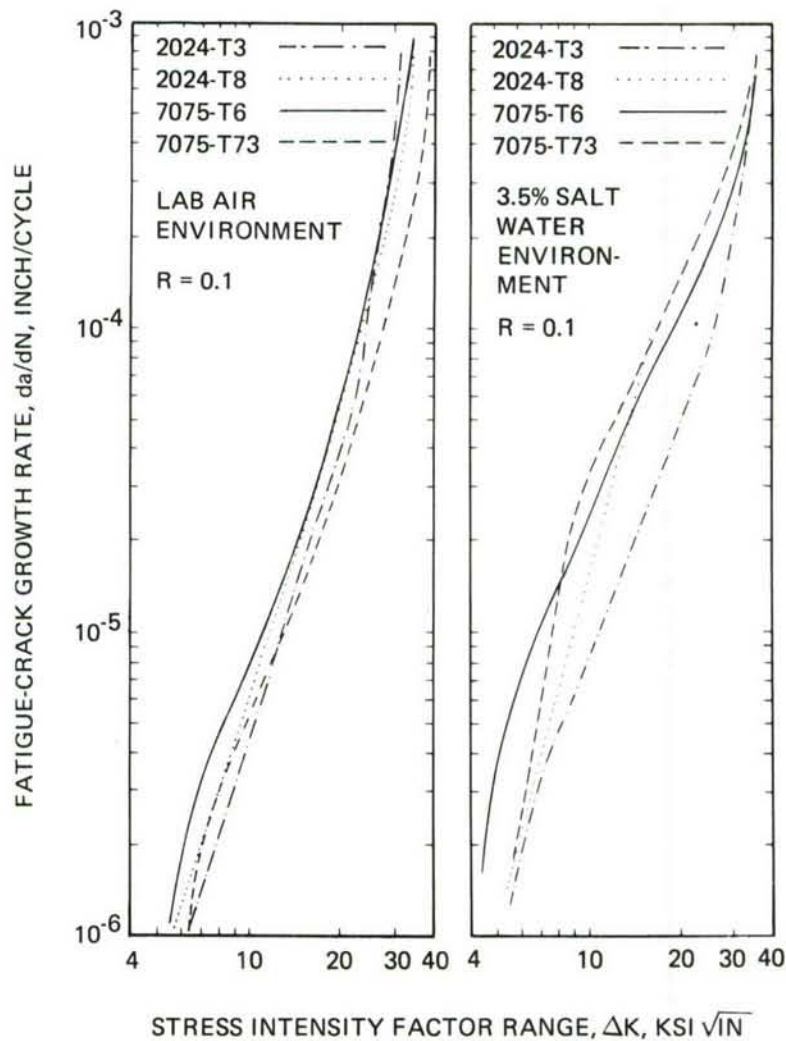
FIGURE 10. GENERAL TREND OF FCP BEHAVIOR FOR ALL FOUR CONDITIONS

A part of the as-received 2024-T3 stock was aged to the T8 condition of the same yield strength as that of the 7075-T73 material. Figure 13 (c) shows the precipitate structure of the S' hardening phase. A grain boundary is evident. The orientation of the precipitate is a function of grain orientation. This area of the foil is somewhat unusual in that no dispersoids are visible. The SAD pattern shows the Al matrix and the S' precipitate. Broad diffuse diffraction spots are reflective of the fine S' precipitates. Figure 13 (d) shows large amounts of dispersoids $(Al_{20}Cu_2Mn_3)$ as well as S' in the background. The grain boundary precipitate seen in this micrograph is most probably the equilibrium S phase. The microstructure is considered normal for the T8 condition of the 2024 alloy.
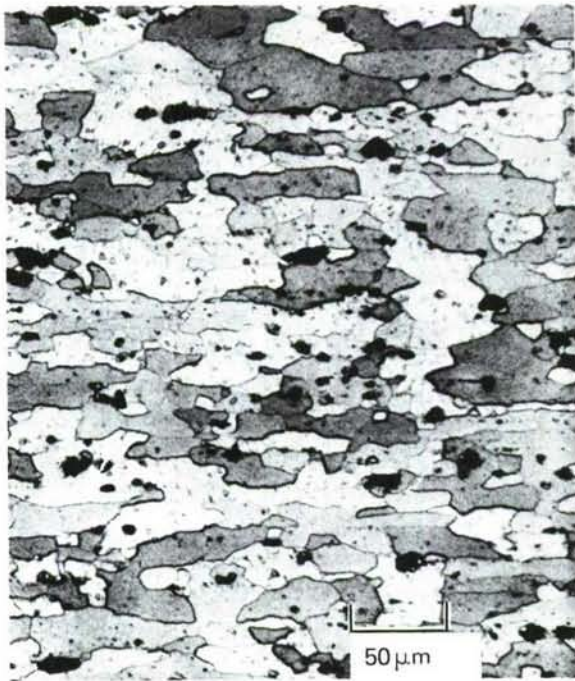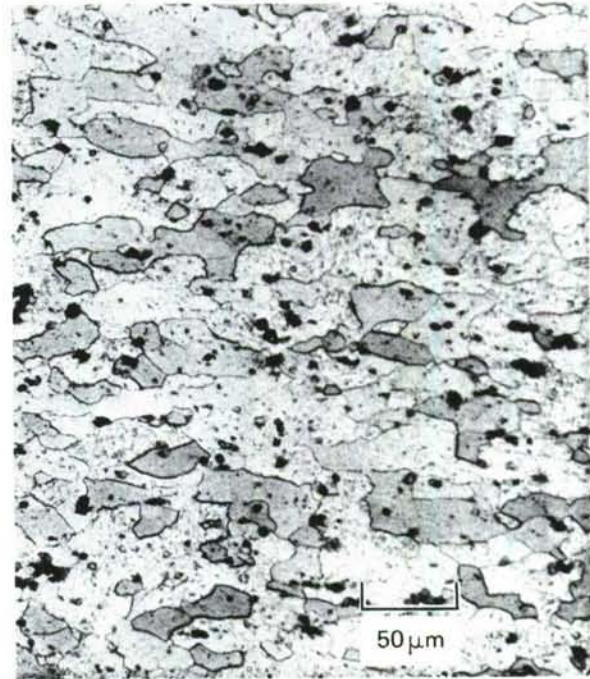
LONGITUDINAL VIEW TRANSVERSE VIEW

(a) 2024-T3 ALLOY
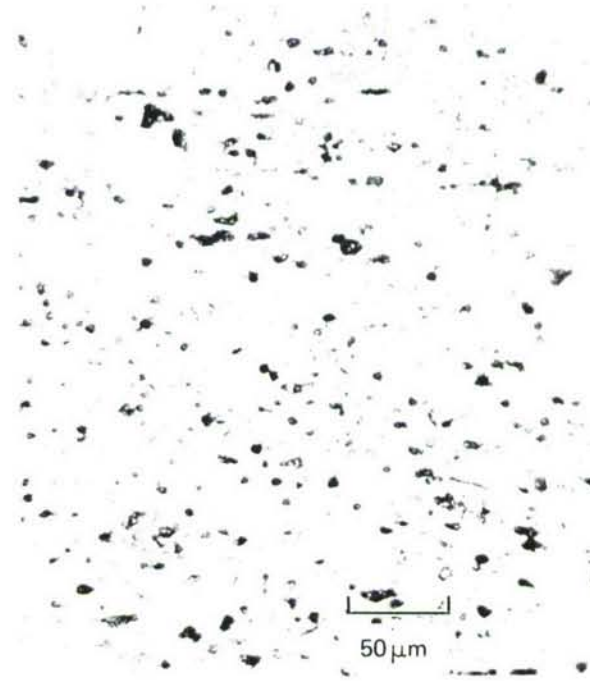
LONGITUDINAL VIEW TRANSVERSE VIEW

(b) 2024-T8 ALLOY

FIGURE 11. MICROSTRUCTURE OF THE 2024 ALLOY — KELLER'S ETCHANT
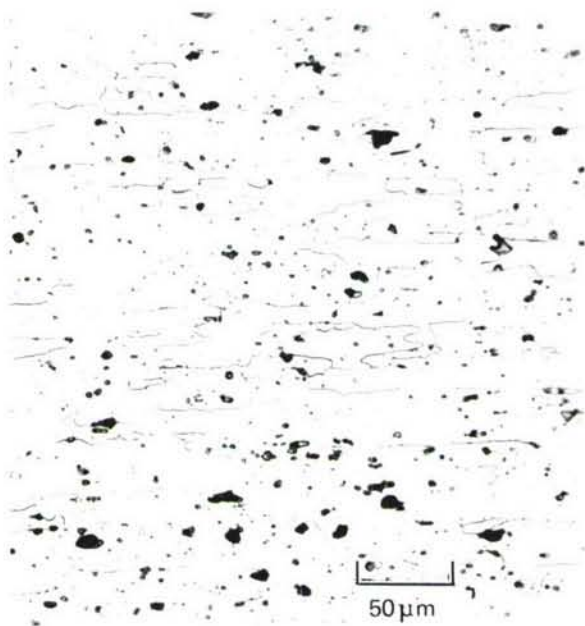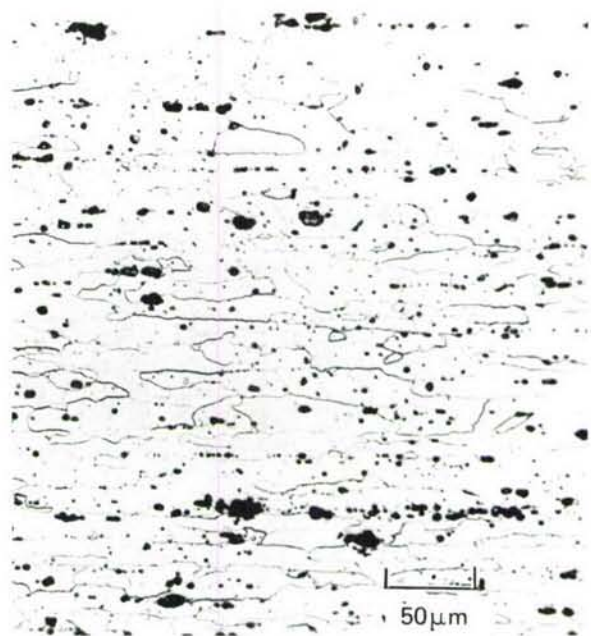
LONGITUDINAL VIEW   TRANSVERSE VIEW

(a) 7075–T6 ALLOY
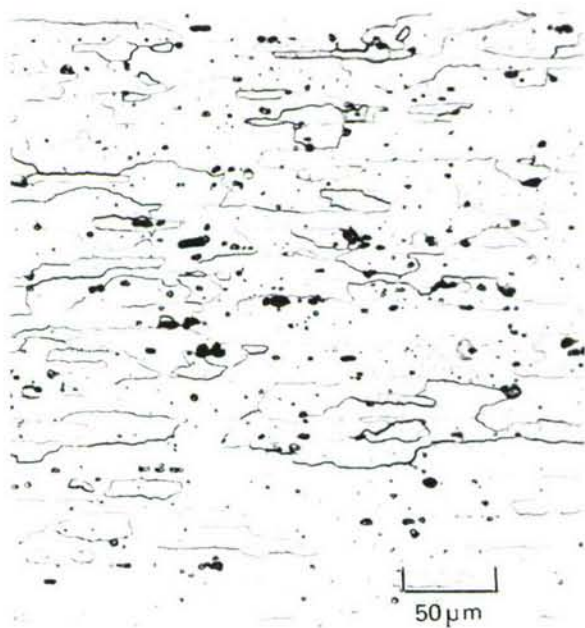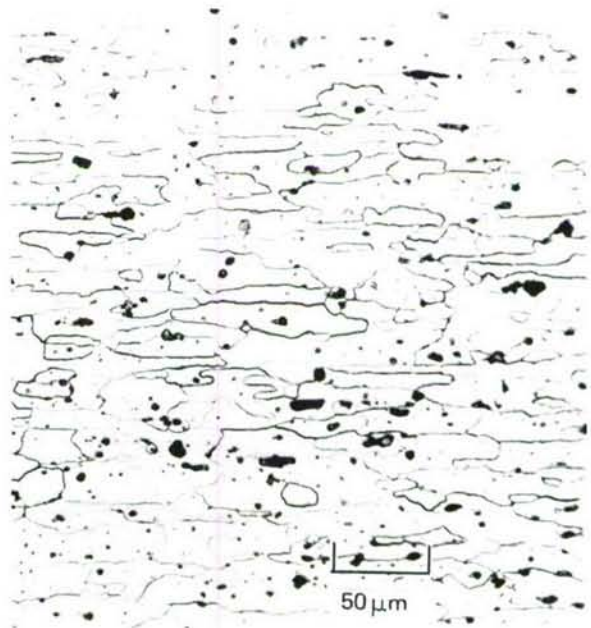
LONGITUDINAL VIEW   TRANSVERSE VIEW

(b) 7075–T73 ALLOY

FIGURE 12. MICROSTRUCTURE OF THE 7075 ALLOY — KELLER'S ETCHANT
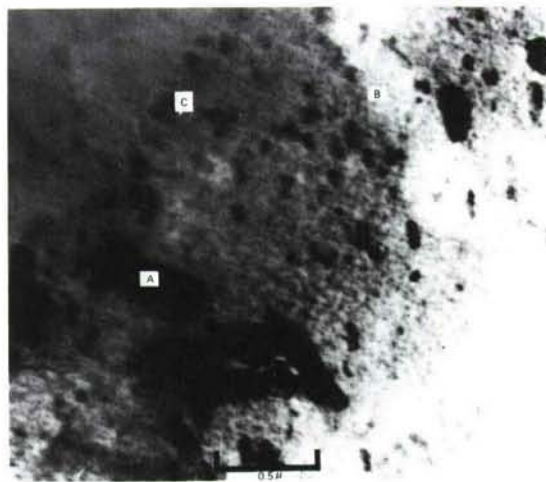
(a) 2024–T3 SHOWING Al_2O_3 (A),
G.P. ZONES (B), AND S' (C)
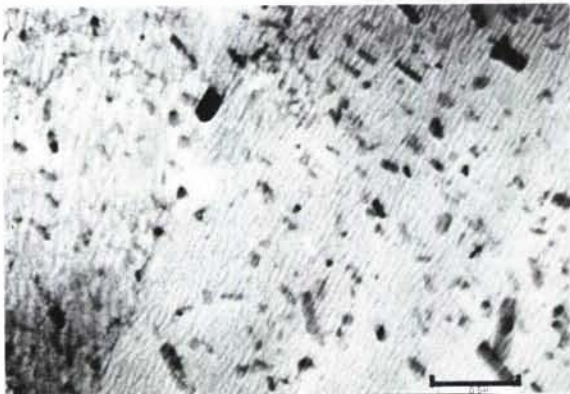
(b) 2024–T3
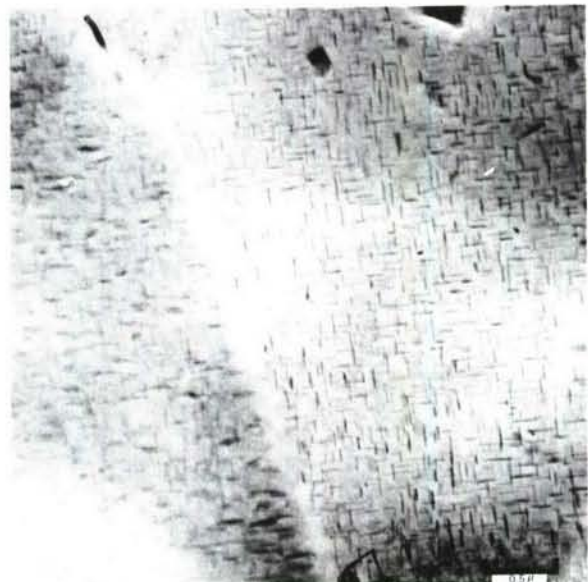
(c) 2024–T8 SHOWING S'
PRECIPITATES
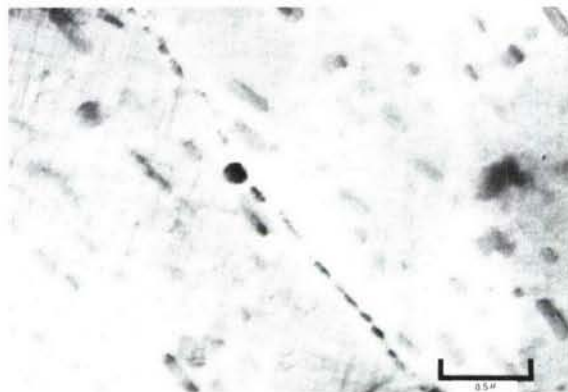
(d) 2024–T8 SHOWING DISPERSOIDS,
S', AND GRAIN BOUNDARY
PRECIPITATION OF S'

FIGURE 13. SUBSTRUCTURE OF BOTH 2024 HEAT TREATMENTS

26

7075 Alloy:

The 7075 alloy is one of the Al-Zn-Mg type. Strengthening in this alloy is due to the precipitation of the η' (transition phase of Mg $(Zn, CuAl)_2$) and the dispersoid phase. Neither of these phases is specifically documented as to crystal structure type, but standard diffraction patterns are catalogued in the ASTM card file index. This enables electron diffraction correlation with thin foils. The normal reported sequence of precipitation in this alloy, in simplified terms, is G.P. zones rich in Mg and Zn on the (111) Al planes $\longrightarrow \eta'$ transition phase $\longrightarrow \eta$. Commercial alloys generally contain significant amounts of Cu. With Cu present, $CuAl_2$ and Al_2CuMg phases can also be detected. The principal hardening phase, however, is the η' phase.

The as-received 7075-T6 condition is revealed in Figure 14 (a). Figure 14 (a) shows primarily η' precipitates and dispersoids. The needle-like structure was identified by SAD as η'. No evidence of dislocation structure was seen.

The 7075-T73 alloy in the present investigation was obtained by aging a portion of the as-received 7075-T6 stock. Since this is an over-aged condition, the precipitate size and distribution would be expected to be greater than in the T6 condition. Figure 14 (b) shows two areas relatively high in η' phase. Traces of the dispersoid phase were also detected.

The observed substructures of 7075-T6 and T73 alloys are representative of typical commercial materials.

Failed FCP Test Specimens

The metallurgical and substructural changes due to constant-amplitude FCP were investigated by obtaining thin foils from the area immediately below the fracture surfaces of failed specimens. These studies indicated the effects of microstructure and composition on FCP behavior and provided baseline data for retardation studies. These studies were used to determine and understand the microstructural changes occurring due to the overload cycle during retardation tests as compared to those occurring due to constant-amplitude load cycles. Electron fractography, as described in the next section, was performed on the fracture faces to show a two-dimensional effect of striation character and propagation phenomena.

The existence of G.P. zones and precipitates in the Al-Cu alloy system tends to inhibit the formation of distinct slip markings and dislocation-cell structures. No overwhelming evidence of distinctive cellular formation or operative slip mechanisms
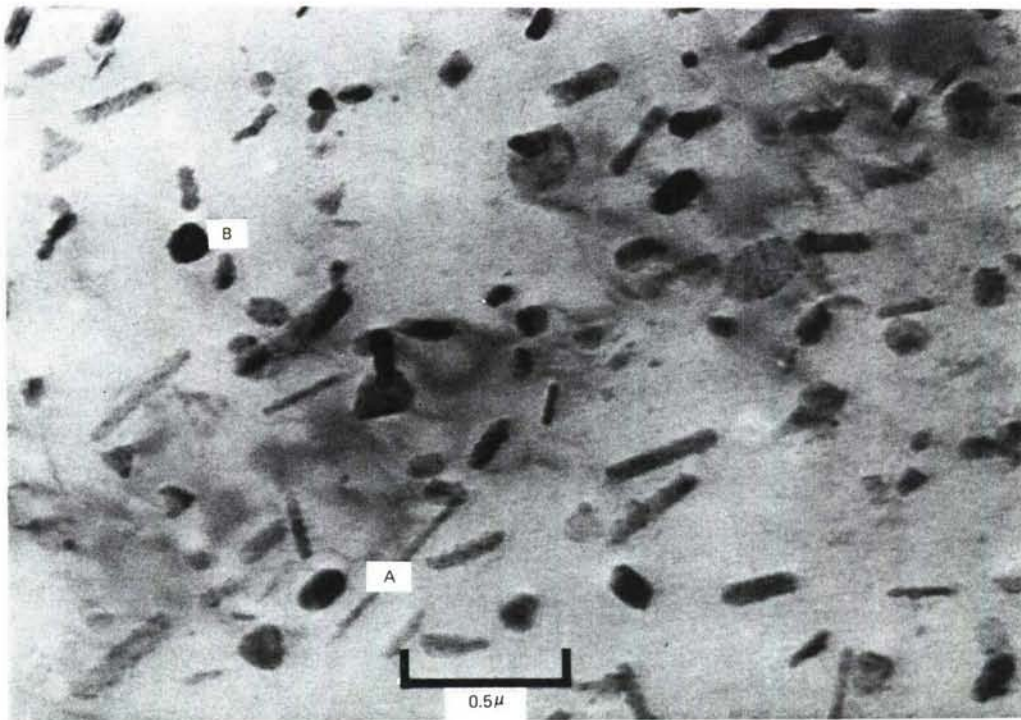
(a) 7075-T6
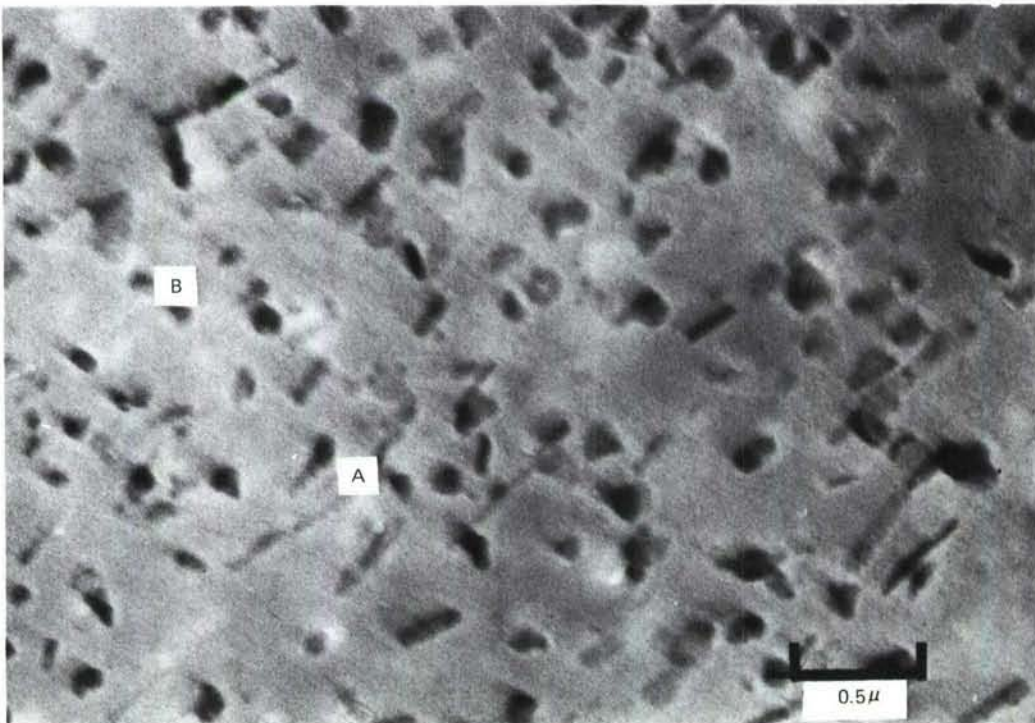
(b) 7075-T73

FIGURE 14. SUBSTRUCTURE OF 7075-T6 AND T73 SHOWING
η' (A) AND DISPERSOID (B)

was observed in the FCP baseline foils examined. The mechanism of fatigue in both the 2024 and 7075 alloys is greatly influenced by the presence of dispersoids, hardening precipitate phase, and constituent particles [22-24]. The nucleation of cracks at constituent particles is most likely the result of dislocation pile-up at the inclusions. Under alternating stress, pile-ups will occur on both sides of an inclusion and give rise to fresh crack initiation. Deformation is primarily one of limited dislocation movement due to the presence of large amounts of precipitates and dispersoids. The mean free path of dislocations would be too small to allow formation of finite cell structure. Hence, one can expect large concentrations of dislocation loops and forests along the crack propagation path.

2024-T3 Alloy:

The observation of foils parallel to the fracture surface in this alloy revealed many dislocation interactions with the various second phase particles such as shown in Figure 15 (a), where dislocation pile-ups occurred around a rather large dispersoid particle. Evidence of grain boundary dislocation pile-up was seen in Figure 15 (b). G.P. zones and equilibrium S particles at grain boundaries as well as in the matrix were also visible. Isolated, pinned dislocations were seen attached to the S particles (Figure 15 (c)). Dislocation tangles and dislocation loops along probable slip planes were also evident. As already mentioned, the deformation at the crack-tip is primarily one of limited dislocation movement due to the presence of various types of particles. Microcracks grow either by a ripple mechanism or by a more complex combination of ductile and cleavage mechanisms. The general character of the fracture surface as reported in the next section indicated a more ductile type of propagation for the T3 condition as compared to the T8 condition. This may be explained in terms of the amount and concentration of precipitate particles, the T8 having a greater amount of precipitates which are primarily S'. The G.P. zones in the T3 condition could pin dislocations but would still allow a greater degree of freedom for dislocation movement.

2024-T8 Alloy:

Examination of foils from position 2 in Figure 4 (b) showed more substructural interactions in the T8 condition as a result of FCP than in the T3 condition. Evidence of an increased density of S' precipitates was seen. The fine acicular structure was
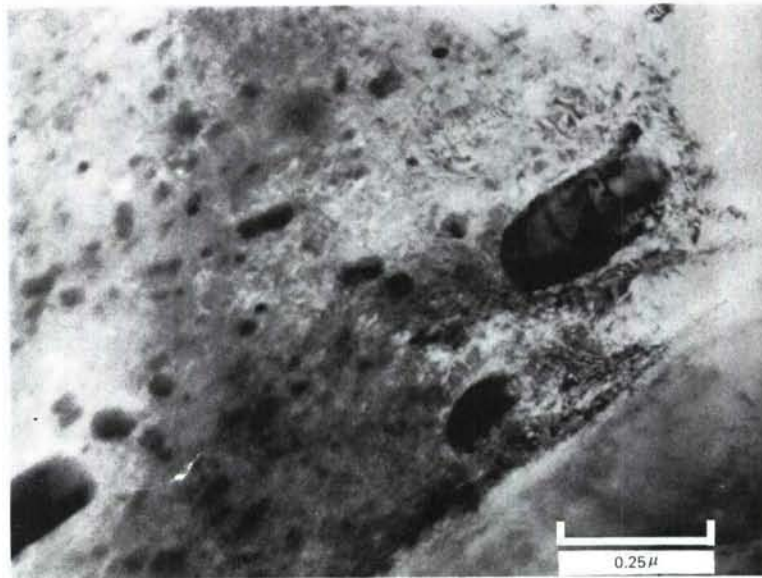
(a) DISLOCATION INTERACTIONS WITH A
DISPERSOID PARTICLE (TOP RIGHT)
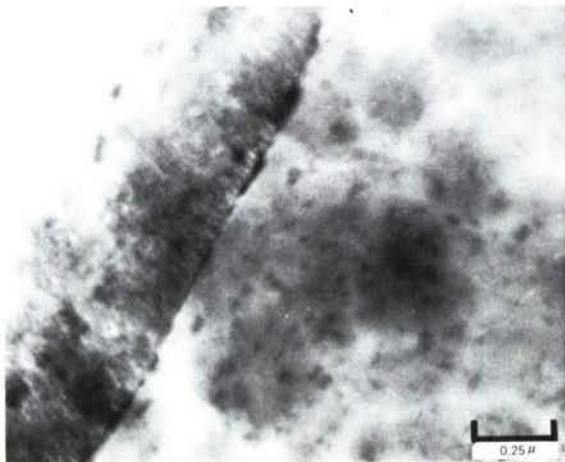
(b) DISLOCATION PILE-UPS AT
GRAIN BOUNDARIES (G.B.)

(c) DISLOCATION PILE-UPS AT
G.B. AND INTERACTIONS WITH
PARTICLES

FIGURE 15. TEM SUBSTRUCTURE BELOW FRACTURE SURFACE OF FAILED
2024–T3 FCP SPECIMENS

30

visible in different directions approaching the triple point grain boundary in Figure 16 (a). No dislocation pile-ups at grain boundaries, as seen in the T3 condition, were evident. Dislocation cell networks established by pinning with the S and S' precipitates were seen, Figure 16 (b). Very fine cellular structures were seen also, Figures 16 (c) and 16 (d). However, these structures did not appear to be related to the precipitation process but rather formed in a relatively precipitate-free area.

It appears that, here too, precipitate morphology played a major role in the damage due to cycling. Striation formation and propagation behavior are of a more brittle nature in the T8 condition than in the T3 condition because of the greater amount of precipitates with smaller mean free path for dislocations, as shown by fractographic studies. The higher degree of secondary cracking found in the T8 condition also indicates increased fracture initiation sites due to increased precipitation.

7075-T6 Alloy:

Examination of foils from the fracture surfaces of 7075-T6 FCP specimens showed considerable variation in substructure and precipitate morphology from one grain to another. G.P. zones and η' phase were predominant in the structure. The G.P. zones range normally from 50 to 200Å in size. The η' phase in the Al matrix, together with a rather large amount of dispersoid particles, can be seen in Figure 17 (a). A faint dislocation cellular substructure can be seen in the background in the top micrograph. There is no high degree of dislocation interaction with the precipitates. Selected area diffraction, in this case, showed only the Al matrix with very faint indications of the η' phase.

At a lower magnification, Figure 17 (b), large dislocation cells were seen. They were "peppered" with G.P. zones and the precipitation hardening phase. The fatigue-crack generally grows perpendicular to these cells. However, very few independent dislocations were apparent. In some of the areas, there was a large number of precipitates.

It has been proposed that crack nucleation can be associated with inclusions in the material. The possibility of overaging, increases in G.P. zone size, and formation of new strain-induced G.P. zones has also been proposed [24]. Comparison of the as-received and FCP conditions reveals an increase in size and number of G.P. zones as a result of cycling. The possible occurrence of overaging could result in softening at the crack tip and thus allow increased plastic deformation.

(a)
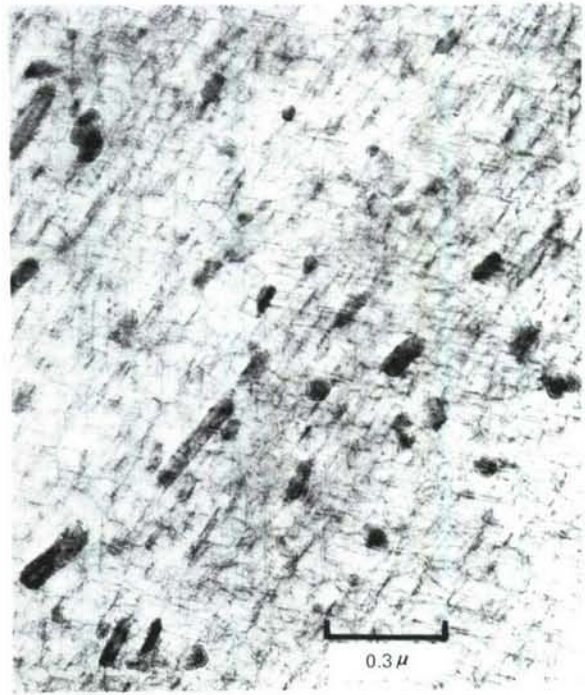
(b)
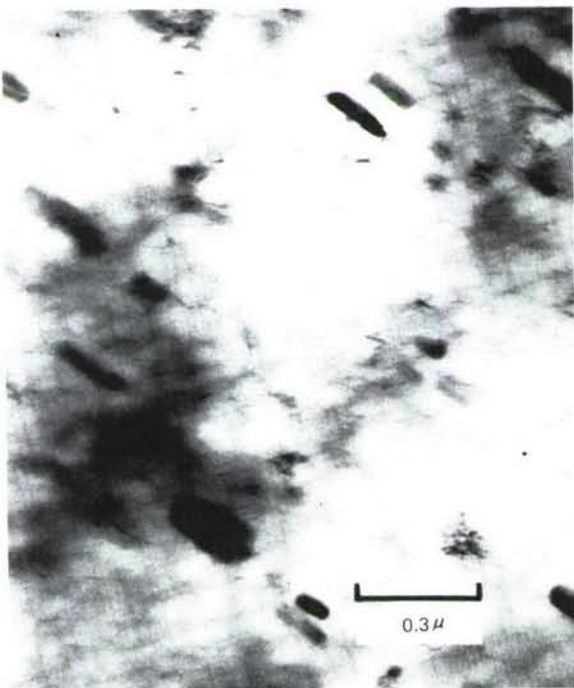
(c)
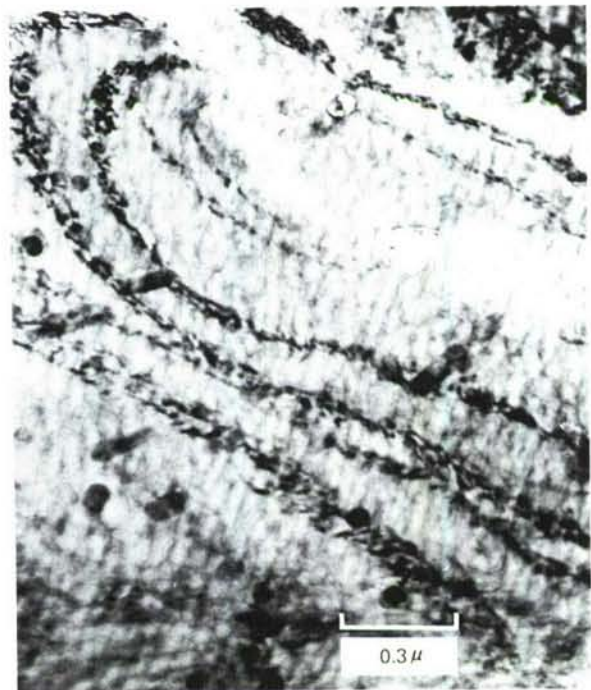
(d)

FIGURE 16. TEM SUBSTRUCTURE BELOW FRACTURE SURFACE OF FAILED
2024-T8 FCP SPECIMEN SHOWING DISLOCATION INTERACTIONS AT GRAIN
BOUNDARIES, DISLOCATION CELL FORMATION, AND PRECIPITATE MORPHOLOGY

32
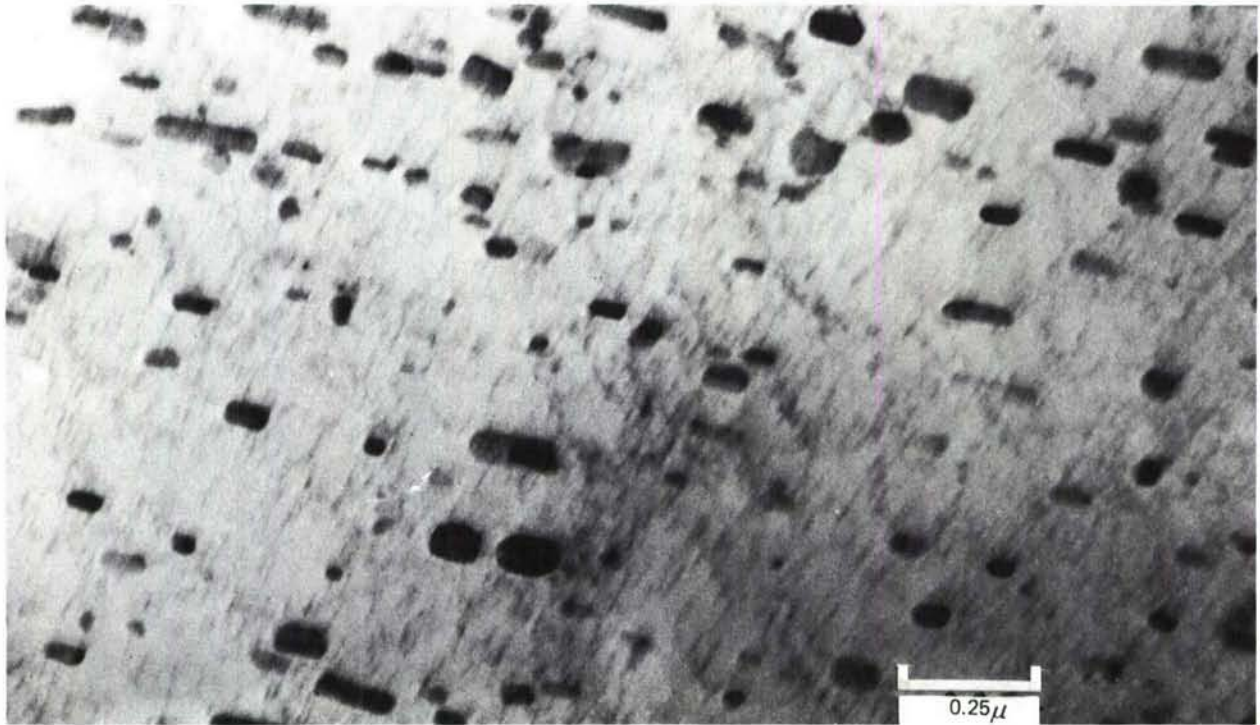
(a)
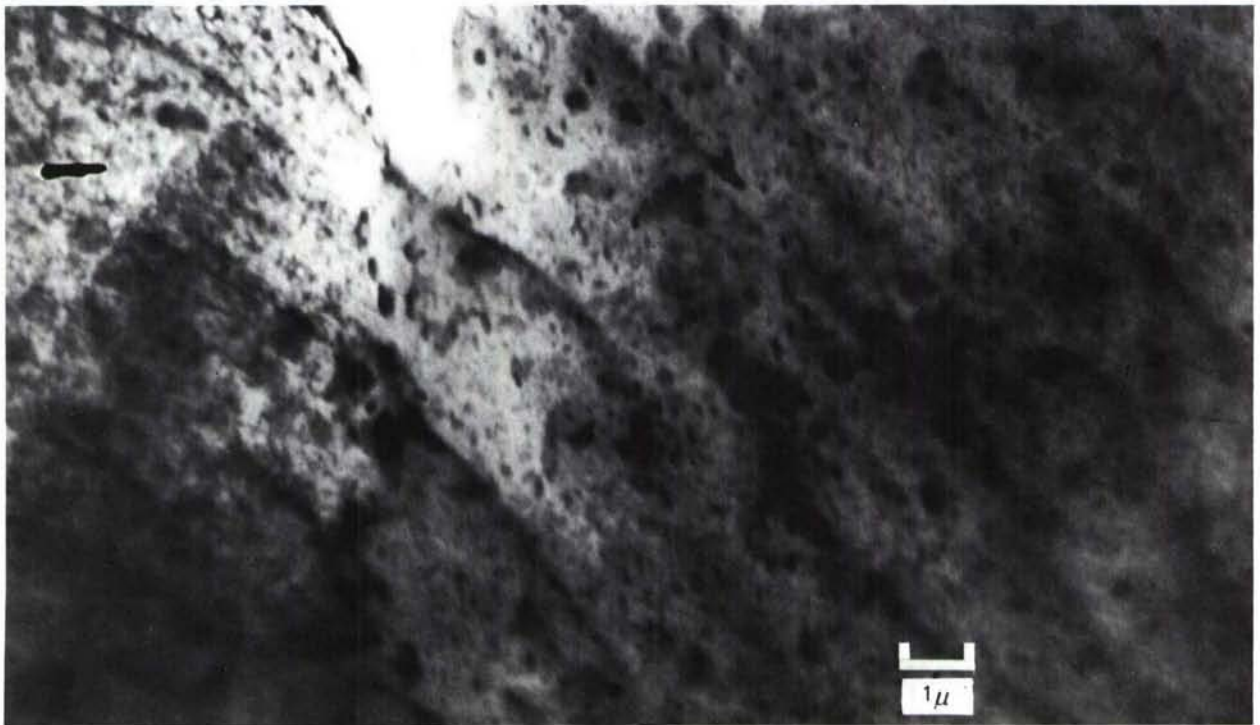
(b)

FIGURE 17. DISLOCATION INTERACTIONS AND PRECIPITATE DISTRIBUTION
IN A FAILED 7075-T6 FCP SPECIMEN

33

7075-T73 Alloy:

Thin foil examination of failed FCP specimens in this alloy revealed an increase in the amount of precipitate. Very fine particles were evident in the background in the micrographs of Figure 18. These are enlarged G.P. zones similar to those observed in the T6 condition. Precipitation was greatest in the (100) orientation. However, from the foils oriented in the (110) plane, fine pinned dislocations and general dislocation tangles were seen. This type of structure was not prevalent over the entire specimen, however. High dislocation densities can be seen in micrographs in Figure 18. This would indicate a heavily deformed zone. Comparison of the FCP substructure with the as-received T73 structure showed a substantial increase in the amount of G.P. zones and dislocation tangles. A classic example of crack initiation due to dislocation pile-ups at an inclusion is seen in Figure 18.

Thus, in the 7075 alloy, precipitation increases under fatigue loading. Both the T6 and T73 conditions showed this behavior, with the T73 showing a larger increase. Dislocation cell structures and interactions were evident in the T6 and T73 conditions, with the greater amount occurring in the T73 condition.

In general, these results showed that precipitates played a predominant role in the fatigue damage, while dislocation interactions played a lesser role except for the 2024-T3 alloy where dislocation interactions were equally important.

6. FRACTOGRAPHIC CHARACTERIZATION

The fractographic features of the failed FCP specimen surfaces were observed with the scanning electron microscope (SEM) to show fatigue-crack interactions with the microstructural features as well as to observe the striation spacings and relate them to crack-growth rates. These results provided a reference state to determine the changes in fractographic features due to overload cycles.

Figure 19 shows SEM fractographs of the fracture surfaces of the 2024-T3 and T8 baseline FCP specimens. The artificial aging of 2024-T3 to the T8 condition results in a higher yield strength and lower ductility compared to the T3 condition. Comparison of Figures 19 (a) and 19 (c), tested at approximately the same stress-intensity factor range, reveals a difference in the appearance of the fracture surfaces. The fractograph in Figure 19 (a) shows extensive branching of the crack in directions other than that of the primary growth direction. Also, the fracture surface is rougher in appearance (compared to Figure 19 (c)), indicating a more ductile failure. This is further illustrated by comparing Figures 19 (b) and 19 (d). Here, even at a somewhat

34
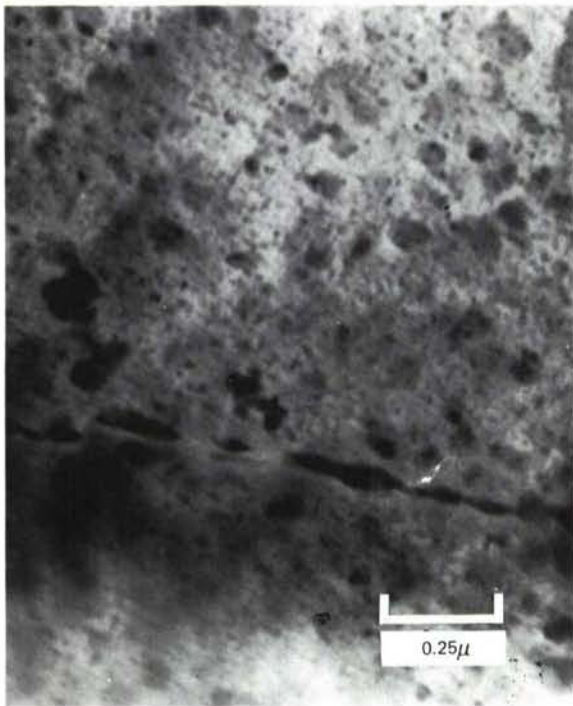
(a) EXTENSIVE INCREASE
IN PRECIPITATION
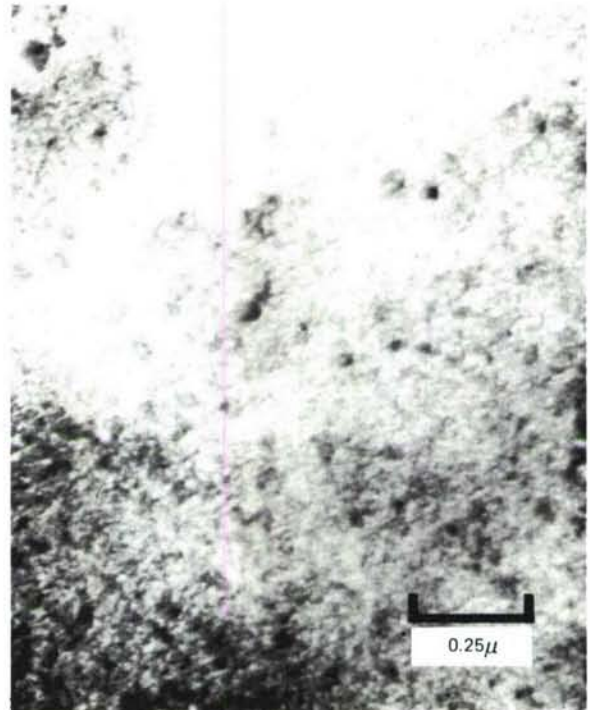
(b) EXTENSIVE INCREASE
IN PRECIPITATION
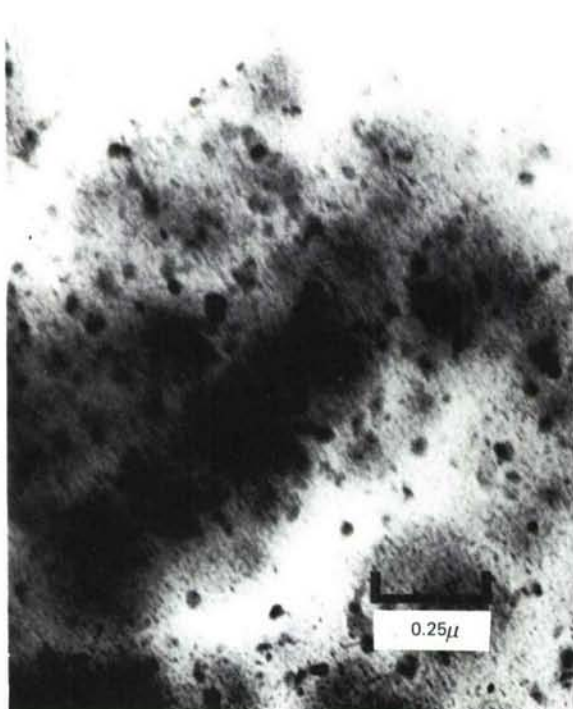
(c) PRECIPITATION AND
DISLOCATION INTERACTIONS
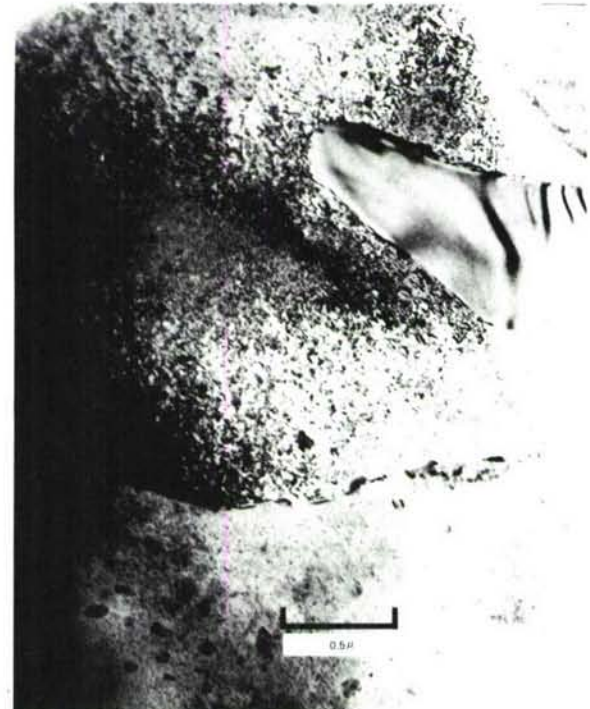
(d) DISLOCATION PILE-UPS GIVING RISE TO CRACK-
INITIATION AROUND A SECOND-PHASE PARTICLE

FIGURE 18. SUBSTRUCTURES FROM A FAILED 7075–T73 FCP SPECIMEN SHOWING
EXTENSIVE INCREASE IN PRECIPITATION AND DISLOCATION INTERACTIONS
DUE TO CYCLING

CRACK-GROWTH
DIRECTION

(a) 2024–T3 ALLOY
ΔK = 12.6 KSI $\sqrt{IN.}$
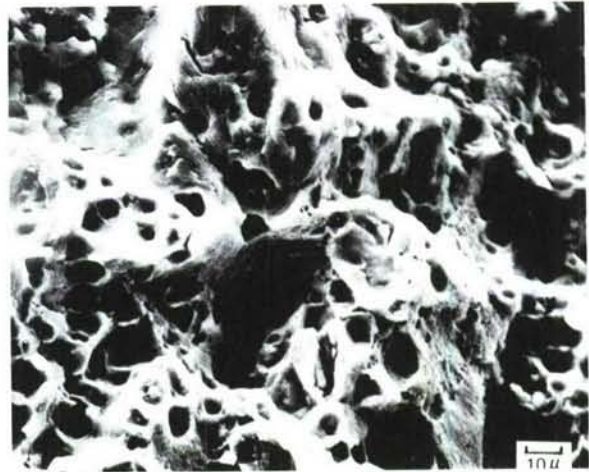
(b) 2024–T3 ALLOY
ΔK = 19.5 KSI $\sqrt{IN.}$
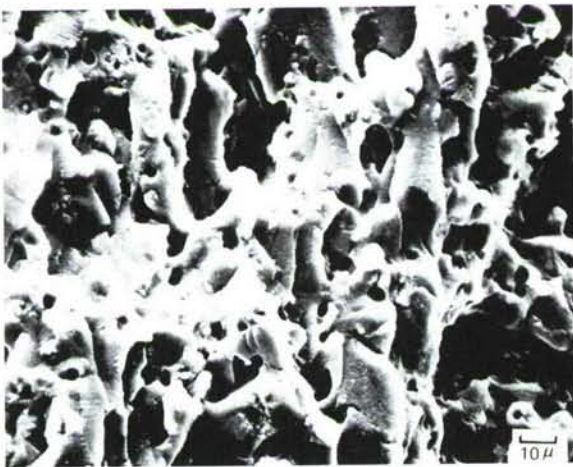
(c) 2024–T8 ALLOY
ΔK = 11.7 KSI $\sqrt{IN.}$
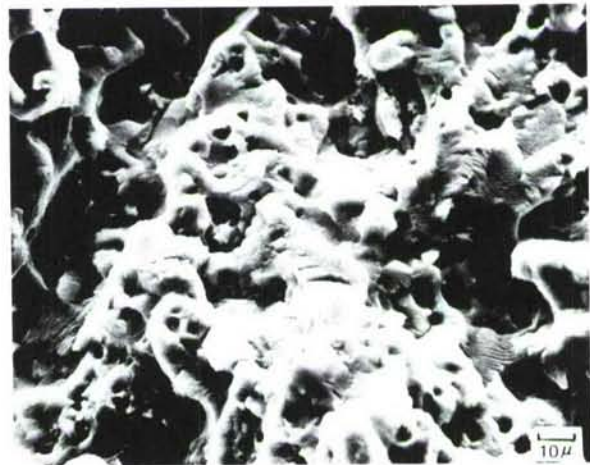
(d) 2024–T8 ALLOY
ΔK = 23.3 KSI $\sqrt{IN.}$

FIGURE 19. FRACTOGRAPHS FROM 2024–T3 AND 2024–T8 ALLOYS
AFTER BASELINE FCP TESTS

lower stress-intensity range, the T3 specimen exhibits a ductile failure compared to the T8 alloy where a mixed mode fracture with less ductility is evident. The 7075-T6 and T73 exhibit fatigue fracture surfaces similar to the 2024-T8.

The effect of second phase particles on fatigue crack propagation can also be seen in Figures 19 and 20. The interaction of the fatigue crack with grain boundaries can be seen in Figure 20. The interaction of the crack with a particle results in the change in direction of local crack-propagation, with the occurrence of secondary branching around the particle. After propagating around the particle, the two branches join again into one propagation front. These particles are often dislodged from the fracture surface during failure and this results in the presence of small hemispherical holes dispersed across the fracture surface.

Striation spacings as a function of the stress-intensity factor were determined from the SEM fractographs of the baseline FCP specimens and compared with the measured crack-growth rates. The fatigue striations were generally discernible above 3×10^{-6} inch/cycle where measurements were made. These results are also shown as solid points in the FCP curves in Figure 9 (a). The results show a reasonable agreement between micro and macro crack-growth rates.

B. EFFECTS OF SINGLE OVERLOADS ON CRACK-GROWTH BEHAVIOR

1. RETARDATION TEST RESULTS

The retardation results were analyzed as indicated in Figure 21, which shows the important parameters that are commonly used to characterize the overload-affected crack-growth behavior. They are:

$$a^* = \text{affected crack-length}$$

$$N^* = \text{number of cycles during growth of } a^*$$

$$r_1 = \text{steady-state crack-growth rate before overload}$$

$$r_2 = \text{steady-state crack-growth rate after overload}$$

Figure 22 shows the crack-length versus number of cycles for each alloy after single overload cycles at a baseline P_{max} of 500 lbs. and an overload ratio of 2.0. These are typical of all the tests run. As seen from these results, the crack-growth

37

(a) 2024-T3 ALLOY

CRACK-GROWTH
DIRECTION

1 μ

(b) 7075-T6 ALLOY

2 μ
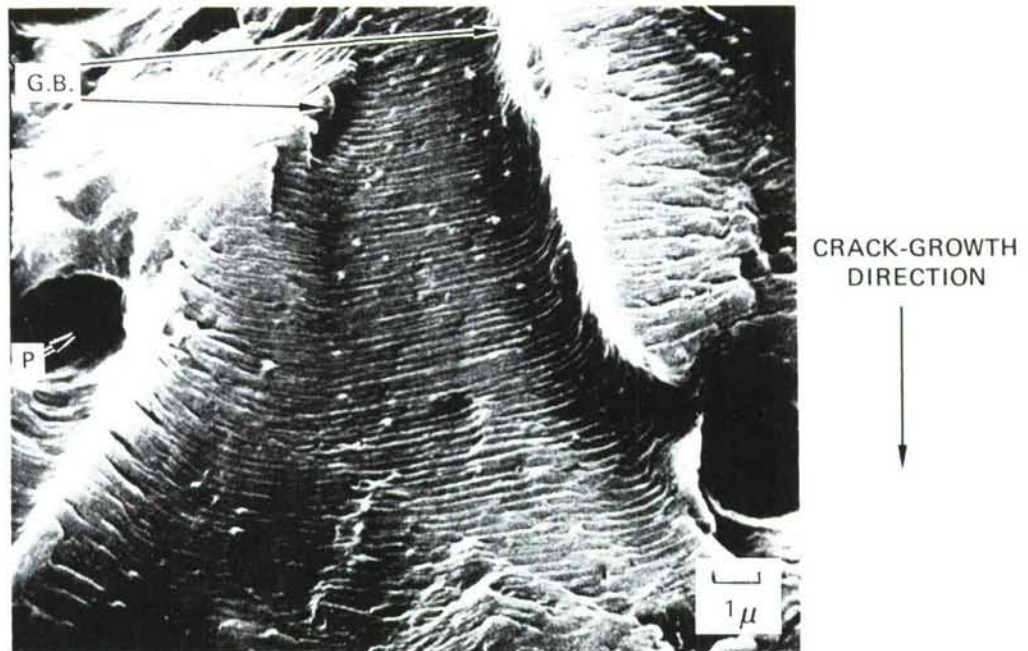
FIGURE 20. FRACTOGRAPHS FROM THE FAILED FCP SPECIMENS SHOWING
INTERACTIONS OF GRAIN BOUNDARY (G.B.) AND SECOND PHASE
PARTICLES (P) WITH CRACK-FRONT
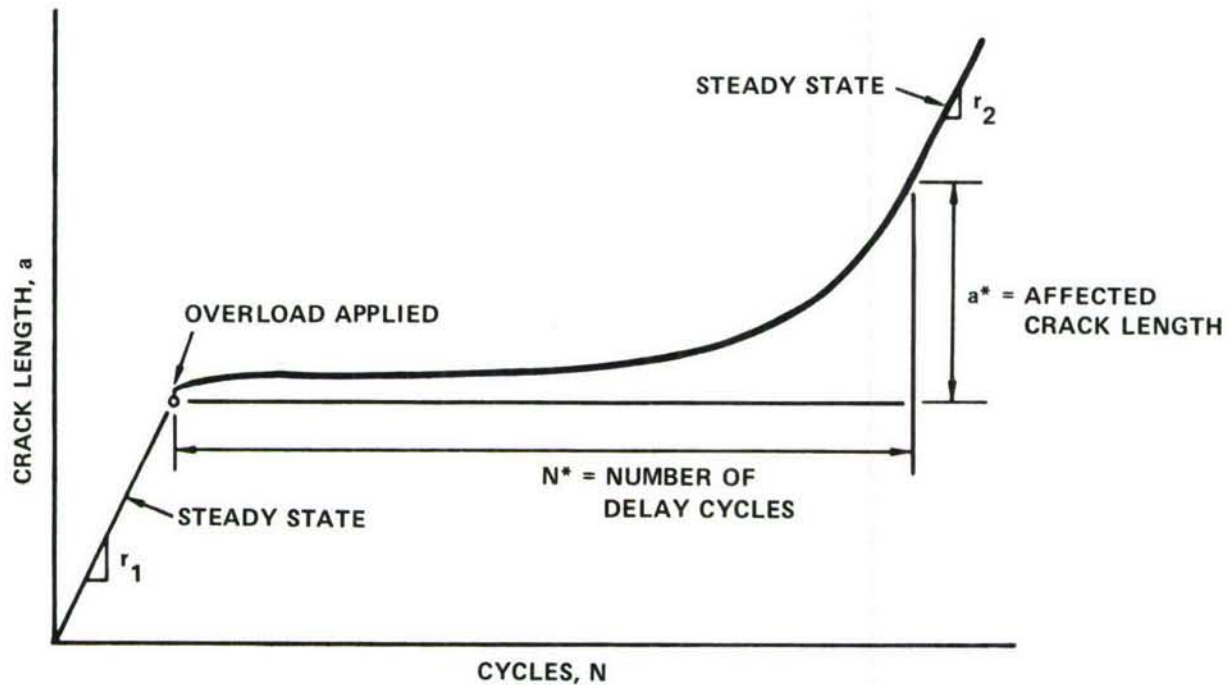
FIGURE 21. CRACK-GROWTH RATE CURVE RESULTING FROM APPLICATION OF A SINGLE OVERLOAD

had reached a steady state after a given overload cycle prior to the application of the next overload cycle. This was further confirmed by da/dN versus a results of the type shown in Figure 23, which were obtained in the majority of cases. Due to some inherent scatter in the crack-growth rate and tunneling after the overload cycle, a small difference in number of delay cycles between any two tests should not be considered as significant. (This scatter was reflected in the measurement of crack-growth rates in the vicinity of the overload cycle. This scatter was generally less for the tests at the higher P_{max} values, as indicated by the fact that the changes in the slopes of a versus N curves due to the overload cycles were more clear-cut and unambiguous for the tests at 800 and 1000 lbs. compared to the test at 500 lbs.

Tables V and VI summarize all the test results obtained in this phase of the program. The measured values of a* can be compared with the size of the overload plastic-zone (R_p), shown in Tables V and VI. The R_p values were calculated from a

39
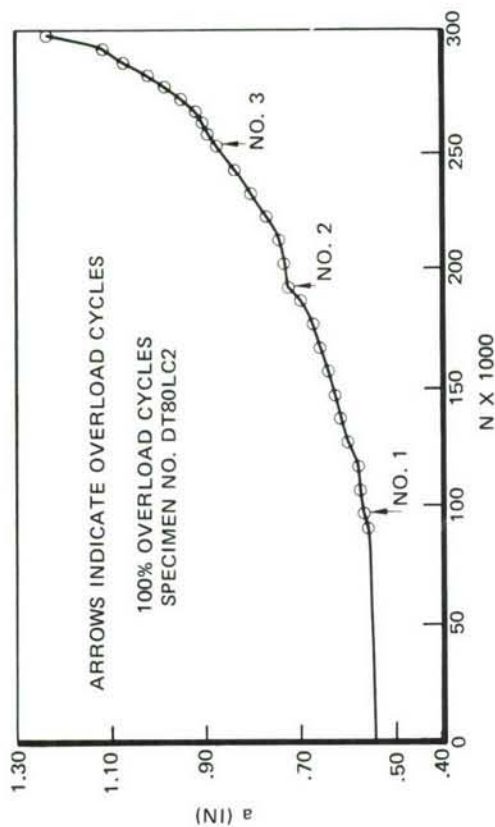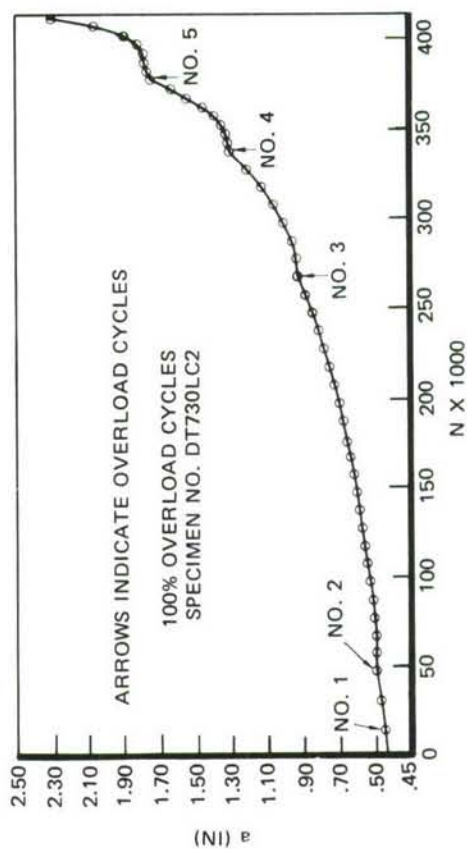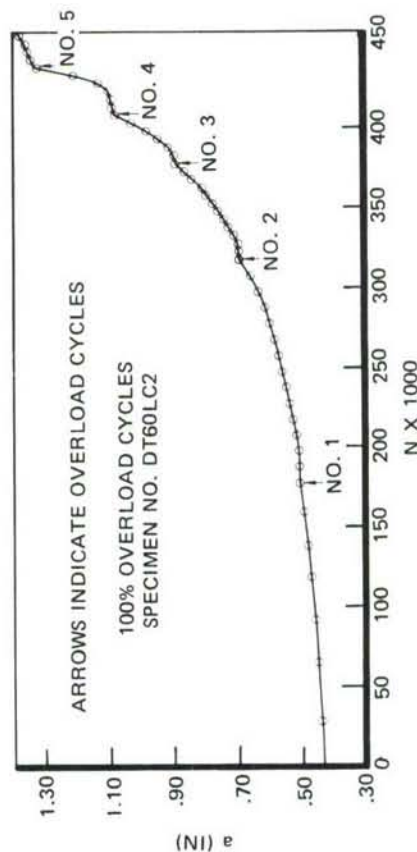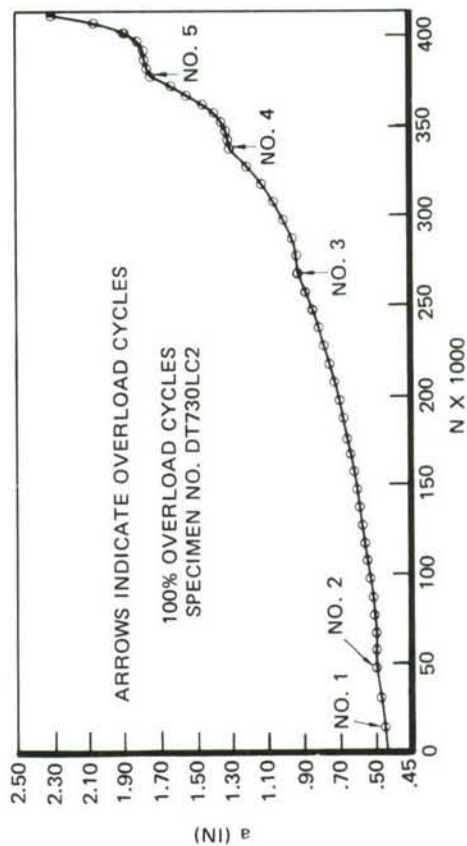
FIGURE 22. TYPICAL CRACK-LENGTH VS NUMBER OF CYCLES FOR EACH ALLOY AT A P_{MAX} OF 500 LBS AND OLR OF 2.0

40
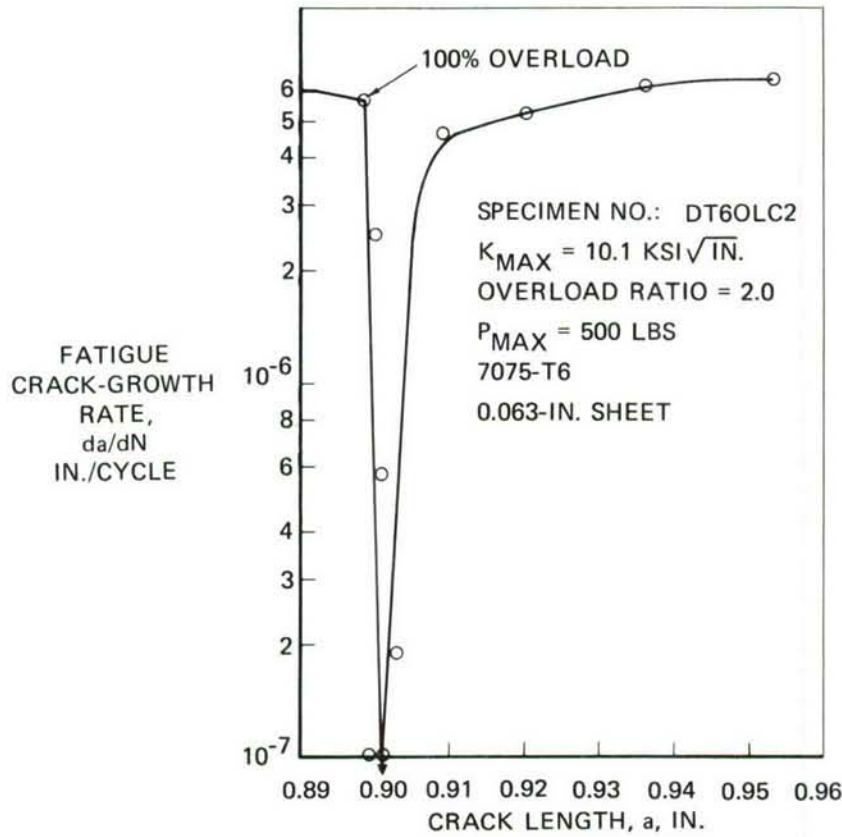
FIGURE 23. INFLUENCE OF 100% OVERLOAD ON SUBSEQUENT CRACK-GROWTH RATES IN AIR FOR 7075-T6

simplified Irwin formula for plastic zone under a plane-stress condition, as shown below:

$$R_p = \frac{1}{\pi} \left(\frac{K_o}{\sigma_{ys}} \right)^2 \tag{4}$$

where K_o is overload stress-intensity factor.

The validity of the existence of plane-stress condition at the crack-tip was confirmed by interferometry, as will be described later. The increase in R_p and $a*$ values with increase in OLR and K_{max} is in agreement with each other considering the approximate nature of expression (4) and $a*$.

TABLE V. SUMMARY OF RETARDATION RESULTS IN AIR FOR 0.063 INCH THICK 2024-T3 AND T8 ALLOYS

SPECIMEN NO.	P_{MAX} (LBS)	K_O/K_{MAX} (OLR)	a_i (IN)	K_{MAX} (KSI $\sqrt{IN}$)	a^* (IN)	$R_p{}^1$	N^* (1000)	ACCL^2
			2024-T3					
DT3OLC1	500	1.5	.5696	6.1	0.0114	0.010	55	a
			.7064	7.6	0.0152	0.015	20	a
			.8660	9.7	0.0236	0.025	12.5	c
DT3OLC2		2.0	.5696	6.1	0.0314	0.018	240	a
			.711	7.7	0.0440	0.028	145	b
			.848	9.4	0.0400	0.042	130	a
DT3OLC3		2.5	.5696	6.1		0.027	Arrest	a
			.7132	7.7		0.044	Arrest	b
			.8402	9.3		0.064	Arrest	b
DT3OLC81	800	1.5	.5596	9.7	0.0304	0.025	15	b
			.7420	12.8	0.0475	0.043	9	a
			.9244	16.9	0.0585	0.076	8	a
DT3OLC81-2		1.5	.58	10.0	0.030	0.027	12.5	c
			.80	14.0	0.070	0.053	12.5	b & c
			1.04	20.2	0.160	0.111	9.0	c
DT3OLC82		2.0	.5696	9.8	0.0790	0.045	120	a
			.7064	12.1	0.0775	0.069	110	b
			.8432	14.9	0.1053	0.100	110	b
DT3OLC82-2		2.0	.57	9.8	0.062	0.046	110	b
			.79	13.8	0.106	0.092	85	b & c
			1.03	19.9	Failed Before Recovery			b & c
DT3OLC83		2.5	.5668	9.8		0.071	Arrest	a
			.7976	13.9		0.140	Arrest	b
			1.0256	19.8		0.290	Arrest	b
DT3OLC11	1000	1.5	.5582	12.0	0.0433	0.038	12.5	a
			.7862	17.1	0.0768	0.077	10	b
			1.0142	24.2	Failed Before Recovery			b & c
DT3OLC12		2.0	.5696	12.2	0.1391	0.070	95	a
			.7984	17.4	Specimen Grip Failure			b
			2024-T8					
DTSOLC1	500	1.5	.5696	6.1	0.0104	0.007	12.5	a
			.7292	7.9	0.0028	0.012	5	a
			.9587	11.4	0.0043	0.024	2	a
DTSOLC2		2.0	.5696	6.1	0.0327	0.013	30	b
			.7307	7.9	0.015	0.021	20	b
			.8789	9.8	0.0421	0.033	15	b
DTSOLC3		2.5	.573	6.2	0.0216	0.021	55	b
			.734	7.9	0.0280	0.033	65	b
			.869	9.7	0.0620	0.050	115	b
DTSOLC4		3.0	.572	6.1	0.043	0.029	315	b
			.772	8.3	0.039	0.053	370	b
			.976	11.1		0.095	Arrest	b
DTSOLC81	800	1.5	.5696	9.8	0.0106	0.018	4	b
			.7976	13.9	0.0448	0.037	4	a
			1.0279	19.8	0.0684	0.075	2	b
DTSOLC82		2.0	.5696	9.8	0.0428	0.033	15	a
			.7986	14.0	0.1240	0.067	20	a
			1.0256	19.8	Failed Before Recovery			
DTSOLC83		2.5	.5696	9.8	0.0806	0.051	115	a
			.7976	13.9	0.1664	0.100	120	b
			1.0256	19.8	Failed During Overload Cycle			
DTSOLC11	1000	1.5	.5696	12.2	0.0289	0.029	4	a
			.7999	17.4	0.0190	0.058	0.7	b
			1.0264	24.7	Failed Before Recovery			b
DTSOLC12		2.0	.5696	12.2	0.1052	0.051	20	a
			.7976	17.4	Failed Before Recovery			b

1 - Plane-stress Overload Plastic-zone
2 - a = No crack growth during overload cycle
　　b = Crack growth during overload cycle
　　c = Initial acceleration after the overload cycle

SPECIMEN NO.	P_{MAX} (LBS)	K_O/K_{MAX} (OLR)	a_i (IN)	K_{MAX} (KSI$\sqrt{IN}$)	a^* (IN)	$R_p{}^1$	N^* (1000)	ACCL[2]
				7075-T6				
DT6OLC1	500	1.5	.5696	6.1	0.0110	0.005	17.5	a
			.7074	7.6	0.0100	0.0078	6	b
			.8472	9.3	0.0120	0.012	4	a
DT6OLC2		2.0	.5112	5.6	0.0038	0.0075	25	a
			.6983	7.4	0.0106	0.013	12.5	a
			.8989	10.1	0.0213	0.024	10	a
			1.0889	13.7	0.1262	0.045	25	b
			1.3306	20.4	Failed Before Recovery			b & c
DT6OLC3		2.5	.5696	6.1	0.0428	0.014	350	a
			.7976	8.7	0.0894	0.028	130	a
			1.0256	12.3			Arrest	a
DT6OLC81	800	1.5	.5368	9.2	0.0092	0.011	2	a
			.6022	10.3	0.0228	0.014	3	a
			.7010	11.9	0.0435	0.019	4	a
DT6OLC81-2		1.5	.57	9.8	0.017	0.013	3	a & c
			.79	13.8	0.036	0.026	3	b
			1.05	20.6	0.050	0.057	2	b & c
DT6OLC82		2.0	.5696	9.8	0.0342	0.023	12.5	b
			.7976	13.9	0.0950	0.046	17.5	a
			1.0271	19.8	Failed Before Recovery			b & c
DT6OLC82-2		2.0	.57	9.8	0.026	0.023	12.5	b
			.79	13.8	0.029	0.045	12.5	b
			1.03	19.9	Failed Before Recovery			a
DT6OLC83		2.5	.5696	9.8		0.036	Arrest	b
DT6OLC11	1000	1.5	.5504	11.9	0.0342	0.019	5	c
			.7776	16.9	0.0266	0.038	2	c
			1.0064	23.9	0.1018	0.077	2	b
DT6OLC12		2.0	.5696	12.2	0.0692	0.036	20	a
			.7976	17.4	0.1702	0.072	20	b
			1.0256	24.7	Failed Before Recovery			b & c
				7075-T73				
DT73OLC1	500	1.5	.5696	6.1	0.0122	0.0072	17.5	a
			.7132	7.7	0.0091	0.0100	6	a
DT73OLC2		2.0	.5012	5.4	0.0190	0.010	55	a
			.7170	7.7	0.0251	0.020	25	a
			.9055	10.2	0.0433	0.036	20	b
			1.1290	14.6	0.0707	0.073	25	b & c
			1.5052	28.0	Failed During Overload Cycle			
DT73OLC3		2.5	.5796	6.2	0.0198	0.021	90	b
			.8076	8.9	0.0418	0.042	85	a
			1.0356	12.6	0.1892	0.085	165	b
DT73OLC4		3.0	.57	6.1		0.029	Arrest	b
			.79	8.7		0.059	Arrest	b
DT73OLC81	800	1.5	.5596	9.7	0.0100	0.018	4	b
			.7876	13.7	0.0210	0.036	3	a
			1.0384	20.1	0.0884	0.078	4	b
DT73OLC82		2.0	.5906	10.1	0.0722	0.035	20	a
			.8214	14.4	0.1092	0.071	17.5	b & c
			1.0494	20.4	1.082	0.140	17.5	b & c
DT73OLC83		2.5	.5696	9.8	0.0704	0.051	130	a
			.7976	13.9	0.1666	0.100	180	b
			1.0256	19.8		0.210	Arrest[3]	b
DT73OLC11	1000	1.5	.5596	12.1	0.0213	0.028	4	a
			.7876	17.1	0.0722	0.056	5	b & c
			1.0156	24.3	0.1284	0.110	3	b & c
DT73OLC12		2.0	.5596	12.1	0.0669	0.050	17.5	b
			.7876	17.1	0.1467	0.100	20	b
			1.0156	24.3	0.2863	0.200	27.5	b

1 - Plane-stress Overload Plastic-zone
2 - a = No crack-growth during overload cycle and no initial acceleration
    b = Crack-growth during overload cycle
    c = Initial acceleration after the overload cycle
3 - Test stopped at 400,000 cycles

The data obtained have been analyzed to provide information concerning:

- Effect of different overload ratios on the retardation behavior.

- Delayed retardation, initial acceleration, and occurrence of crack-growth during overload cycle.

- Effect of K_{max} on the retardation behavior at a given overload ratio.

- Effect of strength level on the retardation behavior for a given alloy.

- Effect of metallurgical factors on the retardation behavior at a constant yield strength in two alloys.

- Effect of strength-level and microstructure differences on the retardation behavior.

- Crack-arrest behavior.

These results are described below.

Effect of Overload Ratio

Even from a cursory examination of Table VII, it is apparent that the magnitude of the overload ratio is the single most dominating factor in determining the number of delay cycles in these alloys. Figure 24 shows the effect of overload ratio (OLR) on delay cycles at K_{max} values of 6.1 and 9.8 ksi $\sqrt{in}$. obtained from tests at two different P_{max} values. These are typical of results at other K values as well. In these and subsequent figures showing retardation behavior, whenever the stress-intensity level for any particular data point was significantly different from those of other points, it was shown as a number in parenthesis next to that particular data point. Retardation behavior is generally related to the overload plastic-zone size which under plane-stress conditions is given by expression (4). The number of delay cycles becomes increasingly high at higher OLR because of the higher residual stresses and increased plastic-zone size at the crack-tip. The affected crack length and calculated R_p both are indicated in Tables V and VI, and the general agreement between them clearly indicates that, with an increase in OLR, the number of delay cycles will go up at a given K_{max}.

44

TABLE VII. COMPARISON OF RETARDATION BEHAVIOR IN AIR FOR THE FOUR ALLOYS
AT DIFFERENT OVERLOAD RATIOS (OLR)

ALLOY	σ_{ys} (KSI)	K_{MAX} (KSI$\sqrt{IN.}$) APPROX.	1.5 OLR		2.0 OLR		2.5 OLR		3.0 OLR	
			a* (IN.)	N* (x1000)	a* (IN.)	N* (x1000)	a* (IN.)	N* (x1000)	a* (IN.)	N* (x1000)
2024-T3	51.7	6.1[1]	.0114	55	.0314	240	Arrest			
2024-T8	61.2	6.1[1]	.0104	12.5	.0327	30	.0216	55	.043	315
7075-T6	73.1	6.0[1]	.0110	17.5	.0038	25	.0428	350		
7075-T73	60.8	6.0[1]	.0122	17.5	.0190	55	.0198	90	Arrest	
2024-T3	51.7	7.7[1]	.0152	20	.0440	145	Arrest			
2024-T8	61.2	8.0[1]	.0028	5	.015	20	.0280	65	.039	370
7075-T6	73.1	7.9[1]	.0100	6	.0106	12.5	.0894	130		
7075-T73	60.8	8.2[1]	.0091	6	.0251	25	.0418	85	Arrest	
2024-T3	51.7	9.5[1]	.0236	12.5	.0400	130	Arrest			
		9.8[2]	.0304	15	.079	120	Arrest			
		9.9[2]	.030	12.5	.062	110				
2024-T8	61.2	10.3[1]	.0043	2	.0421	15	.0620	115		
		9.8[2]	.0106	4	.0428	15	.0806	115		
7075-T6	73.1	10.6[1]	.0120	4	.0213	10	Arrest			
		9.6[2]	.0092	2	.0342	12.5	Arrest			
		9.8[2]	.017	3	.026	12.5				
7075-T73	60.8	11.4[1]			.0433	20	.1892	165		
		9.9[2]	.0100	4	.0722	20	.0704	130		
2024-T3	51.7	13.3[2]	.0475	9	.0775	110	Arrest			
		13.9[2]	.070	12.5	.106	85				
2024-T8	61.2	13.9[2]	.0448	4	.1240	20	.1664	120		
		12.9[2]	.0435	4	.095	17.5				
7075-T6	73.1	13.8[2]	.036	3	.029	12.5				
7075-T73	60.8	14.0[2]	.0210	3	.1092	17.5	.1666	180		

1 - P_{max} = 500 pounds

2 - P_{max} = 800 pounds
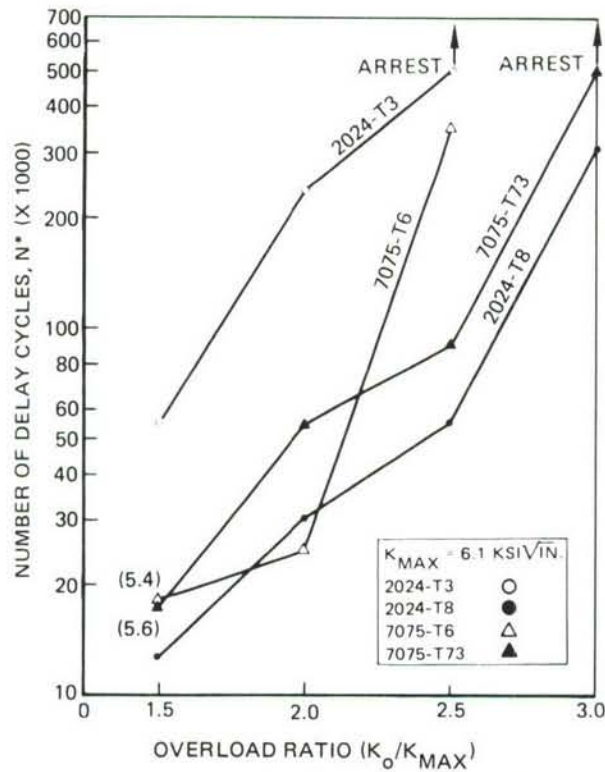
(a) P_{MAX} (K_{MAX}) = 500 LBS (6.1 KSI $\sqrt{IN}$)
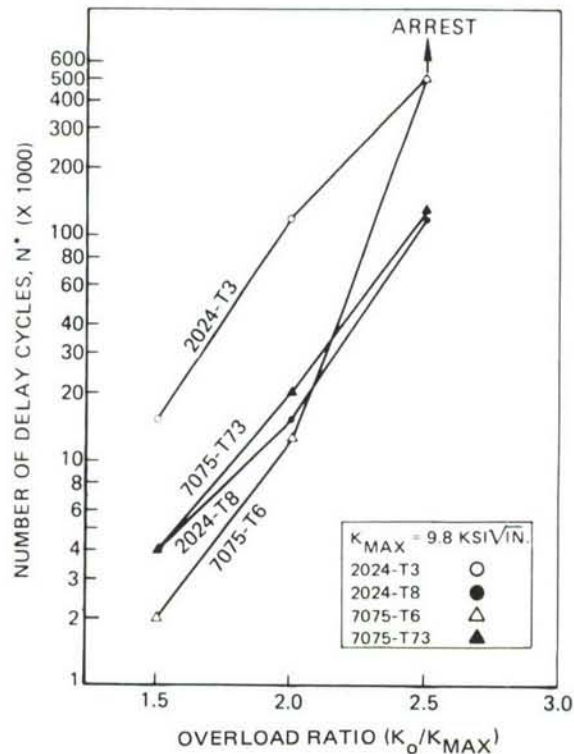
(b) P_{MAX} (K_{MAX}) = 800 LBS (9.8 KSI $\sqrt{IN.}$)

FIGURE 24. EFFECT OF OVERLOAD RATIO (OLR) ON NUMBER OF DELAY CYCLES

46

Transient Crack-Growth Behavior During and Immediately After the Overload Cycle

The details of crack-growth behavior during and immediately after the overload cycles were also observed. For this purpose, the crack-length immediately before and after the overload-cycle was measured. Subsequent to the overload cycle, the crack-length was measured after 10, 20, 50, 100, 200, 300, 500, 700, 1000, 1500, and 2000 constant-amplitude cycles during the first 2,000 cycles of testing. Thus, adequate measurements were made to determine initial acceleration, delayed retardation, the occurrence of crack-growth during the overload cycle, etc. These observations are summarized and presented in the right hand column of Tables V and VI. Although no clear-cut and unambiguous trend was observed, a few conclusions can be drawn from these results. In most cases, neither initial acceleration nor crack-growth during the overload cycle was observed at low OLR and low K_{max} values. At higher K_{max} or higher OLR, crack-growth during the overload cycle was observed. In most cases, at high K_{max} and high OLR values, both initial acceleration and crack-growth during the overload cycle were observed with the exception of those tests where crack-arrest occurred. For a given alloy system such as 2024 or 7075, the heat treatment with lower strength has a stronger tendency to exhibit transient behavior. Whenever crack-growth occurred during the overload cycle, its value was higher than expected for the applied K_o. Since the transient behavior occurs over a very small crack-increment, various factors tend to obscure a unique conclusion. The microscopic inhomogeneity of the alloy, such as an inclusion particle at the crack-tip during the overload cycle, can give rise to inconsistencies in the transient behavior. The occurrence of tunneling and inherent scatter of the crack-growth rate make it still more difficult to obtain a definite conclusion. Nevertheless, our results indicate that the transient behavior can be neglected for life prediction, since it occurs primarily at higher OLR and higher K values where the overall retardation is large and where the contribution of the transient behavior to the number of delay cycles is minimal.

Effect of K_{max} at a Given Overload Ratio

Figures 25 through 27 show the amount of delay for each of the four alloys as a function of baseline K_{max} at a given overload ratio. For the 2024-T3 alloy, the N* value decreased with an increase in K_{max} at the OLR of 1.5 and 2.0, while at the OLR of 2.5 crack-arrest occurred at all of the K_{max} values tested. For the 2024-T8

47
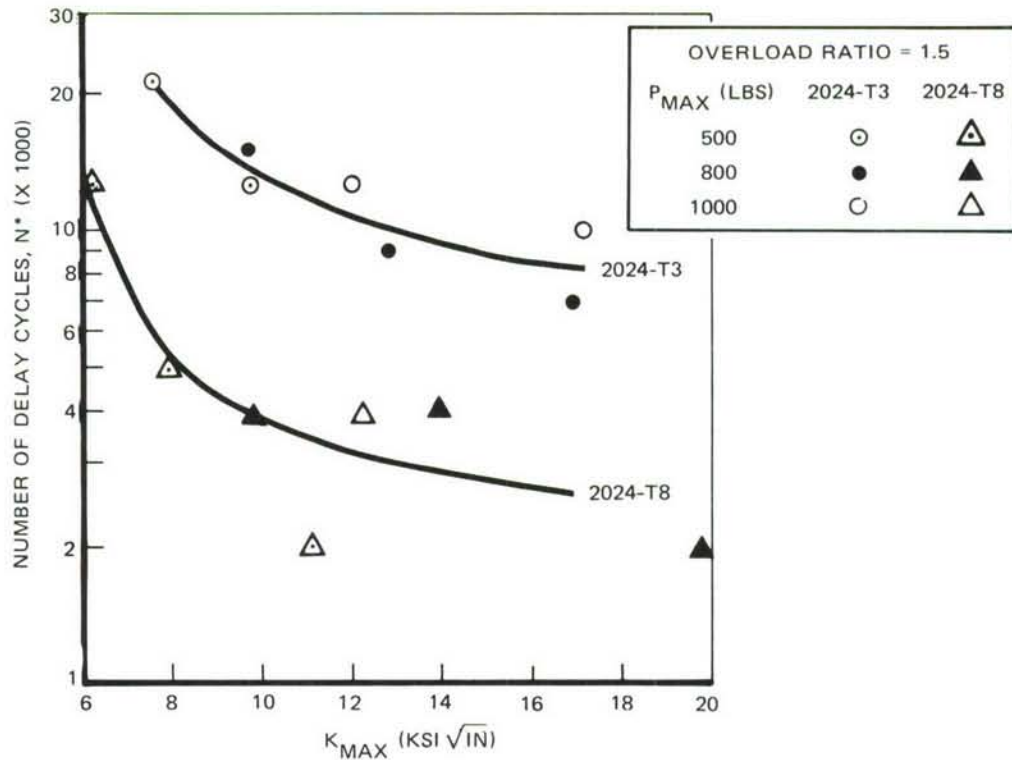
(a) 2024 ALLOY
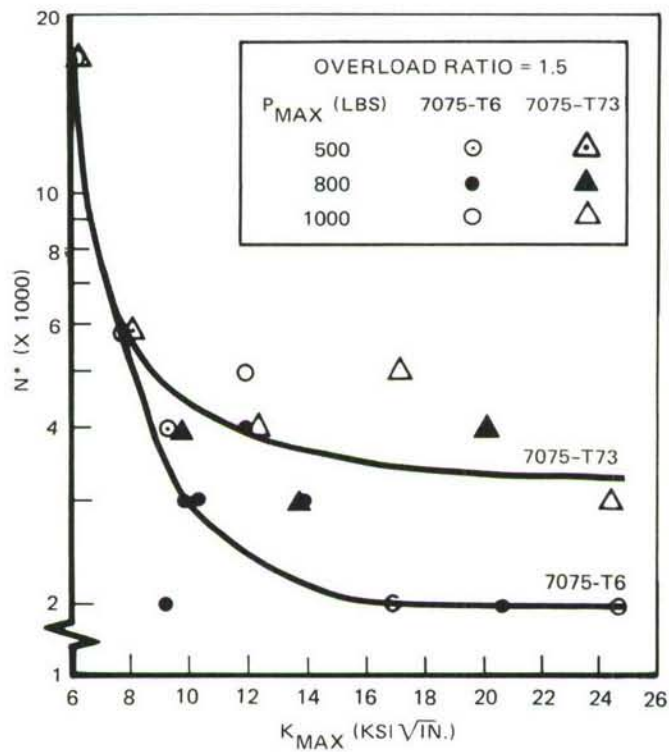
(b) 7075 ALLOY

FIGURE 25. NUMBER OF DELAY CYCLES AS A FUNCTION OF BASELINE
STRESS-INTENSITY FACTOR IN AIR AFTER AN OVERLOAD
RATIO OF 1.5

48
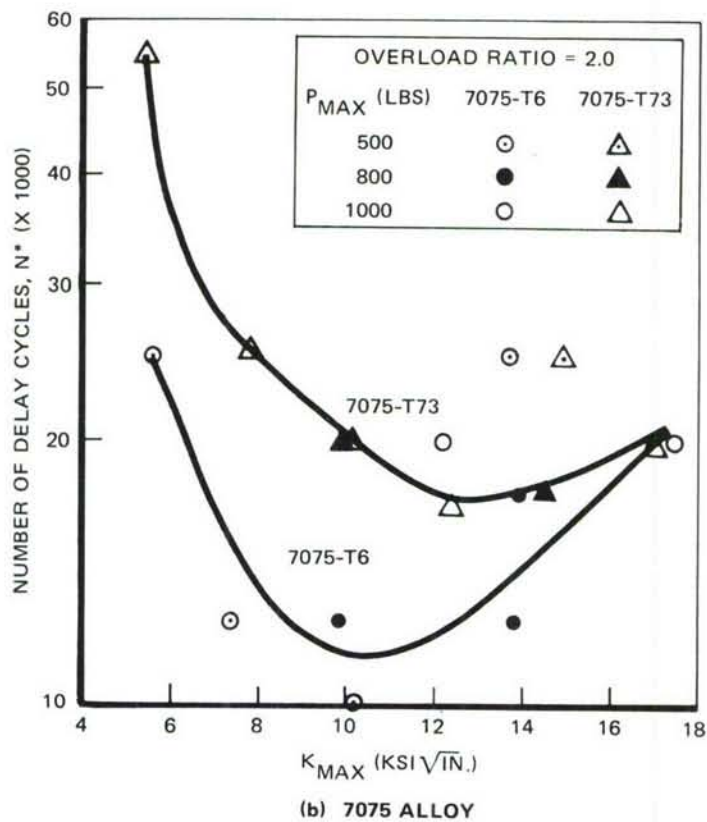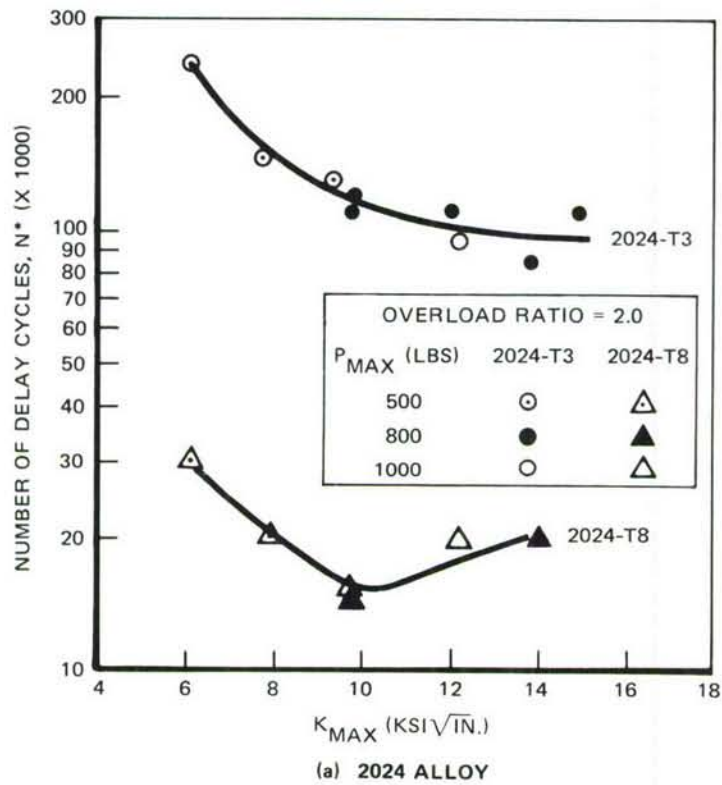
FIGURE 26. NUMBER OF DELAY CYCLES AS FUNCTION OF BASELINE
STRESS-INTENSITY FACTOR IN AIR AFTER AN OVERLOAD
RATIO OF 2.0

49

(a) 2024 ALLOY

(b) 7075 ALLOY
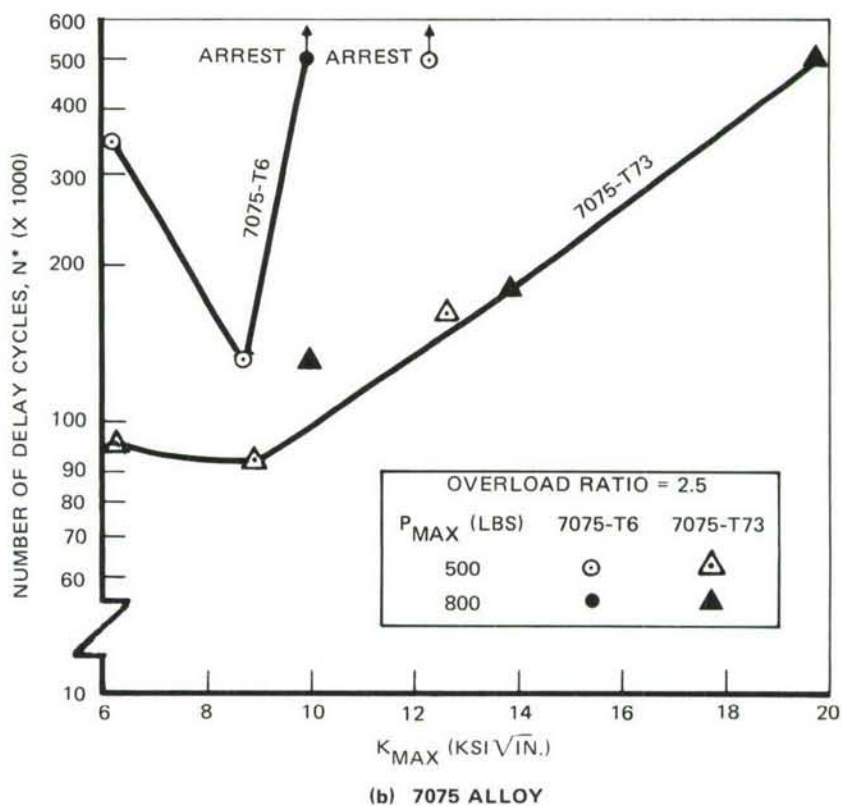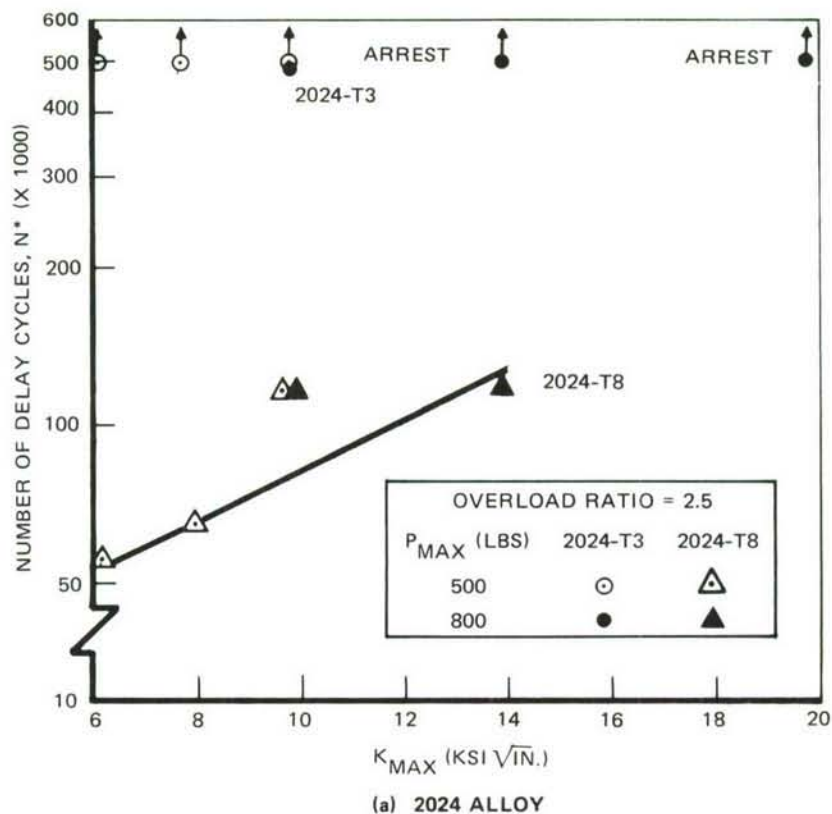
FIGURE 27. NUMBER OF DELAY CYCLES AS A FUNCTION OF BASELINE
STRESS-INTENSITY FACTOR IN AIR AFTER AN OVERLOAD
RATIO OF 2.5

50

alloy, at the OLR of 1.5, the N^* decreased with an increase in K_{max} until it reached an apparent plateau at an approximate K_{max} of 15-18 ksi $\sqrt{in.}$ At OLR of 2.0, the N^* versus K_{max} curve for the 2024-T8 alloy reaches a minimum at a K_{max} of 10-12 ksi $\sqrt{in.}$, after which the N^* goes up with an increase in K_{max}. The K_o (overload stress-intensity factor) values for the plateau at 1.5 OLR and the minimum at 2.0 OLR are at approximately 20-23 ksi $\sqrt{in.}$ after which the N^* value goes up. The behavior of the 7075-T6 and T73 is similar to that of the 2024-T8 alloy. At an OLR of 2.5, the minimum occurs at a K_{max} of approximately 8 ksi $\sqrt{in.}$ for the 7075-T6 and 7075-T73 alloys. The corresponding K_o for the minimas are also around 20 ksi $\sqrt{in.}$ These results indicate that around a K_o of 20 ksi $\sqrt{in.}$, the N^* versus K_{max} behavior changes for the 7075 alloy. In the 2024-T8 alloy, at 2.5 OLR, no minimum in the N^* versus K_{max} curve was observed. The N^* simply increased with increase in K_{max}. Hence at 2.5 OLR, for the 2024-T8 alloy, either there is no minimum in the N^* versus K_{max} curve or the minimum is at a K_{max} of 6 ksi $\sqrt{in.}$ or lower.

These results show that the effect of K_{max} on N^* at a given OLR depends on the alloy and the actual value of OLR. The N^* value decreases with an increase in K_{max} at low OLR until it reaches a plateau, while at higher OLR, it goes through a minimum. Also, for a given K_{max}, the baseline P_{max} has no significant effect on the number of delay cycles (Table VII).

Effect of Strength Level

The effect of the alloy strength level on the retardation behavior for a given composition can be determined from Table VII and also by comparing 2024-T3 with 2024-T8 (Figures 25(a), 26(a), and 27(a)), and 7075-T6 with 7075-T73 (Figures 25(b), 26(b), and 27(b)). The relative behavior of 7075-T6 and 7075-T73 at 2.5 OLR is somewhat different and is discussed under the Crack-Arrest Section. In the 2024 alloy, the T3 condition with a yield strength of 51.7 ksi produced much greater delay than the T8 condition with a yield strength of 61.2 ksi. In the 7075 alloy, the T73 (σ_{ys} = 60.8 ksi) condition produced slightly better retardation behavior than the T6 condition (σ_{ys} = 73.1 ksi). This increase in the number of delay cycles with a decrease in yield strength is expected because the yield strength affects plastic-zone size, as shown in equation (4). At a given K_o, the crack has to go through a larger plastic-zone for an alloy with a

lower yield strength under otherwise identical conditions. This requires a higher number of load cycles. The increased plastic-zone size was reflected by an increase in affected crack-length as the yield strength decreased. The interferometry measurements to be described later also confirmed this. In general, the alloys do rank in terms of their retardation behavior according to their yield strengths with the 2024-T3 showing the maximum delay. These results are similar to those found by Gallagher and Hughes[25].

Effect of Metallurgical Factors

The effect of metallurgical factors on retardation behavior at a constant yield strength was determined by comparing the behavior of 2024-T8 and 7075-T73. As seen in Table VII, both of these alloys have essentially the same yield strength. Hence, according to the various models, they should show consistently similar retardation behavior under identical test conditions. However, by comparing the N* and a* values, it seems that the 7075-T73 alloy exhibits a slightly higher number of delay cycles in most of the cases. This is probably due to the differences in microstructure and cyclic hardening exponents as listed in Table VIII.

Effect of Strength Level and Microstructure Differences

The yield strength differences between the 2024-T3 and T8, and between the 7075-T6 and 7075-T73, are approximately the same. However, the difference in retardation behavior between the two sets (2024-T3 versus 2024-T8 and 7075-T6 versus 7075-T73) are not similar. The two conditions of 2024 alloys show a much greater difference in retardation behavior than the two conditions of 7075 alloy, as shown in Figures 26 and 27. These figures are from the results obtained at an overload ratio of 2.0 and 2.5. At an overload ratio of 1.5 (Figure 25), the difference between 7075-T6 and T73 was minimal, while that between 2024-T3 and T8 was still considerable. This appears to be due to a combined effect of yield strength and metallurgical (microstructure and/or cyclic hardening exponent) differences.

A qualitative analysis, as shown in Table VIII, was performed to analyze the observations. From this table, we concluded that, although the yield strength or microstructural differences in themselves alone influence the retardation behavior,

TABLE VIII. EFFECT OF VARIOUS FACTORS ON RETARDATION

| ALLOYS | CHEMICAL COMPOSITION[1] | METALLURGICAL | | YIELD STRENGTH | DIFFERENCES IN RETARDATION BEHAVIOR |
		MICRO-STRUCTURAL FEATURES[2]	CYCLIC HARDENING EXPONENT[3]		
7075-T6 vs 7075-T73	Similar	Similar (Primarily η' in both)	Similar	Different (73.1 vs 60.8 ksi)	SMALL[4]
7075-T73 vs 2024-T8	Different	Different (Primarily η' in T73 and S' in T8)	Different	Similar (60.8 vs 61.2 ksi)	SMALL[5]
2024-T3 vs 2024-T8	Similar	Different (Primarily G.P. zones in T3 and S' in T8)	Different	Different (51.7 vs 61.2 ksi)	LARGE[6]

1. The 7075-T6 and T73 conditions obtained from the 7075-T6 sheet, and the 2024-T3 and T8 conditions obtained from the 2024-T3 sheet.
2. See Figures 13 and 14 and Sections III A and III G.
3. See Table III.
4. See Figures 25(b) and 26(b) and Table VII.
5. See Table VII.
6. See Figures 25(a) and 26(a) and Table VII.

the synergistic effect of the two can be much greater. Hence, contrary to existing retardation models, which take only one material parameter (σ_{ys}) into consideration, σ_{ys} alone is not adequate for prediction of fatigue-crack growth under variable amplitude loading for a given test condition. Both the microstructural and yield strength differences should be considered in the development of a better retardation model.

Crack-Arrest Behavior

In this work, a crack was considered to be arrested if no significant measurable crack-growth took place in 500,000 constant-amplitude cycles after the overload cycle. As can be seen from Table VII, there is no case, not even in the 2024-T3 alloy where delay was highest, where crack-arrest was observed at OLR of 2.0 or below. This observation clearly indicates the need for modification of the original Willenborg model which predicts crack-arrest at an OLR of 2.0[17] (See Section IIIB-5 under Northrop Retardation Model). Crack-arrest was observed at either OLR of 2.5 or

3.0, depending on the alloy and K_{max}. For comparison purposes, the results at OLR of 2.5 and 3.0 are listed in Table IX for all the four alloys. In the 2024-T3 alloy, crack-arrest was observed at an OLR of 2.5 for all of the K_{max} values tested. It is possible that, for this alloy, the OLR for crack-arrest is between 2.0 and 2.5 for all the K_{max} values. In the case of the 2024-T8 alloy, an OLR of 3.0 at a relatively high K_{max} (11.1 ksi $\sqrt{in.}$) was required. This was probably due to the higher yield strength and cyclic hardening exponent (Table III) of 2024-T8 compared to 2024-T3.

For the 7075-T73 alloy, crack-arrest was observed at 2.5 OLR at a very high K_{max} value (19.8 ksi $\sqrt{in.}$) and at OLR of 3.0 for all the K_{max} values tested. Since the yield strength of the 2024-T8 and 7075-T73 alloys is the same, the differences in crack-arrest behavior are probably due to the differences in cyclic hardening exponent and microstructure of the alloys. The cyclic hardening exponents influences the "fatigue damage" and its accumulation at the crack-tip during cycling.

The 2024-T3 exhibited the best arrest behavior because all three parameters, i.e., the yield strength, microstructure, and cyclic hardening exponents, are favorable. The 7075-T6 alloy was next and showed a crack-arrest behavior which was somewhat superior to the 7075-T73, and the 2024-T8 alloy was poorest. The large difference between the 2024-T3 and 7075-T6 is due primarily to the large difference in their yield strength values. However, the difference between the 7075-T6 and T73 or 7075-T6 and 2024-T8 is contrary to what one would expect if yield strength alone was the governing factor in retardation. Hence, the other two factors, i.e., microstructure and cyclic hardening exponent play a role here. Based on the comparisons of retardation behavior of 7075-T73 and 2024-T8 alloys, the lower cyclic hardening exponent and 7075 type microstructure tend to favor increased retardation. The cyclic hardening exponent of the 7075-T6 is considerably lower than that for the 2024-T8 and slightly lower than the value for the 7075-T73 alloy (Table III). Hence, it appears that the microstructure and cyclic hardening exponents of the 7075-T6 alloy are more favorable for a higher retardation compared to that for the 7075-T73 and 2024-T8 alloys. At the high OLR values, they more than offset the negative influence of the higher yield strength of the 7075-T6. At low OLR, the 7075-T6 alloy does exhibit the poorest overall retardation behavior.

Hence, these results indicate that, beside the yield strength and the test conditions (K_{max} and OLR), the microstructure and cyclic hardening exponent of an alloy influence its retardation and crack-arrest behavior and, hence, should be considered in development of a better retardation model.

TABLE IX. SUMMARY OF RETARDATION RESULTS IN AIR AT OLR OF 2.5 AND 3.0 FOR 0.063-INCH THICK ALUMINUM ALLOYS

K_O/K_{MAX} (OLR)	P_{MAX} (LBS)	a_i (IN)	K_{MAX} (KSI$\sqrt{IN}$)	a^* (IN)	R_p^1 (IN)	N^* (1000)
			2024-T3			
		(σ_{ys} = 51.7 ksi, n' (cyclic hardening exponent) = 0.06)				
2.5	500	.5696	6.1		0.027	Arrest[2]
		.7132	7.7		0.044	Arrest
		.8402	9.3		0.064	Arrest
	800	.5668	9.8		0.071	Arrest
		.7976	13.9		0.140	Arrest
		1.0256	19.8		0.290	Arrest
			2024-T8			
		(σ_{ys} = 61.2 ksi, n' (cyclic hardening exponent) = 0.13)				
2.5	500	.573	6.2	0.0216	0.021	55
		.734	7.9	0.0280	0.033	65
		.869	9.7	0.0620	0.050	115
	800	.5696	9.8	0.0806	0.051	115
		.7976	13.9	0.1664	0.100	120
		1.0256	19.8	Failed During Overload Cycle		
3.0	500	.572	6.1	0.043	0.029	315
		.772	8.3	0.039	0.053	370
		.976	11.1		0.095	Arrest
			7075-T6			
		(σ_{ys} = 73.1 ksi, n' (cyclic hardening exponent) = 0.07)				
2.5	500	.5696	6.1	0.0428	0.014	350
		.7976	8.7	0.0894	0.028	130
		1.0256	12.3		0.056	Arrest
	800	.5696	9.8		0.036	Arrest
			7075-T73			
		(σ_{ys} = 60.8 ksi, n' (cyclic hardening exponent) = 0.09)				
2.5	500	.5796	6.2	0.0198	0.021	90
		.8076	8.9	0.0418	0.042	85
		1.0356	12.6	0.1892	0.085	165
	800	.5696	9.8	0.0704	0.081	130
		.7976	13.9	0.1666	0.100	180
		1.0256	19.8		0.210	Arrest[3]
3.0	500	.57	6.1		0.029	Arrest
		.79	8.7		0.059	Arrest

1 = Plane-stress overload plastic-zone
2 = No significant measurable crack-growth in 500,000 cycles
3 = Test stopped after 400,000 cycles

2. CRACK-CLOSURE BEHAVIOR

A series of crack-growth tests was performed using SEN specimens to determine the crack-closure changes due to single overload cycles. Two different closure detection techniques on two thicknesses of 7075-T6 were used to provide a more complete, reliable, and meaningful investigation within the scope of the program. Both the electrical potential and the strain gage techniques were used for crack-closure measurements before and after an overload cycle during the delay period. The strain gage technique met the "hysteresis loop" criteria for sensitivity as described by Elber[26]. The details of the experimental techniques used in this program, the results, and a discussion of their importance in retardation was reported in a technical paper entitled "Observation of Crack-Closure Behavior After Single Overload Cycles in 7075-T6 SEN Specimens," to be published in the Journal of Engineering Fracture Mechanics. For completeness, the paper is presented in its entirety as Appendix A. A summary of the results follows.

For the specimen geometry (SEN), alloy (7075-T6), and instrumentation used, we did not detect significant changes in crack-closure as the cycling progressed after the overload cycle even though some crack-closure was taking place during constant-amplitude cycling and crack-closure loads did vary with changes in R values. The small change in crack-closure after the overload cycle was not enough to explain the delay. However, after relaxation for 16 hours, as well as after a high overload ratio, significant crack-closure was observed by the potential method. This crack-closure disappeared within 200 cycles. Nevertheless, the overall conclusion from these observations is that insufficient changes in crack-closure were taking place to account for the observed number of delay cycles. These observations, which appear contrary to the crack-closure hypothesis, are in agreement with some of the other reported results. These results are applicable to the alloy, specimen geometry, thickness, and sensitivity of the instrumentation used in this investigation. This work clearly shows that the crack-closure hypothesis is not universally applicable and should be investigated further.

3. FRACTOGRAPHIC CHANGES

The scanning electron microscope (SEM) was used to determine fractographic characteristics of various failed retardation specimens. The fracture surfaces of

the overload specimens were examined to understand the micromechanisms of crack-growth due to the overload with special attention to:

- The nature of the overload region - the occurrence of stretch-zone dimples, abrasion, etc., and their relationship to the plastic-zone size.

- The dependence of the overload-zone character on the alloy microstructure, its properties, and the stress-intensity level.

- The effect of single overload cycles on the microscopic crack-growth rate as indicated by the changes in striation spacings.

For this purpose, fractographs were obtained from areas (1) before overload, (2) in the overload stretch band, and (3) at several locations in the retardation zone, as shown in Figure 28. This figure shows a composite of fractographs taken from a 7075-T6 specimen. The testing conditions are indicated in the figure. The overload cycle manifested itself as a stretch band across the thickness of failed specimens in almost all the cases, as indicated in Figure 28. Fractographs 1 and 2 show transgranular dimples characteristic of overload rupture. Fractograph 3A exhibits an area of apparent cleavage failure. Facets in fractographs 4B and 5C have fatigue striations which could be seen very clearly at higher magnifications. In addition to the overload dimples, cleavage, and fatigue striations, areas of inclusion fracture are visible in most fractographs.

In this particular specimen, changes in striation spacings, as illustrated in Figure 29, were seen. In this figure, the point of overload was used as a reference point and fractographs were obtained at points before and after the overload. The details of testing and distance of points from the overload location are shown in the figure. The striation spacings were correlated with the measured da/dN, as shown in Figure 30. In this case, there was good agreement between the measured da/dN and the striation spacings. However, striations were not observed at crack-growth rates below 3×10^{-6} in./cycle. Also, no striations were observed immediately after the overload cycle. The lack of discernable striations in these cases could be due to abrasion or due to the difficulty in resolving striations associated with relatively low crack-growth rates or due to a change in crack-propagation mode or a combination of all these factors. Because of this, neither well defined striations nor changes in striation spacings after each overload were seen. These and other observed differences in fractographic features due to overload cycles are described below.

CRACK-GROWTH DIRECTION

OVERLOAD STRETCH ZONE

BASELINE P_{MAX} (K_{MAX}): 500 LBS (13.7 KSI $\sqrt{IN.}$)
OVERLOAD RATIO: 2
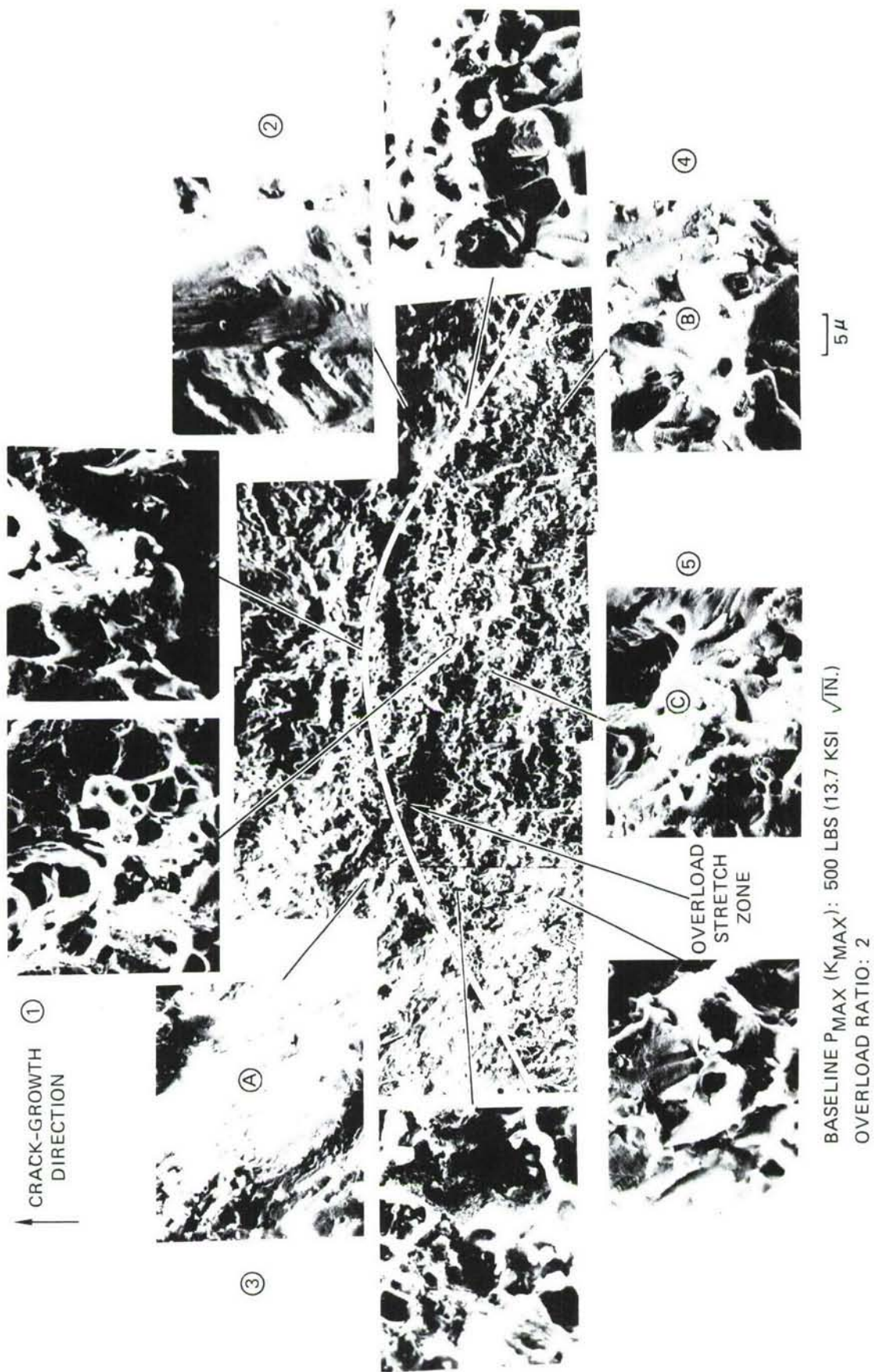
FIGURE 28. FRACTOGRAPHIC CHANGES DUE TO A 100% OVERLOAD CYCLE IN 7075-T6 ALLOY

58

BEFORE OVERLOAD =-0.014-IN.

OVERLOAD REGION = 0

BEYOND OVERLOAD = +0.009-IN.

+0.012-IN.

+0.018-IN.

1μ

+0.042-IN.

+0.047-IN.

+0.058-IN.

BASELINE P$_{MAX}$ (K$_{MAX}$) : 500 LBS (13.7 KSI $\sqrt{IN.}$)
OVERLOAD RATIO: 2
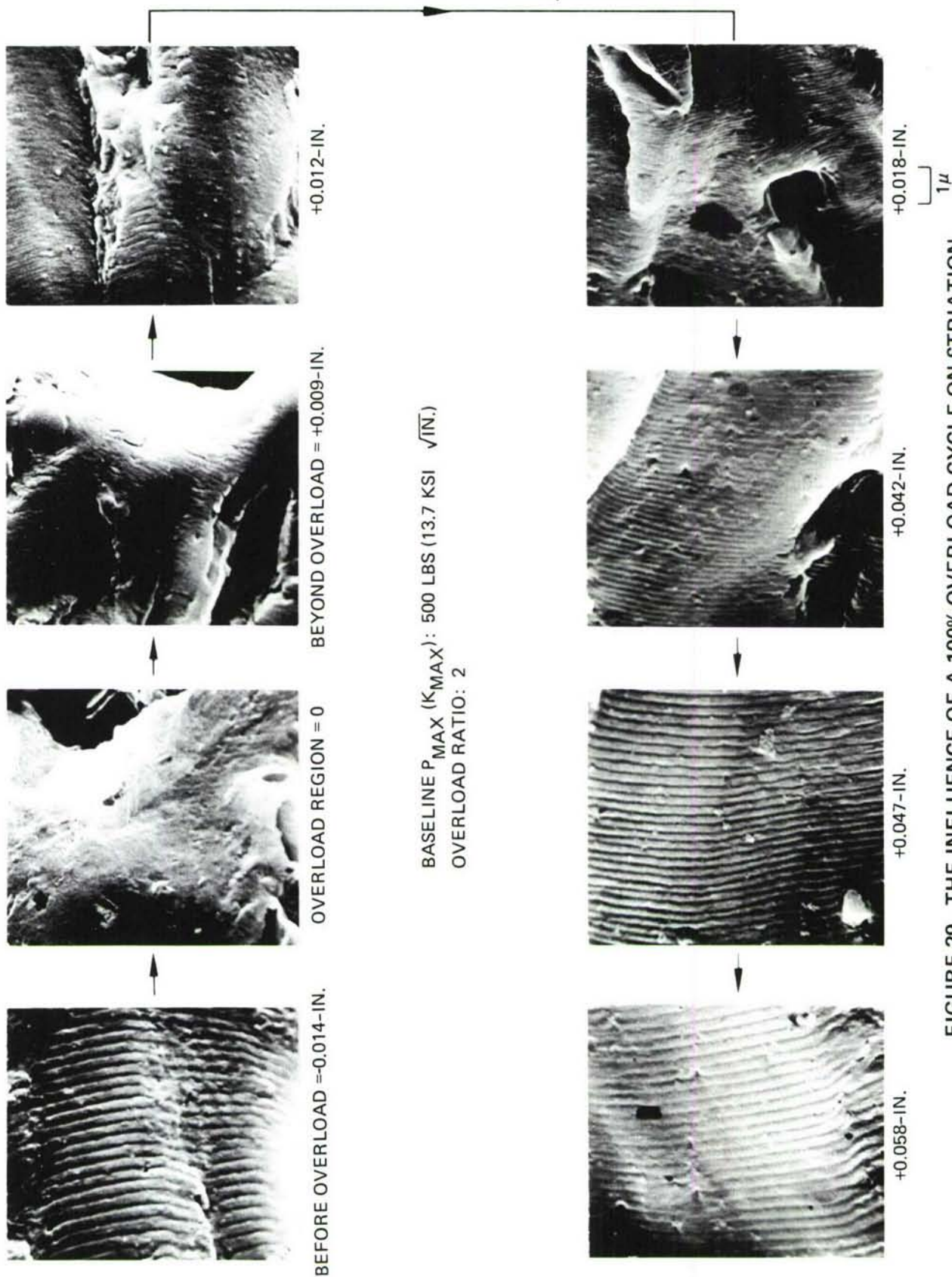
FIGURE 29. THE INFLUENCE OF A 100% OVERLOAD CYCLE ON STRIATION
SPACINGS IN 7075-T6 ALUMINUM ALLOY

59
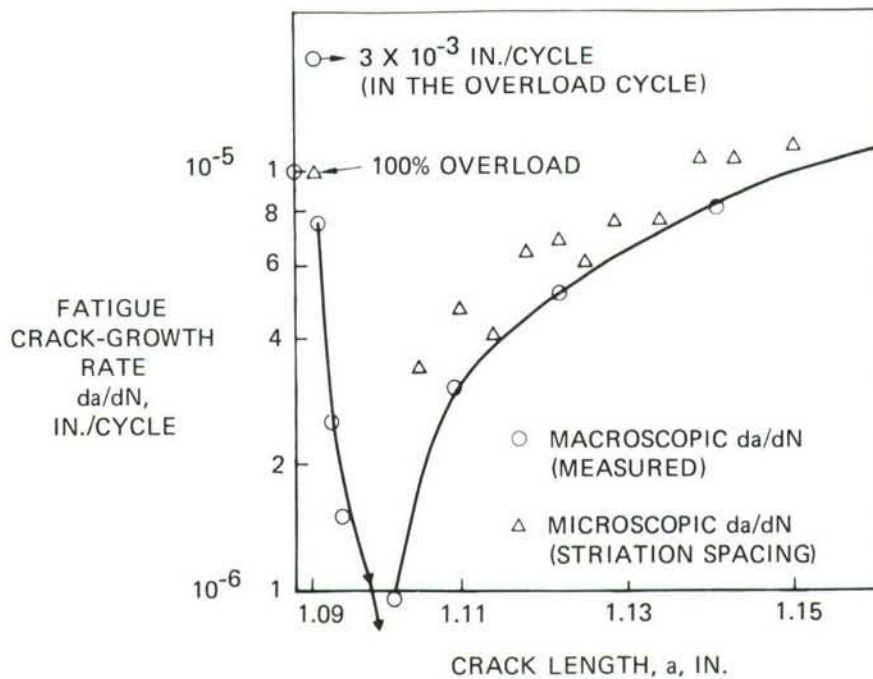
FIGURE 30. INFLUENCE OF 100% OVERLOAD ON SUBSEQUENT CRACK-GROWTH RATES IN AIR FOR 7075-T6 ALLOY

2024 Alloy

Figure 31 shows composite fractographs of the single overload regions obtained from two 2024-T3 and T8 retardation specimens at an OLR of 2.0 and K_{max} of 17.4 ksi $\sqrt{in.}$ The testing conditions were identical for the two specimens. The overload band or stretch zone (marked with arrows, A and B) associated with the incremental crack-growth during the rising-load portion of the overload cycle is marked by a heavily dimpled region. The tunneling effect (arrows C and D) in the stretch zone, as shown in both of the composites in Figure 31, is due to the relatively plane-strain condition along the midsection of the specimen. Immediately following the stretch marking is the retardation zone marked by a rather smooth topography, characteristic of a very low FCP rate. As one proceeds further away from the overload region, the topography of the fracture surface becomes increasingly similar to that which was present before the overload due to the recovery of the constant amplitude crack-growth rate.

60
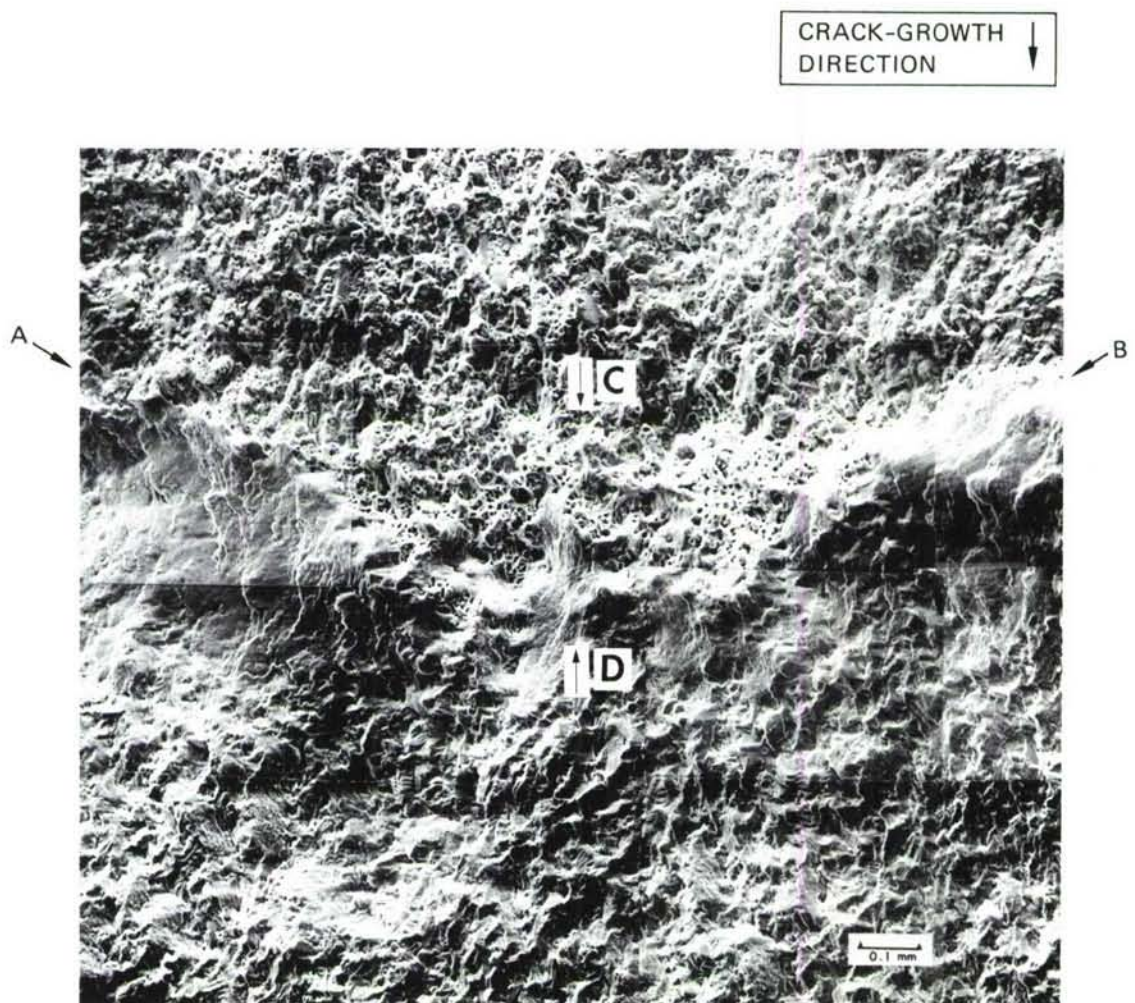
(a) 2024-T3

BASELINE P_{MAX} (K_{MAX}) = 1000 LBS (17.4 KSI $\sqrt{IN.}$)
OVERLOAD RATIO (OLR) = 2.0

**FIGURE 31. FRACTOGRAPHIC FEATURES IN THE VICINITY OF A 100% OVERLOAD
MARKING IN 2024 ALLOY**
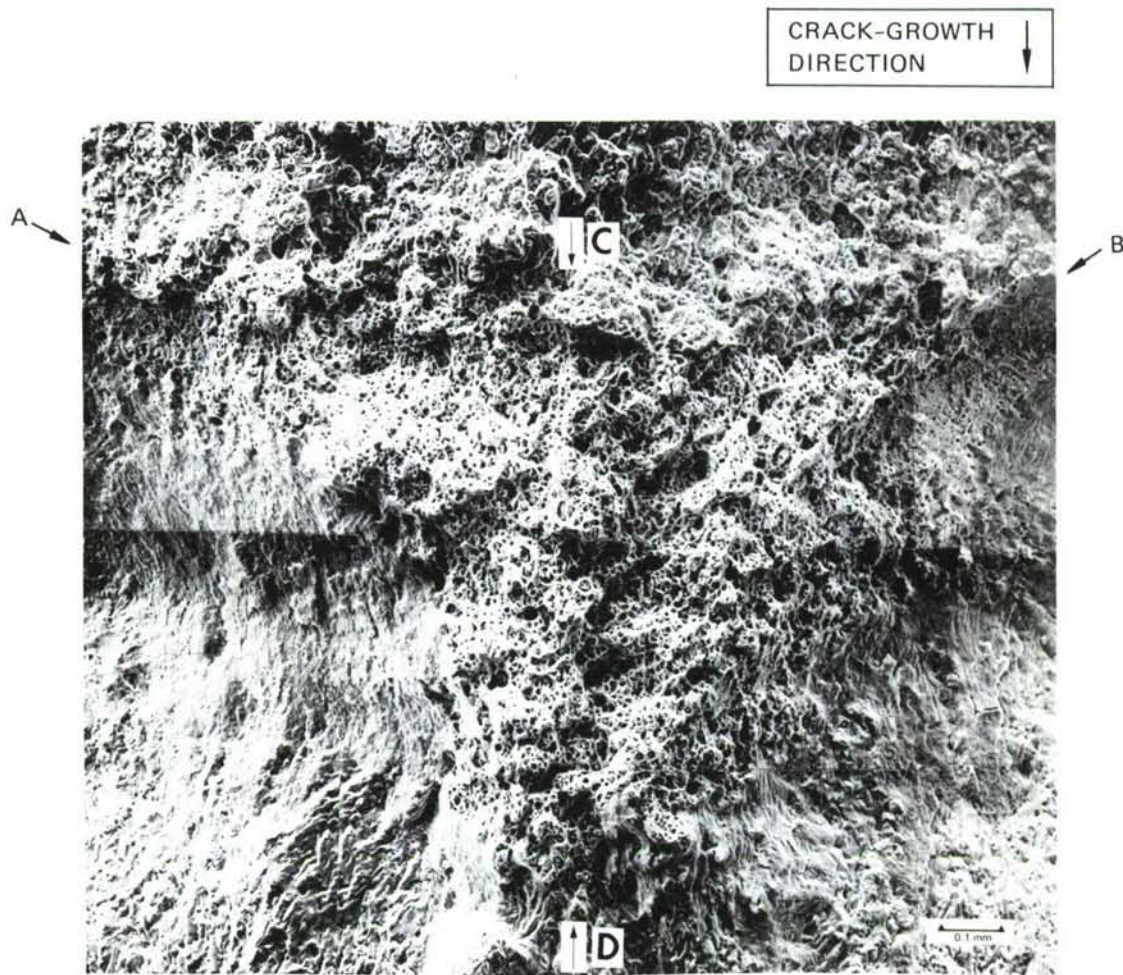
(b) 2024–T8

BASELINE P_{MAX} (K_{MAX}) = 1000 LBS (17.4 KSI $\sqrt{IN.}$)
OVERLOAD RATIO (OLR) = 2.0

FIGURE 31. FRACTOGRAPHIC FEATURES IN THE VICINITY OF A 100% OVERLOAD
MARKING IN 2024 ALLOY (Continued)

In comparing overload regions under similar conditions in the T3 and T8 conditions, the most obvious difference is the larger width of the dimpled region in the T8 compared to that in the T3. This could be attributed to two factors; one is the higher crack-growth rate in the T8 condition at the same overload stress-intensity factor as compared to that for the T3 condition, and the other is the lower fracture toughness in the T8 condition which causes more sub-critical crack-growth during the rising-load portion of the overload cycle.

The effect of the stress-intensity level on the size and nature of the overload region in 2024 can be seen in the fractographs shown in Figure 32. As would be anticipated, the width of the overload stretch zone and the associated retardation region increases with increasing K level, progressing from a thin line at low stress intensity levels (Figure 32 (a) and (c))to a wide band of overload exhibiting tunneling at higher K values (Figure 31). Figure D-11 of Appendix D also shows similar results for the 2024-T3 at three different K levels. Tunneling is visible in Figure 32(d) for the 2024-T8 specimen where the K level is not much higher than that for the T3 specimen in Figure 32(b). This probably occurred because in the T8 condition, the overload K is a large fraction of the fracture toughness.

7075 Alloy

Figure 33 shows composites of fractographs from the single overload regions of the 7075-T6 and T73 retardation specimens at an OLR of 2.0 and K_{max} of 17.4 ksi$\sqrt{in.}$ Both fractographs exhibit the dimpled stretch zone and the ensuing retardation region of smooth topography. Comparison of the two fractographs in Figure 33 shows slightly more tunneling in the T6 condition than in the T73 condition. The difference in tunneling here is less than that between the 2024-T3 and T8 conditions (Figure 33 (a) and (b)).

In comparing the size of tunneling and dimpling in 2024 alloy with the 7075 alloy, the zone-size of the 7075-T6 and T73 fall in between those for the 2024-T3 and T8. The overload region, including dimpling, seen in both the 7075-T6 and T73 alloys, is larger than that in the 2024-T3 and smaller than that of the 2024-T8. This behavior is in agreement with the delay behavior observed during testing. The 2024-T8 alloy shows the least amount of delay, while the 2024-T3 alloy shows maximum delay with the 7075-T6 and T73 alloys showing slightly higher delay than the 2024-T8 alloy.

63

CRACK-GROWTH
DIRECTION
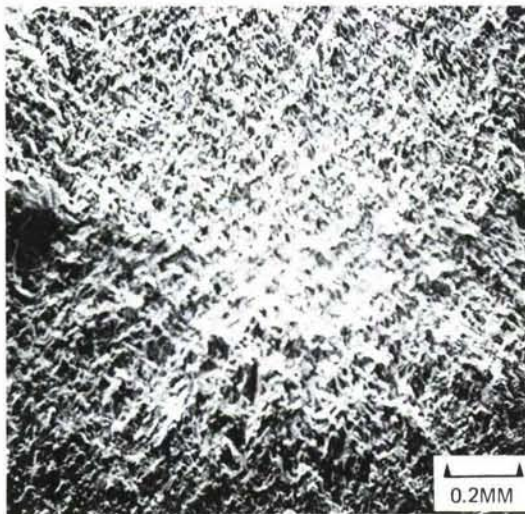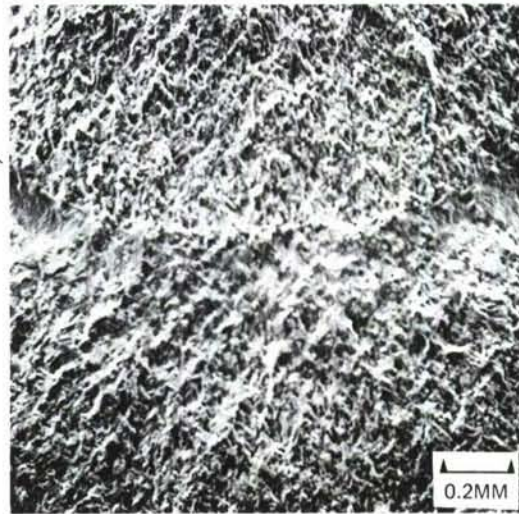
(a) 9.8 KSI $\sqrt{\text{IN.}}$

(b) 12.1 KSI $\sqrt{\text{IN.}}$

2024-T3
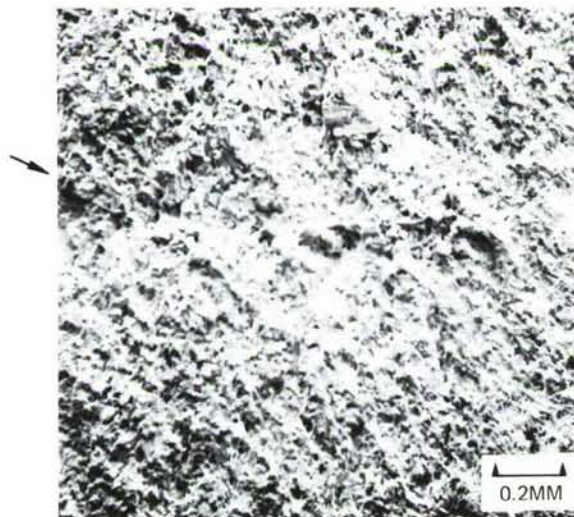
(c) 9.8 KSI $\sqrt{\text{IN.}}$
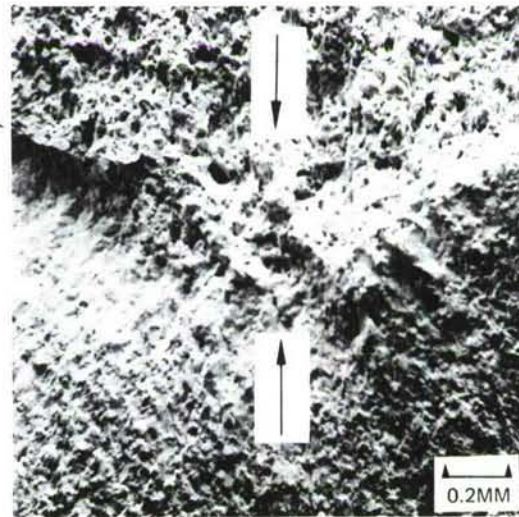
(d) 14.0 KSI $\sqrt{\text{IN.}}$

2024-T8

BASELINE P_{MAX} = 800 LBS

OVERLOAD RATIO = 2.0

FIGURE 32. FRACTOGRAPHS SHOWING EFFECT OF BASELINE STRESS-INTENSITY (K_{MAX}) AFTER A 100% SINGLE OVERLOAD CYCLE IN 2024

64

A B
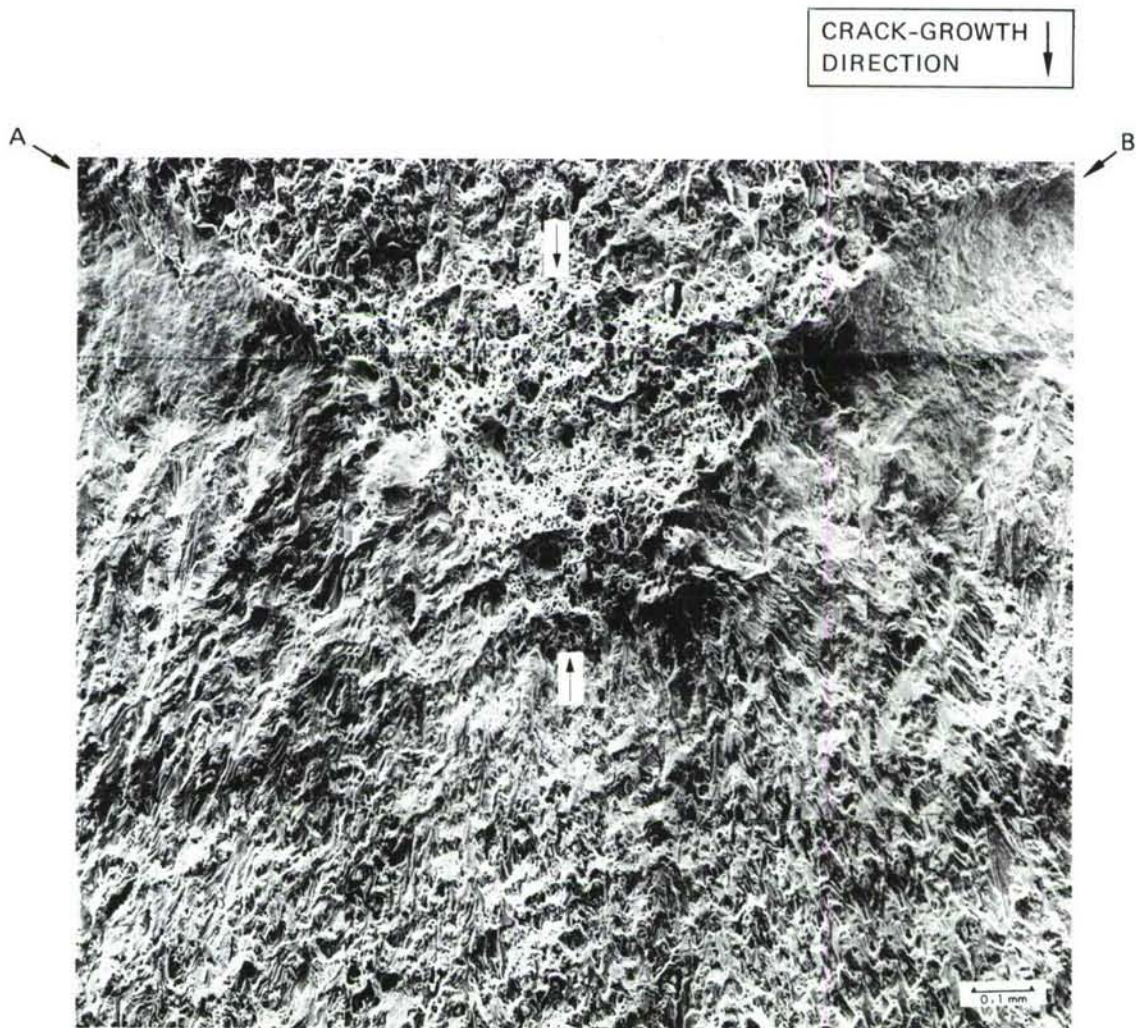
(a) 7075-T6

BASELINE P_{MAX} (K_{MAX}) = 1000 LBS (17.4 KSI $\sqrt{IN.}$)
OVERLOAD RATIO (OLR) = 2.0

FIGURE 33. FRACTOGRAPHIC FEATURES IN THE VICINITY OF A 100% OVERLOAD
CYCLE MARKING IN 7075 ALLOY
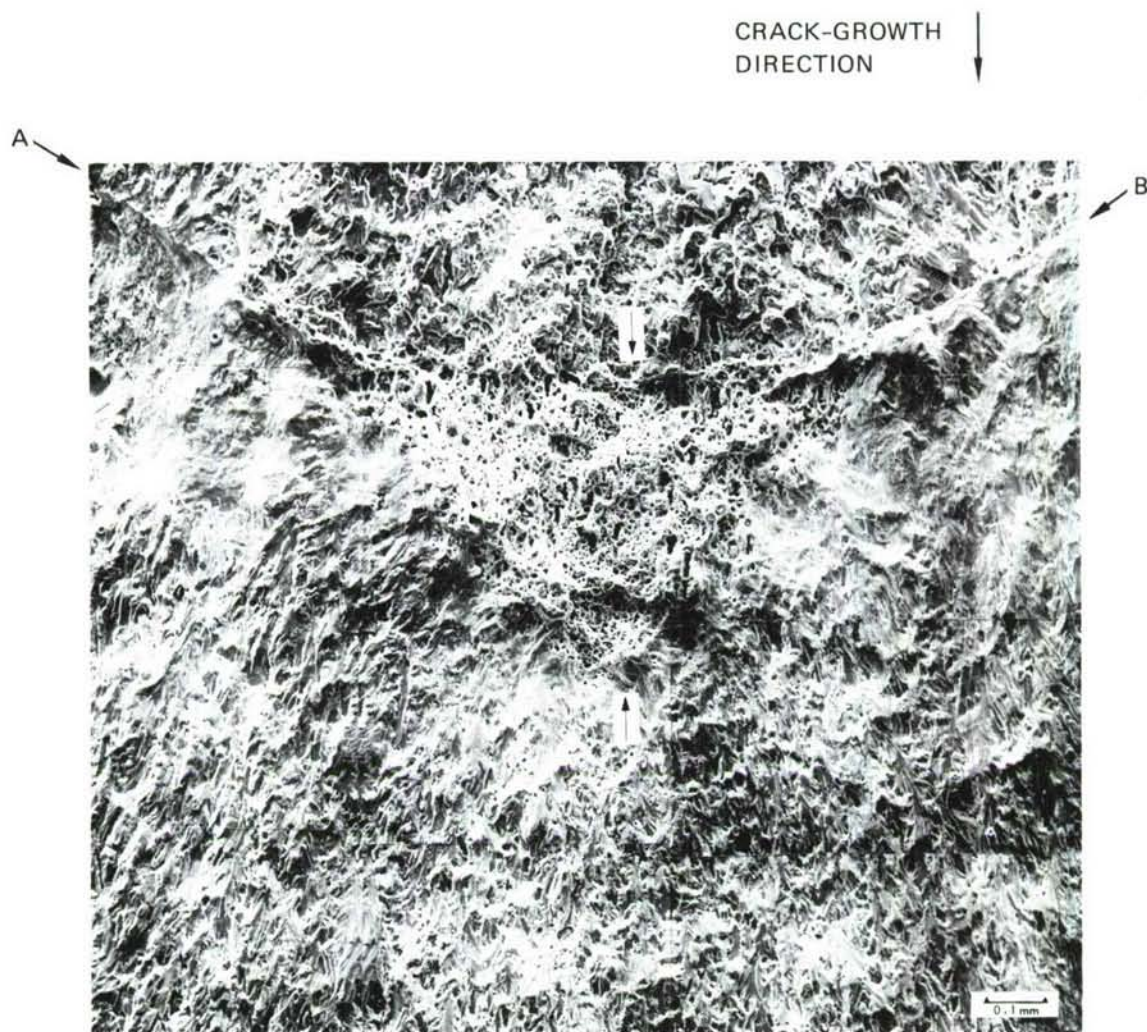
(b) 7075–T73

BASELINE P_{MAX} (K_{MAX}) = 1000 LBS (17.1 KSI $\sqrt{IN.}$)
OVERLOAD RATIO (OLR) = 2.0

FIGURE 33. FRACTOGRAPHIC FEATURES IN THE VICINITY OF A 100% OVERLOAD
CYCLE MARKING IN 7075 ALLOY (Continued)

The effect of stress-intensity level on the size and nature of the overload region in the 7075-T6 and T73 alloys can be seen in the fractographs in Figure 34. Figure C-9 of Appendix C also shows similar results for the 7075-T6 at three different K_{max} levels. As expected, there is more dimpling and tunneling at the higher K levels. Here, as in Figure 32 for the 2024 alloys, the increased stress-intensity was obtained by increasing the crack-length at the same baseline load. The differences in the over-load stretch markings become much more striking when the differences in the K_{max} levels are large, as shown in Figures 31 (b) and 35. Here, the K_{max} varied from 8 to 17 ksi $\sqrt{in.}$ with three different baseline P_{max} values while the crack-lengths at the overload cycle were essentially the same. Figure 35 (a) shows a somewhat faint overload marking due to a single overload cycle with an overload ratio of 2.0 at a baseline load of 500 lbs. and a crack-length of 0.731-in. The width of the retardation zone is not readily apparent in this case, whereas in Figure 35 (b), more extensive dimples and clear-cut markings are seen with a P_{max} of 800 lbs. at the same overload ratio and crack-length as that used for Figure 35 (a) because of the higher K value (14 ksi $\sqrt{in.}$ versus 8 ksi $\sqrt{in.}$). Here, the smooth retardation zone is easily seen. A comparison of the region preceeding the overload cycle in Figure 35 (a) and (b) reveals a rougher surface in Figure 35 (b) than in Figure 35 (a) due to the higher applied load. This is caused by more tearing as the crack propagates with the higher load. Figure 31b shows the overload region in the 2024-T8 alloy at a baseline load of 1000 lbs. with the same crack-length and an overload ratio of 2.0. The occurrence of extensive dimpling and tunneling during the overload cycle is evident. The overload marking is much more pronounced with the high load because of the higher K level (17.4 ksi $\sqrt{in.}$). Also, the fracture surface prior to the overload cycle shows a marked resemblance to an overload mode of crack propagation with a lower incidence of striations observed at high magnifications.

As discussed in the earlier part of this section, changes were seen in striation spacings, as illustrated in Figure 30. The striation spacings were correlated with the measured da/dN values in several selected specimens. Some of these results are shown in Figures 36 and 37. As indicated earlier, at crack-growth rates below 3×10^{-6} in./cycle, striations were not observed. Also, no striations were observed imme-diately after the overload cycle. Nevertheless, for the specimens in which striations were discerbible, the agreement between measured da/dN and striation spacings was reasonably good.

CRACK-GROWTH
DIRECTION
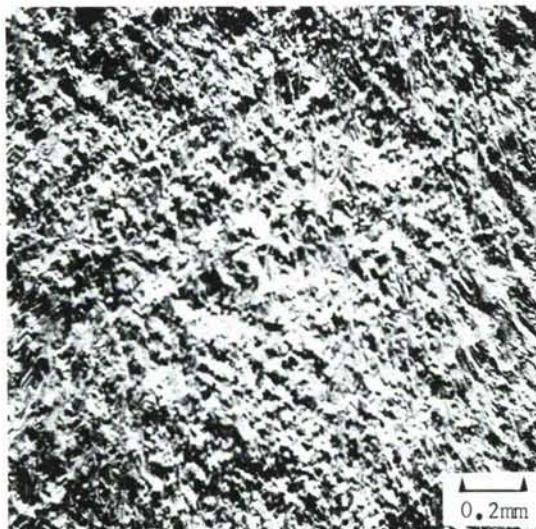
(a) 9.8 KSI √IN.
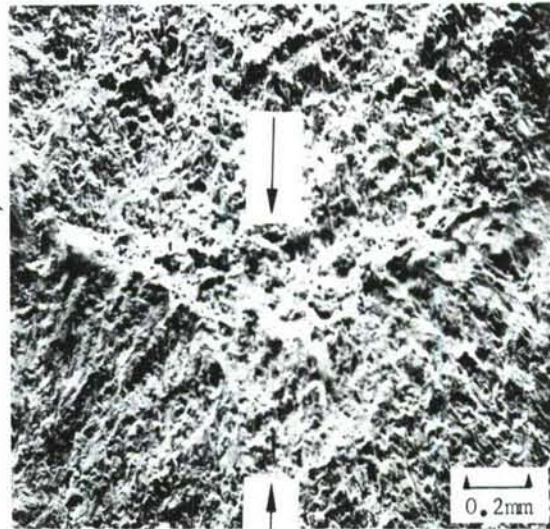
(b) 13.9 KSI √IN.

7075-T6
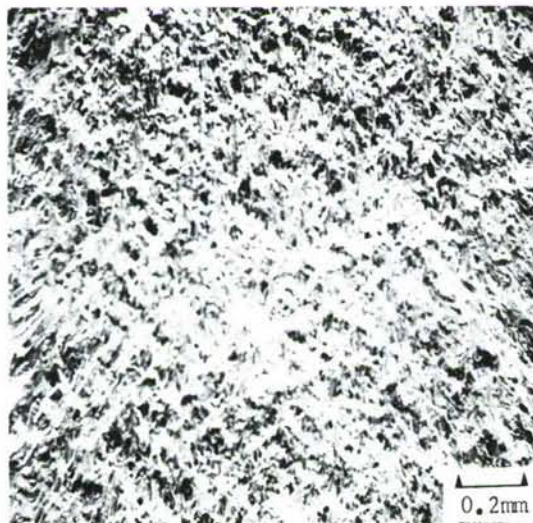
(c) 10.1 KSI √IN.
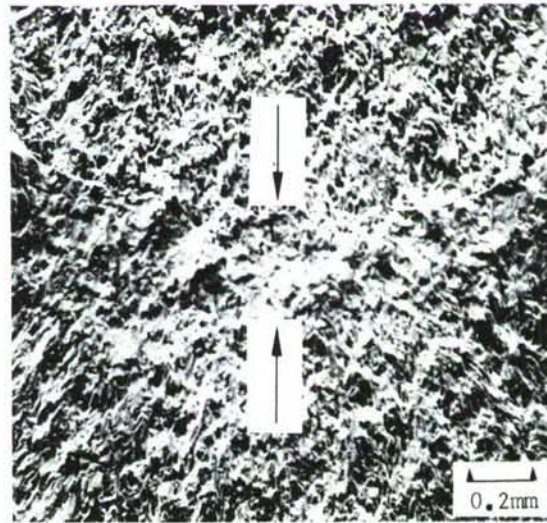
(d) 14.4 KSI √IN.

7075-T73

BASELINE P_{MAX} = 800 LBS

OVERLOAD RATIO = 2.0

FIGURE 34. FRACTOGRAPHS SHOWING EFFECT OF BASELINE STRESS-INTENSITY
(K_{MAX}) AFTER A 100% OVERLOAD CYCLE IN 7075

68
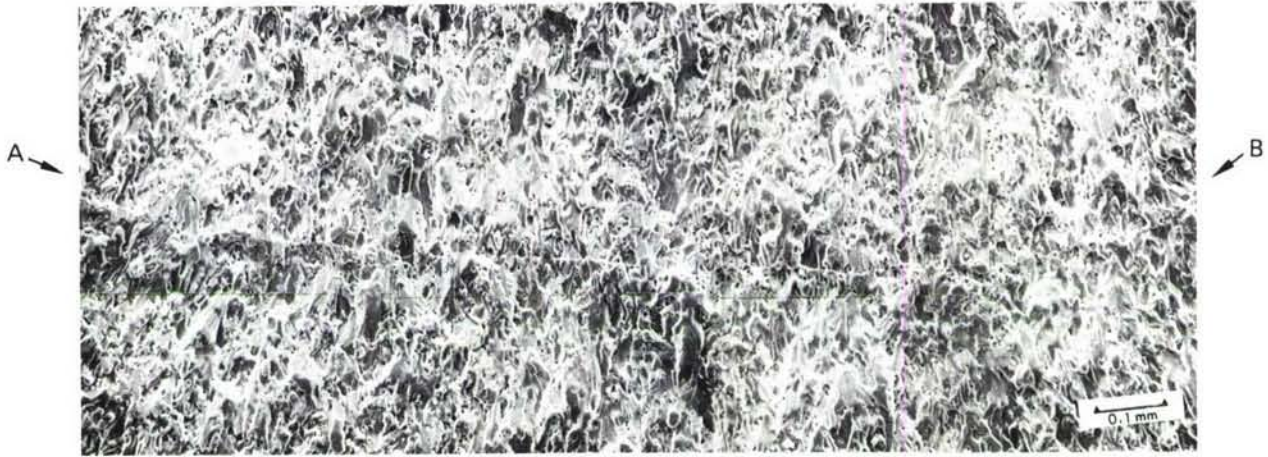
(a) BASELINE P_{MAX} (K_{MAX}): 500 LBS (7.9 KSI $\sqrt{IN.}$)
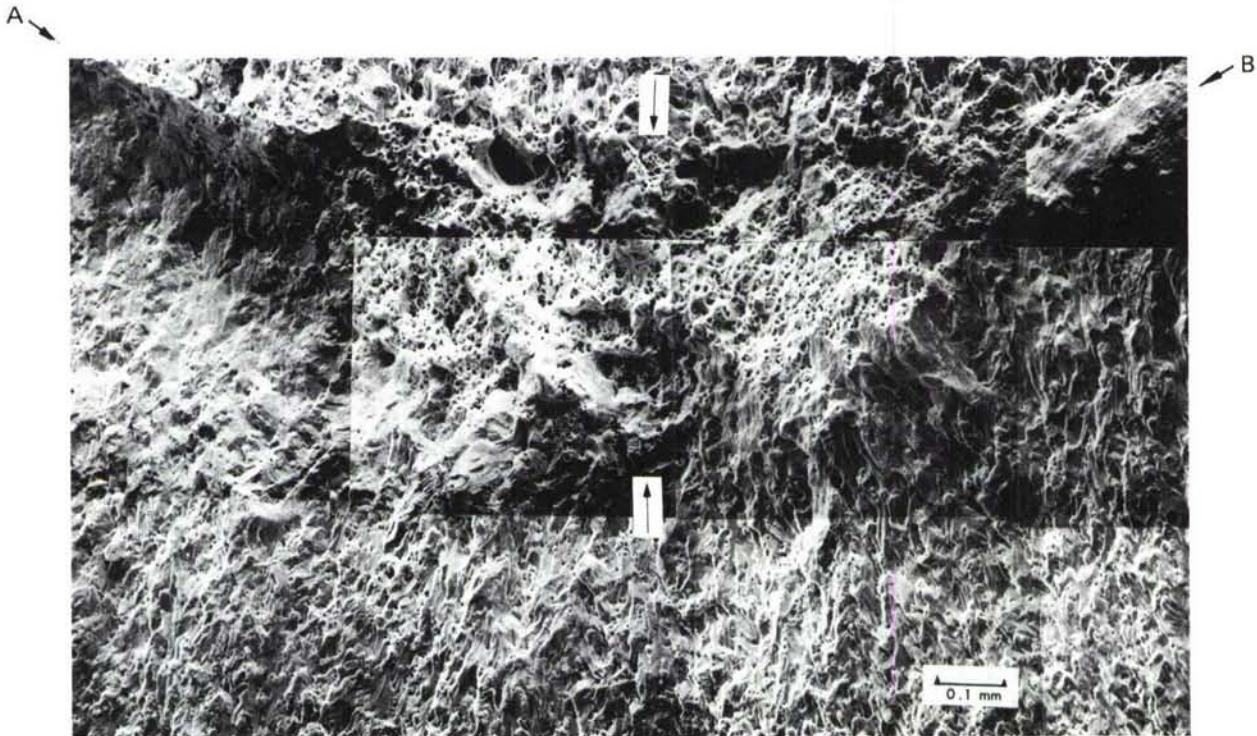
(b) BASELINE P_{MAX} (K_{MAX}): 800 LBS (13.9 KSI $\sqrt{IN.}$)

FIGURE 35. FRACTOGRAPHIC FEATURES IN THE VICINITY OF A 100% OVERLOAD
CYCLE (OLR = 2.0) IN 2024-T8
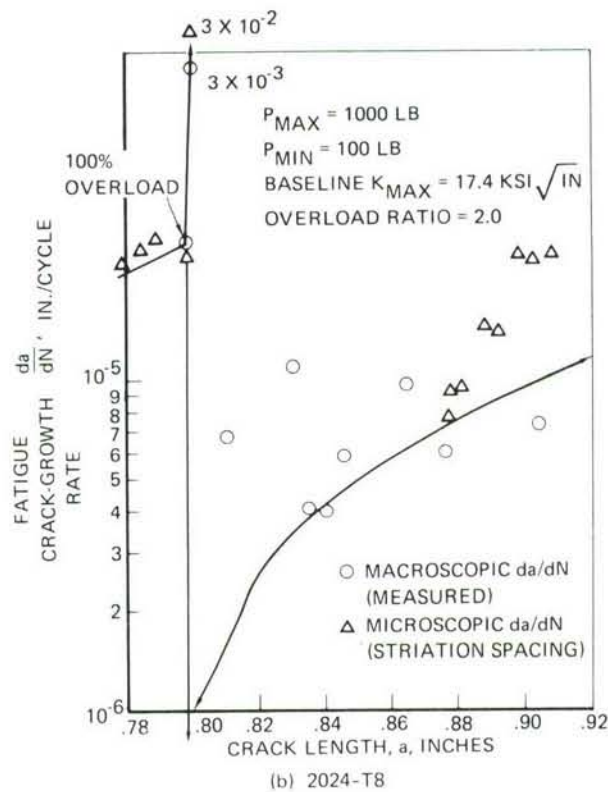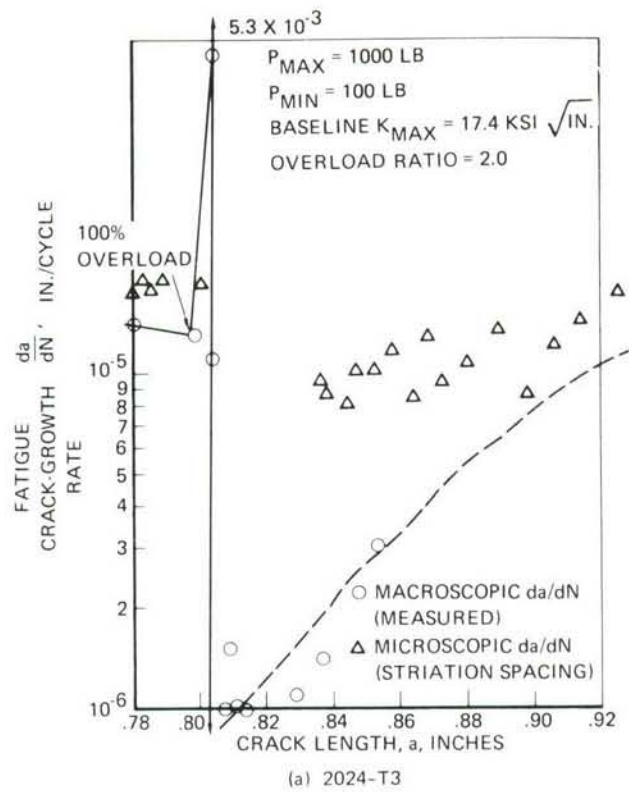
FIGURE 36. THE INFLUENCE OF 100% OVERLOAD CYCLE ON SUBSEQUENT
CRACK-GROWTH RATES IN AIR FOR 2024 ALLOY

70
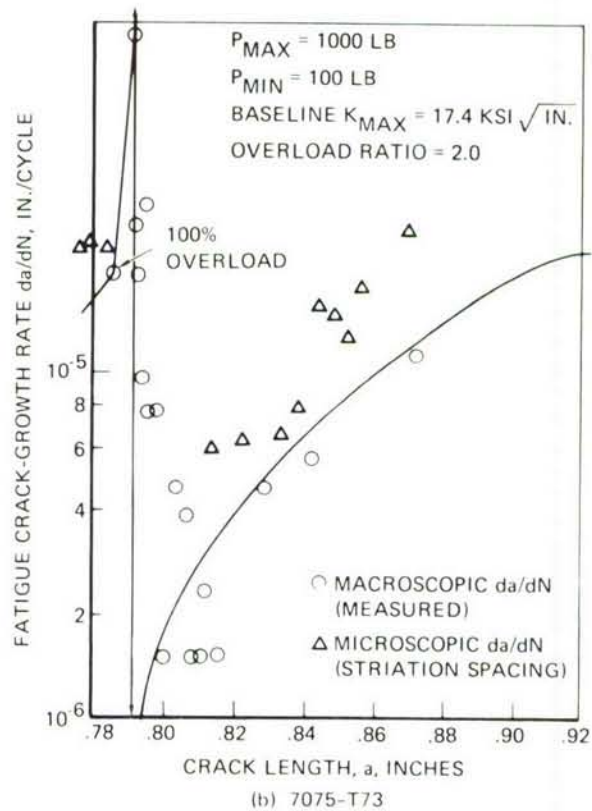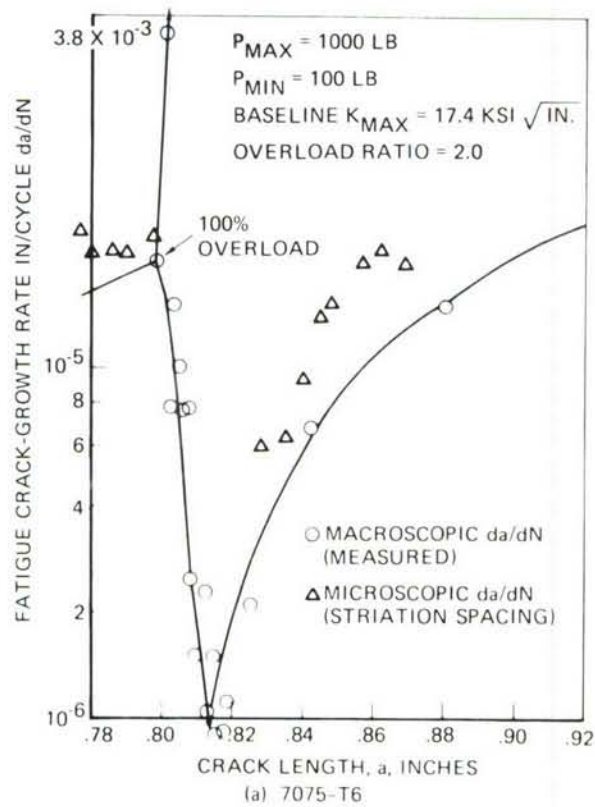
FIGURE 37. THE INFLUENCE OF 100% OVERLOAD CYCLE ON SUBSEQUENT
CRACK-GROWTH RATES IN AIR FOR 7075 ALLOY

4. INTERFEROMETRY STUDIES

Plastic-zone sizes were determined for cyclic loading and an experimental correlation was made between observed plastic-zones, fatigue-crack retardation and the affected crack-length (a*) to establish the importance of the plastic zone with regard to FCP and retardation. An optical interference technique was found to give a reliable measurement of the plastic-zone size, under plane-stress conditions, for the 0.063-in. thick SEN specimens. Figure 38 shows interference patterns obtained from five 7075-T6 SEN specimens with different overload cycles. In all of these specimens, the crack was grown to a length of 0.8-in. under constant-amplitude load cycling with a maximum load of 800 lbs. and an R of 0.1 (K_{max} at 0.8 in. = 13.9 ksi $\sqrt{in.}$). Interference patterns were normally obtained at zero load and within 8 hours of the application of overload cycle. For this work, the boundary outlining changes in fringe patterns at the crack-tip was used to define the plastic-zone. Differences between the various overload strain patterns and plastic-zone sizes at the crack-tip of the specimens are clear. Even though the fringe direction and width in a given specimen can change by minor adjustments of the interference microscope, the plastice-zone size estimate using interference patterns remained unchanged.

The measured plastic-zone sizes were in good agreement with the calculated values for the 7075-T6 alloy as shown in Figure 39. The overload plastic-zone size was calculated using the simplified formula, for the plane-stress condition, given below:

$$R_p = \frac{1}{\pi} \left(\frac{K_o}{\sigma_{ys}} \right)^2 \tag{4}$$

Similar interferometry patterns were obtained at selected overload ratios for all four alloys. Table X summarizes the measured overload plastic-zone sizes from these observations. For comparison, the calculated plane-stress plastic-zone sizes are also listed in this Table. The agreement between the measured and the calculated plastic-zone sizes for all four alloys is reasonably good. Based upon the above expression, (4), the plastic-zone sizes for 7075-T73 and 2024-T8 alloys after a given K_o should be the same. The measured plastic-zone sizes for the 2024-T8 alloy were consistently smaller than those for the 7075-T73 alloy at the same K_o values, and hence, could not be attributed to experimental scatter. These differences are probably due to the microstructure and cyclic hardening exponent values of the two alloys. The 2024-T8 has a higher cyclic hardening exponent (0.13) than does the 7075-T73 alloy (0.09). The smaller plastic-zone size of the 2024-T8 alloy is probably responsible for the poor retardation behavior of the 2024-T8 alloy as compared to the 7075-T73 alloy of the same yield strength.
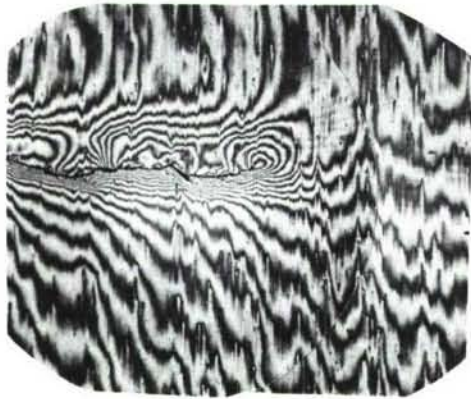
(a) OLR = 1.0
(NO OVERLOAD)
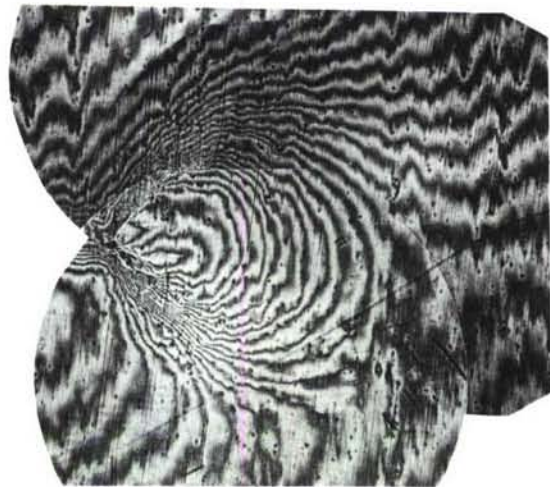
(b) OLR = 1.5

(c) OLR = 1.8

(d) OLR = 2.0
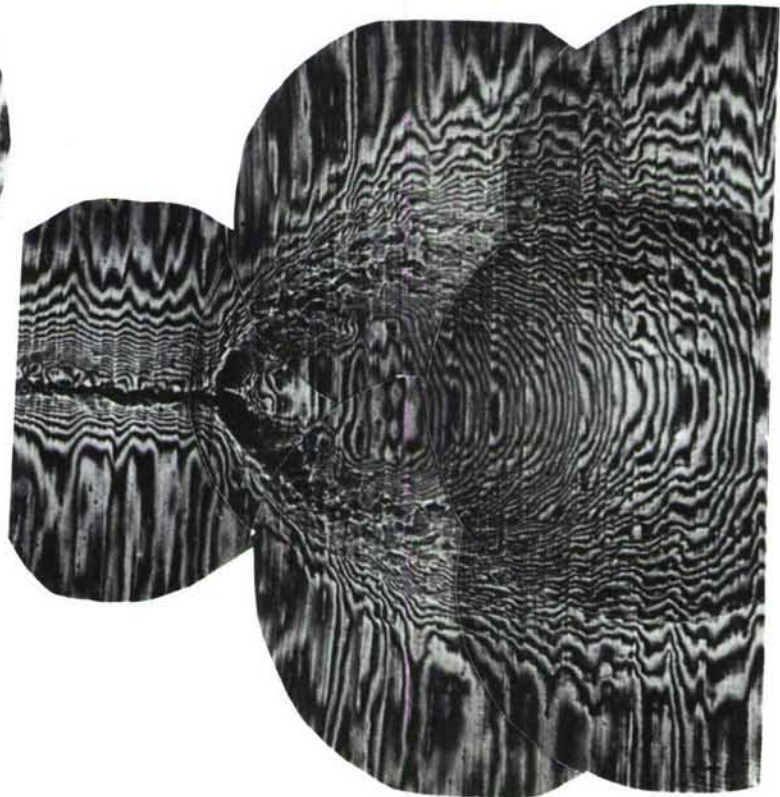
(e) OLR = 2.5

P_{MAX} (K_{MAX}) = 800 LBS (13.9 KSI $\sqrt{IN.}$)

CRACK-LENGTH = 0.800-IN.

0.3MM

FIGURE 38. OPTICAL INTERFERENCE PATTERNS AT THE CRACK-TIP OF
7075-T6 SEN SPECIMENS AFTER DIFFERENT OVERLOAD CYCLES

73
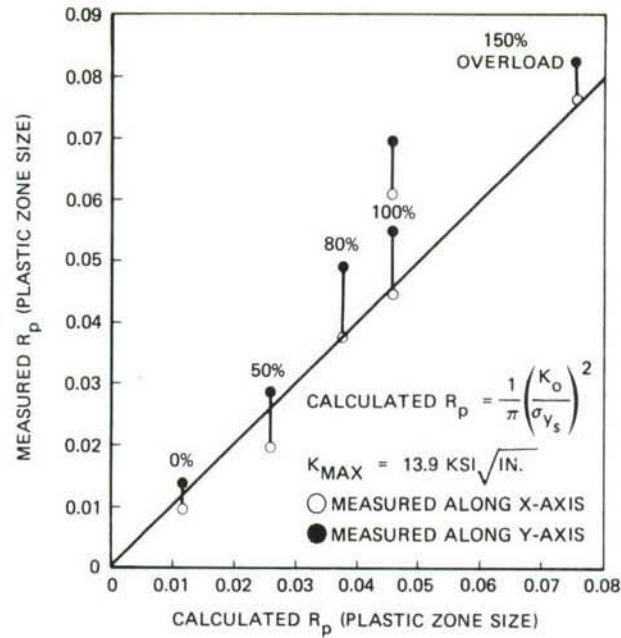
FIGURE 39. COMPARISON OF CALCULATED AND MEASURED PLASTIC-ZONE SIZES IN 7075-T6, 0.063-IN. THICK SEN SPECIMENS AFTER DIFFERENT OVERLOADS

TABLE X. A COMPARISON OF CALCULATED AND MEASURED
PLASTIC-ZONE SIZES FOR THE FOUR TEST ALLOYS

ALLOY	P_{max} (lbs)	K_{max} (ksi $\sqrt{in.}$)	SPECIMEN NO.	K_o/K_{max} (OLR)	CALCULATED R_p (In.)	MEASURED R_p APPROX. IN.	
						X ORIENTATION	Y ORIENTATION
7075-T6	800	13.9	INT-LW-0	1.0	.0115	0.01	0.014
			INT-LW-50	1.5	.0259	0.02	0.028
			INT-LW-80	1.8	.0373	0.038	0.05
			INT-LW-100	2.0	.0460	0.046	0.065
			DT6INT2	2.0	.0460	0.0605	0.069
			DT6INT1	2.5	.0719	0.077	0.081
	500	8.7	DT6INT3	2.0	.0182	0.0171	0.025
7075-T73	800	13.9	DT73INT2	2.0	.0666	0.067	0.077
			DT73INT1	2.5	.1040	0.084	0.088
	500	8.7	DT73INT3	2.0	.0263	0.022	0.0313
2024-T3	800	13.9	DT3INT2	2.0	.0920	0.087	0.087
			DT3INT1	2.5	.1438	0.114	0.112
	500	8.7	DT3INT3	2.0	.0365	0.030	0.0389
2024-T8	800	13.9	DT8INT2	2.0	.0657	0.057	0.060
	500	8.7	DT8INT3	2.0	.0260	0.0195	0.0247

NOTE 1: Calculated $R_p = \frac{1}{\pi}\left(\frac{K_o}{\sigma_{ys}}\right)^2$

NOTE 2: ORIENTATION:

NOTE 3: All the measurements were made on 0.063 in. thick SEN specimens at a crack-length of 0.8 in.

74

The importance of the plastic-zone in retardation was determined by correlating the changes in interference patterns as the crack passed through the plastic-zone with the observed crack-growth behavior. For this purpose, interference patterns were obtained (a) immediately after the overload cycle, (b) when the crack was halfway through the plastic-zone, and (c) when the crack was beyond the plastic-zone. The retardation behavior of these specimens was also measured. Figures 40 and 41 show the correlation of these data for the 7075-T6 alloy after a 50% and an 80% overload cycle, respectively. The figures show the excellent correlation between the retardation behavior, the affected crack-length, and the overload plastic-zone. The overload plastic-zone has been outlined in these figures. As seen, the maximum retardation developed before the crack was halfway through the plastic-zone, and recovery was complete once the crack was completely out of the plastic-zone. Results for a 7075-T6 specimen after a 100% overload cycle are shown in Figure D-10 of Appendix D. Similar correlations were obtained for the other alloys at selected overload ratios.

Thus, the interferometry results clearly show the applicability of this technique for indicating how the crack-growth behavior changes as the crack progresses through the plastic-zone under plane-stress conditions, and they also confirm that the retardation occurs in the overload plastic-zone.

5. NORTHROP RETARDATION MODEL

This section briefly describes the background and development of a new crack-growth retardation model based in part on the test data generated in this program. Compared to the existing models, this model more accurately represents crack-growth experienced in this program and other recent test programs conducted at Northrop.

Although the new model is intended to eventually replace the Willenborg model,[17] at present it has been added to the Northrop crack-growth computer program (NORCRAK) as an option which can be specified by the user of the program.

Background - Willenborg Retardation Model

Engineers have realized for some time that both microscopic fatigue damage and macroscopic crack growth can be temporarily retarded by the application of a high load that imparts beneficial residual stresses in the damaged area. With further application of lower loads, this zone of residual stress decays or is eventually penetrated and non-retarded (crack growth) eventually resumes.
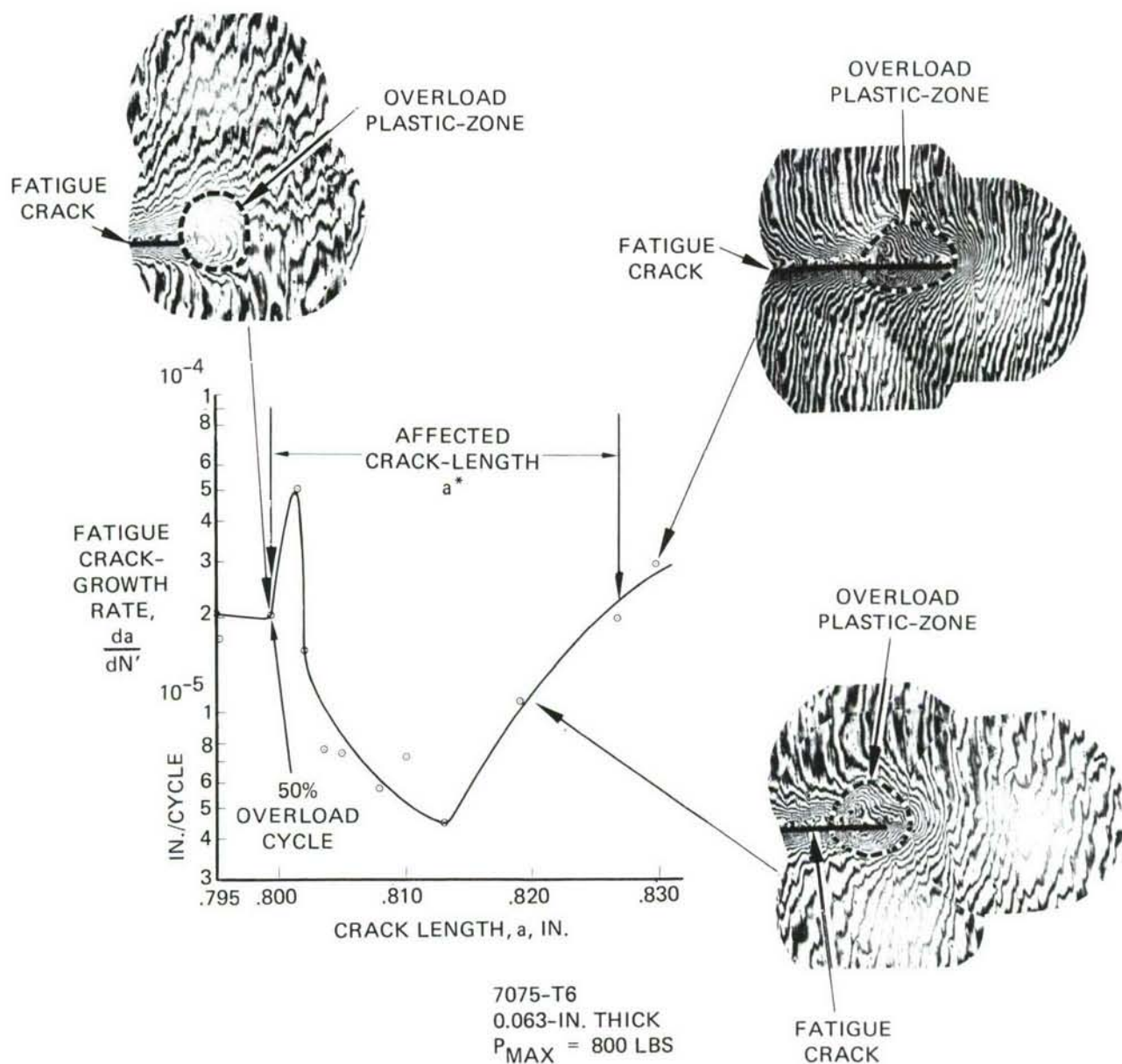
FIGURE 40. INTERFERENCE PATTERNS AT DIFFERENT STAGES OF
CRACK-GROWTH AFTER A 50% OVERLOAD CYCLE
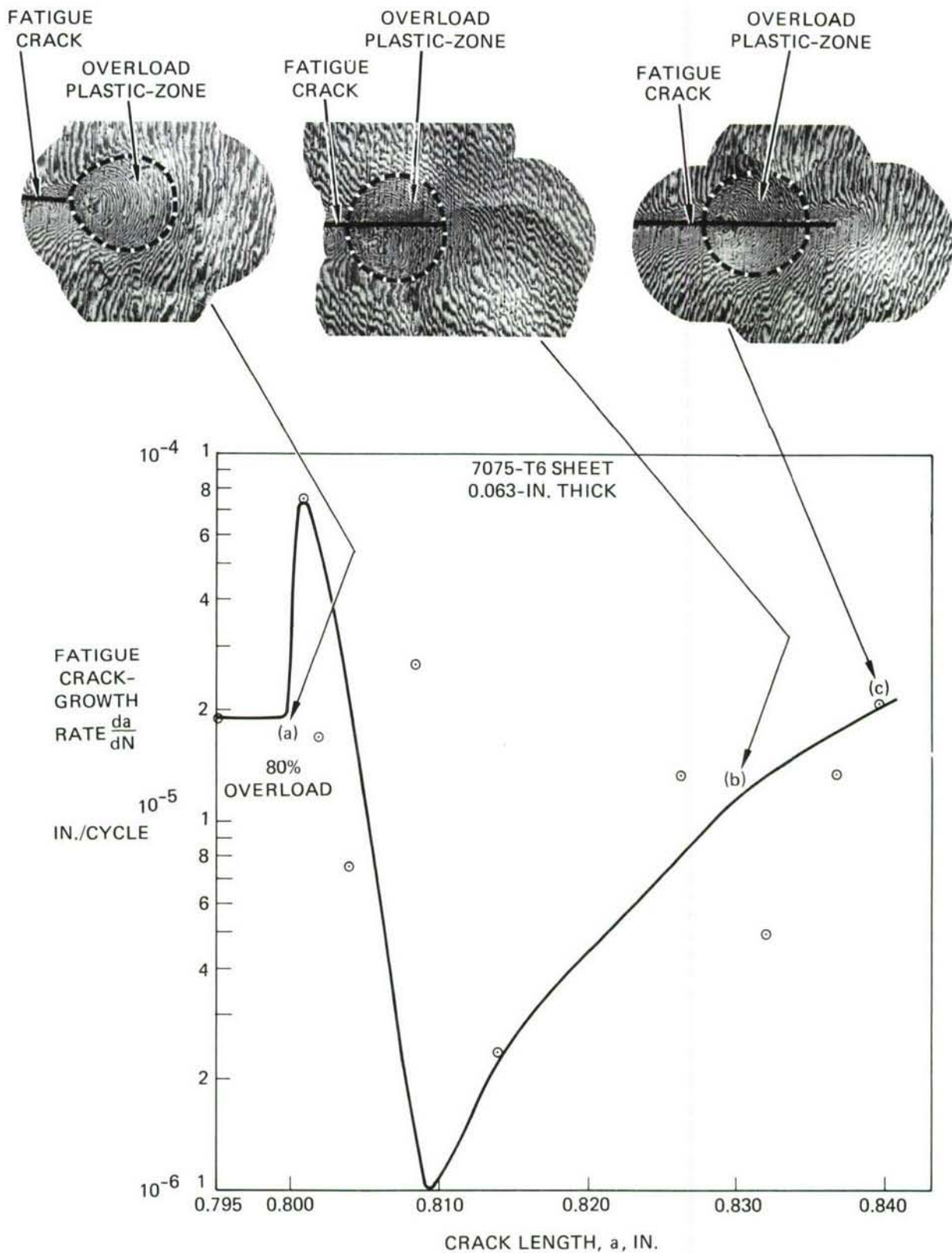
FIGURE 41. INTERFERENCE PATTERNS AT DIFFERENT STAGES OF
CRACK-GROWTH AFTER AN 80% OVERLOAD CYCLE

77

Several methods of accounting for this temporary residual stress from high loads have been developed. For crack-growth analysis one of the more popular approaches was developed by Willenborg[17] and incorporated into the crack-growth analysis programs named CRACKS and CRACKS II developed by the Air Force.

Known as the Willenborg retardation model, this method can be used to calculate the size of the zone of yielded metal immediately ahead of the crack tip. When the plastic zone calculated for a particular load is smaller than the plastic zone remaining from previous loads, the crack-growth for that load is reduced. As the smaller loads cause the crack to grow through the large plastic zone, the retardation decays until the crack advances without retardation.

This process is shown in Figure 42. The diagram on the left shows the assumed condition immediately after an overload cycle which has left a plastic zone of dimension R_p. Then a number of smaller loads are applied, advancing the crack to the position shown on the right.

Willenborg Nomenclature:

R_p = plastic-zone size due to overload cycle

RE = remaining distance across plastic zone after a period of cyclic crack-growth

R_y = calculated plastic zone size for the next load being investigated
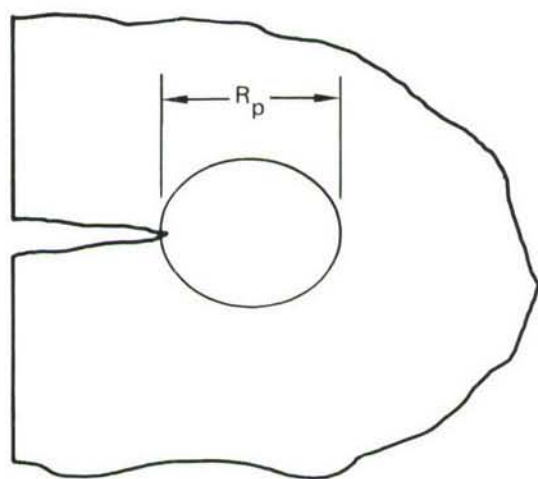
PLASTIC-ZONE DUE TO
OVERLOAD CYCLE
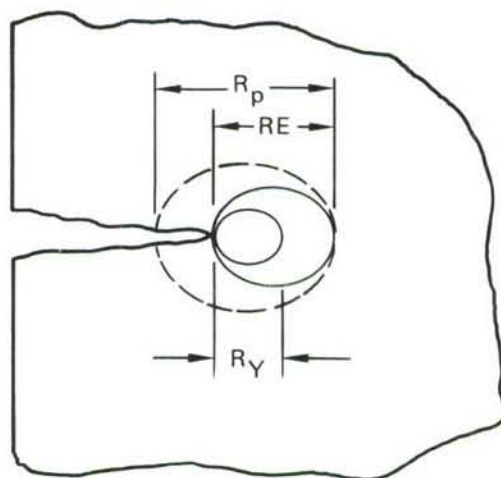
AFTER PERIOD OF CRACK-GROWTH

FIGURE 42. SCHEMATIC OF WILLENBORG MODEL

An accepted expression for plastic-zone radius is:

$$R_p = \frac{K^2}{N_R \pi \sigma_y^2} \qquad \text{where } N_R \text{ varies from 2 for plane stress} \atop \text{to 6 for plane strain} \qquad (5)$$

After a period of cyclic crack growth as shown on the right above:

$$RE = \frac{K^2_{req'd}}{N_R \pi \sigma_y^2} \qquad \text{where } K_{req'd} \text{ is the stress intensity required} \atop \text{to reach the previous plastic zone boundary.} \qquad (6)$$

Willenborg states that if R_y for the next load is less than RE, the stress intensity for the next should be reduced by the amount it falls short of reaching RE.

$$K_{next(effective)} = K_{next} - (K_{req'd} - K_{next}) = 2 K_{next} - K_{req'd} \qquad (7)$$

Solving for $K_{req'd}$ from the previous equation (6) and substituting the equation above (7) leads to:

$$K_{next(eff)} = 2K_{next} - \sigma_y \sqrt{RE \times N_R \times \pi} \qquad (8)$$

Figure 43 shows retardation behavior based on the Willenborg model as a function of K_{next}, $K_{effective}$, and $K_{required}$:

The Willenborg model states that any load causing a plastic zone less than 50% of the load required to extend the plastic zone will have no crack-growth. For loads between 50% and 100% of that required to extend the plastic zone, retardation varies from fully arrested at 50% to fully unretarded crack-growth at 100% as shown in Figure 43.

Test results in this program (Tables V and VI) and elsewhere [25] show that crack-growth is not arrested for 50% loads (OLR = 2.0) and, depending on the specimen, the load level, and the alloy, perhaps not even arrested for 40% loads (OLR = 2.5). For 2024-T8 alloy, an overload ratio of 3.0 (33-1/3% of load) at a relatively high K was required to fully arrest the crack-growth. Comparison of the test results with the Willenborg model also showed that the Willenborg model predicts crack-growth lower than the actual crack-growth for loads up to 60% to 70%, and higher crack-growth for loads from 70% to 100%, of the overload as shown schematically in Figure 43.

PREDICTED CRACK-GROWTH
LOWER THAN ACTUAL

PREDICTED CRACK-GROWTH
HIGHER THAN ACTUAL

$$Y = \frac{K_{EFFECTIVE}}{K_{MAX.}} = \frac{K_{EFF}}{K_{NEXT}}$$

$$X = \frac{K_{MAX}}{K_{REQ'D}} = \frac{K_{NEXT}}{K_{REQ'D}}$$
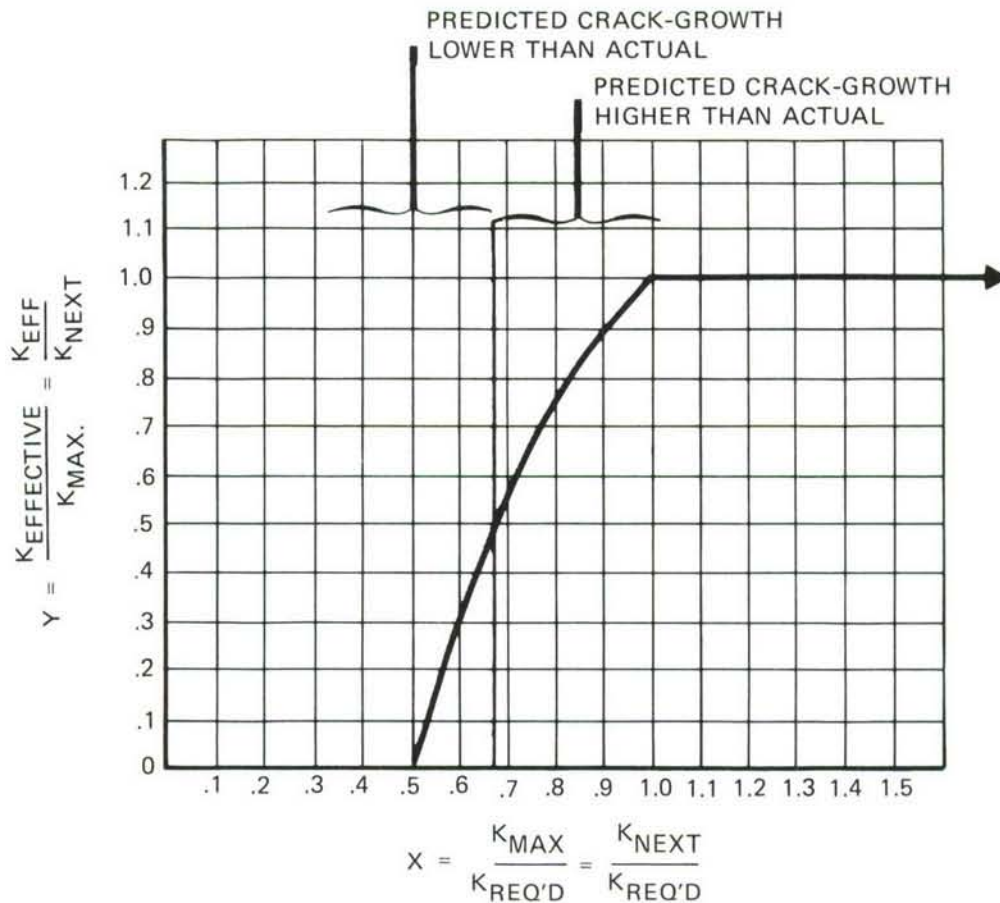
FIGURE 43. WILLENBORG RETARDATION CURVE

The problem is compounded by the fact that for many cases where the $K_{effective}$ is reduced to the range of 0 to 4 ksi $\sqrt{in.}$, the crack-growth (da/dN) rate is below 10^{-8} in./cycle and a region that may contain considerable experimental scatter. The constant-amplitude da/dN vs ΔK data used is prediction is normally curve fitted to a Forman relationship[17]. The nature of the Forman curve in the low da/dN region, however, is always conservative, and for most spectra the cumulative error resulting from this conservatism may not be significant.

The Northrop Model

The Willenborg curve as shown in Figure 44 has a decreasing slope as the crack advances through the plastic zone. This quality appears to be contradictory to most of the test data obtained at Northrop. To improve this feature of the model, numerous first and second order retardation curves were derived and evaluated by comparing test results with the Northrop computer predictions for crack-growth. The test results

80

in this overload retardation program were best matched with the second order curve shown in Figure 44 below.

This curve is based on the second order equation:

$$(x-a) = c(y-b)^2 \quad \text{where } x = \frac{K_{max}}{K_{req'd}} \quad \text{and } y = \frac{K_{eff}}{K_{max}} \tag{9}$$

a, b, and c are constants determined experimentally.

Reasonable agreement between analysis and test were obtained with the following constants:

a = 1.008

b = 1.10

c = 0.8333

By substituting these values in equation (9) and solving for K_{eff}, the following equation is obtained:

$$x = 0.8333 (y-1.1)^2 + 1.008 \tag{10}$$
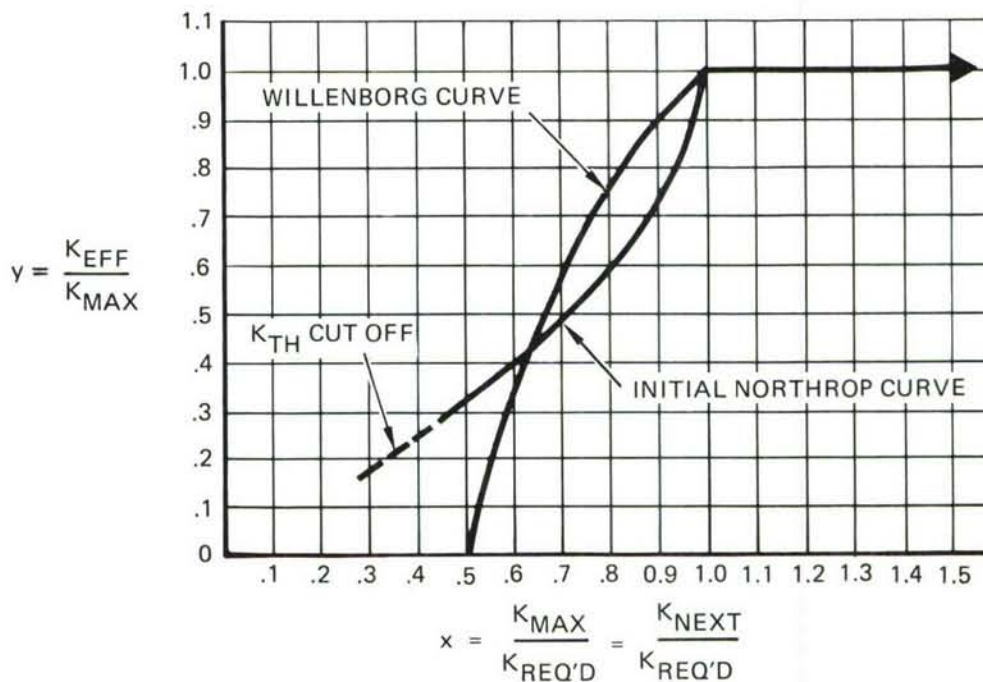
FIGURE 44. NORTHROP RETARDATION MODEL

If this equation is transformed into the parameters represented by x and y:

$$K_{max\ eff} = K_{max} \left[1.1 - \sqrt{\frac{1.008 \left(\dfrac{K_{max}}{K_{req'd}} \right)}{0.8333}} \right] \qquad (11)$$

This curve differs considerably from the Willenborg retardation curve, giving less retardation for low values of K and more retardation for values approaching $K_{required}$. One significant feature of the curve is that total crack arrest is not reflected in the curve. No curve could be found that would accurately represent the differing crack arrest levels from different tests. Evidently crack arrest is not a unique function of the overload ratio as already discussed in III B-1 but it may depend upon an absolute value of a threshold K. When the above curve is used in conjunction with a reasonable threshold K in the NORCRAK crack-growth computer program, remarkably good correlation is achieved with experimental data.

In addition, some retardation testing in this program has shown that what appears to be crack arrest may prove simply to be severely retarded crack-growth. If such "crack arrest" testing is continued at the crack arrest load levels, detectable crack-growth may eventually occur and accelerate through the plastic zone.

Comparison With Test Results

Figure 45 shows the comparison of computer analyses with actual test results from this program at overload ratios of 1.5 and 2.0, respectively. The computer analysis assumed a threshold value of 1.5 ksi $\sqrt{in.}$ for ΔK, and used Forman constants obtained from the FCP curve for 7075-T6 alloy (Figure 9(c)).

In these figures, there is reasonable agreement between test and analysis. Figure 46 shows the comparison for an overload ratio of 2.5 where apparent crack arrest was achieved after the first overload. Crack-growth was then achieved by raising the load for a few thousand cycles. In the test, the second overload again caused apparent crack arrest, but eventually crack-growth resumed and the specimen failed. Analytically, this second temporary crack arrest could not be rationally represented.
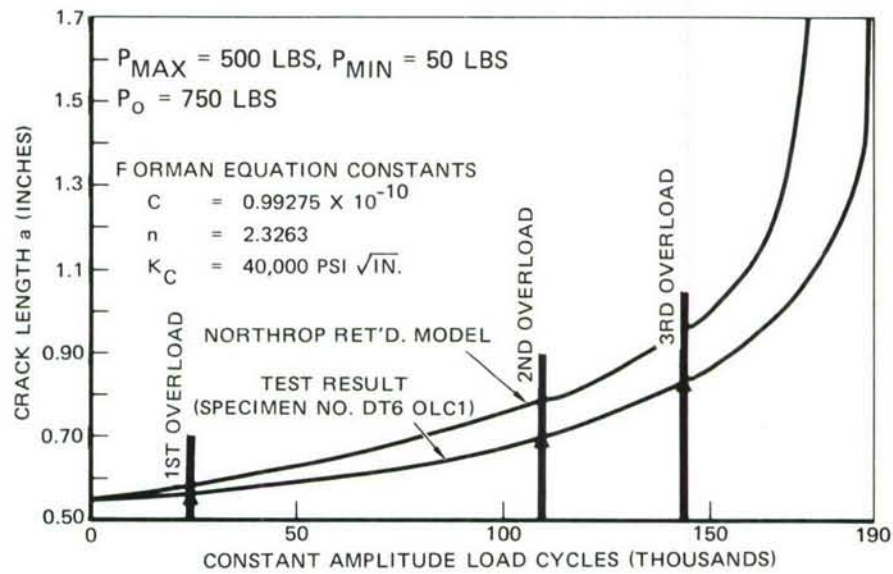
(a) 1.5 OLR
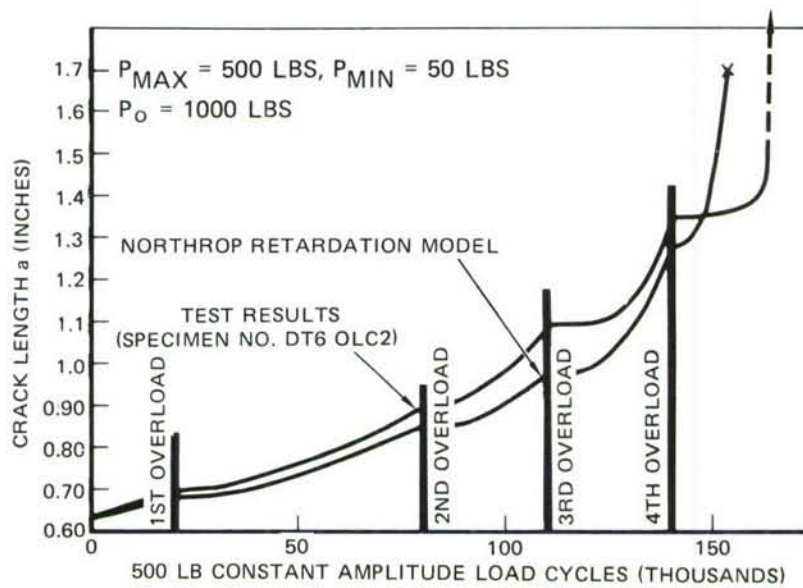
(b) 2.0 OLR

FIGURE 45. COMPARISON OF MEASURED CRACK–GROWTH WITH
THAT PREDICTED IN 7075–T6 AT OLR OF 1.5 AND 2.0
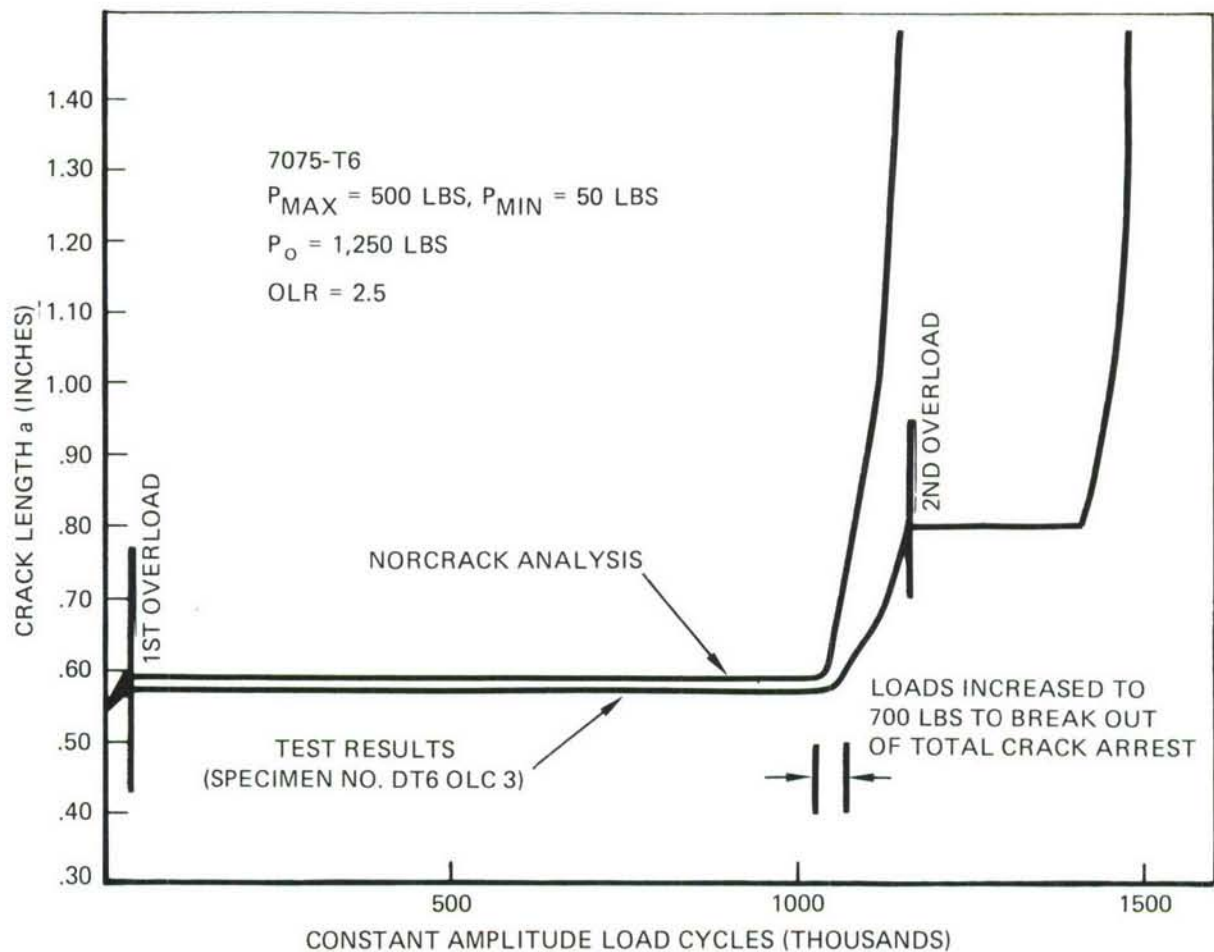
FIGURE 46. COMPARISON OF MEASURED CRACK-GROWTH WITH THAT PREDICTED IN 7075-T6 AT OLR OF 2.5

Refinement of Retardation Model

The result of this program and other parallel test programs at Northrop have demonstrated that the retardation phenomenon, including the decay of crack arrest, are not yet fully understood. The Northrop retardation model is undergoing a continuous process of evolution in order to provide a broader agreement with the test results. Continued spectrum testing will lead to further modifications and refinement in the NORCRAK retardation model.

C. EFFECTS OF FREQUENCY ON RETARDATION BEHAVIOR

To determine whether there are any significant effects of frequency changes on fatigue-crack growth under variable amplitude loading, tests were performed on 0.063-inch SEN specimens of 7075-T6 and 2024-T8 alloys in air and saltwater. The tests in air were conducted at 0.5, 5, and 15 Hz while the tests in saltwater were performed at 0.5, 1, and 15 Hz. A baseline P_{max} of 500 lbs at a P_{min}/P_{max} of 0.1, and single overload cycles with overload ratios (OLR) of 1.5 and 2.0 were used for this work. No major effects of changes in frequency on the retardation behavior were observed for the two alloys investigated.

The results and their discussion have been submitted to the International Journal of Fracture as a research report which is presented in its entirety as Appendix B.

D. EFFECTS OF SALTWATER ON RETARDATION BEHAVIOR

The 2024-T8, 7075-T6, and 7075-T73 alloys were investigated in laboratory air and 3.5% NaCl solution to investigate the effects of a corrosive environment on the retardation behavior of aluminum alloys. The same test frequencies were used in both environments. Single overloads were found to cause a decrease in constant-amplitude crack-growth in saltwater just as they did in air. Also, the number of delay cycles increased with each increase in overload ratio (OLR) in saltwater just as they did in air. However, the number of delay cycles was larger in air than in 3-1/2% saltwater, and the difference was higher for the 7075-T6 alloy than it was for the 2024-T8 and 7075-T73 alloys. The results indicated that a given microstructure and its susceptibility to environmental attack are important in determining its fatigue behavior under variable amplitude loading in an aggressive environment. Thus, an alloy which shows superior retardation behavior in air can be inferior to the other alloy in an aggressive environment such as saltwater as was found for the 7075-T6 and 2024-T8 alloys in this investigation. The difference in the retardation behavior of these two alloys in air was very small while in saltwater, the 2024-T8 alloy was distinctly superior to the 7075-T6 alloy.

Environmental attack similar to that which was observed in the saltwater FCP specimens was found by fractographic examination of selected retardation specimens. However, these observations indicated that the general nature of the fractographic features in relation to the OLR and the applied baseline stress-intensity factor is similar in both air and saltwater, except that at the low OLR and low K values the overload markings were not visible in the specimens tested in saltwater.

This lack of overload marking was more common in the 7075-T6 alloy because of its high susceptibility to environmental attack.

The details of these results and their interpretation have been submitted for publication and will be presented at the ASTM symposium on Corrosion Fatigue to be held in November, 1976 at Denver, Colorado. The paper is presented in its entirety as Appendix C.

E. EFFECTS OF CONDITIONS ENCOUNTERED IN A SERVICE LOAD ENVIRONMENT

In order to make the program results more applicable to aircraft service conditions, selected tests were performed to determine the effects of compressive loads and hold-time on the retardation behavior. As a further aid to the understanding and application of retardation behavior, experiments were selectively conducted to determine the effects of multiple overload cycles, exposure to slightly elevated temperatures, and residual stress on retardation behavior. The latter was done by rod peening the surfaces of fatigue pre-cracked specimens. These specimens were then tested to determine if any retardation took place. The results obtained are described below.

1. MULTIPLE OVERLOAD CYCLES

The application of multiple overload cycles has been found to increase the amount of retardation [7, 8, 27]. However, the number of delay cycles increases to a saturation maximum after a certain number of overload cycles. This maximum effect of overload cycles can be reached in as few as 10 or as many as 300 cycles depending on both the alloy and the overload ratio.

In this investigation, the effect of multiple overload cycles was determined by conducting tests at overload ratios of 1.5 and 2.0 on 0.063-in. thick SEN specimens of 2024-T3 alloy. The number of overload cycles used was 10, 50, and 100. Table XI summarizes the results obtained. Single overload cycle results from Table V are also included.

As seen from the table, the number of delay cycles increases with an increase in the number of overload cycles. However, the a* value does not increase correspondingly. This is probably because the a* value is related to the overload plastic-zone size which depends on the last overload cycle. Hence, most of the existing models, such as Wheeler [12] and Willenborg [17], which predict the same retardation behavior after a single or multiple overload cycles, are inaccurate in

86

$$P_{max} = 800 \text{ Pounds}$$

NO. OF OVERLOAD CYCLES	SPECIMEN NO.	K_O/K_{MAX} (OLR)	a_i (IN)	K_{MAX} (KSI $\sqrt{}$ IN)	a^* (IN)	N^* (1000)	ACCL[1]
1	DT3OLC81-2	1.5	.58	10.0	.030	12.5	c
			.80	14.0	.070	12.5	b & c
			1.04	20.2	.160	9	c
10	IT3MUL1		.57	9.8	.017	20	a
			.79	13.8	.050	12.5	b & c
			1.03	19.9	.075	12.5	b & c
50	IT3MUL3		.57	9.8	.018	12.5	b
			.79	13.8	.079	17.5	b & c
			1.038	20.1	.133	15	b
100	IT3MUL2		.57	9.8	.016	17.5	b
			.79	13.8	.092	25	b
			1.03	19.9	.220	20	b
1	DT3OLC82-2	2.0	.57	9.8	.062	110	b
			.79	13.8	.106	85	b & c
			1.03	19.9	Failed Before Recovery		
10	IT3MUL4		.57	9.8	.086	205	b
			.79	13.8	.098	310	b
			1.03	19.9	Arrest[2]		b
50	IT3MUL6		.57	9.8	Arrest[2]		b
			.79	13.8	Arrest[2]		b
100	IT3MUL5-3		.58	10.0	Arrest[2]		b
			.80	14.0	Arrest[2]		b
			1.040	20.2	Failed in Grips		b
100	IT3MUL5-4		.79	13.8	Arrest[2]		b

1 - a No crack-growth during overload cycle and no initial acceleration
    b Crack-growth during overload cycle
    c Initial acceleration after the overload cycle
2 - No measureable crack-growth in 500,000 cycles

predicting multiple overload effects. They are based on the use of an overload plastic-zone size which does not change significantly due to multiple overload cycles. However, the a^*/N^* value decreases, which indicates that the effective stress-intensity is much lower in the multiple overload tests. The residual compressive stress at the crack-tip is probably much lower in the multiple overload tests. The residual compressive stress at the crack-tip is probably much higher in specimens with higher numbers of overload cycles. Optical interference patterns did not show a difference in strain distribution in the vicinity of the crack-tip for single and multiple overload cycles even though the overload plastic-zone size at the crack-tip was not much different. A detailed interference study may shed more light on this aspect.

In all of these tests, the crack grew during the application of the multiple overload cycles as shown in the right hand column of Table XI. Initial crack acceleration was also observed in a majority of the non-arrest tests.

Fractographic observations also indicated differences in the nature of the overload region between single and multiple overload specimens. With multiple overload cycles, the striations representing each of the multiple overloads could be seen. The width of the retardation zone, W, at the crack-tip appeared to be the same. As an example, Figure 47 shows a comparison of overload marking between two 2024-T3 specimens, one with 1 and the other with 10 overload cycles. In this case, the width of the zone, W, which is related to the overload plastic-zone is essentially the same. However, the change in topography is much more striking in the multiple overload specimens.

Just after the overload marking, the depth of the smooth zone, shown as D, appears to be much greater for the multiple overload specimen. At higher magnification (Figures 48 and 49) ten striations as well as extensive abrasion (A) can be seen in the multiple overload specimen. These results tend to support the crack-closure hypothesis for multiple overload effects even though as discussed earlier, in single overload tests, there is a conflict between the theory and experimental observations. The crack-closure concept for explaining multiple overload results has been described in detail [8, 15, 27]. According to this concept, the crack-closure increases with an increase in the number of overload cycles. This may explain the increased abrasion (A in Figure 49) and the increased height of the "cliff" (D in Figure 47) caused by the multiple overload cycles. The crack-closure theory predicts a saturation or an equilibrium value after a sufficient number of overload cycles has been applied which may explain the limited number of overload cycles which cause the maximum retardation. Thus, it appears that the observed results can best be explained based upon the crack-closure theory. However, a similar argument can also be made based upon the saturation of residual compressive stress at the crack-tip with increased multiple overload cycles. Since crack-closure is a manifestation of residual stresses at the crack-tip, either of the two concepts appears valid for explaining these data. There is need to conduct reliable and sensitive crack-closure measurements under multiple overload cycles to confirm the crack-closure hypothesis. Nevertheless, these test results clearly indicate the need for the incorporation of multiple overload effects in prediction models to obtain a more accurate prediction of fatigue-life under variable amplitude loading.
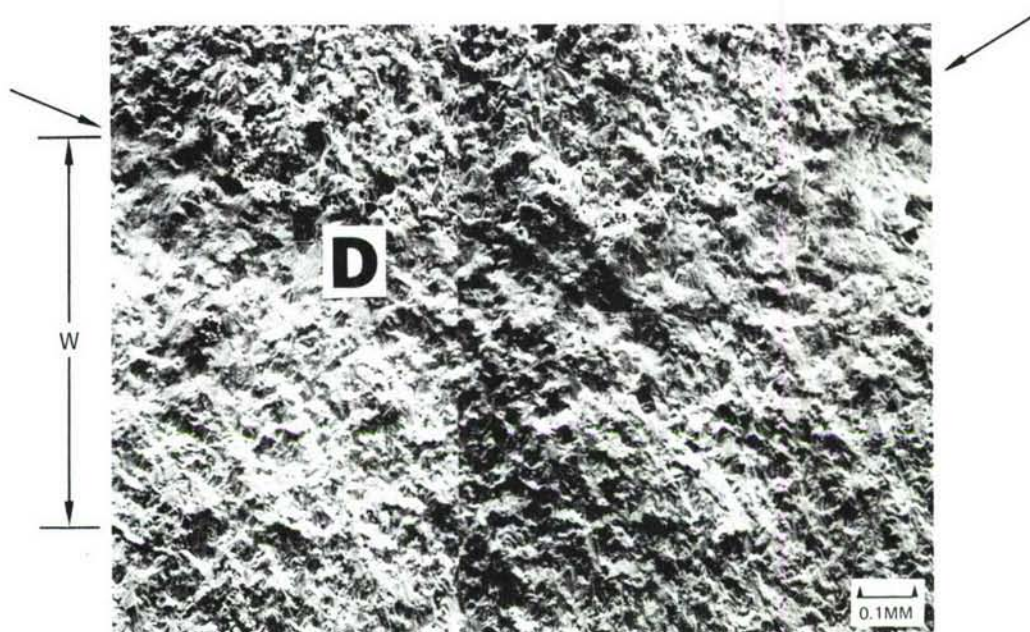
(a) 1 OVERLOAD CYCLE

CRACK-GROWTH
DIRECTION
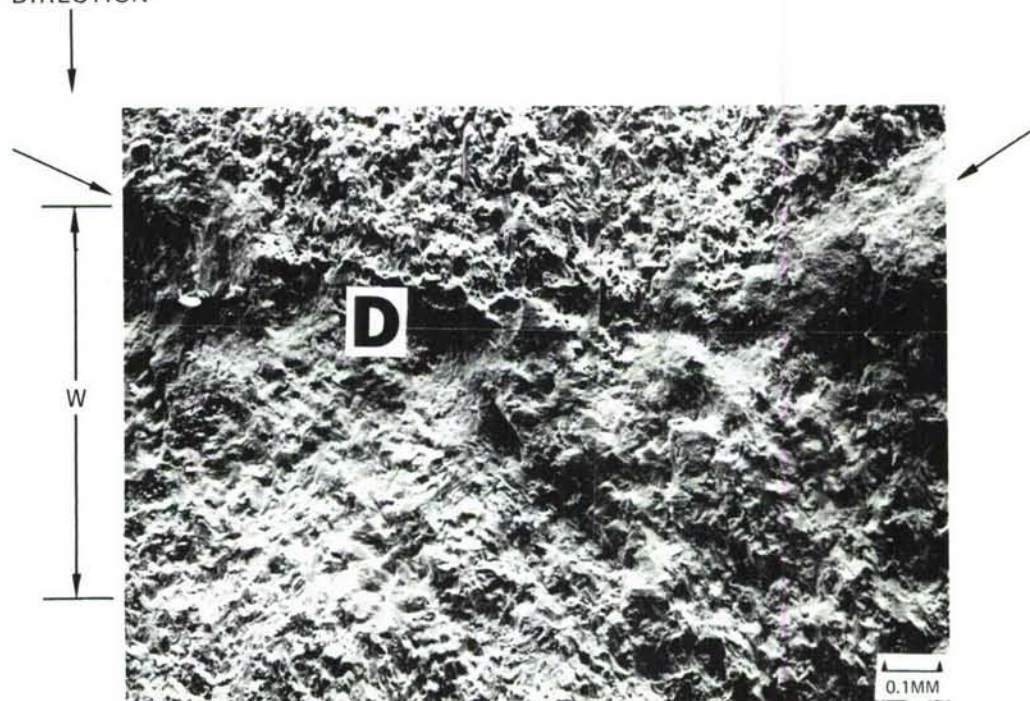
(b) 10 OVERLOAD CYCLES

BASELINE P_{MAX} (K_{MAX}) = 800 LBS (9.8 KSI $\sqrt{IN.}$)

OVERLOAD RATIO = 2.0

FIGURE 47. EFFECT OF MULTIPLE OVERLOAD CYCLES ON OVERLOAD MARKING IN 2024-T3 ALLOY

CRACK-GROWTH
DIRECTION

0.02MM

FIGURE 48. A HIGH MAGNIFICATION VIEW OF THE CENTER REGION OF FIGURE 47(a)

CRACK-GROWTH
DIRECTION
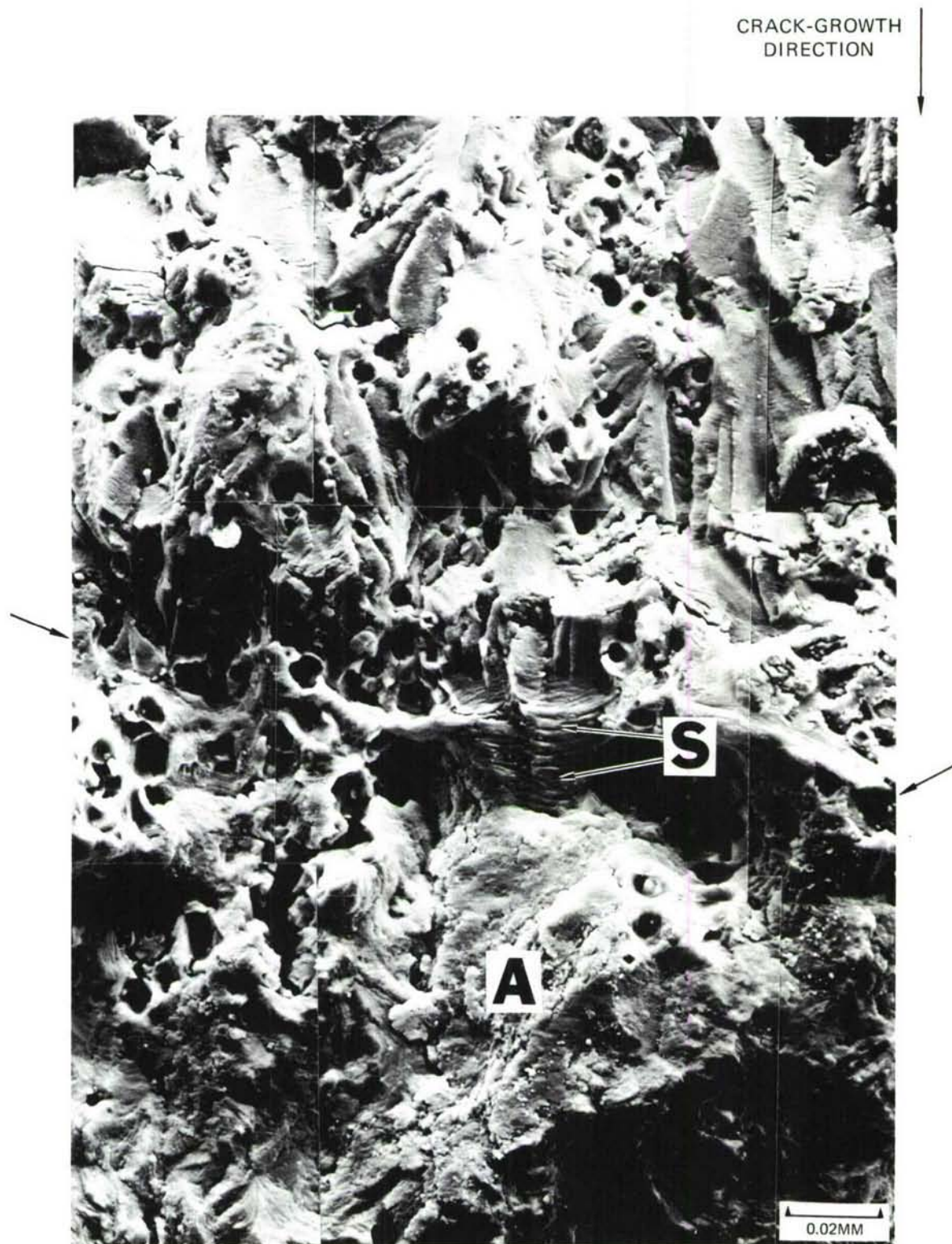
FIGURE 49. A HIGH MAGNIFICATION VIEW OF THE CENTER REGION OF
FIGURE 47(b) SHOWING STRIATIONS IN OVERLOAD REGION

91

2. THERMAL EXPOSURE AFTER OVERLOAD CYCLE

High speed aluminum aircraft structures can occasionally be exposed to elevated temperatures at least as high as 200F. Hence, a study of the effect of temperature exposure, after the application of a high stress cycle, on the retardation behavior at room temperature is important. In a preliminary investigation, Raju, et al[28], found that annealing at elevated temperatures could eliminate retardation. Since annealing does not significantly affect crack-blunting, they concluded that blunting was not a significant factor in retardation, but annealing can reduce the residual stresses at the crack-tip and, hence, change the stress distribution in the region through which the fatigue-crack must grow.

For this work, 2024-T3 and 7075-T6 alloys were selected based on single overload results from Section IIIB. Single-edge-notched specimens, 0.063-inch thick, were tested at overload ratios of 1.5 and 2.0 at a baseline P_{max} of 800 lbs. The specimens were exposed either to 176F (80C) or 248F (120C) for 1 hour shortly after the application of the overload cycle. After the temperature exposure, the specimens were tested under constant-amplitude load cycling in the same manner as before the overload cycle.

Table XII summarizes the results of tests which were performed to determine the effects of thermal exposure on retardation behavior. The plastic-zone size, which depends on permanent plastic deformation, should not change due to exposure to these relatively low temperatures (176F or 248F). Hence, the affected crack-length (a*) does not show any trend with thermal exposure under otherwise identical test conditions. There does appear to be a small decrease in the number of delay cycles due to thermal exposure. In order to further evaluate the effect of exposure on retardation, the effective crack-growth in the retardation zone, a*/N*, was calculated. For comparison purposes, the a*/N*, as well as the N* values for corresponding tests, are listed in Table XIII. As seen, there is a decrease in N* and a trend towards an increase in a*/N* with exposure for the higher K values. This is probably due to the fact that, at the higher K values, the plastic strain energy is much higher and, hence, it can be relieved more easily by thermal exposure. This aspect is analogous to the relationship between coldworking, recrystallization, and grain growth.

TABLE XII. SUMMARY OF TESTS TO DETERMINE EFFECTS OF
THERMAL EXPOSURE ON RETARDATION BEHAVIOR

P_{max} = 800 Pounds

| TEMP. OF EXPOSURE[1] F (C)	SPECIMEN NO.	K_O/K_{MAX} (OLR)	a_i (IN)	K_{MAX} (KSI $\sqrt{IN}$)	$a*$ (IN)	$N*$ (1000)	ACCL[2]
			2024-T3				
None	DT3OLC81-2	1.5	.58	10.0	.030	12.5	c
			.80	14.0	.070	12.5	b & c
			1.04	20.2	.160	9	c
176 (80)	IT3EXPO1		.57	9.8	.012	12.5	b
			.79	13.8	.025	6	b
			1.03	19.9	.082	8	b & c
248 (120)	IT3EXPO2		.57	9.8	.040	12.5	b
			.79	13.8	.025	6	b & c
			1.03	19.9	.015	0.7	a & c
None	DT3OLC82-2	2.0	.57	9.8	.062	110	b
			.79	13.8	.106	85	b & c
			1.03	19.9	Failed Before Recovery		b & c
176 (80)	IT3EXPO3		.57	9.8	.093	75	b
			.79	13.8	--	--	-
			1.03	19.9	.182	50	b & c
248 (120)	IT3EXPO4		.57	9.8	.012	75	a
			..79	13.9	.139	55	b
			1.03	19.9	--	--	-
			7075-T6				
None	DT6OLC81-2	1.5	.57	9.8	.017	3	a & c
			.79	13.8	.026	3	b
			1.05	20.6	.050	2	b & c
176 (80)	IT6EXPO1		.57	9.8	.007	2	a
			.79	13.8	.017	1.5	b
			1.03	19.9	.072	2	a & c
248 (120)	IT6EXPO2		.58	10.0	.016	3	b & c
			.80	14.0	.033	3	b & c
			1.04	20.2	.004	0.1	a
None	DT6OLC82-2	2.0	.57	9.8	.026	12.5	b
			.79	13.8	.029	12.5	b
			1.03	19.9	Failed Before Recovery		a
176 (80)	IT6EXPO3		.57	9.8	.053	12.5	b
			.79	13.8	.075	10	b
			1.03	19.9	Failed Before Recovery		b
248 (120)	IT6EXPO4		.57	9.8	.020	6	a
			.79	13.8	.082	8	b & c
			1.03	19.9	Failed Before Recovery		b & c

1 – Time of Exposure: 1 Hour
2 – a = No crack growth during overload cycle and no initial acceleration
    b = Crack growth during overload cycle
    c = Initial acceleration after the overload cycle

TABLE XIII. EFFECT OF THERMAL EXPOSURE ON THE RETARDATION BEHAVIOR OF 2024-T3 AND 7075-T6 ALLOYS

K_o/K_{max} (OLR)	K_{max} (ksi $\sqrt{\text{in.}}$)	N* (x1000)			a^*/N^* (x10^{-6} in./cycle)		
		No Exposure	1.0 hr. at 176F (80C)	1.0 hr. at 248F (120C)	No Exposure	1.0 hr. at 176F (80C)	1.0 hr. at 248F (120C)
				2024-T3			
1.5	9.9	12.5	12.5	12.5	2.4	1.0	3.2
	13.9	12.5	6.0	6.0	5.6	4.2	4.2
	20.1	9.0	8.0	0.7	17.8	10.3	21.4
2.0	9.8	110	75	75	0.6	1.2	0.8
	13.9	85	--	55	1.2	----	2.5
				7075-T6			
1.5	9.9	3	2	3	5.7	3.5	5.3
	13.9	3	1.5	3	8.7	11.3	11.0
	20.2	2	2	0.1	25.0	36.0	40.0
2.0	9.8	12.5	12.5	6	2.1	4.2	3.3
	13.8	12.5	10	8	2.3	7.5	10.3

Although complete elimination of crack-growth delay was not observed in these tests, the thermal exposure produced a definite decrease in the number of delay cycles at high K values. Perhaps, exposure to a somewhat higher temperature would have completely eliminated the observed delay. However, in this investigation, the maximum temperature was limited so as not to change the metallurgical structure significantly. Figure 50 shows optical microstructures taken both before and after thermal exposure. No differences in the microstructures can be seen. The dimpling and crack-tip blunting can be seen in these micrographs. At a higher magnification, what appears to be a small extension of the crack-tip plasticity can be seen after exposure in the micrograph in Figure 50(d) as an increase in dark etching area (shown by arrow). This extension should have caused an increase in crack delay, if blunting was the primary controlling factor in retardation.

Changes in the interferometry pattern due to thermal exposure, were evaluated for one specimen. An optical interference pattern was obtained at the crack-tip after the overload cycle but before thermal exposure, while another pattern was obtained from the same specimen after thermal exposure at 248F (120C) for 1 hour. The plastic-zone size was the same in both cases.

(a)   0.1MM

(b)   0.04MM
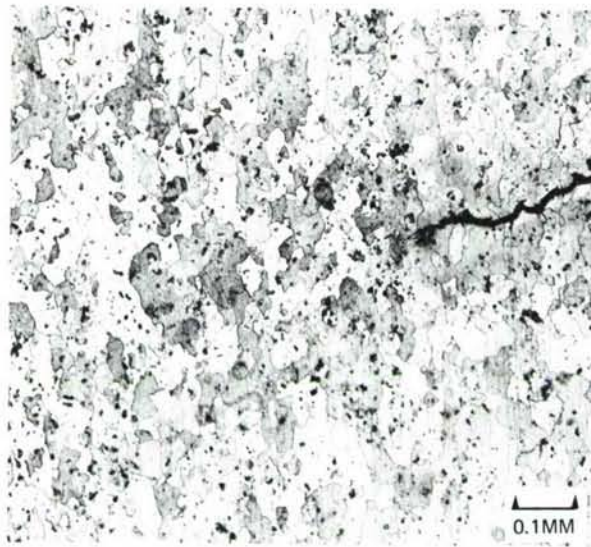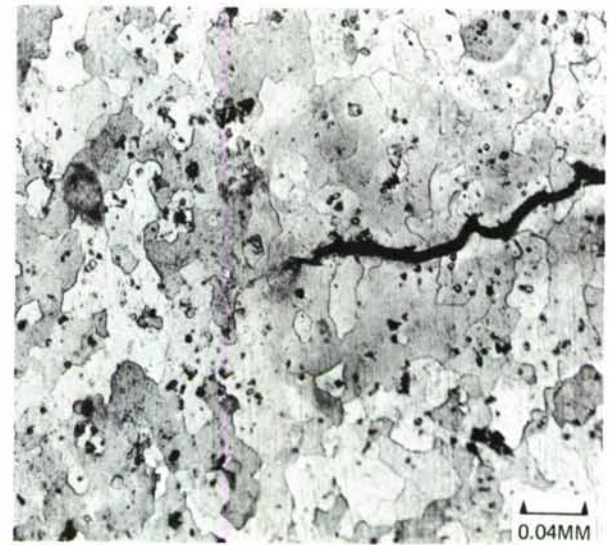
BEFORE EXPOSURE AND AFTER OVERLOAD CYCLE

(c)   0.1MM

(d)   0.04MM
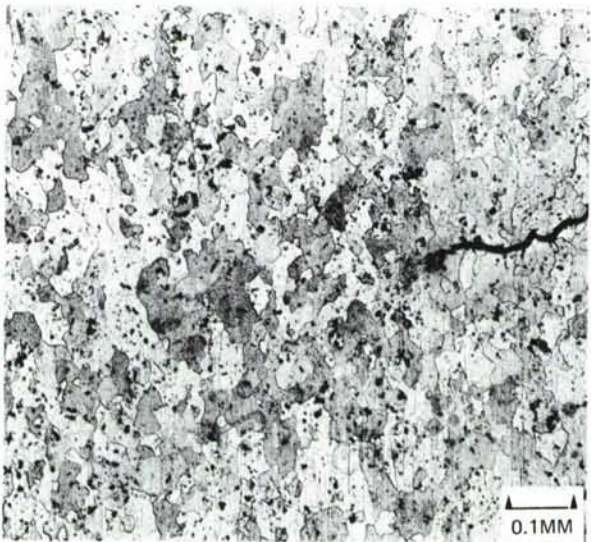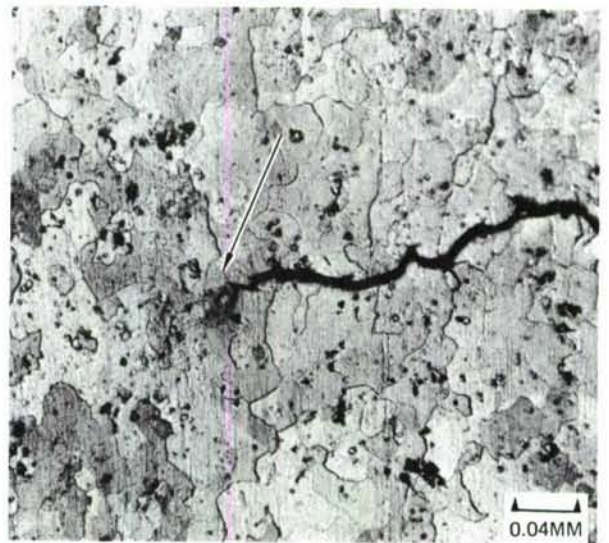
AFTER EXPOSURE AT 248F (120C) FOR 1 HR

$$P_{MAX} (K_{MAX}) = 800 \text{ LBS } (14 \text{ KSI} \sqrt{\text{IN.}})$$

FIGURE 50. EFFECT OF THERMAL EXPOSURE ON CRACK-TIP PLASTIC
DEFORMATION (BLUNTING AND "DIMPLING") AFTER A 100% OVERLOAD
CYCLE IN 2024-T3 ALLOY

95

$$P'_{max} = 4000 \text{ Pounds}$$

COMPRESSIVE LOAD (LBS)	SPECIMEN NO.	a_i (IN)	K_{MAX} (KSI $\sqrt{\text{IN}}$)	K^1_{COMP} (KSI $\sqrt{\text{IN}}$)	a^* (IN)	N^* (x1000)	a^*/N^* ($\times 10^{-6}$ IN/ CYCLE)	ACCL[2]
			Overload Ratio	1.5				
0	HT6THK1	.5924	6.4	0	.0023	8	2.9	a
		.7292	7.9	0	.0061	5	12.2	a
		.8660	9.8	0	.0030	1.5	20.0	a
-400	GT651COM1	.56	6.1	-.61	.002	5	4.0	a
		.82	9.1	-.91	.010	4	25.0	a
		1.09	13.8	-1.38	0	0	--	a & c
-2000	GT651COM2	.57	6.1	-3.1	.005	10	5.0	a
		.79	8.7	-4.4	.025	6	41.7	a
		1.03	12.6	-6.3	--	0	--	b
			Overload Ratio	2.0				
0	HT6THK2	.5924	6.4[3]	0	--	--		a
		.7292	7.9	0	.027	9	30.0	a
		.8660	9.8	0	.0129	3	43.0	a
-400	GT651COM3	.57	6.1	-.61	.021	65	3.2	a
		.79	8.7	-.87	.019	12.5	15.2	b
		1.03	12.6	-1.26	.035	12.5	28.0	b
-2000	GT651COM4	.57	6.1	-3.1	.030	90	3.3	a
		.79	8.7	-4.4	.039	10	39.0	a
		1.03	12.6	-6.3	.075	15	50.0	b & c
-2000	GT651COM4-2	.56	6.1	-3.1	.068	60	11.3	b
		.787	8.7	-4.4	.058	12.5	46.4	b & c
		1.000	12.0	-6.0	.060	10.0	60.0	a & c

1 - K_{COMP} = For comparison only - not a valid LEFM number.

2 - a = No crack growth during overload cycle
    b = Crack growth during overload cycle
    c = Initial acceleration after overload cycle

3 - Crack grew only on one surface - making data invalid.

load cycle. However, the specimen interior is affected by the compressive load as evidenced by a comparison of the fractographic features from the mid-thickness regions of the retardation specimens tested both with and without a compressive load.

Figure 52 shows fractographs from the mid-thickness area of 0.5-in. thick retardation specimens tested with and without a compressive load. As seen in Figure 52, the depth of "cliff" (D) at the overload marking is much higher in the specimen which experienced the compressive load. High magnification views from both of these specimens (Figures 53 and 54) show these differences much more clearly. The
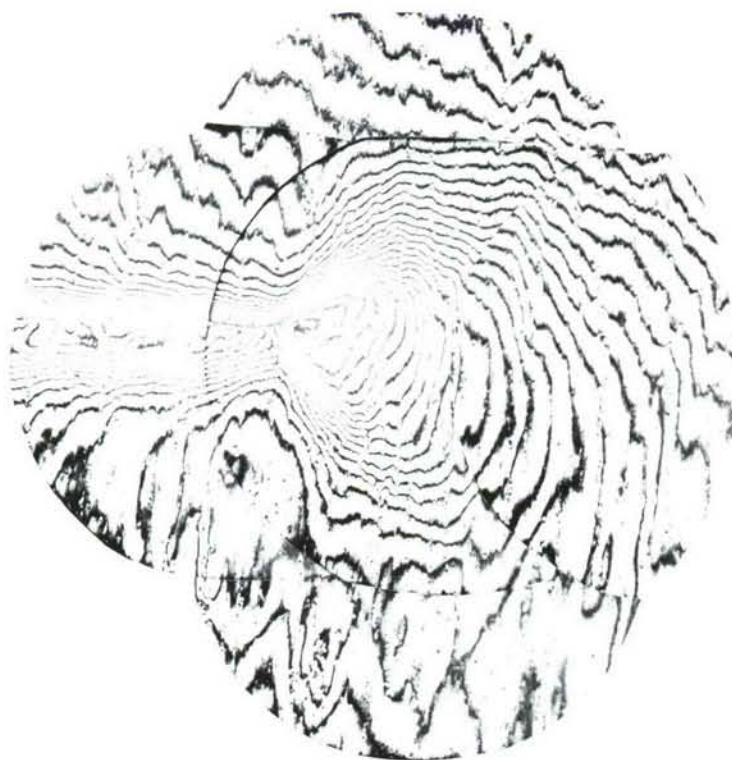
(a) AFTER THE OVERLOAD CYCLE BUT BEFORE COMPRESSIVE LOAD

0.3MM
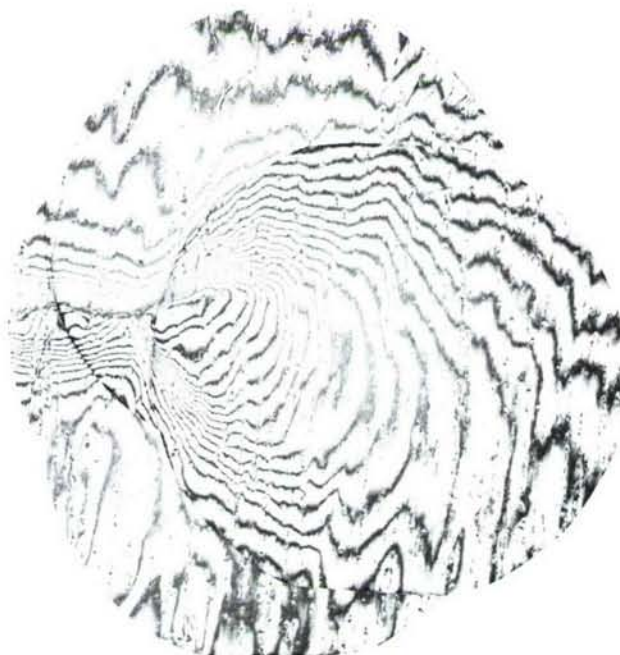
(b) AFTER A COMPRESSIVE LOAD OF 2,000 LBS

$$P_{MAX} (K_{MAX}) = 4,000 \text{ LBS } (12.0 \text{ KSI} \sqrt{IN.})$$

CRACK-LENGTH = 1 IN.

FIGURE 51. EFFECT OF COMPRESSIVE LOAD CYCLE ON THE SURFACE INTERFERENCE PATTERN DUE TO A 100% OVERLOAD CYCLE IN A 0.5-IN. THICK 7075-T651 SEN SPECIMEN

(a) NO COMPRESSIVE LOAD, K_{MAX} = 10 KSI $\sqrt{IN.}$
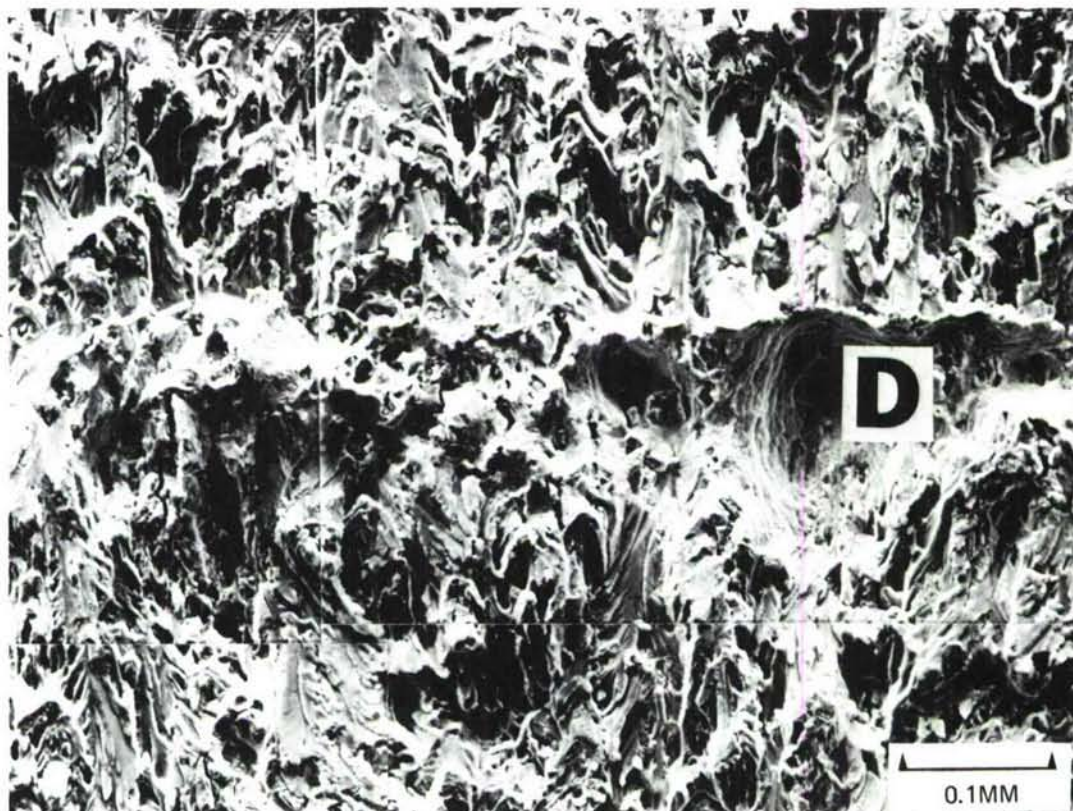
(b) COMPRESSIVE LOAD = 2,000 LBS, K_{MAX} = 12.0 KSI $\sqrt{IN.}$

BASELINE P_{MAX} = 4,000 LBS

OVERLOAD RATIO = 2.0

FIGURE 52. EFFECT OF COMPRESSIVE LOAD CYCLE ON THE FRACTOGRAPHIC
FEATURES IN MID-THICKNESS REGION OF A 0.5-IN. THICK 7075-T651 SEN SPECIMEN

99

CRACK-GROWTH
DIRECTION

0.01MM
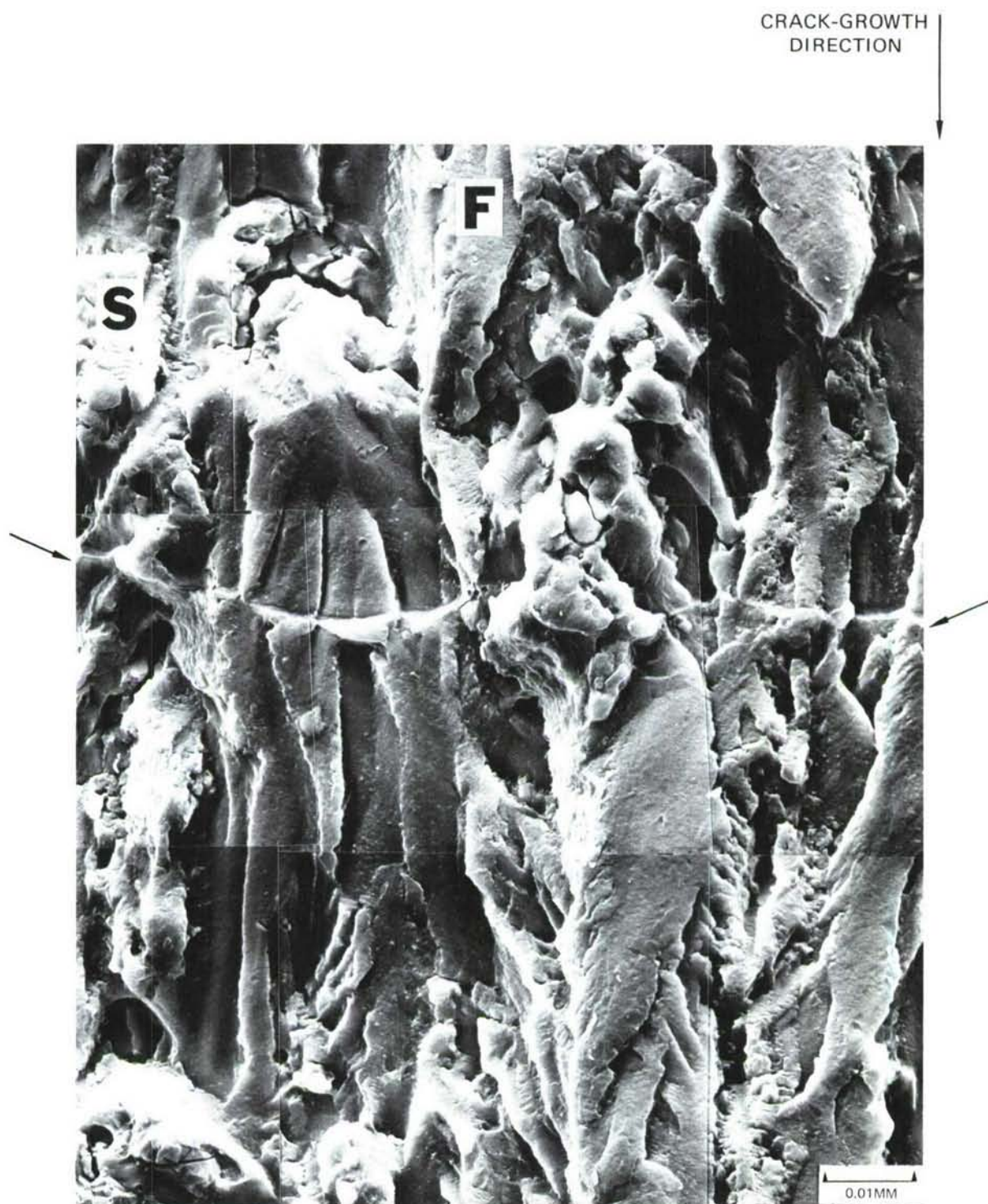
FIGURE 53. A HIGH MAGNIFICATION VIEW OF CENTER REGION OF FIGURE 52 (a)

CRACK-GROWTH
DIRECTION

F

S

0.01MM
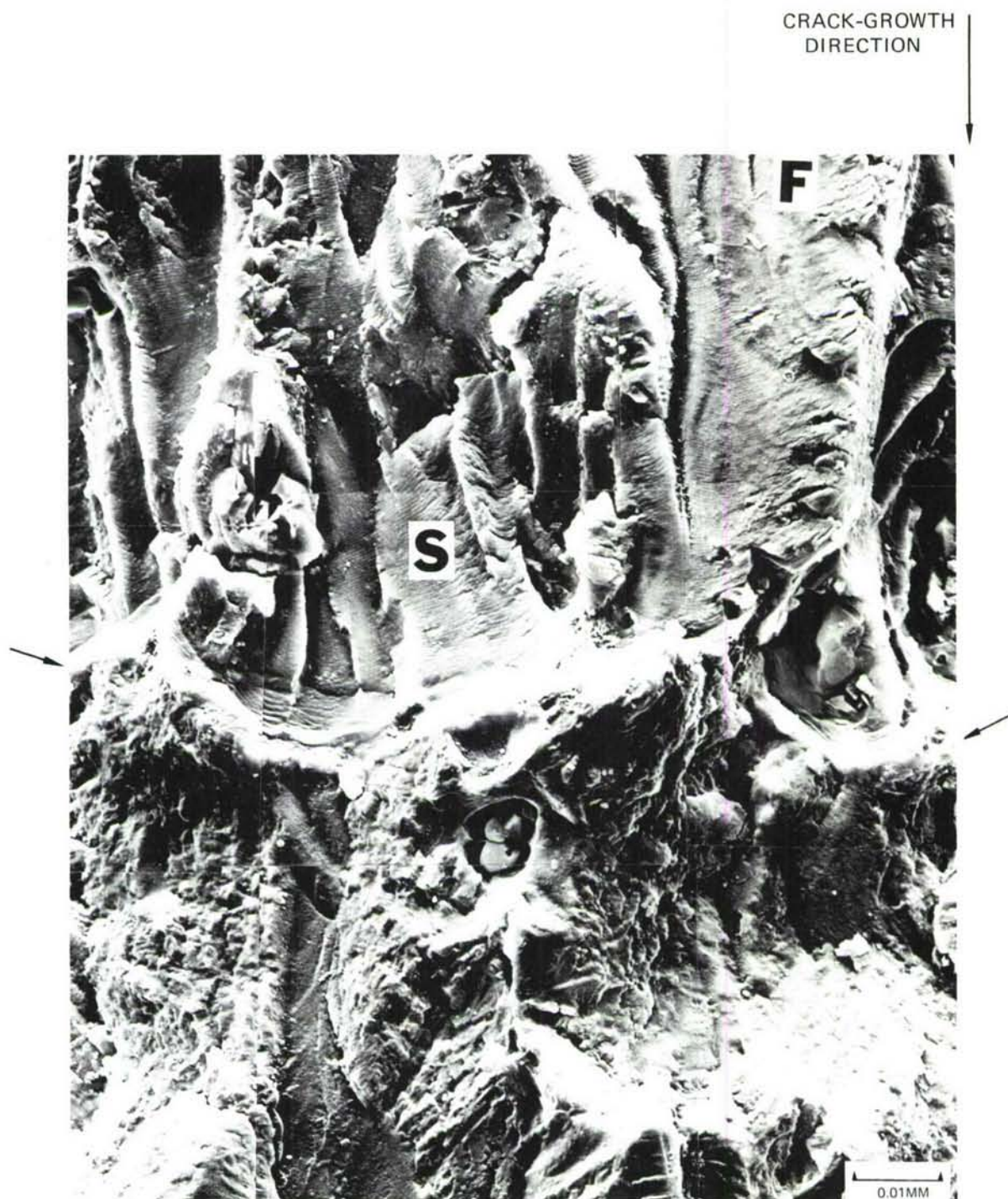
FIGURE 54. A HIGH MAGNIFICATION VIEW OF CENTER REGION OF FIGURE 52 (b)

101

striations (S) and fatigue facets (F) before the overload cycle marking can be seen in both the specimens tested with and without the compressive load cycle. After both an overload cycle and a compression load cycle, the fracture surface shows considerable abrasion. Differences in the height of the "cliff" can be seen between the two specimens. The fractographic features are considerably rougher in the specimen with compressive load.

Thus, the compressive load cycle affects the crack propagation in the mid-thickness region, while the surface plastic-zone at the crack-tip remains essentially the same. Because of these complex features, no definitive conclusions can be made concerning the effect of compressive load on delay cycles. However, the effective crack-growth rate in the retardation zone tends to increase with compressive load.

4. ROD-PEENING AT THE CRACK-TIP

Experiments were conducted to determine if the compressive stresses introduced by tensile overloads could be simulated by peening in the crack-tip area of fatigue-precracked specimens. Rod-peening was chosen rather than shot-peening because it has been shown that it produces compressive-stresses to a greater depth[34]. Initially, two 0.063-inch thick 2024-T8 SEN specimens were used for our investigation. The fatigue-crack was grown to 0.8-inch under constant amplitude loading at an R of 0.1 and P_{max} of 800 lbs. These specimens were rod-peened with two different sets of peening parameters as shown in Table XV. The residual stresses measured by a Rigaku strain-flex analyzer are also shown in this Table. Subsequently, crack-growth experiments were performed. For comparison purposes, additional specimens without any rod-peening were tested under otherwise identical conditions.

Figure 55(a) shows the effects of rod-peening on fatigue-crack growth behavior. Rod-peening accelerated fatigue-crack propagation. In order to confirm this surprising observation, additional tests were run on three 7075-T6 specimens. Two of these were rod-peened while the third was not rod-peened. Table XV shows rod-peening parameters, while Figure 55(b) shows a versus N results for these specimens. Here too, rod-peening accelerated the FCP. This increase in FCP could be due to any combination of the following reasons:

1. It is possible that the tensile stresses introduced in the unpeened area (area outside peened zone) of side 2 (Table XV) were harmful.

2. Buckling and distortion of this thin specimen caused sufficient bending stresses to reduce the crack-growth resistance.

TABLE XV. ROD PEENING PARAMETERS AND RESIDUAL STRESSES IN ROD-PEENED SPECIMENS

| ALLOY | SPEC. NO. | PEENING PARAMETERS | RESIDUAL STRESS — KSI | | | |
| | | | SIDE 1 | | SIDE 2 | |
			PEENED	UNPEENED	PEENED	UNPEENED
2024-T8	1-IT8	25 psi/0.031 Tip Radii	-39.9	-18.2	-29.1	+20.4
	2-IT8	35 psi/0.031 Tip Radii	-24.8	- 2.3	-29.1	+ 6.9
7075-T6	1-IT6	25 psi/0.031 Tip Radii	-50.7	0	-50.7	+16.0
	2-IT6	35 psi/0.031 Tip Radii	-59.8	- 2.3	-43.8	+ 6.9

3. The severe plastic deformation in the crack-tip area due to rod-peening has **work**-hardened the material to an embrittled condition.

Nevertheless, these results clearly demonstrate that the crack-tip residual stresses introduced by tensile overloads cannot be simulated by peening.

5. HOLD-TIME AT LOW LOADS

The hold-time at low stress levels can allow some localized relaxation of residual stresses around the crack tip. This occurs even though at room temperatures in a relatively non-aggressive laboratory environment, no gross creep or environmental effects are expected. In Ti-6Al-4V alloy, a small decrease in delay cycles by holding at the minimum load (P_{min}) has been reported.[11]

In this work, it was decided to simulate the hold-time studies with stresses experienced by an aircraft while cruising or when the aircraft is on the ground in readiness for a flight. To accomplish this, the specimens were kept in the test machine at P_{mean} for various selected times.

SEN specimens of 0.063-inch thick 2024-T3 and 7075-T6 alloys were tested at OLR of 1.5 and 2.0 at a baseline P_{max} of 800 lbs and R of 0.1. Hold-times at the P_{mean} of 1, 8, and 16 hrs. after each overload cycle were used. Table XVI summarizes these results. In order to further evaluate the effect of hold-time on retardation, the effective crack-growth in the retardation zone, a*/N*, was also calculated. For
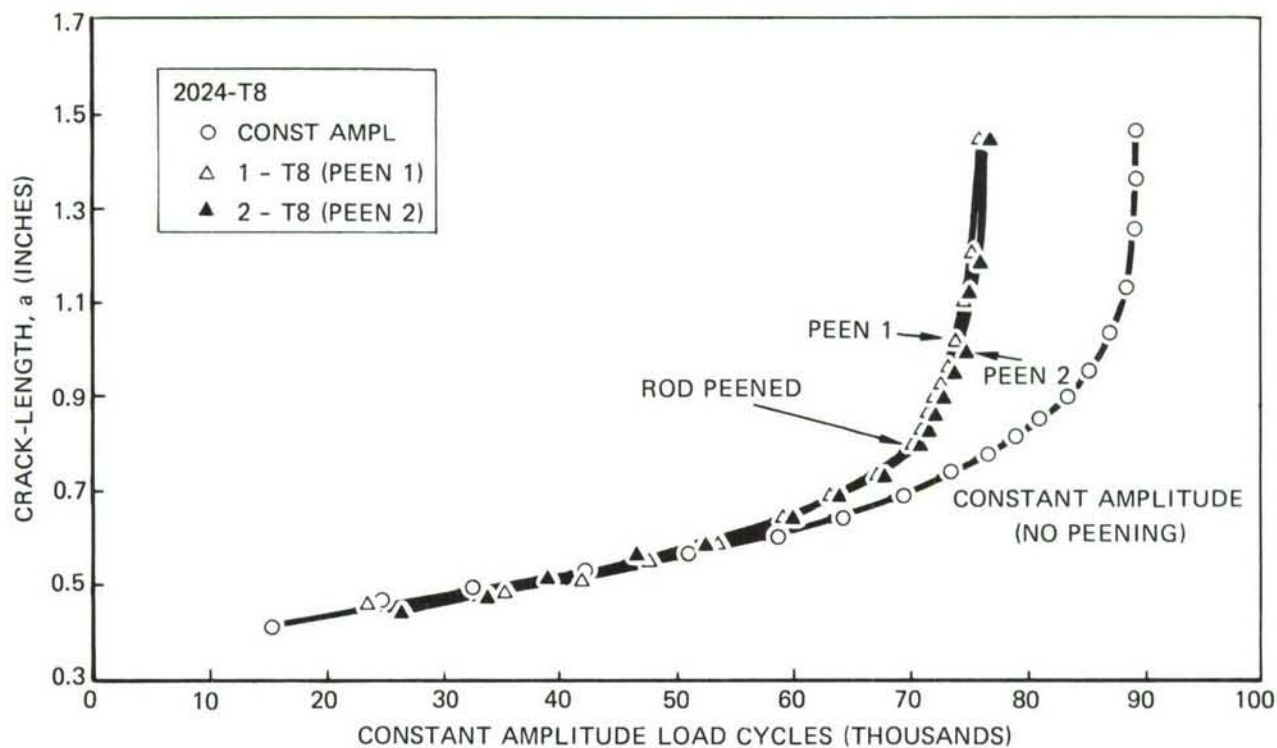
(a) 2024-T8
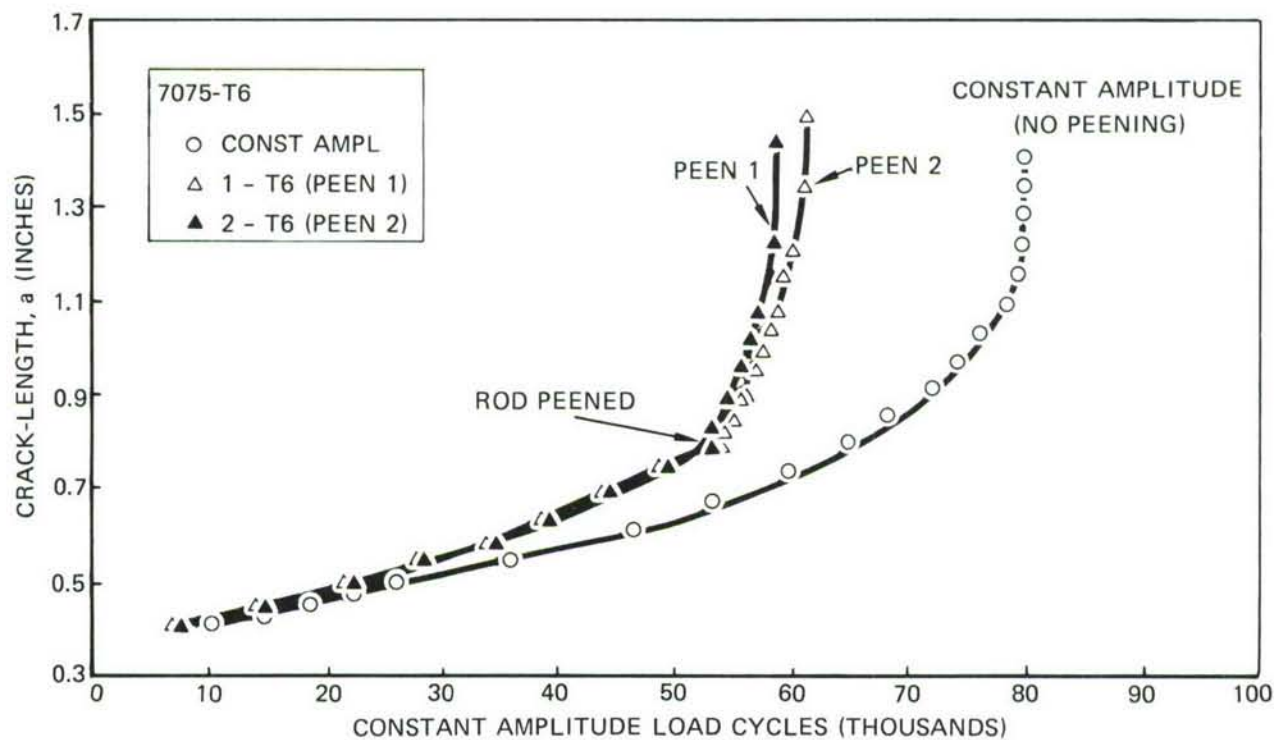
(b) 7075-T6

FIGURE 55. EFFECT OF ROD-PEENING ON FATIGUE-CRACK GROWTH
BEHAVIOR OF 2024-T8 AND 7075-T6 ALLOYS

comparison purposes, both the N* and a*/N* values for corresponding tests are listed in Table XVII. As seen, there is no definite trend, either in a*/N* or in N* with hold-time. As already stated, a small difference between any two tests should not be considered significant because of the statistical nature of the retardation behavior unless that difference exists in a series of tests, i.e. unless a pattern is observed.

A cursory look at Table XVI or XVII may indicate that at OLR of 1.5, N* does not change with hold-time for either 2024-T3 or 7075-T6 while at OLR of 2.0, for 7075-T6, the N* is higher after a hold-time of 16 hours contrary to anticipation. This apparent observation is misleading because the a*/N* values show a small increase with hold-time which would indicate less retardation. The reason for the higher N* was that in this particular test sub-surface crack-growth took place; i.e., the crack was not visible on the surface while it was growing in the interior as indicated by "dimpling" on the surface. At approximately 22,000 cycles, it popped to the surface. This was reflected in fractographic features as well as by initial acceleration and crack-growth during the overload cycle (right-hand column, Table XVI). These features are probably responsible for a redistribution of residual stresses at the crack-tip in such a way that the affected area is increased and the residual stress is decreased, which could explain the observed behavior. With the 2024-T3 alloy at OLR of 2.0, there is considerably more inconsistency in the retardation behavior. It is probably due to the relatively low yield strength of the 2024-T3 alloy combined with holding at the mean load after a high OLR, which caused crack-blunting and/or redistribution of stresses. Hence, no conclusion can be reached based on these tests. However, the results here clearly show that, in analysis and interpretation of all retardation test results except for the very basic spectrum, both the N* and a*/N* values be used, as otherwise, one can reach misleading conclusions.

Fractography was performed on selected specimens to identify differences in fracture topography in the mid-thickness region, as was found for the compressive load tests, even though the surface plastic-zones did not appear different. Initial acceleration was frequently observed for the 7075-T6 alloy with hold-time. This acceleration was probably due to sub-critical crack-growth in the center of the specimen during the hold-time period in this alloy. Figure 56 shows the mid-thickness region of the retardation specimen without any hold-time. In this figure, there is excessive dimpling in and beyond the overload zone, while with hold-times of 1 and 16 hours, relatively smooth regions of sub-critical crack-growth were seen. Figure 57 obtained from the mid-thickness region of the retardation specimen with a hold-time

TABLE XVI. SUMMARY OF TESTS TO DETERMINE EFFECTS OF HOLD-TIME ON RETARDATION BEHAVIOR

$$P_{max} = 800 \text{ Pounds}$$

HOLD TIME[1] (HRS)	SPECIMEN NO.	K_O/K_{MAX} (OLR)	a_i (IN)	K_{MAX} (KSI $\sqrt{IN}$)	a^* (IN)	N^* (1000)	ACCL[2]
			2024-T3				
0	DT3OLC81-2	1.5	.58	10.0	.030	12.5	c
			.80	14.0	.070	12.5	b & c
			1.04	20.2	.160	9.0	c
1	GT3HOLD1		.57	9.8	.029	12.5	b
			.79	13.8	.056	10	b & c
			1.03	19.9	.148	8	b & c
8	GT3HOLD3		.57	9.8	.035	15	b
			.79	13.8	.050	10	a & c
			1.03	19.9	.113	8	a & c
16	GT3HOLD2		.58	10.6	.031	12.5	a
			.784	13.7	.060	15	a & c
			1.041	20.2	.096	8.0	a & c
0	DT3OLC82-2	2.0	.57	9.8	.062	110	b
			.79	13.8	.106	85	b & c
			1.03	19.9	Failed Before Recovery		b & c
1	GT3HOLD4[3]		.57	9.8			
			.795	13.9			
			1.032	19.9			
8	GT3HOLD6		.56	9.7	.015	55	b & c
			.79	13.8	.315	120	a & c
			1.03	19.9	Failed Before Recovery		
16	GT3HOLD5		.57	9.8	.050	75	a & c
			.79	13.8	.027	30	a & c
			1.03	19.9	Failed Before Recovery		b
			7075-T6				
0	DT6OLC81-2	1.5	.57	9.8	.017	3	a & c
			.79	13.8	.036	3	b
			1.05	20.6	.050	2	b & c
1	GT6HOLD1		.57	9.8	.013	3	a
			.79	13.8	.029	3	a & c
			1.04	20.2	.03	2	b
8	GT6HOLD3		.57	9.8	.015	3	b
			.79	13.8	.032	3	b
			1.035	20.0	.038	2	b
16	GT6HOLD2		.57	9.8	.013	3	b
			.79	13.8	.021	1.5	b
			1.03	19.9	.048	2	b & c
0	DT6OLC82-2	2.0	.57	9.8	.026	12.5	b
			.79	13.8	.029	12.5	b
			1.03	19.9	Failed Before Recovery		a
1	GT6HOLD4		.57	9.8	.025	10	b & c
			.79[3]	13.8	--	--	a & c
			1.032	19.9	Failed Before Recovery		b & c
8	GT6HOLD6		.57	9.8	.031	15	a
			.79	13.8	.064	17.5	b
			1.03	19.9	Failed Before Recovery		b & c
8	GT6HOLD6-2		.57	9.8	.029	10	a & c
			.79	13.8	.046	10	a & c
			1.03	19.9	Failed Before Recovery		a
16	GT6HOLD5[4]		.57	9.8	.095	25	a
			.79	13.8	.110	25	b
			1.03	19.9	Failed Before Recovery		b & c

1 - Hold-Time load P_{mean} (440 pounds)

2 - a = No crack-growth during overload cycle
   b = Crack-growth during overload cycle
   c = Initial acceleration after the overload cycle

3 - Crack-branching, - Invalid data.

4 - Subsurface crack-growth

TABLE XVII. EFFECT OF HOLD-TIME ON RETARDATION BEHAVIOR

P_{max} = 800 lbs.

K_o/K_{max} (OLR)	K_{max} (ksi $\sqrt{in.}$)	N* (1000) HOLD TIME, HOURS				a*/N* (10^{-6} in/cycle) HOLD TIME, HOURS			
		0	1	8	16	0	1	8	16
					2024-T3				
1.5	10.0	12.5	12.5	15	12.5	2.4	2.3	2.3	2.5
	13.9	12.5	10.0	10	15	5.6	5.6	5.0	4.0
	20.0	9.0	8.0	8	8	17.8	18.5	14.1	12.0
2.0	9.8	110	-	55	75	0.6	-	0.3	0.7
	13.8	85	-	120	30	1.2	-	2.6	0.9
					7075-T6				
1.5	9.8	3	3	3	3	5.7	4.3	5.0	4.3
	13.8	3	3	3	1.5	12.0	9.7	10.7	14.0
	20.1	2	2	2	2	25.0	15.0	19.0	24.0
2.0	9.8	12.5	10	10/15[1]	25[2]	2.1	2.5	2.9/2.2[1]	3.8
	13.8	12.5	-	10/17.5[1]	25[2]	2.3	-	4.6/3.7[1]	4.4

1. Duplicate Test
2. Sub-Surface Crack-Growth

of 1 hour shows this. However, in the 2024-T3 alloy, the fractographic features were similar between specimens with and without hold-time. This was so because even without a hold-time in the 2024-T3 alloy, either crack-growth occurred during the overload cycle or initial acceleration took place after the overload cycle.

These results did not indicate a consistent trend in hold-time effects on retardation behavior at room temperature and in a non-aggressive environment even though hold-times in an aggressive environment such as 3.5% saltwater at room temperature or at an elevated temperature may significantly affect the delay behavior as reported by Shih and Wei for mill-annealed Ti-6Al-4V alloy[35].

F. EFFECTS OF THICKNESS ON RETARDATION BEHAVIOR

The effect of specimen thickness on retardation behavior was investigated by using 0.5, 0.25, and 0.063-inch thick single-edge-notched specimens of 7075 alloy in the T6 and T73 conditions and 2024 alloy in the T3 and T8 conditions. Single overload cycles were used with two different overload ratios and interferometry was used to measure the surface plastic-zone size. The cyclic hardening exponents for all four materials were determined by obtaining cyclic stress-strain curves using incremental strain-cycling tests on 0.25-inch diameter cylindrical specimens. Test results
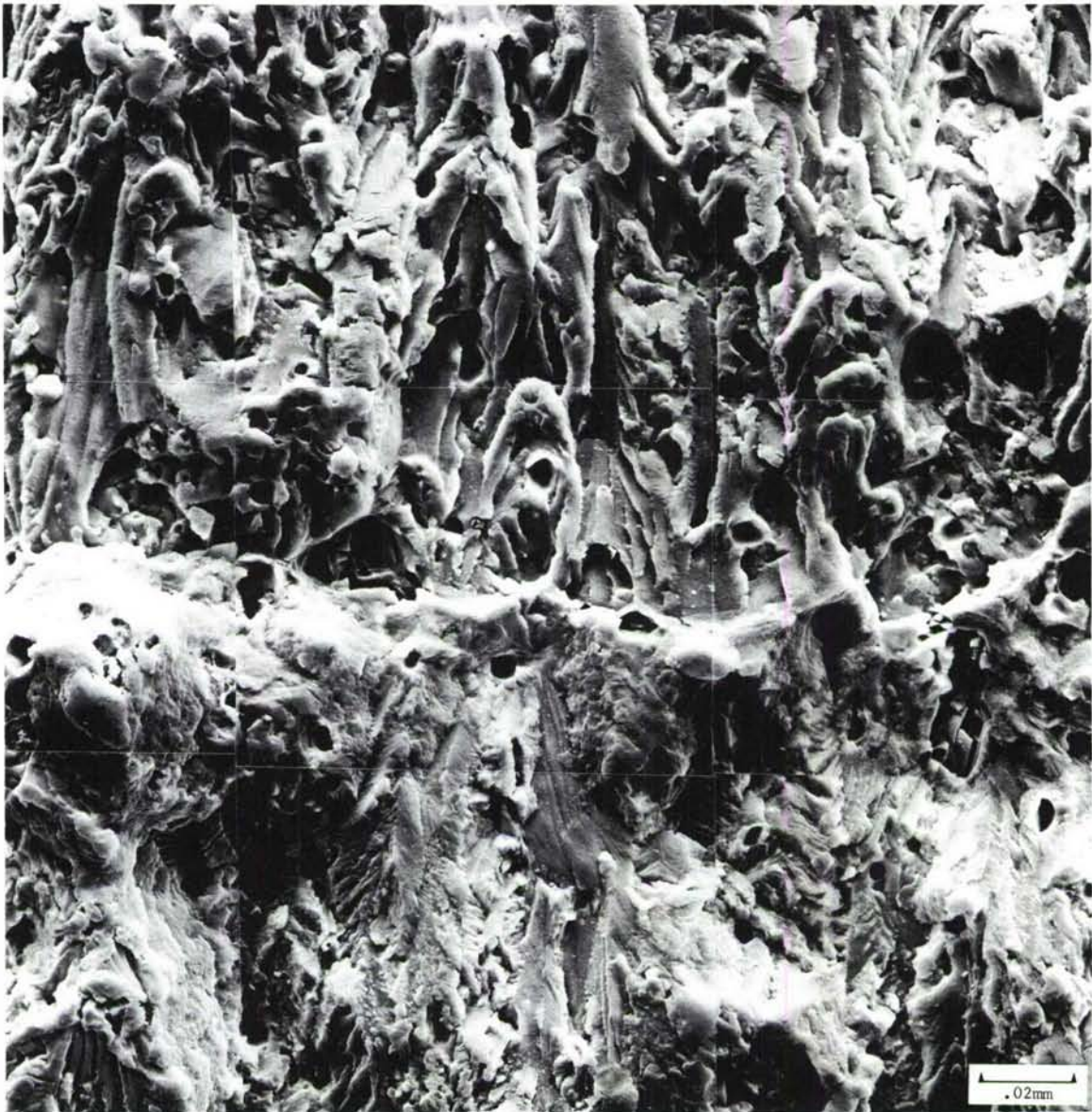
$$P_{MAX} \, (K_{MAX}) \; = \; 800 \text{ LBS } (9.8 \text{ KSI} \sqrt{\text{IN.}})$$

OVERLOAD RATIO = 2.0

FIGURE 57. FRACTOGRAPHIC FEATURES IN THE VICINITY OF A 100%
OVERLOAD MARKING IN THE MID-THICKNESS REGION OF
7075-T6 WITH A HOLD-TIME OF 1 HR

indicated that the amount of retardation decreases with increasing specimen thickness. However, the relative decrease was more predominant in the 7075 alloy and, at the higher overload ratio, 2.0. Only a minor effect of thickness was seen on the retardation behavior for the 2024-T8 alloy, which had a different precipitate morphology and cyclic hardening exponent. Fractography was used to study the micromechanisms of crack-growth. Well-defined striations and changes in the striation spacings after an overload cycle were not seen in all specimens studied, and no striations were observed immediately following the overload cycle. The lack of discernible striations is due to: abrasion, the difficulty in resolving striations associated with relatively low crack-growth rates, a change in crack-propagation mode, or a combination of all of the above factors. However, for the specimens with discernible striations, correlation between measured da/dN and changes in striation spacing was good.

A discussion of these results was presented at the Tenth National Symposium on Fracture Mechanics, Philadelphia, Pa., Aug. 26-28, 1976. The paper is reproduced in its entirety as Appendix D.

G. MICROSTRUCTURAL CHANGES

In order to determine microstructural changes in the overload zone, TEM studies were performed to determine how the crack propagates with reference to intermetallic compounds, precipitates, dislocation tangles and grain morphology. Since foils must be obtained from extremely small localized areas to preserve the plastic zone for TEM studies, a rather thick foil was used for final ion milling after mechanical sectioning and electropolishing. Even though this made the final foil preparation a time-consuming process, there was no other technique available to assure the retention of the desired area.

To evaluate the micromechanism effects, three series of thin foil investigations were performed by:

(a) Mapping of the plastic-zone area in a 7075-T6 and a 2024-T3 retardation specimen after crack-arrest.

(b) Examination of foils removed parallel to the fracture surfaces of retardation specimens as was done for FCP specimens.

(c) Specially designed tests — foils were obtained from the overload plastic-
zone area:

    (i)   After the overload cycle (FIP)

    (ii)   When the crack was halfway through the overload plastic-zone (HTP)

    (iii)   When the crack was beyond the zone. For this purpose, results from
           (b) were used.

In general, the details of the microstructural changes in the retardation speci-
mens were similar to those observed in the failed FCP (constant amplitude) specimens.
Only the magnitude of changes in dislocation and precipitation interactions was larger.
Just as in the FCP specimens, the existence of G.P. zones and precipitates in these
alloy systems tends to inhibit the formation of distinct slip markings and dislocation-
cell structures in retardation specimens. No overwhelming evidence of distinctive
cellular formation or operative slip mechanisms was observed. In fact, it was a
very rare case when a dislocation cellular structure, as shown in Figure 58, was
observed. Here, at a very high magnification, dislocation tangles and cells with faint
G.P. zones in the background can be seen. The G.P. zones can be seen in the back-
ground of the cellular structure as fine discrete areas. This particular area showed
the greatest amount of cell-structure development of all foils examined in the program.
This could have resulted from a precipitate-depleted area where dislocations would move
and interact more freely. This area is from a foil obtained in the plastic zone region of
a 7075-T6 specimen after a 100 percent overload cycle.

The mapping of the plastic-zone area was performed to determine the changes in
the vicinity of the crack-tip area due to the overload cycle. For this purpose, wedge
shaped foils from the plastic-zones of one 7075-T6 and one 2024-T3 specimen after
crack-arrest were obtained. The crack-tip was at the apex of the wedge as shown
below:

SUCCESSIVE LAYERS REMOVED

111
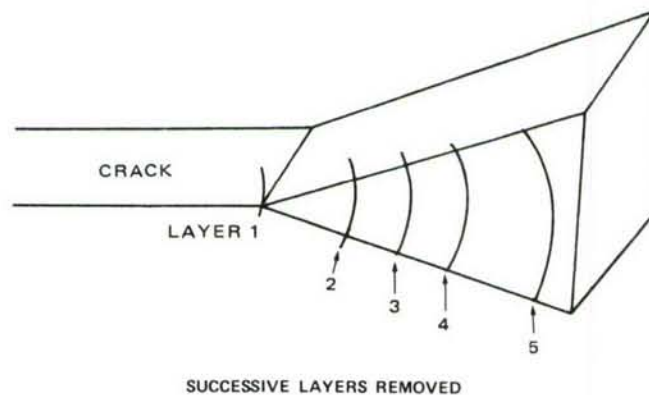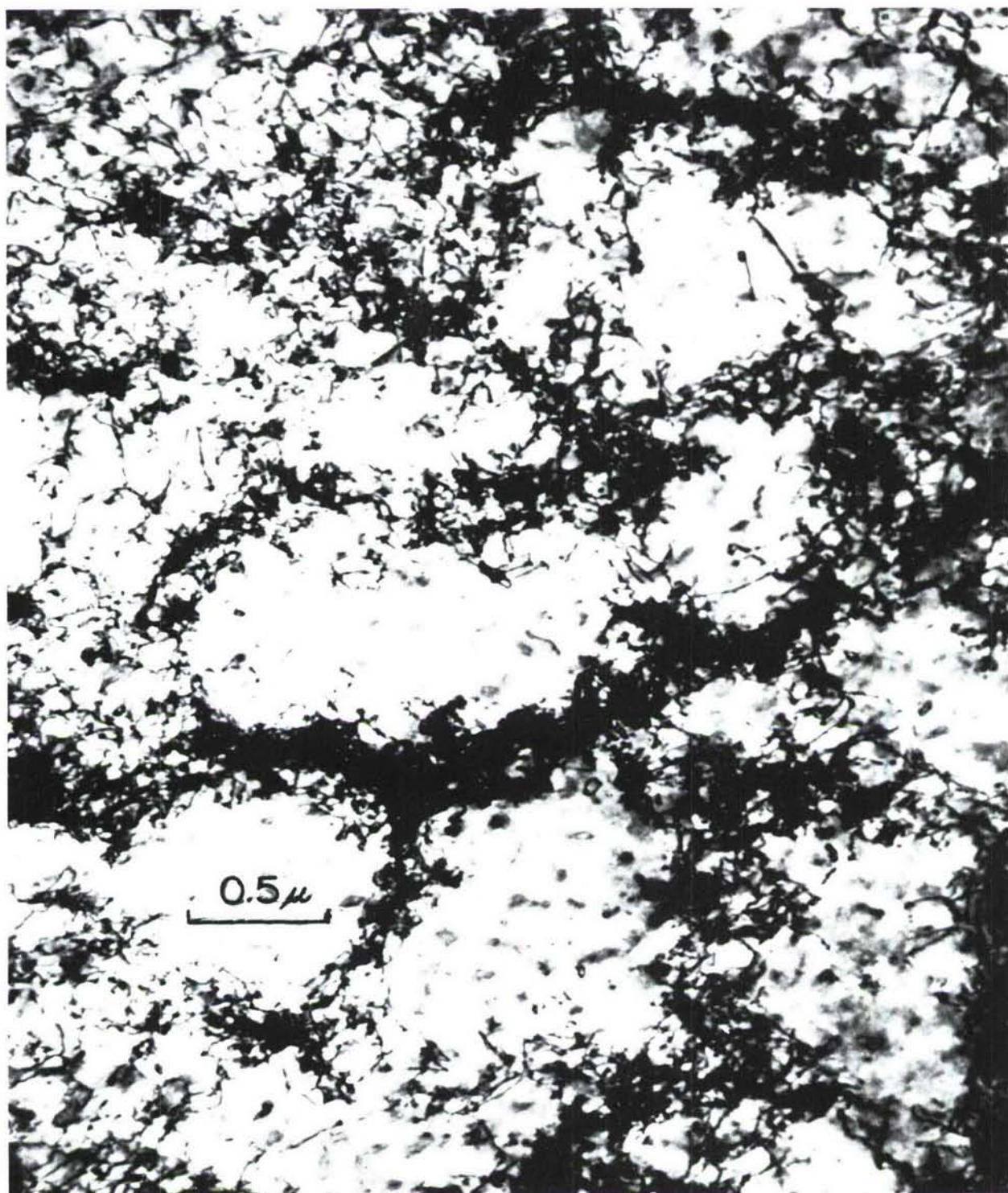
FIGURE 58. DISLOCATION CELL NETWORKS IN THE 100% OVERLOAD REGION
OF A 7075-T6 RETARDATION SPECIMEN

The mapping was then done by removing successive layers of the foil in such a way that the first layer did not contain the overload plastic-zone, while the second layer was just within the plastic-zone, and so on, until we progressed beyond the plastic-zone. We saw both a change in dislocation density and a change in precipitate distribution as the plastic-zone was traversed. In the 2024-T3 alloy, it was primarily the change in dislocation density while in the 7075-T6, the change was both in dislocation density and precipitation. However, in the 2024-T3, there were areas in the central region of the plastic-zone where only an extensive increase in G.P. zones could be seen as shown in Figure 59(a). An interesting feature noted was that the changes due to overload were not maximum at the center of the layers. Figure 59(b) schematically shows the observed pattern. This is probably due to the fact that maximum dislocation movement takes place along the shear slip-planes.

Two failed specimens from each alloy, one with OLR of 1.5 and the other with OLR of 2.5, were selected for obtaining foils from the overload regions of their fracture surfaces. In specially designed tests, an overload cycle (OLR = 2.0) was applied in two specimens of each alloy after growing the crack to 0.8-inch at a P_{max} of 500 pounds. In one of the two specimens of each alloy, the crack was grown approximately halfway through the plastic-zone (obtained from Table X at 8.7 ksi $\sqrt{in}$). Thin foils were then obtained from the crack-tip area of each of the eight specimens (2 specimens x 4 alloys). As already stated, no mechanism differences between the retardation and FCP foils were observed to warrant an extensive analysis and discussion. Table XVIII summarizes these results and lists the salient features of microstructural changes. A review follows.

In the 2024-T3 alloy, foils obtained from the plastic-zone region due to the overload (FIP) showed an extensive increase in dislocation density and some increase in precipitation, primarily very fine G.P. zones (Figure 60 (a)). When the crack was halfway through the plastic-zone (HTP), a similar structure with areas of dislocation tangles was observed (Figure 60(b)-(d)). This included planar and forest dislocations which were confirmed by tilting of the specimen stage when some of them with favorable orientation (g.b = 0) vanished (compare 60 (b) and (d)).

In 2024-T8 FIP, an extensive increase in precipitation (platelets of large S') along crystallographic planes giving a "Widmanstatten" type of pattern was observed (Figure 61(a) and (b)). In Figure 61(b), dislocation tangles at an apparent grain boundary can be seen. In HTP of this alloy, areas with dislocation tangles and finer S' network can be seen in Figure 61(c) and (d). The TEM observations in FIP of
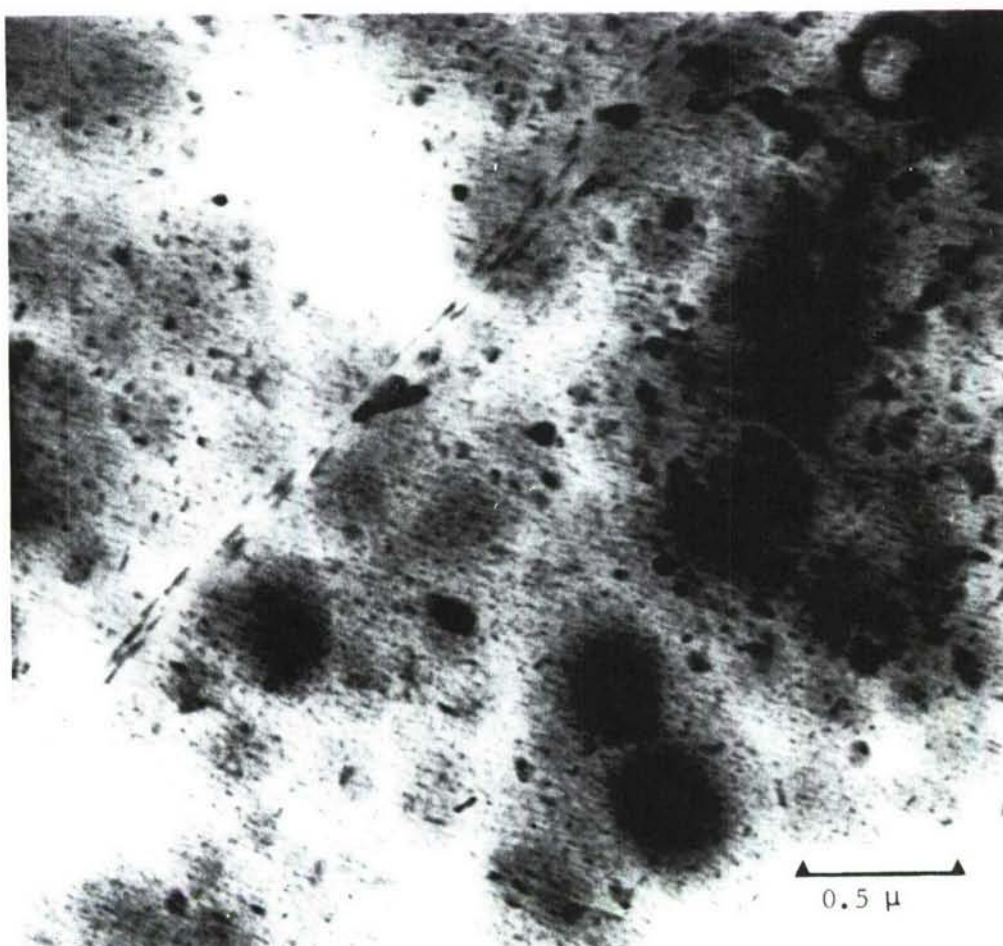
FIGURE 59(a). MICROGRAPH SHOWING EXTENSIVE PRECIPITATION IN A
2024-T3 CRACK-ARREST PLASTIC-ZONE (OLR = 2.5, P_{MAX} = 800 LBS)
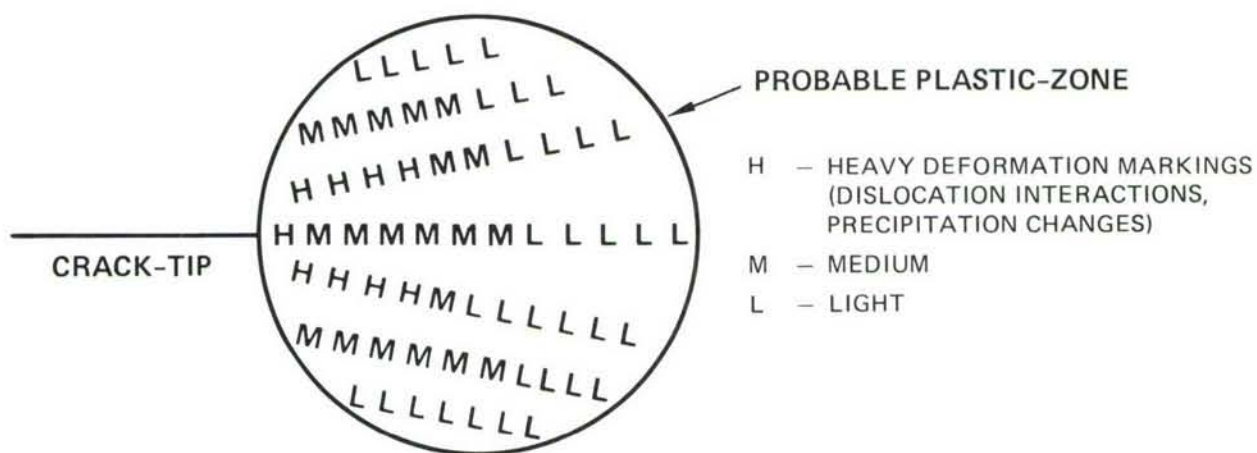
FIGURE 59(b). SCHEMATIC OF CHANGES IN DEFORMATION MARKING OBTAINED
BY MAPPING OF 2024-T3 AND 7075-T6 CRACK-ARREST SPECIMENS
(OLR = 2.5, P_{MAX} = 800 LBS)

TABLE XVIII. SUMMARY OF MICROSTRUCTURAL INVESTIGATION

ALLOY	FOILS PARALLEL TO FRACTURE SURFACES OF FAILED RETARDATION SPECIMENS[1]				SPECIALLY DESIGNED TESTS – FOILS OBTAINED FROM THE PLASTIC-ZONE AREA (PZA)[2]			
	1.5 OVERLOAD RATIO		2.5 OVERLOAD RATIO		IMMEDIATELY AFTER THE OVERLOAD		CRACK HALFWAY THROUGH PZA	
	SPECIMEN NO. (FIG. NO.)	SALIENT FEATURES	SPECIMEN NO. (FIG. NO.)	SALIENT FEATURES	SPECIMEN NO. (FIG. NO.)	SALIENT FEATURES	SPECIMEN NO. (FIG. NO.)	SALIENT FEATURES
2024-T3	DT30LC1 (64(a) & (b))	Dislocation tangles and interactions, G.P. zones.	DT30LC3 (64(a))	Extensive dislocation interactions and G.P. zones.	DT3TEM1 (60(a))	Primarily dislocation tangles and very fine G.P. zones.	DT3TEM2 (60(b)-(d))	Primarily dislocation tangles and areas with G.P. zones. Grain boundary is apparent (b).
2024-T8	DT80LC1 (64(c))	S' ppts along crystallographic planes	DT80LC3 (64(d))	Primarily precipitates with some dislocation tangles.	DT8TEM1 (61(a) & (b))	Array of large S' platelets aligned along crystallographic planes.	DT8TEM2 (61(c) & (d))	Array of smaller S' platelets with some dislocation tangles.
7075-T6	DT60LC1 (65(a))	Dislocation networks and G.P. zones.	DT60LC3	Dislocation networks and G.P. zones.	DT6TEM1 (62(a) & (b))	Dislocation networks, tangles, and G.P. zones. Grain boundary precipitates, peppered matrix.	DT6TEM2 (62(c) & (d))	Dislocation tangles, elongated cells, networks, G.P. zones, and peppered matrix.
7075-T73	DT730LC1 (65(b))	"Peppered" G.P. zones and dislocation tangles. Grain boundary precipitates.	DT730LC3 (65(c))	Fine distribution of G.P. zones and dense dislocation tangles. Grain boundary precipitates.	DT73TEM1 (63(a) & (b))	Dislocation tangles, G.P. zones, Grain boundary dislocation build-up and grain boundary precipitates.	DT73TEM2 (63(c))	Dislocation tangles and G.P. zones.

1) Fracture surface in the vicinity of first overload cycle was used for these foils.
2) For these tests, an overload cycle (OLR = 2.0) was applied at a crack-length of 0.8-in. and P_{max} of 500 lbs.
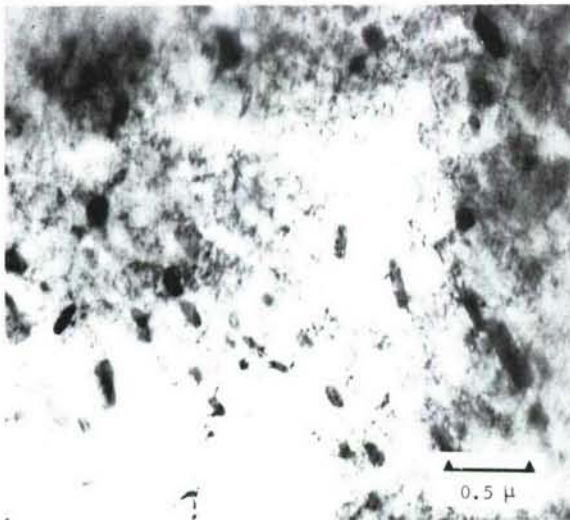
(a) AFTER OVERLOAD
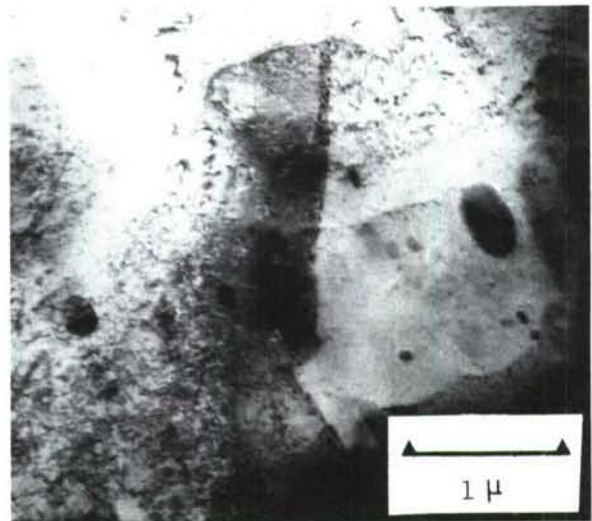
(b) HALFWAY THROUGH PLASTIC-ZONE
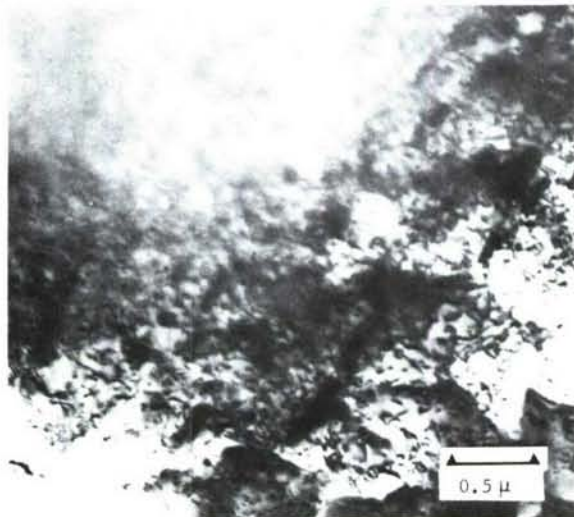
(c) HALFWAY THROUGH PLASTIC-ZONE

(d) HALFWAY THROUGH PLASTIC-ZONE

FIGURE 60. DISLOCATION INTERACTIONS AND PRECIPITATE DISTRIBUTION
IN THE PLASTIC-ZONE AREA OF 2024-T3 SPECIMEN
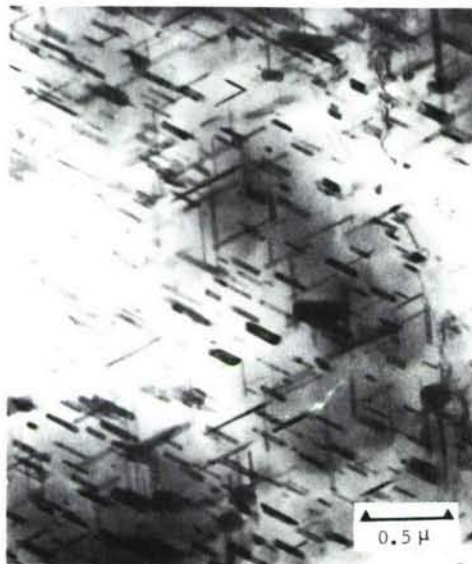
(a) AFTER OVERLOAD
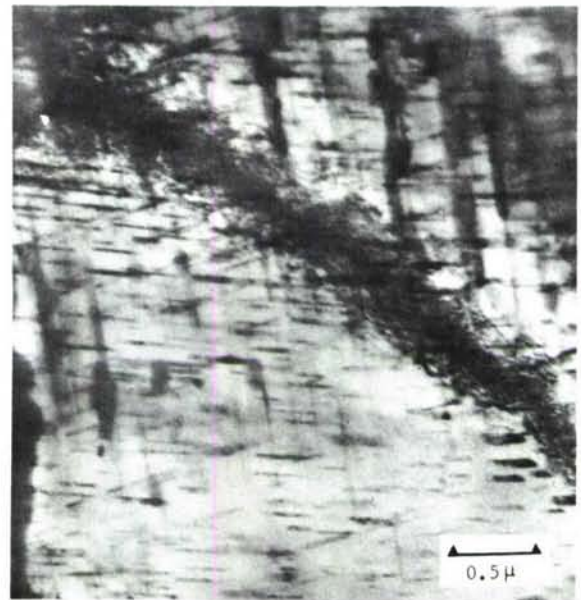
(b) AFTER OVERLOAD
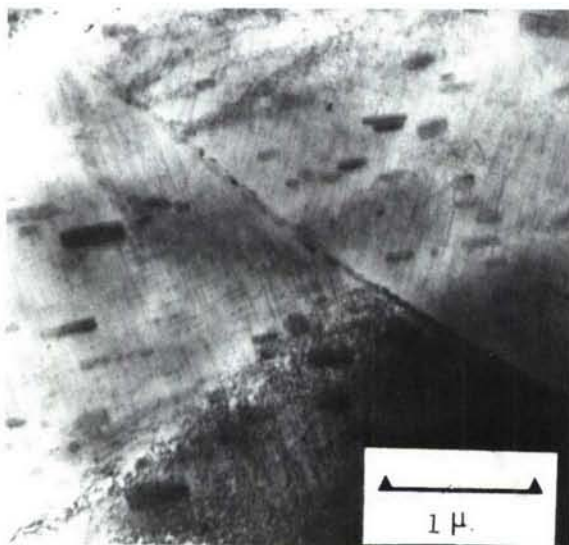
(c) HALFWAY THROUGH PLASTIC-ZONE

(d) HALFWAY THROUGH PLASTIC-ZONE

FIGURE 61. DISLOCATION INTERACTIONS AND PRECIPITATE DISTRIBUTION
IN THE PLASTIC-ZONE AREA OF 2024-T8 SPECIMEN

117

7075-T6 showed extensive increase in G.P. zones which "peppered" the matrix (Figure 62(a) and (b)). Some dislocation marking can also be seen in these micrographs. In the case of HTP (halfway through plastic-zone), dislocation tangles and cells also could be seen (Figure 62(c) and (d)). Both the FIP (Figure 63(a) and (b)) and HTP of the 7075-T73 showed features similar to those for the 7075-T6 alloy. However, the precipitation and dislocation interactions were greater in this alloy.

The examination of foils from sections parallel to the fracture surfaces followed a similar pattern, e.g., Figure 64 shows typical micrographs from the overload plastic-zone areas of 2024-T3 and T8 alloys. The details of the specimen condition are listed in Table XVIII. A heavy dislocation density can be observed in the overload plastic-zone area (Figures 64(a) and (b)). Figure 64(c) shows a corresponding area of the 2024-T8 at the same OLR (1.5). Here, dislocation density is much lower as compared to the 2024-T3 specimen. Instead, the 2024-T8 showed a large density of precipitate particles. Even at an OLR of 2.5 (Figure 64(d)), there was primarily precipitation; the dislocation density was nowhere near that in the 2024-T3 alloy. This difference in microstructure is probably responsible for the difference in the retardation behavior of the two heat treatments of the 2024 alloy. Apparently, the heavy dislocation density inhibits cross-slip necessary for crack-nucleation from the blunted crack-tip, while the heavier density of precipitate particles apparently does not offer significant resistance to crack-nucleation and growth. In fact, they may even make nucleation easier, which could explain why the 2024-T8 alloy has poorest retardation among all four alloys studied. Similar foils from the 7075-T6 and T73 showed both increased dislocation interactions and precipitation. However, the dislocation interactions were less than in the 2024-T3 alloy, while the precipitation changes were not crystallographic and Widmanstatten type as in the 2024-T8 alloy. Figure 65 illustrates this. In the 7075-T6 alloy, at low OLR (1.5), comparatively straight dislocation networks can be seen (Figure 65(a)). Figure 65(b) shows an area from the foil of a 1.5 OLR, 7075-T73 fracture surface. Here, a triple grain boundary with peppery G.P. zones can be seen. Micro-cracks can easily nucleate from these triple points. At the higher OLR (2.5), besides peppery G.P. zones, dislocation tangles can be seen (Figure 65(c)). This could explain why the higher OLR shows higher delay. Thus, the microstructural changes reflect the observed retardation behavior, and they show that the dislocation interactions as observed in 2024-T3 plastic-zone have a much higher resistance to fatigue-crack growth than the precipitation changes observed in 2024-T8.
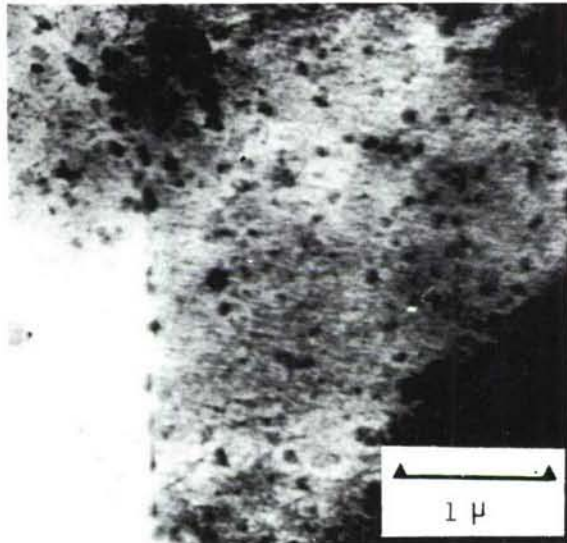
(a) AFTER OVERLOAD
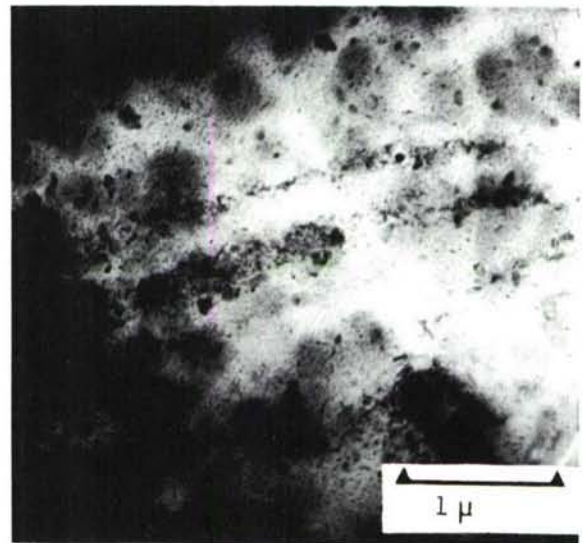
(b) AFTER OVERLOAD
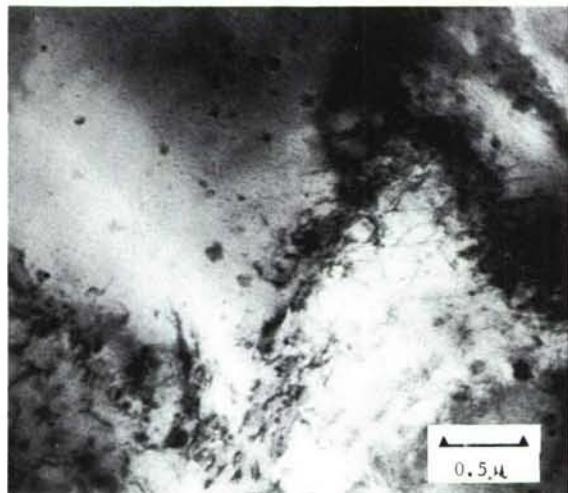
(c) HALFWAY THROUGH PLASTIC-ZONE
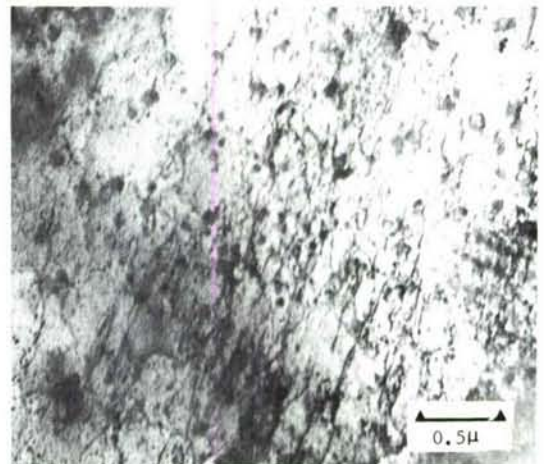
(d) HALFWAY THROUGH PLASTIC-ZONE

FIGURE 62. DISLOCATION INTERACTIONS AND PRECIPITATE DISTRIBUTION
IN THE PLASTIC-ZONE AREA OF 7075-T6 SPECIMEN
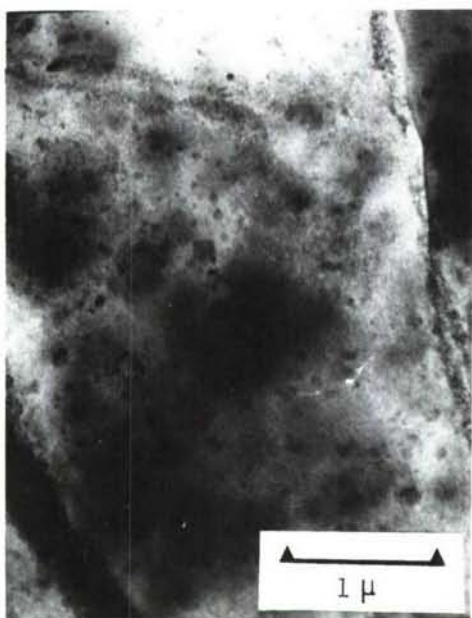
(a) AFTER OVERLOAD
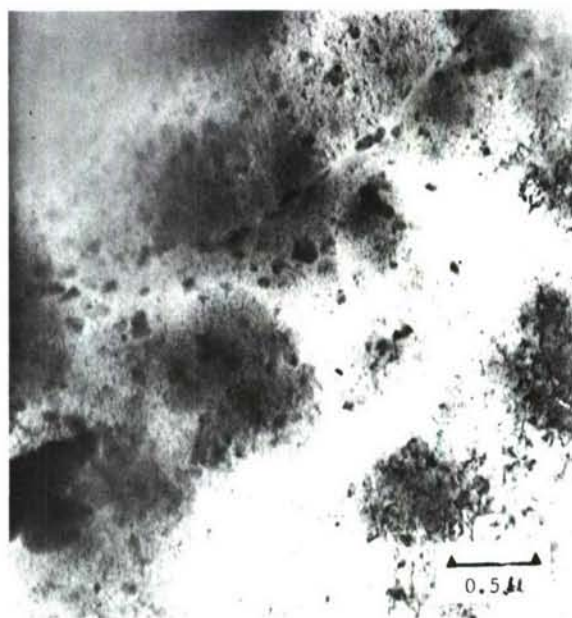
(b) AFTER OVERLOAD
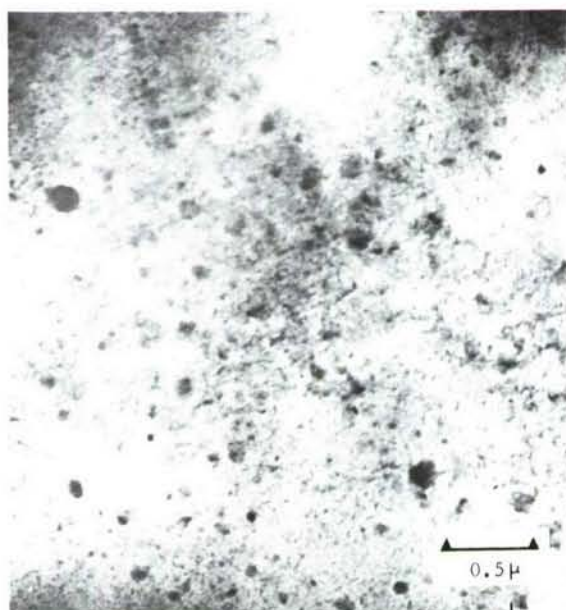
(c) HALFWAY THROUGH PLASTIC-ZONE

FIGURE 63. DISLOCATION INTERACTIONS AND PRECIPITATE DISTRIBUTION
IN THE PLASTIC-ZONE AREA OF 7075-T73 SPECIMEN

(a) 2024–T3 (OLR = 1.5)
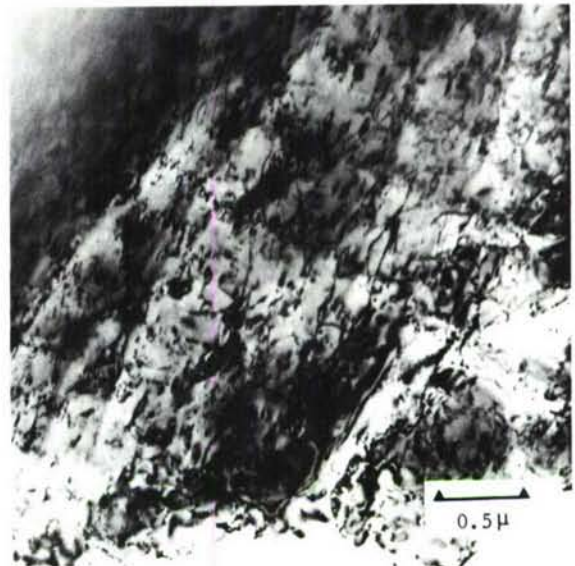
(b) 2024–T3 (OLR = 1.5)
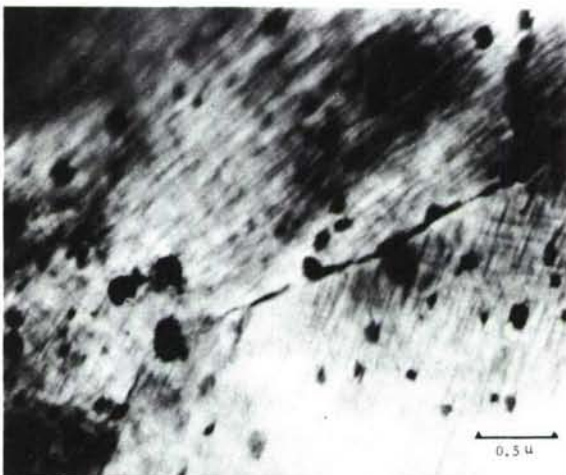
(c) 2024–T8 (OLR = 1.5)
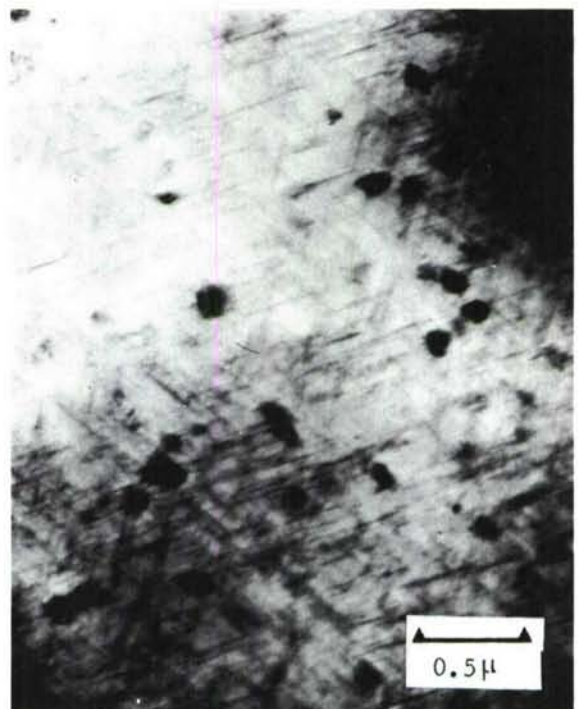
(d) 2024–T8 (OLR = 2.5)

FIGURE 64. DISLOCATION INTERACTIONS AND PRECIPITATE DISTRIBUTION
IN THE OVERLOAD PLASTIC-ZONE AREA OF FAILED 2024 SPECIMENS

121

(a) 7075-T6 (OLR = 1.5)

(b) 7075-T73 (OLR = 1.5)
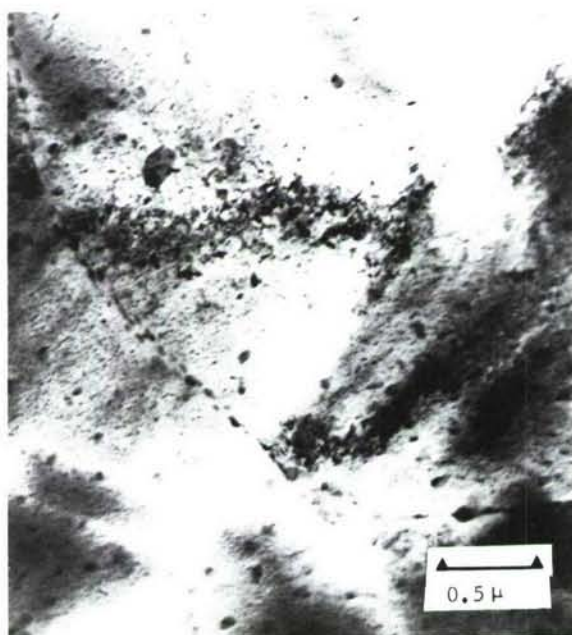
(c) 7075-T73 (OLR = 2.5)

FIGURE 65. DISLOCATION INTERACTIONS AND PRECIPITATE DISTRIBUTION
IN THE OVERLOAD PLASTIC-ZONE AREA OF FAILED 7075 SPECIMENS

The compressive load cycle appeared to produce no dramatic change in the microstructure. Figure 66 shows two areas from a foil obtained from a section parallel to the overload plastic-zone region of the fracture surface of a 7075-T651 retardation specimen with compressive load. Here, compared to the retardation specimens without compressive overload, there are less "peppery" type G.P. zones, even though their sizes are larger. Figure 66(a) shows what appear to be twin or subgrain-boundaries as outlined by fine precipitates, while Figure 66(b) shows two grains, in one of which dislocation tangles and networks can be seen, while in the other probably because of the orientation of the grains $(\vec{g} \cdot \vec{b} = 0)$, no dislocation tangles can be seen.

To summarize, the TEM investigation of thin foils obtained from the overload plastic-zone and area below the fracture surface of 2024-T3 retardation specimens showed extensive increase in dislocation density and their interactions. Similar foils for the 2024-T8 alloy showed increased precipitation of large S' platelets and changes in precipitate morphology without any substantial increase in dislocation interactions. The 7075-T6 and T73 alloys showed both increased dislocation inter-actions and precipitation. However, the increased dislocation interactions were less than those in the 2024-T3 alloy, while the precipitation changes were general versus the Widmanstatten type morphology in the 2024-T8 alloy. Thus, dislocation inter-actions are much more beneficial than precipitation changes in inhibiting fatigue-crack growth as manifested by the relative retardation behavior of the four program materials.

(a) FINE PRECIPITATES AND TWIN OR
SUBGRAIN BOUNDARIES
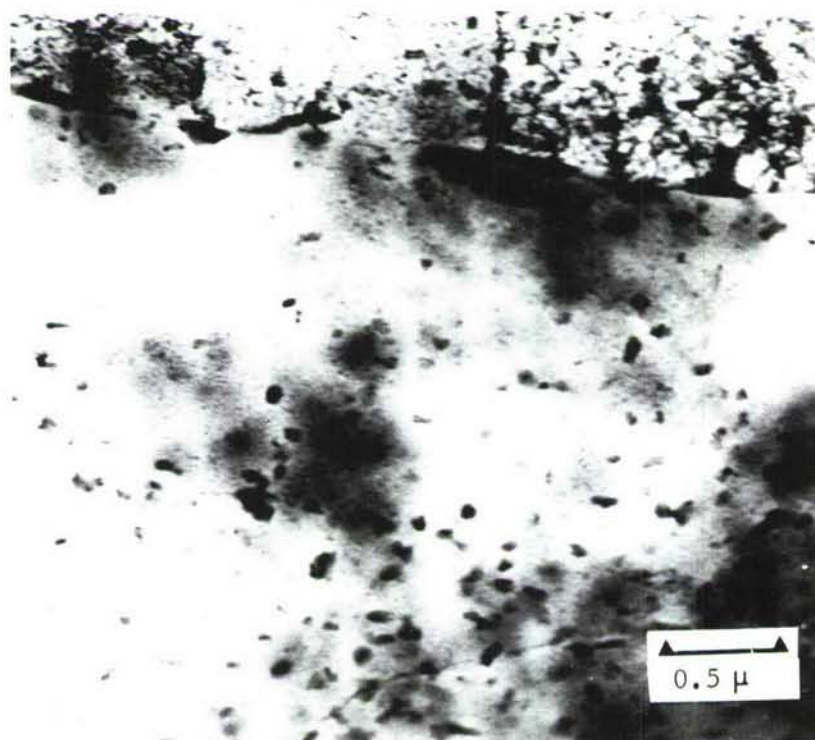
(b) DISLOCATION TANGLES AND
NETWORKS AS WELL AS FINE PRECIPITATES

FIGURE 66. EFFECT OF A COMPRESSIVE LOAD ON MICROSTRUCTURE IN THE
PLASTIC-ZONE AREA (OLR = 2.0) OF A 7075-T651 SPECIMEN

IV. SUMMARY AND CONCLUSIONS

A fundamental investigation was made to determine the important metallurgical and environmental factors that influence fatigue crack retardation behavior in aluminum alloys and to provide a basis for improving retardation prediction techniques. The retardation phenomenon was found to be very complex and dependent on the loading variables as well as material parameters. The results from this program suggest that a phenomenological model for predicting fatigue-crack growth under variable amplitude loading can be developed by taking the various important parameters into account.

Fatigue-crack growth behavior after single overload cycles at different overload ratios was determined for four microstructures with three different yield strengths. The results were correlated with the observed retardation behavior, metallurgical features, fractographic features, and plastic-zone size changes at the crack-tip. In order to determine the effects of microstructure and plastic-zone size changes, which primarily depend upon the yield strength and applied stress intensity factor, two aluminum alloys (2024 and 7075), strengthened by different hardening mechanisms and having different stress-strain characteristics, were used. The use of two heat treatments for each of the alloys (T6 and T73 for 7075, T3 and T8 for 2024) permitted the determination of the effect of strength level and metallurgical factors on the retardation behavior.

Tests were conducted to determine the effects of an aggressive environment (3-1/2 percent saltwater), test frequency, and thickness on the retardation behavior. Selected tests were included to determine the effects of hold-time at low stress levels, compressive load cycles, multiple overload cycles, peening, and exposure to slightly elevated temperatures on the retardation behavior.

The conclusions obtained from this program are summarized below:

1. The magnitude of the overload ratio (OLR) is the most important loading parameter affecting retardation in the 2024 and 7075 alloys. The number of delay cycles (N^*) increases with an increase in OLR.

2. Immediately after the overload cycle, transient crack-growth behavior
    such as initial acceleration, delayed retardation, etc. can be neglected
    for making life predictions, since their effect on the number of delay
    cycles is very small.

3. The effect of baseline K_{max} on N^* at a given OLR depends on the alloy
    and the actual value of OLR. The N^* value decreases with an increase
    in K_{max} until it reaches a plateau, subsequent to which it increases with
    K_{max} depending on the OLR. For a given K_{max} and OLR, the baseline
    P_{max} has no significant effect on the number of delay cycles.

4. In general, the yield strength can be used to rank the retardation behavior
    of the program alloys; the alloy with the lowest yield strength (2024-T3)
    showing maximum delay. However, other factors such as the test environ-
    ment and microstructure can change this ranking as indicated by the salt-
    water results and the next three conclusions.

5. Under identical test conditions, the 7075-T73 generally showed a higher
    number of delay cycles than the 2024-T8 even though they both had the
    same yield strength. The 2024-T3 showed considerably more delay than
    the other three alloys. The 7075-T73 alloy was next with the 2024-T8 and
    7075-T6 showing approximately similar delay behavior.

6. Yield strength differences alone are not adequate for explaining differences
    in retardation behavior. Both the microstructural and yield strength
    differences must be considered in the development of an improved retarda-
    tion model: as an example, the yield strength differences between the
    2024-T3 and T8 and between the 7075-T6 and T73 are approximately the
    same. However, the two conditions of 2024 alloy showed a much greater
    difference in retardation behavior than the two conditions of 7075 alloys.

7. There was no unique value of crack-arrest for the four alloys studied.
    In the 2024-T3 alloy, crack-arrest occurred at 2.5 OLR for all K_{max}
    values. For the other alloys, it was either 2.5 or 3.0, depending on
    the K_{max}. These results indicated that besides the yield strength and
    the test conditions (K_{max} and OLR), the microstructure and cyclic
    hardening exponent of an alloy influence its retardation and crack-arrest
    behavior.

8. For the specimen geometry (SEN), alloy (7075-T6), and instrumentation used, no significant changes in crack-closure were detected as the cycling progressed after the overload cycle even though some crack-closure was taking place during constant-amplitude cycling and crack-closure loads did vary with changes in R values.

9. After relaxation for 16 hours, as well as after a high overload ratio, significant crack-closure was observed by the potential method. This crack-closure disappeared within 200 cycles. Nevertheless, the overall conclusion from crack-closure observations was that insufficient changes in crack-closure were taking place to account for the observed number of delay cycles.

10. The overload cycle manifests itself as a stretch band across the thickness of the failed specimens.

11. The width of the overload stretch zone and associated retardation region increases with increasing K and decreasing thickness, progressing from a thin line at low K levels to a wide band of overload zone exhibiting more dimpling and tunneling at higher K values.

12. The extent of tunneling and dimpling depended on the alloy, its toughness, and mechanical properties. The tunneling and extent of dimpling in the stretch zone was generally larger in the 7075-T6 and T73 alloys than in the 2024-T3 alloy and smaller than in the 2024-T8 alloy. This behavior was in agreement with the delay behavior observed during testing.

13. For the specimens with discernible striations, correlation between measured da/dN rates and changes in striation spacing was good.

14. A good agreement between plastic-zone size measured by interferometry and that calculated under plane stress conditions was found for the 0.063-inch thick specimens of all the four alloys. However, interferometry is not suitable for investigating plane-strain or mixed mode conditions because the interferometry measures surface plastic-zone and, for specimens of any thickness, a plane-strain condition does not exist at the surface.

15. The results showed the applicability of the optical interference technique for investigating the crack-growth behavior as the crack progresses through the plastic-zone under plane-stress conditions and also confirmed that retardation occurs primarily in the overload plastic-zone.

16. Test frequency changes did not produce any major effects on the retardation behavior.

17. Single tensile overload cycles cause retardation of fatigue-crack growth in saltwater just as they do in air. The number of delay cycles increases with increase in overload ratio in both air and saltwater.

18. The number of delay cycles was greater in air than in the 3-1/2 percent saltwater.

19. The effect of an aggressive environment on retardation behavior was much larger in the 7075-T6 alloy than in the 2024-T8 and 7075-T73 alloys.

20. The effect of an aggressive environment on retardation behavior was more predominant at higher overload ratios and could not be attributed to the higher FCP rate associated with the saltwater environment. This was probably due to higher crack-blunting and higher plastic-strain energy at the crack-tip due to severe plastic deformation at the high OLR.

21. The susceptibility of a microstructure to environmental attack was found to be important in determining its fatigue behavior under variable amplitude loading in an aggressive environment. An alloy such as 7075-T6 which shows superior retardation behavior in air can be inferior to the other alloy such as 2024-T8 in an aggressive medium such as saltwater.

22. Environmental attack similar to that which is observed on fracture surfaces of saltwater FCP specimens was found by fractographic examination of saltwater retardation specimens.

23. The application of multiple overload cycles increases retardation. The number of delay cycles increases up to a certain number of overload cycles, after which it reaches a saturation maximum. Multiple overload cycles can manifest themselves as striation bands and increased abrasion in the overload zone.

24. Exposure to 176F (80C) or 248F (120C) was found to cause a decrease in retardation.

25. The effective crack-growth rate in the retardation zone increased due to a compressive load after the overload cycle.

26. The beneficial crack-tip residual stresses introduced by tensile overloads cannot be simulated by rod-peening.

27. Hold-time at low stress levels was found to have no significant effect on the retardation behavior.

28. The number of delay cycles was found to decrease with increase in thickness. However, only a minor effect of thickness was seen on the retardation behavior of the 2024-T8 alloy.

29. Both the $N*$ (delay cycles) and $a*/N*$ (effective crack-growth rate) are useful parameters for analysis and interpretation of retardation test results.

30. Thin foils obtained from the overload plastic-zone and area below the fracture surface of 2024-T3 retardation specimens showed an extensive increase in dislocation density and their interactions. Similar foils for the 2024-T8 alloy showed increased precipitation of large S' platelets and changes in precipitate morphology without any substantial increase in dislocation interactions. The 7075-T6 and T73 alloys showed both increased dislocation interactions and precipitation. However, the increased dislocation interactions were less than those in the 2024-T3 alloy, while the precipitation changes were general versus the Widmanstatten type morphology in the 2024-T8 alloy. Thus, dislocation interactions are much more beneficial than precipitation changes in inhibiting fatigue-crack growth as manifested by the relative retardation behavior of the four program materials.

REFERENCES

1. C. M. Hudson and H. F. Hardrath, "Effects of Changing Stress Amplitude on the Rate of Fatigue-Crack Propagation in Two Aluminum Alloys," NASA TN D-960, September 1961.

2. J. Schijve, "Fatigue Crack Propagation in Light Alloy Sheet Materials and Structures," Report MP-195, National Luchtvaartlaboratorium (Amsterdam), August 1960.

3. C. M. Hudson and K. N. Raju, "Investigation of Fatigue-Crack Growth Under Simple Variable-Amplitude Loading," NASA TN D-5702, March 1970.

4. H. F. Hardrath, "Cumulative Damage," Fatigue – Interdisciplinary Approach, Syracuse University Press, Syracuse, New York, 1964.

5. E. F. J. Von Euw, R. W. Hertzberg, and R. Roberts, "Delay Efforts in Fatigue Crack Propagation," ASTM STP 513, p. 230, 1972.

6. D. M. Corbly and P. F. Packman, "On the Influence of Single and Multiple Peak Overloads on Fatigue Crack Propagation in 7075-T651 Aluminum," Engr. Fract. Mech., Vol. 5, p. 479, 1972.

7. R. H. Gardner and R. I. Stephens, "Subcritical Crack Growth Under Single and Multiple Periodic Overloads in Cold-Rolled Steel," Proc. of Seventh National Symposium on Fracture Mechanics, 1973; published in ASTM STP 559.

8. V. W. Trebules, R. Roberts, and R. W. Hertzberg, "Effect of Multiple Over-Loads on Fatigue Crack Propagation in 2024-T3 Aluminum Alloy," ASTM STP 536, p. 115, 1973.

9. J. Schijve, "Effect of Load Sequences on Crack Propagation Under Random and Program Loading," Engr. Frac. Mech., Vol. 5, p. 269, 1973.

10. J. C. McMillan and R. M. N. Pelloux, "Fatigue Crack Propagation Under Program and Random Loads," ASTM STP 415, p. 505, 1967.

11. O. Jonas, and R. P. Wei, "An Exploratory Study of Delay in Fatigue-Crack Growth," Int. J. of Fracture Mechanics, Vol. 7, p. 116, 1971.

12. O. E. Wheeler, "Spectrum Loading and Crack Growth," Trans. ASME, Journal of Basic Engineering, Paper No. 71-Met-X.

13. H. F. Hardrath and A. T. McEvily, "Proceedings of the Crack Propagation Symposium," Vol. I, Cranfield, England, October 1961.

14. W. T. Mathews, F. I. Barratta, and G. W. Driscoll, "Experimental Observations of a Stress Intensity History Effect Upon Fatigue-Crack Growth Rate," Int. J. of Fract. Mech., Vol. 7, p. 224, 1971.

15. W. Elber, "The Significance of Fatigue Crack Closure," ASTM STP 486, p. 230, 1971.

16. R. E. Jones, "Fatigue-Crack Growth Retardation After Single-Cycle Peak Overload in Ti-6Al-4V Titanium Alloy," University of Dayton, M. S. Thesis, April 1972.

17. J. Willenborg, R. M. Engle, and H. A. Wood, "A Crack Growth Retardation Model Using an Effective Stress Concept," TM-71-1FBR, WPAFB, Ohio, 1971.

18. R. W. Landgraf, JoDean Morrow, and T. Endo, "Determination of the Cyclic Stress-Strain Curve," Journal of Materials, JMLSA, Vol. 4, No. 1, March 1969, p. 176.

19. G. R. Chanani, "Retardation of Fatigue Crack-Growth in 7075 Aluminum Alloy," Met. Eng., Quarterly, Feb. 1975, p. 40.

20. A. Szirmae and R. M. Fisher, "Specimen Damage During Cutting and Grinding," ASTM STP 372, p. 3, 1964.

21. B. Gross, J. E. Srawley, and W. F. Brown, Jr., "Stress Intensity Factors for a Single-Edge-Notch Tension Specimen by Collocation of a Stress Function," NASA TND-2395, August 1964.

22. J. C. Grosskreutz and G. G. Shaw, "Mechanisms of Fatigue in 1100-0 and 2024-T4 Aluminum," AFML TR-65-127, 1965.

23. J. C. Grosskreutz and G. G. Shaw, "Mechanisms of Fatigue in 7075-T6 Aluminum," AFML TR-66-96, 1966.

24. L. H. Glassmann and A. J. McEvily, Jr., "Effects of Constituent Particles on the Notch Sensitivity and Fatigue-Crack-Propagation Characteristics of Aluminum-Zinc-Magnesium Alloys," NASA TN D-928, 1962.

25. J. P. Gallagher and T. F. Hughes, "The Influence of Yield Strength On Overload Affected Fatigue-Crack Growth Behavior in 4340 Steel," AFFDL-TR-74-28, 1974.

26. W. Elber, "Discussion on 'The Effects of Rest-Time on Fatigue Crack Retardation and Observations of Crack Closure'," presented at the ASTM Symposium on Fatigue-Crack Growth Under Spectrum Loads, Montreal, June 1975.

27. P. D. Bell and M. Creager, "Crack-Growth Analysis for Arbitrary Spectrum Loading," AFFDL-TR-74-129, October 1974.

28. K. N. Raju, V. Ningiah, and B. V. S. Rao, "Effect of Exposure to Elevated Temperatures on Delay in Crack Growth Due to a High Stress Cycle," Int. of J. Fract. Mech., Vol. 8, p. 99, 1972.

29. J. Schijve and D. Broek, "The Results of a Programmed Test on a Gust Spectrum with Variable Amplitude Loading," Aircraft Eng. Vol. 34, p. 314, 1962.

30. J. Schijve, D. Broek, and P. de Rijk, "Crack Propagation Under Variable Amplitude Loading," NLR Report M2094, January 1962.

31. B. M. Hillberry, W. X. Alzos and A. C. Skat, Jr., "The Fatigue Crack Propagation Delay Behavior in 2024-T3 Aluminum Alloy Due to Single Overload/Underload Sequences," AFFDL-TR-75-96, 1975.

32. R. C. Rice and R. I. Stephens, ASTM STP 536, P. 95, 1973.

33. W. J. Mills and R. W. Hertzberg, Eng. Fract. Mech., Vol. 7, p. 705, 1975.

34. R. E. Rosas, "Study to Determine Stress Profile of Rod-Peened Aluminum Structural Alloys versus Shot-Peened Material," Northrop MRDR-248 under NASA contract No. NAS-8-31563, Project No. 50823.

35. T. T. Shih and R. P. Wei, "The Influence of Chemical and Thermal Environments on Delay in a Ti-6A1-4V Alloy," presented at the ASTM Symposium on Fatigue Crack Growth Under Spectrum Loads, Montreal, Canada, June 23-24, 1975, to be published in STP 595.

APPENDIX A

OBSERVATION OF CRACK-CLOSURE-BEHAVIOR AFTER SINGLE OVERLOAD CYCLES IN 7075-T6 SINGLE-EDGE-NOTCHED SPECIMENS*

I. INTRODUCTION

It is well established that tensile overloads result in retardation; i.e., a decrease in fatigue-crack growth rate[1-9]. However, the mechanisms of overload retardation have not been well understood. Several mechanisms which have been proposed to explain the observed crack-growth behavior under constant and variable-amplitude loading include residual compressive stresses at the crack-tip[1,4], changes in the crack-tip plastic-zone size[5,6,10], crack-blunting, strain hardening[11], crack-closure[12], or combinations of these. Crack-closure has recently received considerable attention as a means for explaining as well as modeling fatigue-crack growth behavior under spectrum loads. However, very limited work on direct measurements of crack-closure changes during the delay period after an overload cycle has been reported to confirm the importance of crack-closure in retardation. Hence, to establish and understand the role of crack-closure in delay behavior, we used two different experimental techniques to determine changes in crack-closure during the delay period after single overload cycles in 7075-T6 SEN specimens. The two techniques used were the electrical potential and strain gage methods. This paper describes the crack-closure changes detected by these methods.

II. EXPERIMENTAL PROCEDURE

Single-edge notched (SEN) specimens (Figure A-1) with two different thicknesses, 0.063-inch and 0.250-inch, were used for this investigation. The 0.063-inch thickness provided plane-stress conditions at the crack-tip for the overloads used in this investigation, while the 0.250-inch thickness provided a mixed mode or plane strain condition at the crack-tip, depending on the applied stress-intensity range.

---

*To be published in Engr. Fract. Mech.

The effects of single overloads on the fatigue-crack growth behavior were determined on a 20 KIP MTS machine using a simple 2-level spectrum of the type shown in Figure A-2. All of the constant-amplitude load cycles were run at R = 0.1 and F = 5 Hz, while the overload cycles were run at 0.1 Hz. However, frequencies were lowered during crack-closure measurements. The number of constant-amplitude cycles was sufficient for complete recovery of the unretarded crack-growth rate. In these tests, the crack-lengths were measured by printing photo-grids with intergrid spacings of 0.0228-inch. Crack-lengths were then measured to an accuracy of 0.0004-inch by use of a filar eyepiece in a high-magnification traveling microscope. The retardation behavior observed was correlated with the crack-closure changes detected by the strain gage and electrical potential methods.

The strain gage technique was similar to the one used by Schmidt and Roberts[13]. Several different positions of the strain gage, with respect to the crack-tip, were tried during the initial stage of this work. The shapes of the load-displacement curves were dependent upon the location of the gage. However, the position shown in Figure A-3 (center of the gage located 0.05-inch behind the crack-tip) was found to be the optimum location with respect to the allowable strain range of the gage and the greatest sensitivity for measuring crack-closure as the crack surfaces started closing from the tip.

Figure A-4 shows the experimental arrangement for the electrical potential method. A constant-voltage DC power supply was used to apply the electrical potential to SEN specimens for crack-closure studies. Potential change was measured using a digital voltmeter (in microvolts) and a strip chart recorder with proper amplification built into the circuitry. The occurrence of actual physical touching of the crack surfaces (crack-closure) was easily detected by a distinct change in the resistance, resulting in a potential drop indicated on the strip chart recorder and the digital voltmeter. Confirmation of the electrical sensitivity of crack-closure detection was obtained by the insertion of 0.0003-inch thick copper foil into the fatigue crack as close to the tip as possible, while the SEN specimen was under load in the testing machine. When the load was reduced the crack surfaces came in contact with the copper foil, resulting in a distinct change in resistance and a potential drop, thus confirming the electrical sensitivity of the system.

III. RESULTS AND DISCUSSION

The tensile properties for both thicknesses of the 7075-T6 material are listed in Table A-I. The crack-closure tests are summarized in Table A-II, and a description and discussion of the results follow.

CLOS1: 1st Overload Cycle

The number of delay cycles, N*, was approximately 25,000 cycles. The number of delay cycles, N*, refers to the number of cycles over which the retardation occurs. Figure A-5 schematically shows how the number of delay cycles was measured. Typical load versus displacement records are shown in Figure A-6. The occurrence of hysteresis loops in the load-displacement curves demonstrates that the strain gage technique is sensitive enough to detect significant crack-closure changes as indicated by Elber[14]. The existence of a hysteresis loop means that loading and unloading curves are not colinear and that the load-displacement relationship is a superposition of a configuration change effect (e.g., crack-closure) on a plastic deformation effect (e.g., deformation at crack-tip) as described in detail by Elber[12]. In these load-displacement curves, crack-opening load is the load at which the records become linear[13].

During the delay period, the shapes of the load-displacement curves essentially remained the same. The small differences between the shapes at different stages of cycling do not indicate sufficient crack-closure to explain the observed retardation behavior for these low stress-intensity tests at low gross-section stresses for the 0.063-inch thick 7075-T6 SEN specimens tested. These preliminary results appear contradictory to observations by other investigators reporting significant crack-closure in surface-flawed[15], compact tension, and center-cracked specimens[12]. As will be described later on, these strain gage observations are further confirmed by electrical resistance measurements; thereby indicating that for the geometry used in the present investigation, significant changes in crack-closure as measured by the actual touching of fracture surfaces did not occur during the delay region produced by an overload cycle. The width of the hysteresis loop in the load-deflection curves in Figure A-6 increased as the crack grew out of the retardation zone, and the slope of the curves; i.e., the compliance changed with increasing crack length, indicating the sensitivity of the gage.

CLOS1: 2nd Overload Cycle

In this case, approximately 430,000 cycles were required for the complete recovery of fatigue-crack growth after the overload cycle. Figure A-7 shows the load-displacement curves measured at selected intervals. In this case, probably because of the longer crack-length, higher overload ratio, and a slightly different gage location (0.060-inch behind crack-tip), there was more non-linearity in the curves. This could

also be due to at least partial closing of the crack at a load higher than that for the first overload cycle. Nevertheless, the overall trend is the same as observed after the previous overload cycle; i.e., no significant changes in crack-closure loads occur as the cycling proceeds after the overload cycle because, regardless of the actual shape of the load-displacement curves, it is the change in the shape that determines changes in crack-closure as the crack progresses through the delay zone. The small change observed is not enough to explain the absence of any measurable growth for at least 150,000 cycles and the delay lasting over 400,000 cycles.

CLOS3: 1st Overload Cycle

In this case, as in all the subsequent tests, both the electrical potential and strain gage methods were used. Here, the load-displacement records obtained by the strain gage method were similar to those shown in Figure A-7, indicating a small change in crack-closure. The electrical potential method, which is more sensitive to detection of contact between crack surfaces, did not exhibit any significant crack-closure as shown in Figure A-8. The sensitivity of the present system in detecting small amounts of crack-closure is somewhat limited. Nevertheless, whenever there was significant crack-closure, the system was sufficiently sensitive to detect it, as evidenced in constant amplitude cycling at various R ratios[16], and also during the third overload cycle on this specimen, as will be described later.

CLOS3: 2nd Overload Cycle

The strain gage results were similar to those observed after the first overload cycle in specimen No. CLOS1, while the potential results were similar to those shown in Figure A-8.

CLOS3: 3rd Overload Cycle

Because of the somewhat unusual behavior observed so far, this test was run in a modified form. Previous results[16, 17] had shown that whenever the constant-amplitude loads were reduced after the crack had been grown by some amount at higher loads, crack closure was observed by the potential method. We ran a test to verify this and found it valid for a few cycles at the lower load level. Hence, the crack in this specimen was grown by approximately 0.1-inch by cycling between 80 and 800 lbs., subsequent to which an overload cycle at a P_{max} of 1200 lbs. was applied. Then, testing was continued between 50 and 500 lbs. for 100,000 cycles, during which period

no measurable crack-growth was observed. The potential results are shown in Figure A-9. Here, during the overload cycle as well as immediately after the overload cycle, a large crack-closure was observed. However, the crack-closure decreased substantially after 10 cycles and was not observed at all within the sensitivity of the system after 1000 cycles. Hence, the crack-closure observed immediately after the overload cycle is not adequate in itself to explain the lack of any measurable crack-growth in 100,000 cycles in the 7075-T6 SEN specimen. The observed crack-closure could be due to the drop of the constant-amplitude P_{max} from 800 to 500 lbs. Nevertheless, this series of observations indicates two things: the capability of the potential method for detecting crack-closure and the lack of extensive crack-closure changes during the entire delay period due to the overload cycle in this specimen.

CLOS4: 1st Overload Cycle

This 0.25-inch thick SEN specimen was tested to find out if thickness had any effect on the crack-closure behavior. An increase in thickness decreases the sensitivity of the potential method for measurement of changes in crack length. The results in this case were similar to those for the first overload in CLOS3, indicating that, with the present system (material, specimen geometry, and instrumentation), crack-closure is not the controlling factor for the retardation behavior.

In this specimen, an unusual behavior was observed. The crack was grown to 0.8-inch and out of the retardation zone and left overnight at zero load before continuing the test. Considerable crack-closure, similar to that in Figure A-9, was observed upon constant-amplitude cycling at P_{max} of 2000 lbs. However, the crack-closure vanished within 200 cycles. Figure A-10 shows this result. This indicates the need for conditioning cracks before testing as well as the influence of relaxation on crack-closure. This relaxation aspect may give rise to somewhat misleading results if a crack is allowed to "stand" before taking the actual crack-closure measurements. In this case, the crack was grown to 0.9-inch before the application of the next overload cycle.

CLOS4: 2nd Overload Cycle

In this case, neither the potential method nor the strain gage showed any significant changes in crack-closure. This was true even immediately after the overload cycle, unlike the specimen No. CLOS3, 3rd overload cycle where some crack-closure changes after an overload cycle at an overload ratio of 2.5 were observed by the

potential method. One of the possible reasons for this observation here could be due to the decreased sensitivity of the potential method because of the increase in thickness of the test specimen. However, the primary conclusion was the same; i.e., no significant changes in crack-closure were taking place during the delay period.

Thus, in these tests, no substantial crack-closure was detected except for the cases where the overload stress-intensity was rather large. Even then, the big change in crack-closure lasted only for a few cycles. These observations, which appear contrary to the crack-closure model for retardation and some of the published results[12, 15], are in agreement with directly measured crack-closure results of Sharpe and others[17, 18] and are applicable to the specimen geometry, alloy, thickness, and sensitivity of the instrumentation used in this investigation.

IV. SUMMARY AND CONCLUSIONS

The electrical potential and strain gage techniques were used for crack-closure measurements before and after an overload cycle during the delay period. The strain gage technique met the "hysteresis loop" criteria for sensitivity as described by Elber. For the specimen geometry (SEN), alloy (7075-T6), and instrumentation used, we did not detect significant changes in crack-closure as the cycling progressed after the overload cycle even though some crack-closure was taking place during constant-amplitude cycling and crack-closure loads did change with changes in R values. The small change in crack-closure after the overload cycle was not enough to explain the delay. However, after relaxation for 16 hours, as well as after a high overload ratio, significant crack-closure was observed by the potential method. This crack-closure disappeared within 200 cycles. Nevertheless, the overall conclusion from these observations is that no substantial changes in crack-closure were taking place to account for the observed number of delay cycles. This observations, which appear contrary to the crack-closure hypothesis are in agreement with some of the other reported results. These results are applicable to the alloy, specimen geometry, thickness, and sensitivity of the instrumentation used in this investigation. This work clearly shows that the crack-closure hypothesis is not universally applicable and should be investigated further.

V. ACKNOWLEDGMENT

REFERENCES

1. G. R. Chanani, "Retardation of Fatigue-Crack Growth in 7075 Aluminum, " Metals Engr. Quarterly, p. 40, February 1975.

2. J. Schijve, "Fatigue Crack Propagation in Light Alloy Sheet Materials and Structures, " Report MP-195, National Luchtvaartlaboratorium (Amsterdam), August 1960.

3. C. M. Hudson and K. N. Raju, "Investigation of Fatigue-Crack Growth Under Simple Variable-Amplitude Loading, " NASA TN D-5702, March 1970.

4. H. F. Hardrath, "Cumulative Damage, " Fatigue — Interdisciplinary Approach, Syracuse University Press, Syracuse, New York, 1964.

5. E. F. J. Von Euw, R. W. Hertzberg, and R. Roberts, "Delay Effects in Fatigue Crack Propagation, " ASTM STP-513, p. 230, 1972.

6. D. M. Corbly and P. F. Packman, "On the Influence of Single and Multiple Peak Overloads on Fatigue Crack Propagation in 7075-T6511 Aluminum, " Engr. Fracture Mechanics, Vol. 5, p. 479, 1972.

7. F. H. Gardner and R. I. Stephens, "Subcritical Crack Growth Under Single and Multiple Periodic Overloads in Cold-Rolled Steel, " Proc. of Seventh National Symposium on Fracture Mechanics, 1973; published in ASTM-STP 559.

8. V. W. Trebules, R. Roberts, and R. W. Hertzberg, "Effect of Multiple Overloads on Fatigue Crack Propagation in 2024-T3 Aluminum Alloy, " ASTM STP-536, p. 115, 1973.

9. J. Schijve, "Effect of Load Sequences on Crack Propagation Under Random and Program Loading, " Engr. Frac. Mech., Vol. 5, p. 269, 1973.

10. G. R. Chanani, S. D. Antolovich, and W. W. Gerberich, "Fatigue Crack Propagation in Trip Steels, " Met. Trans., Vol. 3, p. 2661, 1972.

11. S. D. Antolovich, A. Saxena, and G. R. Chanani, "A Model for Fatigue Crack Propagation, "Engr. Fract. Mech., Vol. 7, p. 649, 1975.

12. W. Elber, "The Significance of Fatigue Crack Closure," ASTM STP-486, p. 230, 1971.

13. R. Roberts and R. A. Schmidt, "Observations of Crack Closure," Int. J. of Fracture Mech., Vol. 8, p. 469, 1972.

14. W. Elber, "Discussion on The Effects of Rest-Time on Fatigue Crack Retardation and Observations of Crack Closure," presented at the ASTM Symposium on Fatigue-Crack Growth Under Spectrum Loads, Montreal, June 1975.

15. O. Buck, J.D. Fransen, and H.L. Marcus, "Spike Overload and Environmental Effects on Fatigue Crack Delay in Al 7075-T651," presented at the ASTM Symposium on Fatigue Crack Growth Under Spectrum Loads, Montreal, June 1975.

16. J.H. FitzGerald, Northrop Corporation, Unpublished Results, 1975.

17. T.T. Shih and R.P. Wei, "A Study of Crack Closure in Fatigue," Engr. Fract. Mech., Vol. 6, p. 19, 1974.

18. W.N. Sharpe, D.M. Corbly, and A.F. Grandt, "The Effects of Rest-Time on Fatigue Crack Retardation and Observations of Crack Closure," presented at the ASTM Symposium on Fatigue Crack Growth Under Spectrum Loads, Montreal, June 1975.

TABLE A-I. TENSILE PROPERTIES OF 7075-T6 ALLOY

THICKNESS INCH	Y.S. KSI	U.T.S. KSI	ELONG. %
0.063	72.8	80.2	12.5
0.25	72.4	78.5	12.6

TABLE A-II. CRACK-CLOSURE TESTS ON 7075-T6 SEN SPECIMENS

SPECIMEN NO.	THICKNESS (IN.)	OVERLOAD RATIO	P_{MAX}	a_i (IN)	METHOD USED*	K_{MAX} KSI $\sqrt{IN.}$
CLOS1 1st Overload Cycle	0.063	2.0	500	0.573	Strain Gage	6.1
CLOS1 2nd Overload Cycle	0.063	2.5	500	0.978	Strain Gage	11.4
CLOS3 1st Overload Cycle	0.063	2.5	500	0.65	Both Strain Gage & Potential	6.9
CLOS3 2nd Overload Cycle	0.063	2.0	500	0.82	Both Strain Gage & Potential	8.9
CLOS3 3rd Overload Cycle	0.063	2.4**	500	1.02	Both Strain Gage & Potential	12.3
CLOS4 1st Overload Cycle	0.25	2.0	2000	0.65	Both Strain Gage & Potential	6.9
CLOS4 2nd Overload Cycle	0.25	2.5	2000	0.90	Both Strain Gage & Potential	10.0

*A new strain gage was bonded and conditioned for a small number of constant-amplitude cycles before the overload cycle.

**Crack was grown between 80 and 800 lbs. before application of the overload cycle with a maximum load of 1200 lbs. After the overload cycle, the cycling was done between 50 and 500 lbs.

144
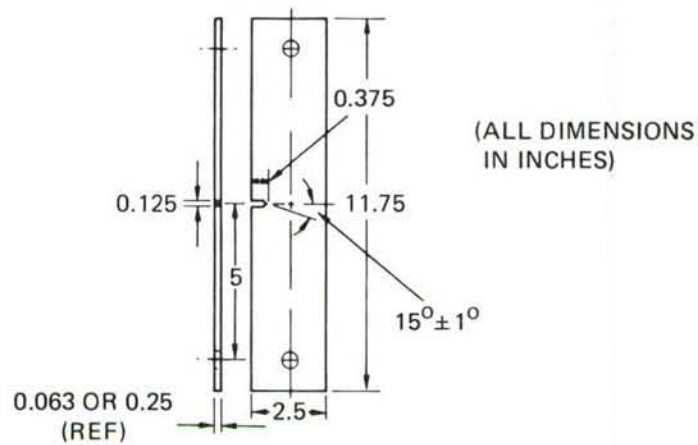
FIGURE A-1. SEN ALUMINUM SPECIMEN, LT (RW) ORIENTATION

$$\text{OVERLOAD RATIO} = \frac{K_O}{K_{MAX}}$$

$$\text{\% OVERLOAD} = \left(\frac{K_O - K_{MAX}}{K_{MAX}}\right) \times 100$$
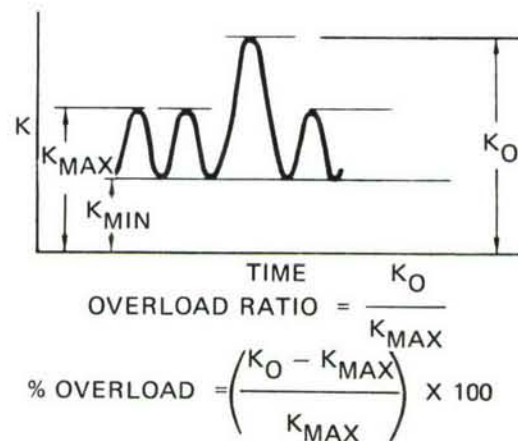
FIGURE A-2. SCHEMATIC REPRESENTATION OF THE TEST SPECTRUM
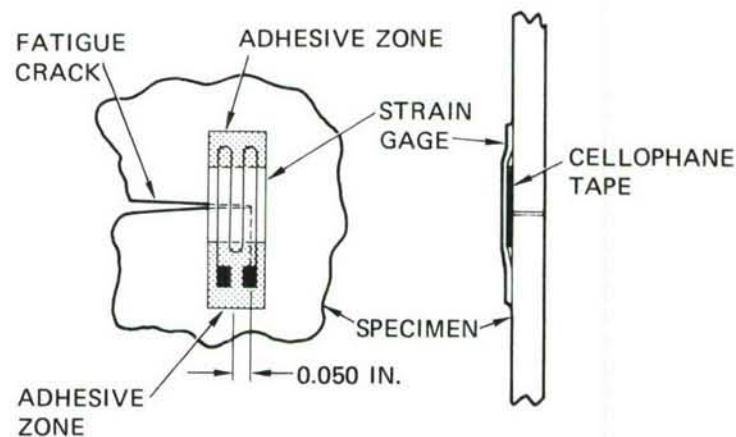
FIGURE A-3. POSITION OF STRAIN GAGE FOR CLOSURE MEASUREMENTS
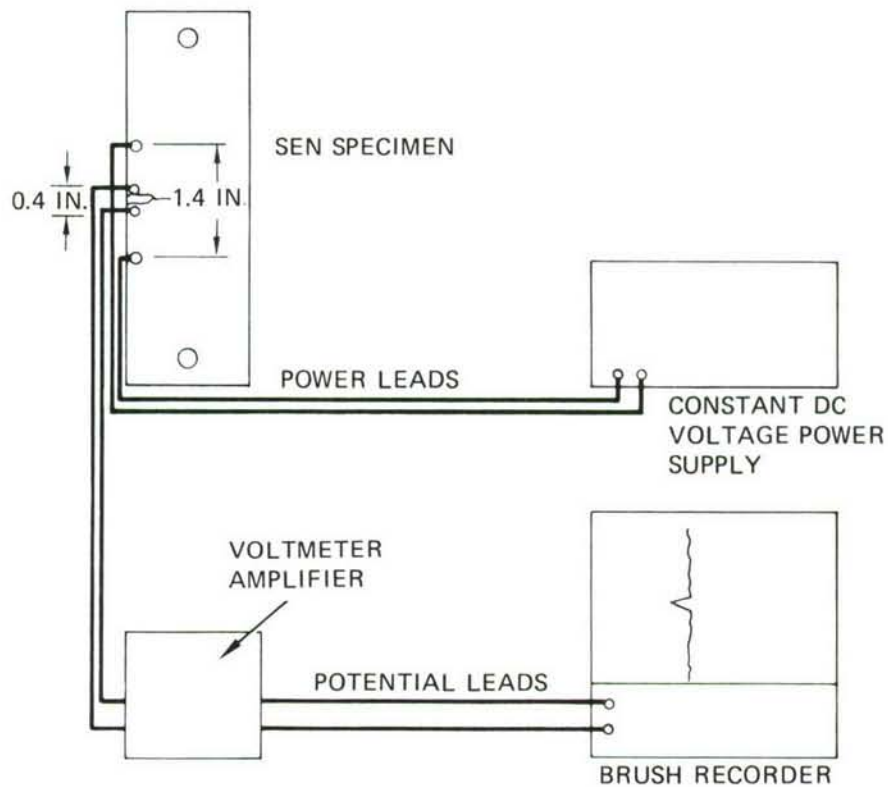
FIGURE A-4. EXPERIMENTAL ARRANGEMENT FOR ELECTRICAL POTENTIAL METHOD
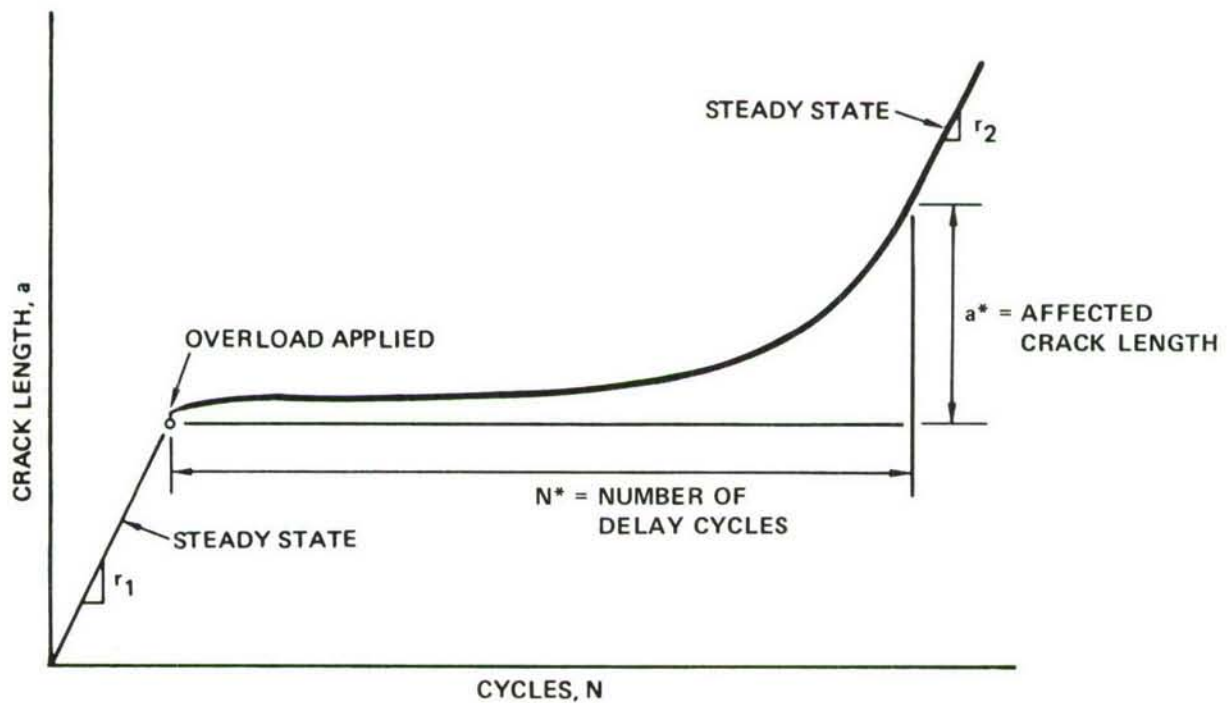
FIGURE A-5. CRACK-GROWTH RATE CURVE RESULTING FROM APPLICATION
OF A SINGLE OVERLOAD

146
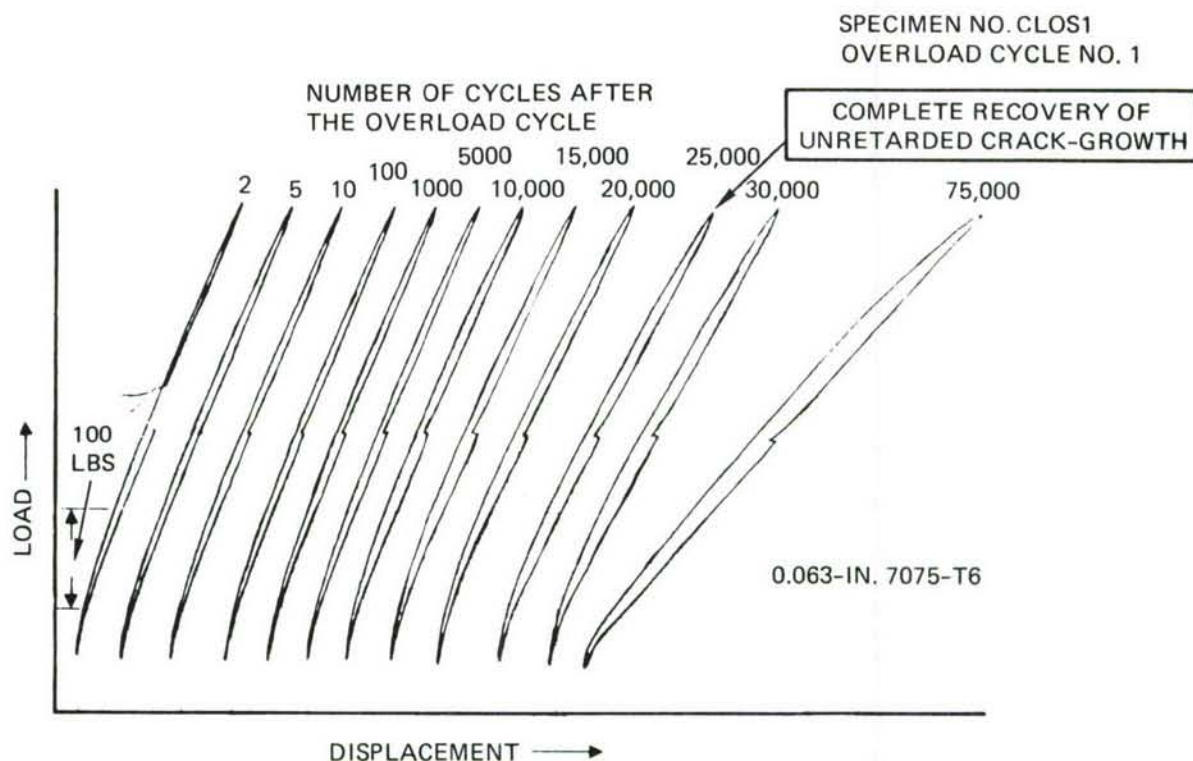
FIGURE A-6. LOAD VS DISPLACEMENT AT INTERVALS DURING FATIGUE TESTING — OVERLOAD RATIO OF 2
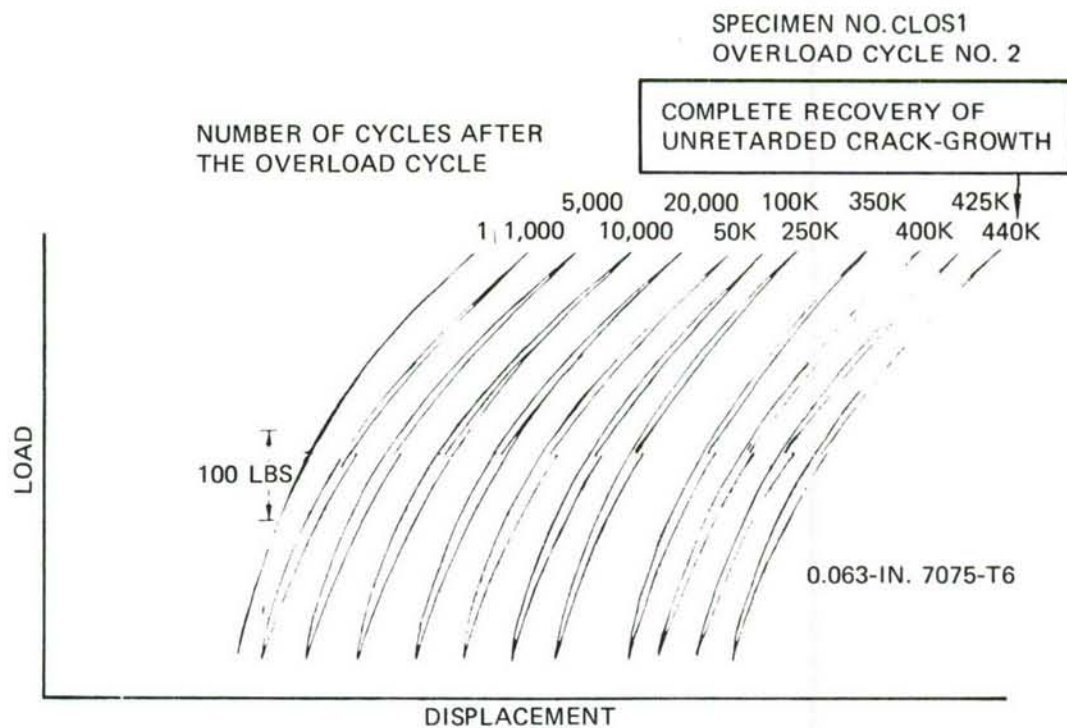
FIGURE A-7. LOAD VS DISPLACEMENT AT INTERVALS DURING FATIGUE TESTING — OVERLOAD RATIO OF 2.5
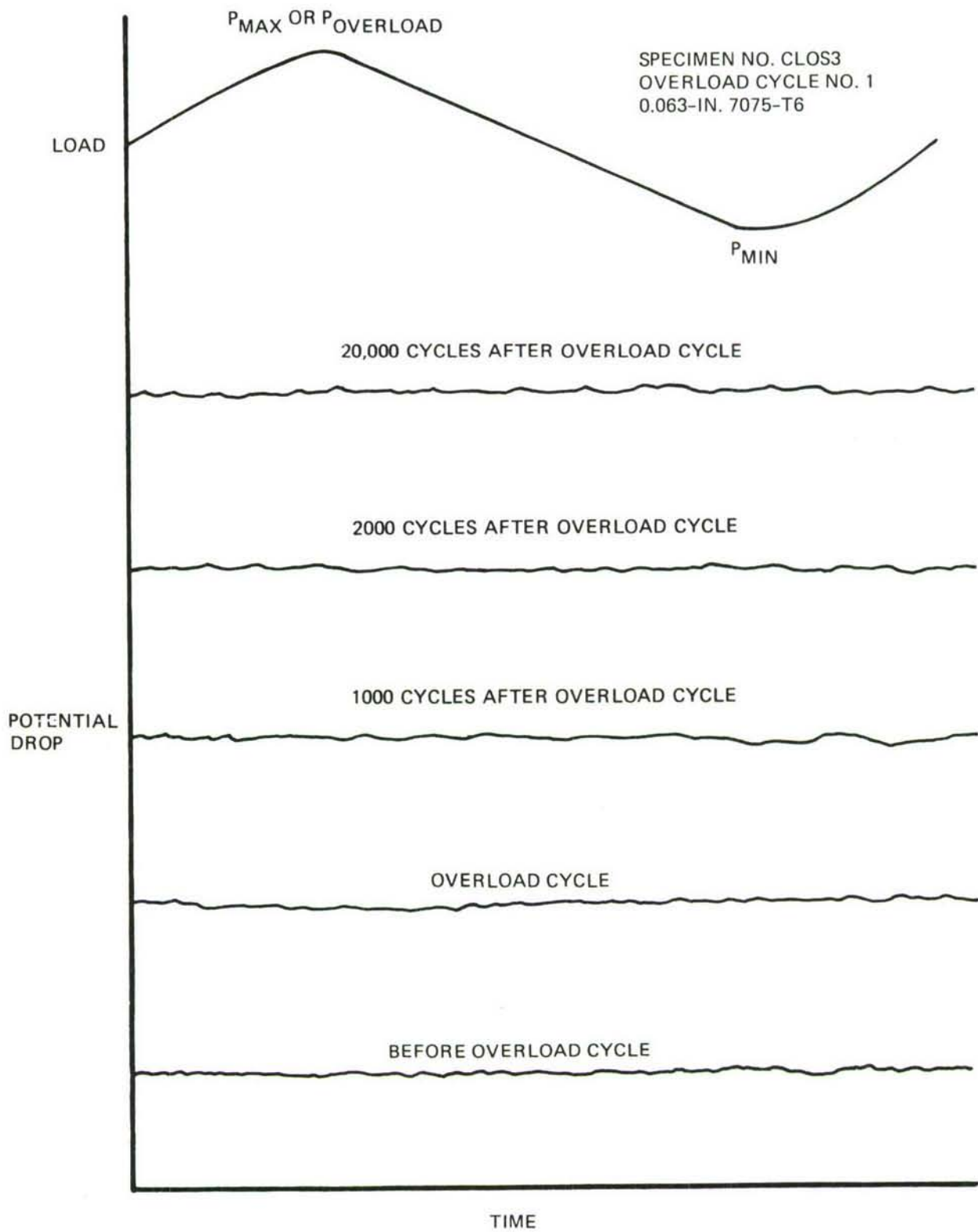
FIGURE A-8. POTENTIAL VS LOAD DURING AND AFTER OVERLOAD CYCLE
SHOWING NO CRACK-CLOSURE

148
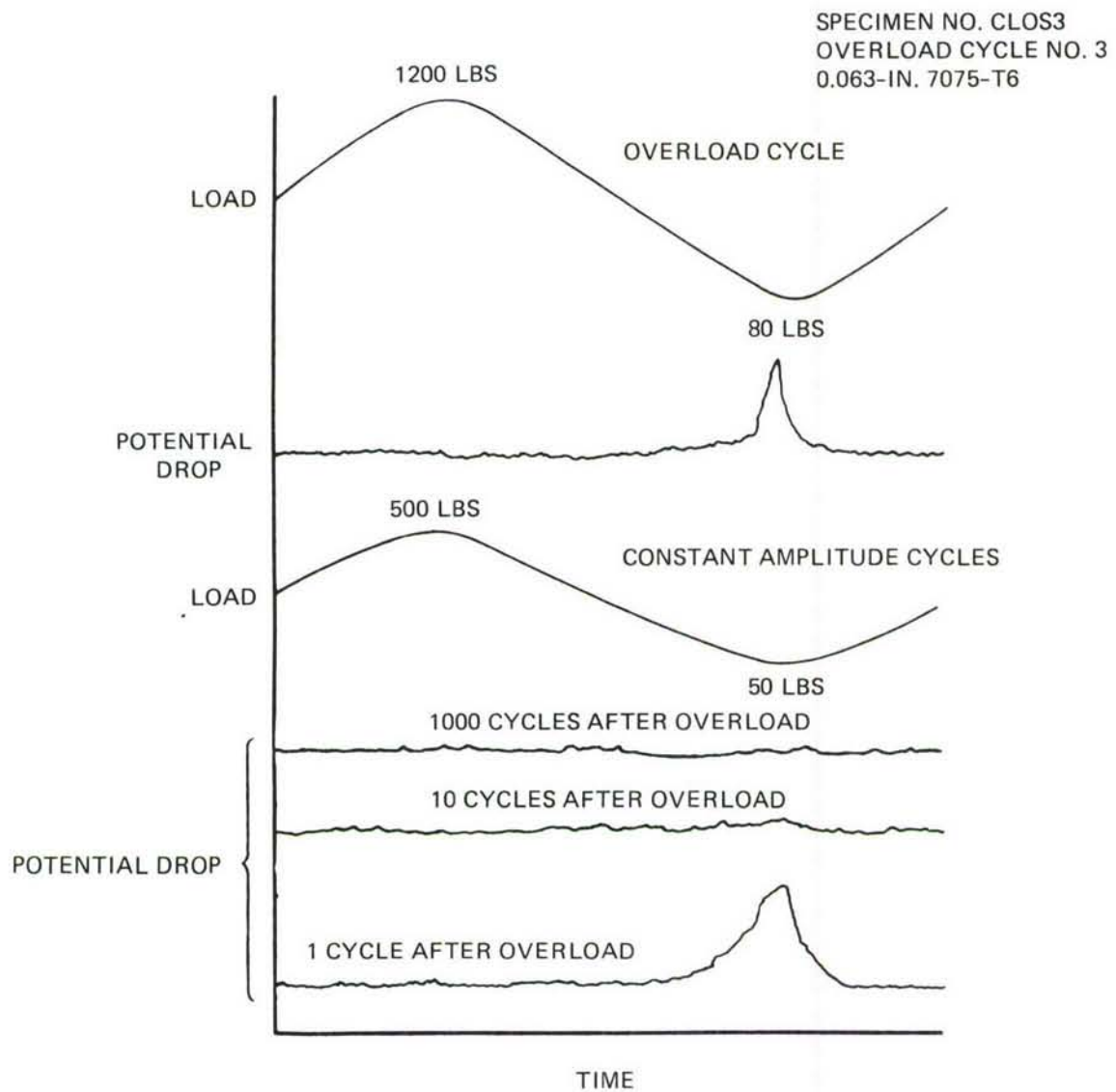
FIGURE A-9. POTENTIAL VS LOAD DURING AND AFTER OVERLOAD
CYCLE — SHOWING CRACK-CLOSURE

149
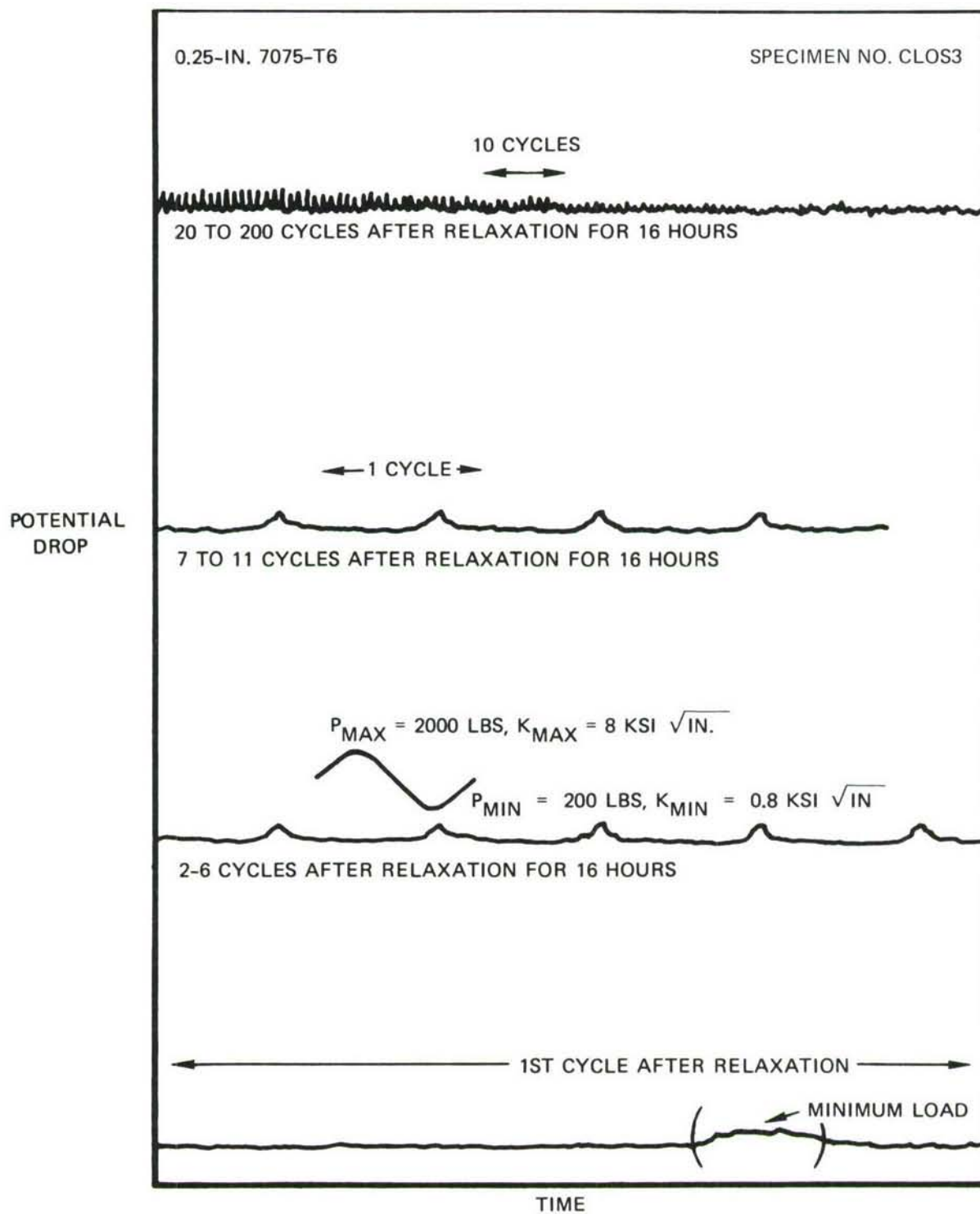
FIGURE A-10. EFFECT OF RELAXATION ON CRACK-CLOSURE

APPENDIX B
EFFECT OF TEST FREQUENCY ON THE RETARDATION BEHAVIOR
OF 7075-T6 and 2024-T8 ALLOYS*

The effects of test-frequency changes on constant-amplitude fatigue-crack growth rates have not been found to be significant in aluminum alloys[1]. To determine whether there are any significant effects of frequency changes on fatigue-crack growth under variable amplitude loading, tests were performed on 0.063-inch by 2.5-inch by 11.75-inch SEN specimens of 7075-T6 and 2024-T8 alloys in air and saltwater. The tests in air were conducted at 0.5, 5, and 15 Hz, while the tests in saltwater were performed at 0.5, 1, and 15 Hz. For the saltwater tests, we selected a frequency of 1 Hz rather than the 5 Hz used for the tests in air because, in saltwater, a small change in the low frequency range is expected to have a much larger effect on retardation than it does in air. A baseline constant-amplitude load (P_{max}) of 500 lbs. at a P_{min}/P_{max} of 0.1, and single overload cycles with overload ratios (OLR) of 1.5 and 2.0 were used for this work. The number of constant-amplitude cycles applied after the single overload cycle was always sufficient for complete recovery of the unretarded crack-growth rate. Details of both the spectrum and the test method are described elsewhere[2]. In order that each specimen would be tested under otherwise identical conditions, the overload spike (K_{OL}) was normally applied at the same approximate crack length (a_i) for each test frequency. Table B-I summarizes these results.

As seen in Table B-I, the number of delay cycles (N*) increased with increasing OLR. In general, at a given overload ratio, the number of delay cycles decreased as the baseline stress-intensity increased, even though the affected crack-length (a*), shown in Table B-I, increased. This was probably due to a higher baseline crack-growth rate and a faster recovery of the unretarded crack-growth rate at higher K values, which caused the crack to grow through the overload plastic-zone in relatively fewer cycles.

Figure B-1 shows the influence of frequency change on the number of delay cycles (N*) for both the 2024-T8 and 7075-T6 alloys. In this figure, whenever the stress-intensity factor for any particular data point was significantly different from the other

---

* To be published in Int. J. of Fracture.

151

points on the curve, that value is shown in parenthesis next to that point. As expected, the N* values were generally greater in air than in saltwater. These results do not indicate any major trend in the test frequency effect on the retardation behavior of the two alloys investigated. These results are in general agreement with the constant-amplitude fatigue-crack growth results in aluminum alloys. Hall, et al[1], reported little or no effect by reducing the test frequency from 1 to 0.1 Hz on the FCP rates for 7075-T651 alloy in several aggressive environments.

Some small differences in retardation behavior due to frequency changes can be noted from our tests. In some cases, an initial acceleration and crack growth occurred during the overload cycle (Table B-I). Although no general statement can be made based on these limited tests, it appears that crack-growth during the overload cycle was generally observed in higher frequency tests. A surprising aspect of these results is that it appears that the number of delay cycles does not follow any pattern for the saltwater tests at the three frequencies used, while in air, there appears to be some trend. It appears that, in air, the maximum delay is observed at 5 Hz. This aspect is contrary to what one would expect. This minor anomaly could be due to experimental scatter in the data. Some of the delay is due to the differences in K_{max}. For some of the tests at 5 Hz, the K_{max} levels were not identical to the corresponding tests at the other two frequencies. When these K_{max} differences are taken into account, points A and B in Figure B-1 will move down, indicating less of a frequency effect. This adjustment is based on the observation that, for the test conditions used in this work, N* goes down as K_{max} goes up. Nevertheless, no such adjustment is necessary for the tests at K_{max} of 6.1 ksi $\sqrt{in.}$ where it appears that the maximum delay in air is at 5 Hz. The small decrease in delay cycles at 0.5 Hz could be due to a small amount of relaxation at the lower frequency, while at 15 Hz, there may be a small amount of local heating at the crack-tip. Further work needs to be performed to resolve these points.

No differences of any significance were noted between the fractographic features of the specimens tested at different frequencies. This is best illustrated in Figure B-2 which shows fractographs obtained from two retardation specimens of 2024-T8 alloy tested in saltwater at 0.5 Hz and 15 Hz, respectively. The overload cycles resulted in stretch-bands across the thickness of the failed specimens in almost all the cases. The dimpled region in the overload band or stretch zone is associated with the incremental crack-growth during the increasing portion of the overload cycle. The tunneling effect in the stretch zone is due to the relatively plane-strain condition along the

midsection of the specimen. Immediately following the stretch marking is the retardation zone marked by a rather smooth topography, characteristic of a very low FCP rate. As one proceeds further away from the overload region, the topography of the fracture surface becomes increasingly similar to the surface before the overload due to the recovery of the constant-amplitude crack-growth rate. As noted, these features were similar for all tests in one medium at both low and high frequencies, although the overload stretch zone and the associated retardation region were larger with higher applied K levels. This increase in stretch band size is a direct manifestation of the overload plastic-zone size which increases with increase in K. There were differences in the fractographs between specimens failed in air and in saltwater due to differences in corrosiveness of the two media.

It was thought that some of the differences in the number of delay cycles could be due to the basic difference in the crack-growth rate of specimens tested at different frequencies. For this purpose, the decrease in the average da/dN values in the affected crack-length region was compared for each test. This was calculated by obtaining da/dN from the retardation tests once crack-growth had stabilized and dividing it by a*/N* obtained from Table B-I. When these values were plotted as a function of frequency, no general trend was observed.

These tests did not indicate any major frequency-change effects on retardation behavior in the two aluminum alloys investigated. Further investigation is required to confirm these observations for other aluminum alloys and to provide an understanding of the observed behavior.

ACKNOWLEDGMENTS

REFERENCES

1. L. R. Hall, R. W. Finges, and W. F. Spurr, "Corrosion Fatigue Growth in Aircraft Structural Materials," AFML-TR-204, September 1973.

2. G. R. Chanani, Met. Engr. Quarterly, February 1975, p. 40.

TABLE B-I. RETARDATION RESULTS AT DIFFERENT FREQUENCIES

P_{MAX} = 500 LBS

OLR, K_O/K_{MAX}	FREQ. (HZ)	2024-T8 ALLOY					7075-T6 ALLOY				
		a_i (IN)	K_{MAX} (KSI $\sqrt{IN}$)	a^* (IN)	N^* (1000)	ACCL[1]	a_i (IN)	K_{MAX} (KSI $\sqrt{IN}$)	a^* (IN)	N^* (1000)	ACCL[1]
					LABORATORY AIR						
1.5	0.5	0.570	6.1	0.006	8	a	0.560	6.0	0.005	4	a
		0.690	7.4	0.014	8	a	0.790	8.6	0.012	4	a
		0.790	8.6	0.005	3	a	1.020	12.2	0.018	3	a
		1.030	12.4	0.018	2	a					
	5	0.570	6.1	0.010	12.5	a	0.570	6.1	0.011	17.5	a
		0.729	7.9	0.003	5	a	0.707	7.6	0.010	6	b
		0.959	11.1	0.004	2	a	0.847	9.3	0.012	4	a
	15	0.570	6.1	0.004	5	a	0.570	6.1	0.003	5	a
		0.790	8.6	0.007	3	a	0.790	8.6	0.010	3	b
		1.030	12.4	0.005	0.5	a	1.030	12.4	0.016	2	b
2.0	0.5	0.570	6.1	0.010	17.5	a	0.560	6.0	0.013	15	a
		0.790	8.6	0.014	10	a	0.780	8.4	0.017	10	b
		1.030	12.4	0.068	15	b	1.020	12.2	0.068	25	b
	5	0.570	6.1	0.033	30	b	0.511	5.6	0.004	25	a
		0.731	7.9	0.015	20	b	0.698	7.4	0.011	12.5	a
		0.879	9.8	0.042	15	b	0.899	10.1	0.021	10	a
							1.089	13.7	0.126	25	b
							1.331	20.4	Failed before recovery		b & c
	15	0.570	6.1	0.013	20	a	0.570	6.1	0.007	15	b
		0.790	8.6	0.032	17.5	a	0.790	8.6	0.021	10	b
		1.030	12.4	0.087	17.5	b	1.030	12.4	0.058	17.5	b
					3.5 PERCENT NaCl						
1.5	0.5	0.570	6.1	0.004	4	a	0.570	6.1	0.010	4	a
		0.798	8.7	0.002	3	a	0.790	8.6	0.014	1.5	a
		1.026	12.3	0.011	2	a	1.030	12.4	0.011	0.5	b
	1	0.58	6.1	0.006	6	a	0.570	6.1	0.010	5	a
		0.80	8.7	0.009	2	b	0.798	8.7	0.014	2	a
		1.04	12.5	0.019	2	b	1.026	12.3	0.016	1	a
	15	0.570	6.1	0.010	8	a	0.560	6.0	0.008	3	a
		0.790	8.6	0.015	4	a	0.780	8.4	0.012	2	a
		1.032	12.4	0.005	1	a	1.044	12.7	0.023	1	a
2.0	0.5	0.570	6.1	0.005	15	a	0.558	6.0	0.013	8	a
		0.798	8.7	0.005	6	a	0.780	8.4	0.021	5	a
		1.026	12.3	0.066	10	a	1.020	12.2	0.061	8	a
	1	0.570	6.1	0.010	12.5	a	0.570	6.1	0.005	6	a
		0.800	8.8	0.024	8	a	0.798	8.7	0.026	5	a
		1.026	12.3	0.089	12.5	a	1.026	12.3	0.063	7	a
	15	0.570	6.1	0.012	10	a	0.570	6.1	0.027	12.5	a
		0.790	8.6	0.021	8	b	0.790	8.6	0.042	8	a
		1.030	12.4	0.085	12.5	b	1.020	12.2	0.195	15	b

1 — a = No crack growth during overload cycle and no initial acceleration.
    b = Crack growth during overload cycle.
    c = Initial acceleration after the overload cycle.
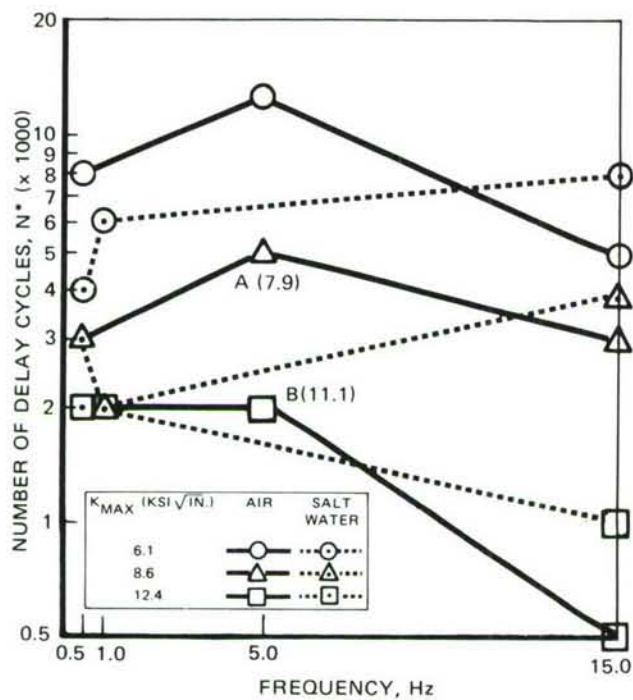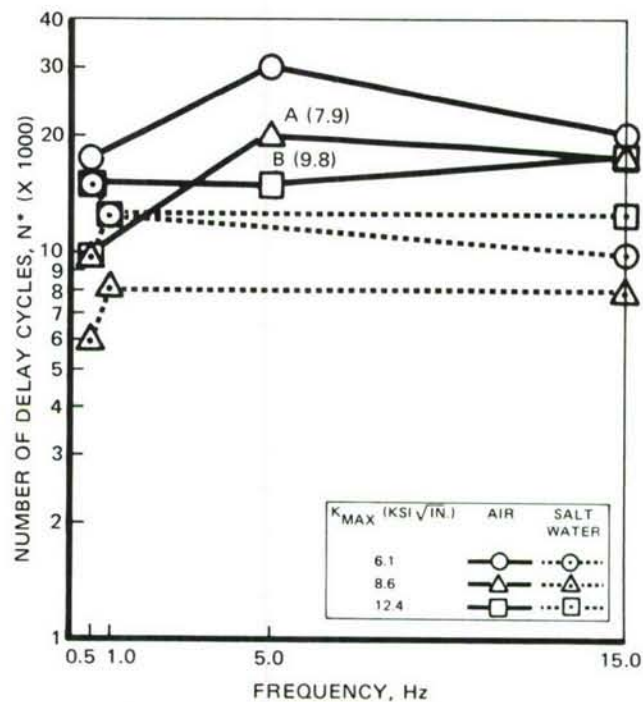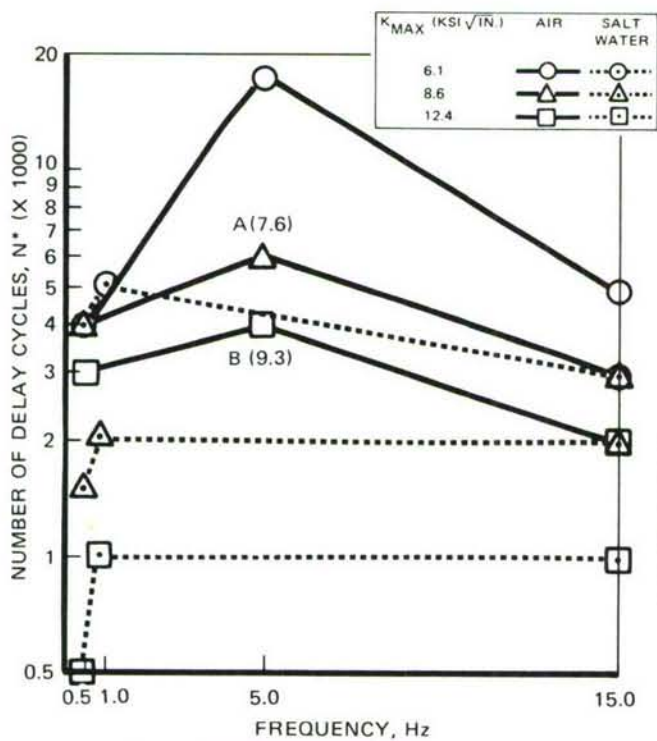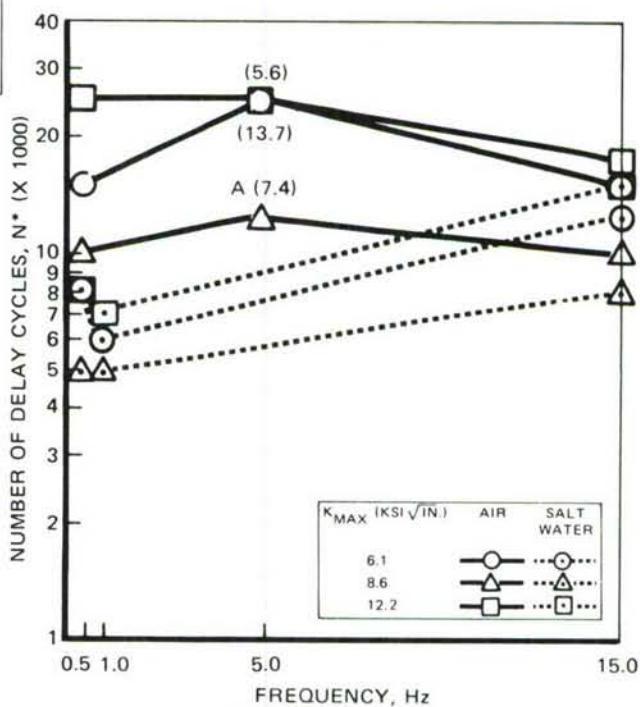
FIGURE B-1. EFFECT OF FREQUENCY ON RETARDATION BEHAVIOR
OF 2024-T8 7075-T6 ALLOYS

155

(a) FREQUENCY = 15 Hz

(b) FREQUENCY = 0.5 Hz

CRACK-GROWTH DIRECTION

OVERLOAD MARKINGS
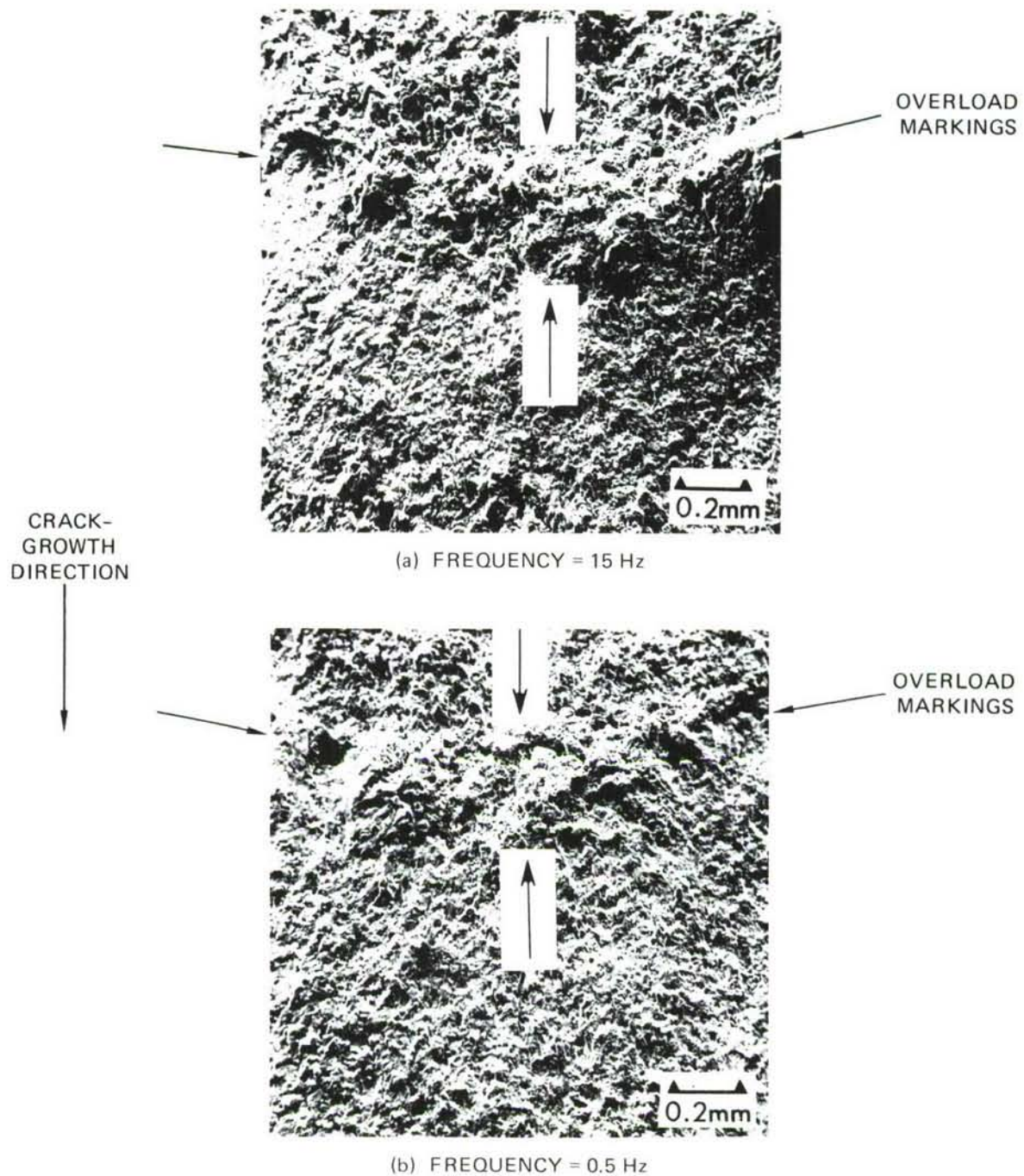
CRACK LENGTH AT OVERLOAD = 1.03 IN.
K_{MAX} = 12.3 KSI $\sqrt{IN.}$

P_{MAX} = 500 LBS
OVERLOAD RATIO = 2.0

FIGURE B-2. EFFECT OF FREQUENCY ON FRACTOGRAPHIC FEATURES IN THE VICINITY OF AN OVERLOAD CYCLE WITH AN OLR OF 2.0 IN 2024-T8

APPENDIX C

INVESTIGATION OF EFFECTS OF SALTWATER ON
RETARDATION BEHAVIOR OF ALUMINUM ALLOYS*

I. INTRODUCTION

The important parameters that can influence fatigue-crack growth are the nature of cyclic stresses at the crack-tip, the metallurgical structure and properties of the material, and the environmental conditions at the crack-tip. Considerable theoretical and experimental work has been performed to determine the crack-growth behavior of various materials under constant-amplitude loading. Recent efforts have concentrated on determining the effects of variable amplitude loading on crack-growth behavior[1-13]. Research in the last decade or so has shown that load sequences have a considerable effect on fatigue-crack propagation (FCP)[4-13]. In particular, the application of a single overload or a few cycles at high tensile loads causes retardation; that is, a decrease in the fatigue-crack growth rate[4-13]. However, the influence of an aggressive environment on the retardation behavior has received very little attention. It is generally recognized that an aggressive environment accelerates the constant-amplitude crack-growth rates. Nevertheless, it is not well known as to how the environment affects the retardation behavior. Furthermore, the various models which have been developed to predict FCP behavior under variable amplitude loading are based on constant-amplitude data and plastic-zone size changes at the crack-tip[14-19]. Since the aggressive environment can both accelerate the constant-amplitude crack-growth rate and remove a portion of the plastic zone during the delay period, it is necessary to establish its effect on the prediction models. This investigation was conducted to determine the influence of an aggressive environment on the retardation behavior of aluminum alloys and to provide information that can be used to predict, with better accuracy, the fatigue life of an aircraft structure under service conditions.

---

* To be presented at the Symposium on Corrosion Fatigue, November 1976, Denver, Colorado.

In this investigation, the 2024-T8, 7075-T6, and 7075-T73 alloys were tested in both air and saltwater. The 3-1/2% saltwater solution was selected as the aggressive environment because it has been shown to be one of the most aggressive of the typical aircraft test environments[20]. Single overload cycles with three different overload ratios (OLR) were used in this work. Fractography was performed to determine the influence of an aggressive environment on the fracture topography of failed retardation specimens and to provide an understanding of failure mechanisms in an aggressive medium with simple variable-amplitude loading.

II. EXPERIMENTAL

The 2024 and 7075 alloys were procured in the T3 and T6 conditions, respectively. Part of the as-received 7075-T6 material was heat treated to the T73 condition to avoid minor compositional variables, which could otherwise obscure the effects of different 7075 alloy heat treatments on the retardation behavior. The as-received 2024-T3 material was heat treated to the 2024-T8 condition of the same yield strength as that of the 7075-T73 material. For this purpose, sample blanks of the 2024-T3 were heat treated using different times at a temperature of 375F to produce variations in tensile properties within the T8 specification. From the various times and temperatures investigated, an aging treatment of 96 hours at 375F was selected as the best treatment because it produced an average yield strength of 61.2 ksi which was within 1% of that obtained with the 7075-T73 alloy (60.8 ksi).

Single-edge notched (SEN) specimens in the LT orientation, as shown in Figure C-1, were used for this investigation. Single overload cycles with overload ratios of 1.5, 2.0, and 2.5 were used as shown in Figure C-2. All tests were conducted with a baseline P_{max} of 500 lbs. and an R ratio (P_{min}/P_{max}) of 0.1 in a controlled laboratory environment (72±5F and 50±5% relative humidity). The constant-amplitude load cycles for tests in air were applied at a frequency of 5 Hz while those for tests in saltwater were applied at 1 Hz. The overload cycles in both media were applied at 0.1 Hz. After the overload cycle the number of constant-amplitude cycles applied was sufficient for complete recovery of the unretarded crack-growth rate. The crack-lengths were measured to a minimum accuracy of ±0.002 inch with the aid of imprinted photogrids (intergrid spacings of 0.020 inch) and a filar eyepiece in a high-magnification traveling microscope. The saltwater retardation tests were conducted on a 24-hour basis to avoid the difficulty of measuring crack-tip positions on an excessively corroded surface.

Constant-amplitude FCP tests were conducted in both air and saltwater on SEN specimens obtained from the same lot of material as was used in the retardation studies to evaluate the effects of an overload cycle on FCP.

Fractographic examination of the constant-amplitude FCP and retardation specimens tested both in air and saltwater was performed with a Cambridge S4-10 scanning electron microscope (SEM). Fracture surfaces were cleaned by replication and then gold-shadowed before the SEM examination.

III. RESULTS AND DISCUSSION

The tensile properties of the three alloys used in this investigation are listed in Table C-1. The selection of these three conditions provides information about the effect of susceptibility of a microstructure to environmental attack on retardation behavior (susceptible 7075-T6 versus relatively immune 7075-T73 and susceptible 7075-T6 versus relatively immune 2024-T8).

Figure C-3 shows the trend of the constant-amplitude FCP curves obtained for all three materials in air and saltwater. As expected, the FCP rates in saltwater were faster than those in the air. As described below, data from these curves were used to calculate the degree of retardation, and the specimen fracture surfaces were used to determine the changes in fractographic features due to overload cycles. At low and intermediate crack-growth rates where resistance to environmental attack is important, the 7075-T6 alloy showed the poorest FCP resistance because of the susceptibility of this microstructure to environmental attack.

In most of the retardation tests, the overload cycles were applied at similar crack-lengths in both the air and saltwater tests. This provided a direct comparison of the test ressults which were then analyzed in a similar manner. Table C-II summarizes all of the results obtained. The number of delay cycles, N^*, and the affected crack-length, a^*, refer to the number of cycles and crack-length over which the retardation occurred, respectively. Figure C-4(a) shows schematically how the number of delay cycles and the affected crack-length were measured. Figure C-4(b) shows typical curves of crack-length versus number of cycles for the 7075-T73 alloy in both air and saltwater after single overload cycles with an OLR of 2.5. These curves are typical of all of the tests conducted. Because of the inherent scatter in the crack-growth rate after an overload cycle, particularly for the saltwater tests, a small difference in the number of delay cycles between any two tests should not be considered significant.

These results together with the fractographic results are described and discussed below.

A. RETARDATION TEST RESULTS

As can be seen from Table C-II, the number of delay cycles increased with the increase in the overload ratio for each alloy in both air and saltwater. Figures C-5 through C-7 show the amount of delay for each of the three alloys as a function of the baseline K_{max} at a given overload ratio. At an OLR of 1.5, shown in Figure C-5, the delay cycles decrease with an increase in baseline K_{max}, while at OLR values of 2.0 (Figure C-6) and 2.5 (Figure C-7) there is a minimum in each curve. The number of delay cycles in air reaches the minimum at an approximate K_{max} of 10 and 8 ksi $\sqrt{in.}$ for tests at OLR of 2.0 and 2.5, respectively. The minimum occurs at lower stress-intensity values for the saltwater tests. The minimum in the delay cycle curve, for tests in air, corresponds to a K_o (overload stress-intensity factor) of about 20 ksi $\sqrt{in.}$; at higher values of K_o the N* value goes up. Hence, it is possible that the N* versus K_{max} behavior is somehow related to the value of K_o. This would explain why no minimum number of delay cycles was observed in Figure C-5 for the tests at OLR of 1.5 where K_o did not exceed 20 ksi $\sqrt{in.}$ for any test.

As expected, the number of delay cycles was greater in air than in the 3-1/2% saltwater. The difference in the number of delay cycles between air and saltwater tests was greater for the 7075-T6 alloy than it was for the 2024-T8 and 7075-T73 alloys. These results indicate that an alloy with a corrosion-resistant microstructure can change its retardation ranking, depending on the environment in which it is tested. This is demonstrated by making a comparison between the retardation behavior of 2024-T8 and 7075-T6 alloys in air and saltwater. The difference in the retardation behavior of these two alloys in air was very small, while in saltwater, the 2024-T8 alloy was distinctly superior to the 7075-T6 alloy. This is apparently due to the fact that the 7075-T6 alloy is highly susceptible to environmental attack, while the 2024-T8 alloy is relatively immune. This is best illustrated in Figure C-7 at an OLR of 2.5 where the retardation phenomenon is at its peak.

The affected crack-length, a*, is generally believed to be related to the overload plastic-zone size. The overload plastic-zone size depends on the overload stress-intensity factor (K_o) and increases with increased applied K_o. Hence, a* should also increase with K, as found in most of the cases listed in Table C-II. However, some

inconsistencies do exist in the saltwater data of Table C-II. These could be due either to some complex load-environment-time interaction at the crack-tip or to experimental scatter in data. At higher K values, the environmental attack at the crack-tip is more severe and, hence, a part of the overload plastic-zone may be corroded away, which would explain the observed anomaly in affected crack-lengths.

The differences between the number of delay cycles in air and saltwater may be attributed to the higher constant amplitude crack-growth rates in saltwater. Thus, it takes fewer cycles for a crack to grow through a given overload plastic-zone size in saltwater than in air. If the differences could be completely explained due to this growth-rate difference, then crack-blunting would be a minor factor, as indicated by an examination of preliminary results reported earlier[8] and also as found by Raju, et al[21]. Raju, et al, found that annealing at elevated temperatures eliminated retardation. Since temperature increases do not significantly affect crack-blunting, they concluded that blunting was not a significant factor.

To determine whether or not blunting was a significant factor in the results, the decrease in the average da/dN values in the affected crack-length region was compared for each of the two media. The normalized decrease in crack-growth (also called degree of retardation), R*, is defined as: $R^* = (da/dN)/(a^*/N^*)$. Figure C-8 shows these values for the 7075 alloy for the lowest (1.5) and highest OLR (2.5). The values of a* and N* used to obtain R* were obtained from Table C-II. The constant-amplitude da/dN values were obtained from the da/dN versus ΔK curves shown in Figure C-3. The differences between R* values at OLR of 1.5 and those at an OLR of 2.5 were much less for the 2024-T8 alloy than those shown for the 7075 alloys. Examination of Figure C-8 indicates that the higher constant-amplitude da/dN rates in saltwater can account for some of the differences in the number of delay cycles, particularly at lower OLR values. However, at higher OLR, the higher da/dN rate in saltwater cannot completely account for the observed differences. This could be due either to a high plastic strain energy at the crack-tip, or to a severe plastic deformation at the high OLR or to a higher crack-blunting at the higher OLR or to a combination of both plastic energy and crack-blunting.

At the low OLR, there is less crack-blunting and plastic deformation at the crack-tip and, hence, the corrosion of a plastically deformed crack-tip or resharpening of the blunted crack by an aggressive media does not play an important role, a conclusion reached earlier based on the results at low OLR[8] and also be Raju, et al[21]. However, at high OLR, both the blunting and the plastic deformation at the crack-tip are

161

much greater and, hence, the environmental attack as well as the degree of susceptibility of the alloy to environmental attack can influence the retardation behavior in saltwater. For this reason, the heavily blunted crack at the high OLR is quickly resharpened in the 7075-T6 alloy because of its high susceptibility to environment attack and, as a result, there is much less retardation in saltwater. In 2024-T8 and 7075-T73 alloys, the difference is much less due to their relative immunity to environmental attack. Thus, it would appear that blunting is an important, if not a governing, factor in retardation at high OLR. The high plastic energy density at the higher OLR could also contribute to the observed differences in delay cycles at high OLR. Nevertheless, these tests clearly indicate the importance of a given microstructure and its susceptibility to environmental attack in determining its fatigue behavior under variable amplitude loading in an aggressive environment. Thus, an alloy which shows superior retardation behavior in air can be inferior to the other alloy in an aggressive environment such as saltwater as was found for the 7075-T6 and 2024-T8 alloys in this investigation. The difference in the retardation behavior of these two alloys in air was very small, while in saltwater, the 2024-T8 alloy was distinctly superior to the 7075-T6 alloy.

B. FRACTOGRAPHIC RESULTS

Fractographic examinations of selected FCP and retardation specimens from each alloy tested in both air and saltwater were performed to provide an understanding of the failure mechanisms in an aggressive medium with a simple variable amplitude loading and to determine the influence of an aggressive environment on the nature and size of the overload region. For this purpose, fractographs were obtained (1) before overload, (2) in the overload stretch band, and (3) at several locations in the retardation zone. In general, environmental attack similar to that which was observed in fracture surfaces of saltwater FCP specimens was found by fractographic examination of retardation specimens.

The overload cycle manifested itself as a stretch-band across the thickness of the failed specimens in almost all air tests, while the fracture surfaces of the saltwater retardation specimens showed overload stretch markings only at higher OLR and higher K values. At the lower OLR and lower K values, the overload markings generally were not visible.

The width of the overload-stretch zone and the associated retardation region increased with increased applied K level. In air, it progressed from a barely visible

thin line at low K levels to a wide band of overload zone exhibiting dimpling and tunneling at higher K values. This increase in the stretch band size is a direct manifestation of the overload plastic-zone size which increases with increased K. In saltwater, the overload markings were generally smaller in magnitude and hence were probably removed by the corrosive attack of the saltwater at low OLR values. The nature of the stretch markings in saltwater tests, when visible, was similar to those formed in air.

Figure C-9 shows the results for 7075-T6 alloy at an OLR of 2.5 as a function of K_{max} in air, while Figure C-10 shows similar results in saltwater. These fractographs show, particularly in air, that as the stress-intensity level goes up, the width of the overload zone increases because the plastic-zone size is directly proportional to the square of applied K. The overload band or stretch zone associated with the incremental crack-growth during the rising-load portion of the overload cycle is marked by a dimpled region, as in the center of Figure C-9(c). The tunneling effect seen in the stretch zone of Figures C-9(c) and C-10(c) is due to the relatively plane-strain condition along the midsection of the specimen. Immediately following the stretch marking is the retardation zone marked by a rather smooth topography, characteristic of a very low FCP rate. Proceeding further away from the overload region, the topography of the fracture surface becomes increasingly similar to that which is seen before the overload cycle. This occurs due to the recovery of the constant-amplitude crack-growth rate.

At a baseline K_{max} of approximately 6 ksi $\sqrt{in}$. (i.e., after first overload cycle), a well-defined overload stretch marking was not seen in any of the three alloys tested in saltwater even at an OLR of 2.0. Figure C-11 shows the fractographic results obtained for both air and saltwater tests of the 2024-T8 alloy at an OLR of 2.0 and a K_{max} of 6.1 ksi $\sqrt{in}$. As seen even in the case of the 2024-T8 alloy which is relatively immune to the environmental attack, the overload marking is not distinct in saltwater, while it is very clear for air. At an OLR of 2.5, the overload markings were just barely visible in the saltwater tests of the 7075-T6 alloy because of its high susceptibility to environmental attack (Figure C-10(a)), whereas in air, they were very distinct (Figure C-9(a)).

In the saltwater tests at a baseline K_{max} of approximately 9 ksi $\sqrt{in}$. (second overload cycle) and OLR of 2.0, an overload marking was observed in the 2024-T8 alloy, while a very faint marking was observed in the 7075-T73 alloy, and no marking

was seen for the 7075-T6 alloy. This is probably due to the high susceptibility of the 7075-T6 alloy to environmental attack which allows the overload marking to be corroded away. In the 7075-T6 alloy, both pitting and grain boundary attack were seen.

At a baseline K_{max} of approximately 12 ksi $\sqrt{in.}$ (third overload cycle), the overload markings were visible in saltwater specimens at both OLR of 2.0 and 2.5 even in the 7075-T6 alloy. Figures C-12 through C-14 show typical results of the saltwater tests for the three alloys at the two OLR. At a given OLR, the stretch zone, including dimpling, is larger in the 2024-T8 alloy (Figure C-12) than in 7075-T6 (Figure C-13) and 7075-T73 (Figure C-14) alloys. This observation is similar to that made for testing in air, which indicates that during the overload cycle itself, the environment probably does not play as great a role as it does during the crack-growth phase after the overload cycle. This is evidenced by the corroding away of the overload marking in susceptible 7075-T6 alloy (Figure C-13 (a)). Since these fractographs were obtained from those specimens which had experienced relatively high K values, tunneling can be observed. Again, this behavior is similar to that observed in air. Here too, the 2024-T8 showed the largest amount of tunneling. An increase in OLR from 2.0 to 2.5 at the same baseline K_{max} results in an increase in the stretch zone size, including tunneling just as it did with an increase of K_{max} as shown in Figures C-9 and C-10.

For some of the tests conducted in air, depending on the baseline K, changes in striation spacings were seen across the overload stretch zone. No striations were observed in the area immediately after the overload cycle, nor at crack-growth rates below 3 x 10^{-6} inch/cycle for tests conducted in air. Very few striations were observed in the vicinity of the overload cycle for tests conducted in saltwater. The lack of discernible striations for tests in air could be either due to (1) abrasion, (2) the difficulty in resolving striations associated with the relatively low crack-growth rates, (3) a change in crack-propagation mode, or (4) a combination of all these factors. In the case of the saltwater specimens, the striations probably were not seen, due to the corroding attack of saltwater. The aggressive environment in these tests apparently did not allow the blunting and resharpening mechanisms responsible for striation formation to operate. Nevertheless, for the specimens in which striations were discernible, the agreement between measured da/dN and striation spacings was good.

From these observations, it appears that the general nature of the fractographic features in relation to OLR and K_{max} values is similar in both air and saltwater, except that at the lower OLR and K values the overload markings were not visible in saltwater. This lack of overload marking was more prevalent in the 7075-T6 alloy,

which is highly susceptible to environmental attack. Furthermore, in saltwater tests, the deterioration of fractographic features due to environmental attack was evident and changes in striation spacings were not discernible.

IV. SUMMARY AND CONCLUSIONS

- Single tensile overload cycles cause retardation of fatigue-crack growth in saltwater just as they do in air. The number of delay cycles increased with increased overload ratios in both air and saltwater.

- The number of delay cycles was greater in air than in the 3-1/2% saltwater tests.

- The effect of an aggressive environment on the retardation behavior was much greater in the 7075-T6 alloy than in the 2024-T8 and 7075-T73 alloys.

- The effect of an aggressive environment on the retardation behavior was more predominant at the higher overload ratios where it could not be attributed to the higher saltwater FCP rates alone. This was probably due to more crack-blunting and higher plastic-strain energy at the crack-tip due to severe plastic deformation at the high OLR, i.e., crack-blunting appeared to be an important factor at high OLR, while at low OLR, its contribution was small.

- The susceptibility of a microstructure to environmental attack was found to be important in determining its fatigue behavior under variable amplitude loading in an aggressive environment. An alloy which is superior to another alloy in air can be inferior to the same alloy in an aggressive environment such as saltwater, as was found for the 7075-T6 and 2024-T8 alloys. In air, both these alloys showed a small difference in retardation behavior, while in saltwater, the 2024-T8 was distinctly superior.

- Environmental attack similar to that which is observed on fracture surfaces of saltwater FCP specimens was found on the retardation specimens.

- For tests in air, the overload cycle manifested itself as a stretchband across the thickness of the specimen in almost all of the cases studied. In saltwater, these markings were distinct only at the high OLR and high K values. This lack of distinct overload marking was more common in the 7075-T6 alloy due to its high susceptibility to environmental attack.

165

V. ACKNOWLEDGMENT

REFERENCES

1. J. Schijve, "Fatigue Crack Propagation in Light Alloy Sheet Materials and Structures," Report MP-195, National Luchtvaartlaboratorium (Amsterdam), 1960.

2. C. M. Hudson and K. N. Raju, "Investigation of Fatigue-Crack Growth Under Simple Variable-Amplitude Loading," NASA TN D-5702, March 1970.

3. H. F. Hardrath, "Cumulative Damage," Fatigue — Interdisciplinary Approach, Syracuse University Press, Syracuse, New York, 1964.

4. E. F. J. Von Euw, R. W. Hertzberg, and R. Roberts, ASTM STP-513, p. 230, 1972.

5. D. M. Corbly and P. F. Packman, Engr. Fracture Mechanics, Vol. 5, p. 479, 1972.

6. R. C. Rice and R. I. Stephens, ASTM STP-536, p. 95, 1973.

7. T. T. Shih, PhD Thesis, "Fatigue-Crack Growth Under Variable Amplitude Loading," Lehigh University, 1974.

8. G. R. Chanani, Met. Engr. Quarterly, Vol. 15, p. 40, 1975.

9. O. Jonas and R. P. Wei, Int. J. of Fracture Mech., Vol. 7, p. 116, 1971.

10. E. P. Probst and B. M. Hillberry, "Fatigue Crack Delay and Arrest Due to Single Peak Tensile Overloads," AIAA Paper No. 73-325, March 1973.

11. J. P. Gallagher and T. F. Hughes, "The Influence of Yield Strength on Overload Affected Fatigue-Crack Growth Behavior in 4340 Steel," AFFDL-TR-74-28, 1974.

12. J. Schijve, "Prediction of Fatigue Crack Propagation in Aircraft Materials Under Variable-Amplitude Loading," Presented at the ASTM Symposium on Fatigue-Crack Growth Under Spectrum Loads, Montreal, Canada, June 23-24, 1975.

13. J. Schijve, Engr. Frac. Mech., Vol. 5, p. 269, 1973.

14. O. E. Wheeler: Trans. ASME, J. of Basic Engineering, Paper No. 71-Met-X.

15. J. Willenborg, R. M. Engle, and H. A. Wood: "A Crack Growth Retardation Model Using an Effective Stress Concept," AFFDL-TM-71-1-FBR, WPAFB, Ohio 1971

16. T. R. Porter: Eng. Fract. Mech., Vol. 4, p. 717, 1972.

17. P. D. Bell and M. Creager, "Crack-Growth Analysis for Arbitrary Spectrum Loading," AFFDL-TR-74-129, Oct. 1974

18. S. D. Antolovich, A. Saxena, and G. R. Chanani, Engr. Fract. Mech., p. 649, 1975.

19. G. R. Chanani, S. D. Antolovich, and W. W. Gerberich, Met. Trans., vol. 3, p. 2661, 1972.

20. L. R. Hall, R. W. Finges, and W. F. Spurr, "Corrosion Fatigue-Crack Growth in Aircraft Structural Materials," AFML-TR-204, Sept. 1973.

21. K. N. Raju, V. Ningiah, and B. V. S. Rao, Int. J. and Fract. Mech., Vol. 8, p. 99, 1972.

TABLE C-I. TENSILE PROPERTIES OF THE ALUMINUM ALLOYS

ALLOY AND HEAT TREATMENT	0.2% Y.S. KSI	U.T.S. KSI	% ELONGATION
7075-T6	73.1	80.2	12.5
7075-T73	60.8	71.2	12.3
2024-T8	61.2	68.3	10.0

Note 1:   Flat specimens of 2-inch gage-length were used.
Note 2:   The reported values are an average of three tests.

TABLE C-II. SUMMARY OF RETARDATION RESULTS IN AIR AND SALTWATER[1]

ENVIRONMENT	SPECIMEN NO.	K_O/K_{MAX} (OLR)	a_i (IN)	K_{MAX} (KSI$\sqrt{IN}$)	a^* (IN)	N^* (1000)	ACCL[2]
			2024-T8				
Laboratory Air	DT8ØLC1	1.5	.5696	6.1	.0104	12.5	a
			.7292	7.9	.0028	5	a
			.9587	11.1	.0043	2	a
	DT8ØLC2	2.0	.5696	6.1	.0327	30	b
			.7307	7.9	.015	20	b
			.8789	9.8	.0421	15	b
	DT8ØLC3	2.5	.5734	6.2	.0216	55	b
			.734	7.9	.0280	65	b
			.869	9.7	.0620	115	b
3.5% Salt Water	ET8SWØLC1-2	1.5	.58	6.2	.006	6	a
			.80	8.7	.009	2	b
			1.04	12.5	.019	2	b
	ET8SWØLC2	2.0	.5696	6.1	.01	12.5	a
			.7996	8.8	.0238	8	a
			1.0256	12.3	.0894	12.5	a
	ET8SWØLC3	2.5	.5696	6.1	.0190	35	a
			.7976	8.7	.0626	45	a
			1.0256	12.3	.1140	45	b
			7075-T6				
Laboratory Air	DT6ØLC1	1.5	.5696	6.1	.0110	17.5	a
			.7074	7.6	.0100	6	b
			.8472	9.3	.0120	4	a
	DT6ØLC2	2.0	.5112	5.6	.0038	25	a
			.6983	7.4	.0106	12.5	a
			.8989	10.1	.0213	10	a
			1.0889	13.7	.1262	25	b
	DT6ØLC3	2.5	.5696	6.1	.0428	350	a
			.7976	8.7	.0894	130	a
			1.0256	12.3		Arrest	a
3.5% Salt Water	ET6SWØLC1	1.5	.5696	6.1	.0100	5	a
			.7976	8.7	.0140	2	a
			1.0256	12.3	.0160	1	a
	ET6SWØLC2	2.0	.5696	6.1	.0050	6	a
			.7976	8.7	.0258	5	a
			1.0256	12.3	.0625	7	a
	ET6SWØLC3	2.5	.5696	6.1	.0210	30	a
			.7976	8.7	.0666	35	a
			1.0256	12.3	.2816	40	b
			7075-T73				
Laboratory Air	DT73ØLC1	1.5	.5696	6.1	.0122	17.5	a
			.7132	7.7	.0091	6	a
	DT73ØLC2	2.0	.5012	5.4	.0190	55	a
			.7170	7.7	.0251	25	a
			.9055	10.2	.0433	20	b
			1.1290	14.6	.0707	25	b & c
	DT73ØLC3	2.5	.5796	6.2	.0198	90	b
			.8076	8.9	.0418	85	a
			1.0356	12.6	.1892	165	b
3.5% Salt Water	ET73SWØLC1	1.5	.5696	6.1	.0243	15	b
			.7968	8.7	.0167	2	a
			1.0256	12.3	.0357	1	b
	ET73SWØLC2	2.0	.5696	6.1	.0288	40	a
			.7748	8.4	.0438	20	a
			1.0256	12.3	.1160	12.5	b
	ET73SWØLC3	2.5	.5696	6.1	.0238	35	a
			.7976	8.7	.1230	50	a
			1.0256	12.3	.3065	77.5	a

1 Using 0.063-inch thick SEN specimens at a frequency of 5 Hz for tests in air and 1 Hz for tests in saltwater.
2-a No crack growth during overload cycle and no initial acceleration.
   b Crack growth during overload cycle.
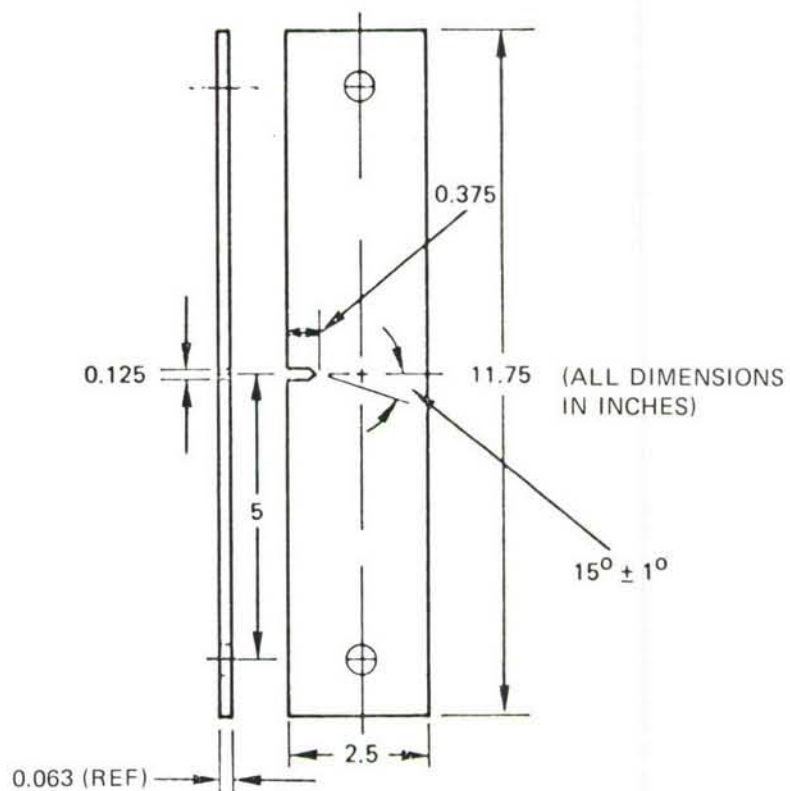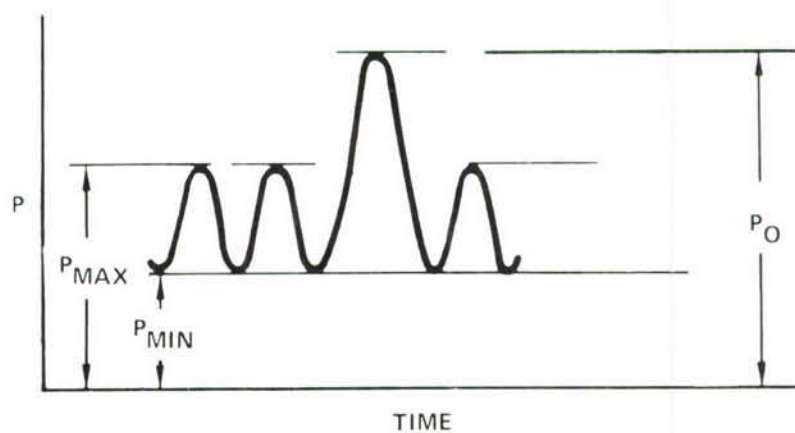   c Initial acceleration after the overload cycle.

FIGURE C-1. SEN ALUMINUM SPECIMEN, LT (RW) ORIENTATION

$$\text{OVERLOAD RATIO} = \frac{P_O}{P_{MAX}}$$

$$\% \text{ OVERLOAD} = \left(\frac{P_O - P_{MAX}}{P_{MAX}}\right) \times 100$$

FIGURE C-2. SCHEMATIC REPRESENTATION OF THE TEST SPECTRUM
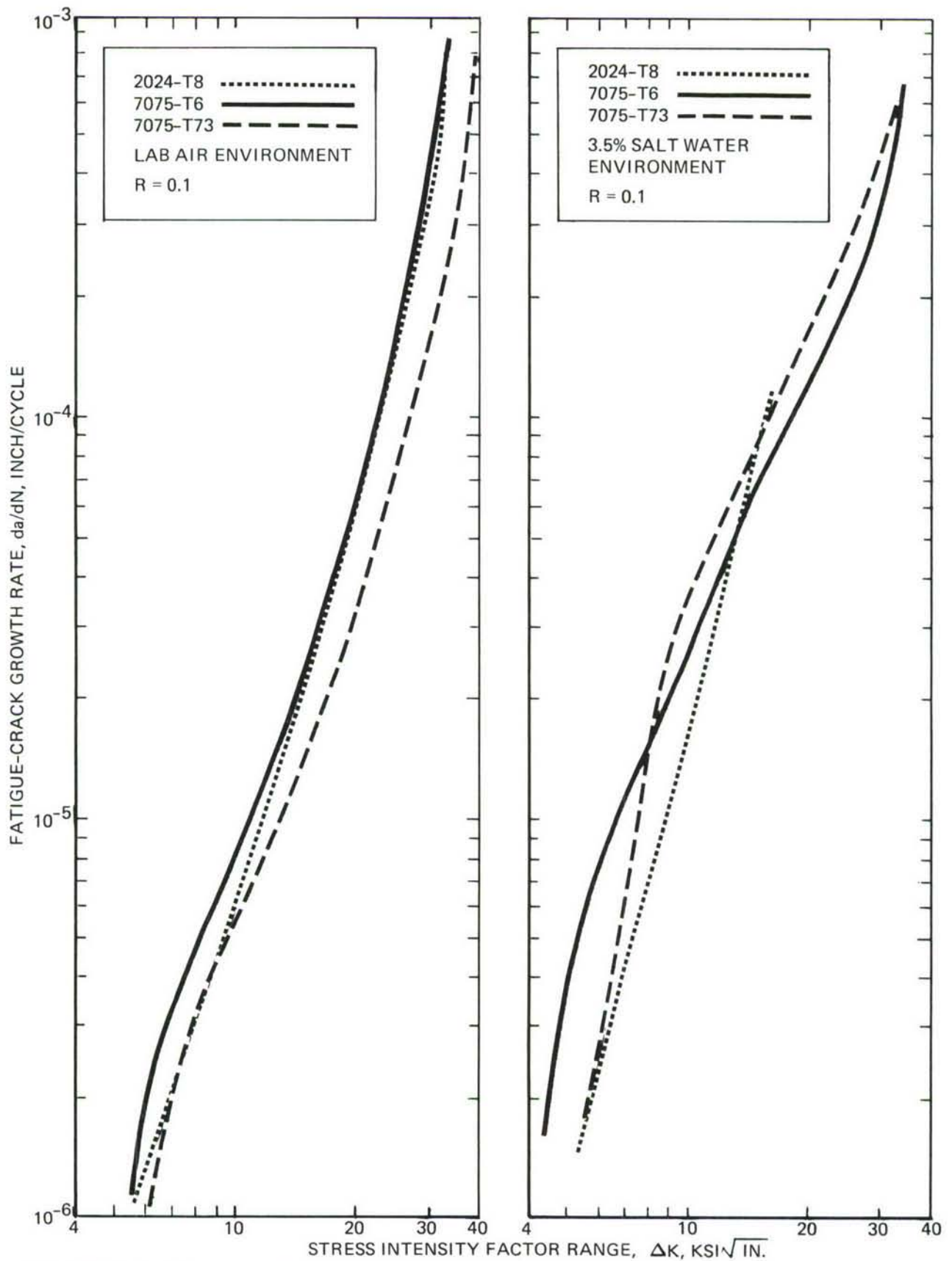
FIGURE C-3. GENERAL TREND OF THE FCP BEHAVIOR FOR ALL THREE MATERIALS

172
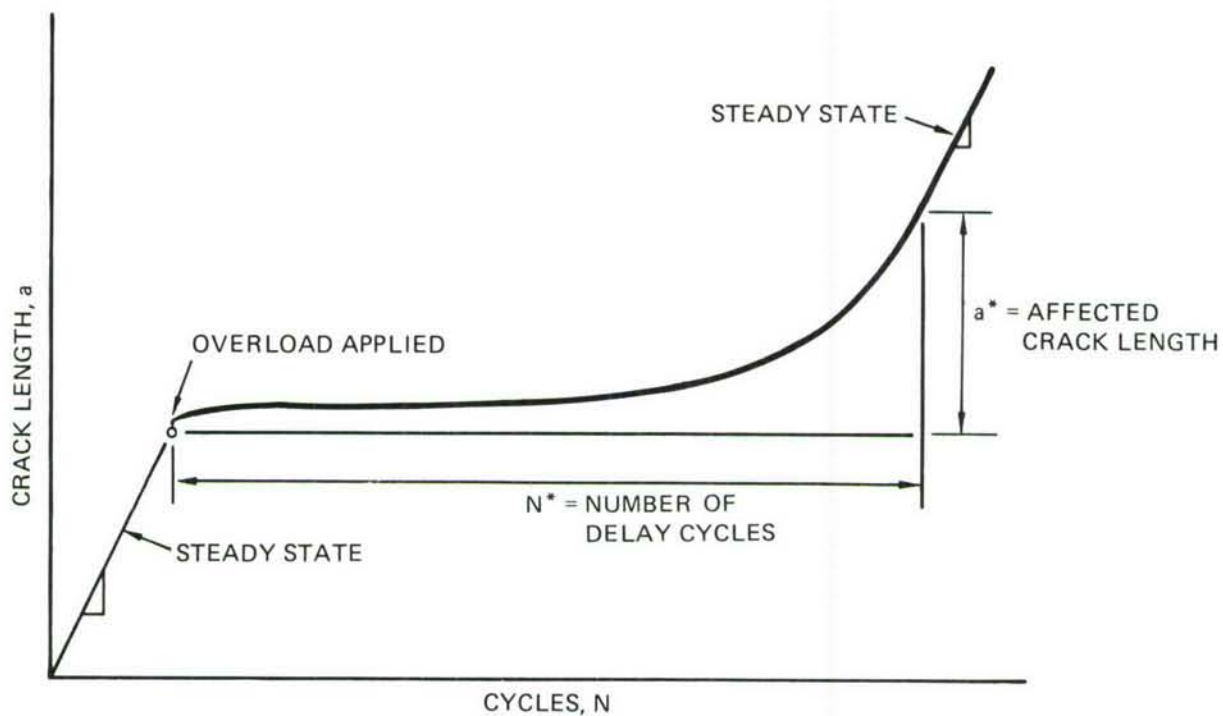
FIGURE C-4(a). CRACK-GROWTH RATE CURVE RESULTING FROM APPLICATION OF A SINGLE OVERLOAD
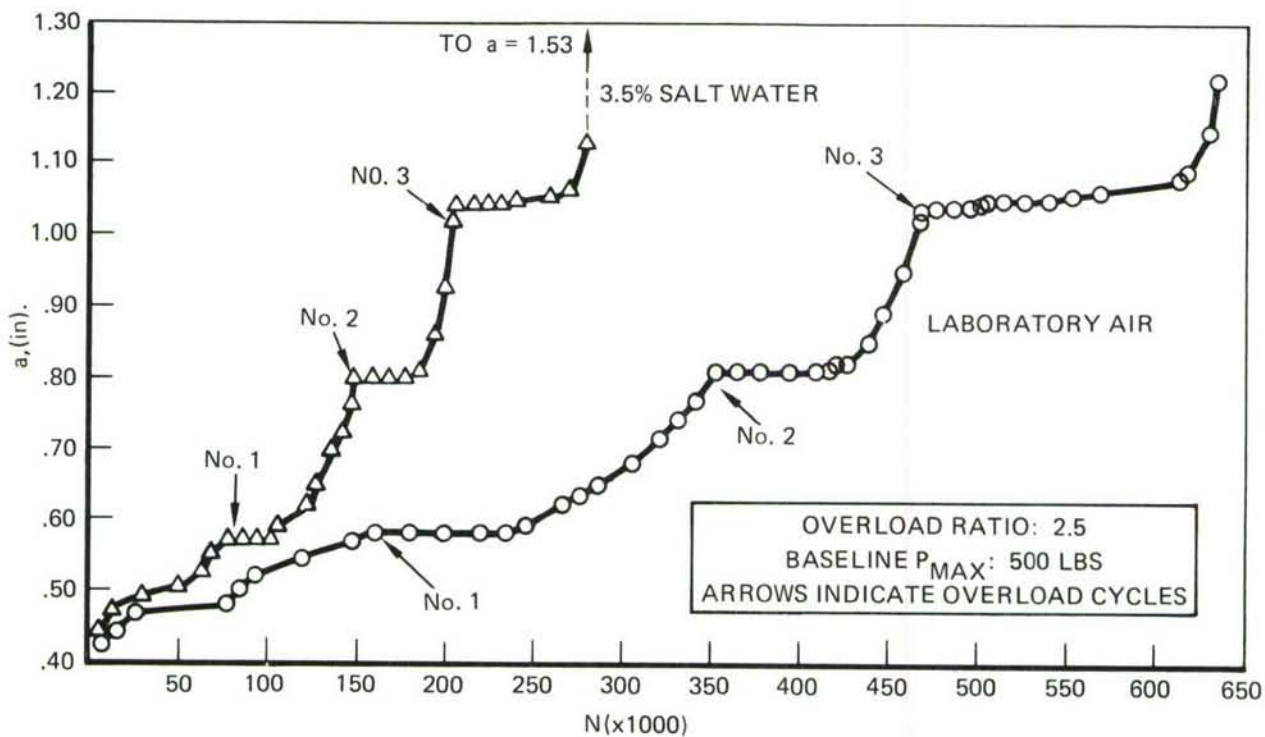
FIGURE C-4(b). CRACK-LENGTH VS NUMBER OF CYCLES FOR 7075-T73 ALLOY AT AN OVERLOAD RATIO OF 2.5 IN BOTH AIR AND SALT WATER
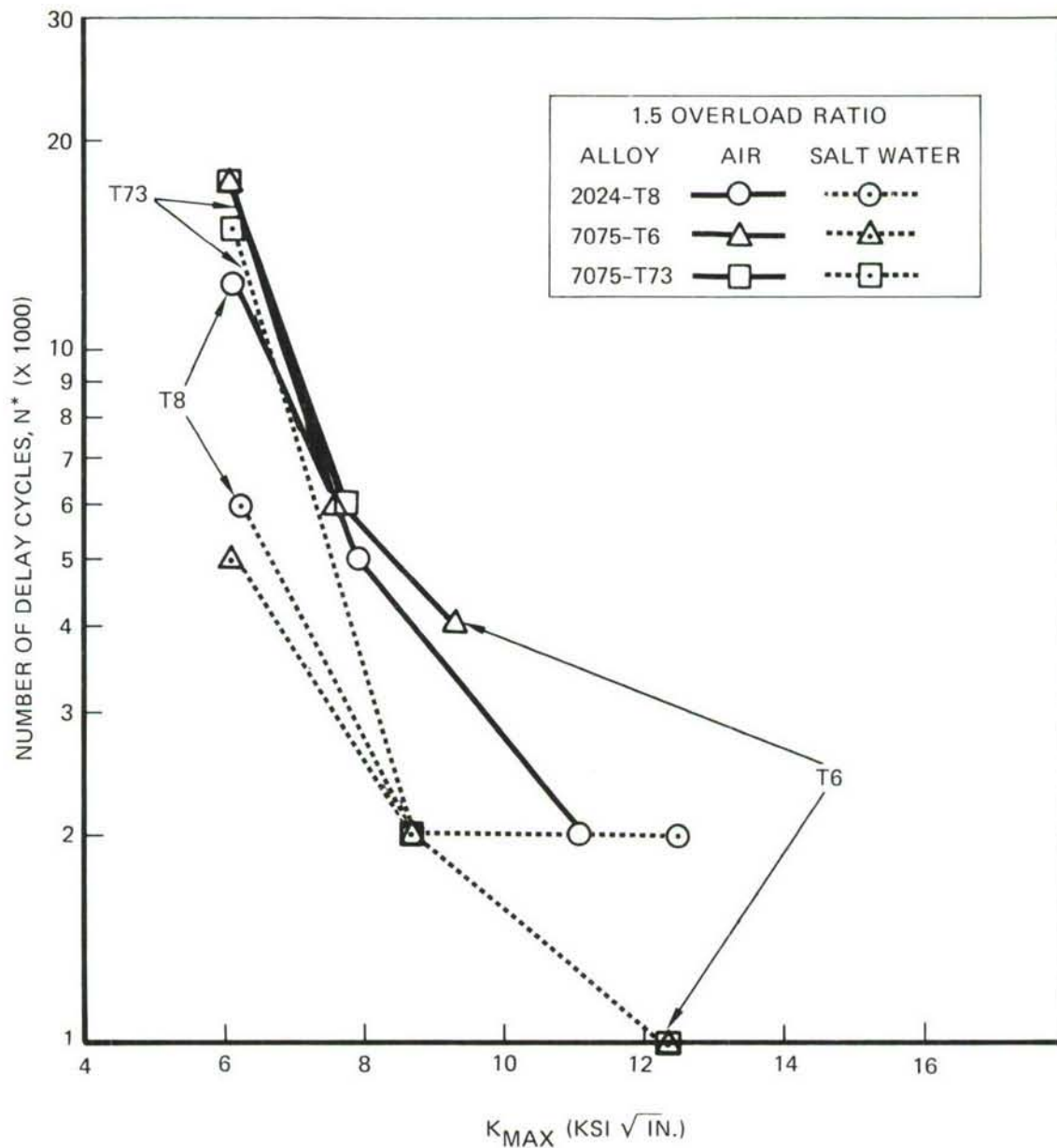
FIGURE C-5. NUMBER OF DELAY CYCLES AS A FUNCTION OF BASELINE
STRESS-INTENSITY FACTOR IN AIR AND 3.5% SALT WATER
AFTER AN OVERLOAD RATIO OF 1.5
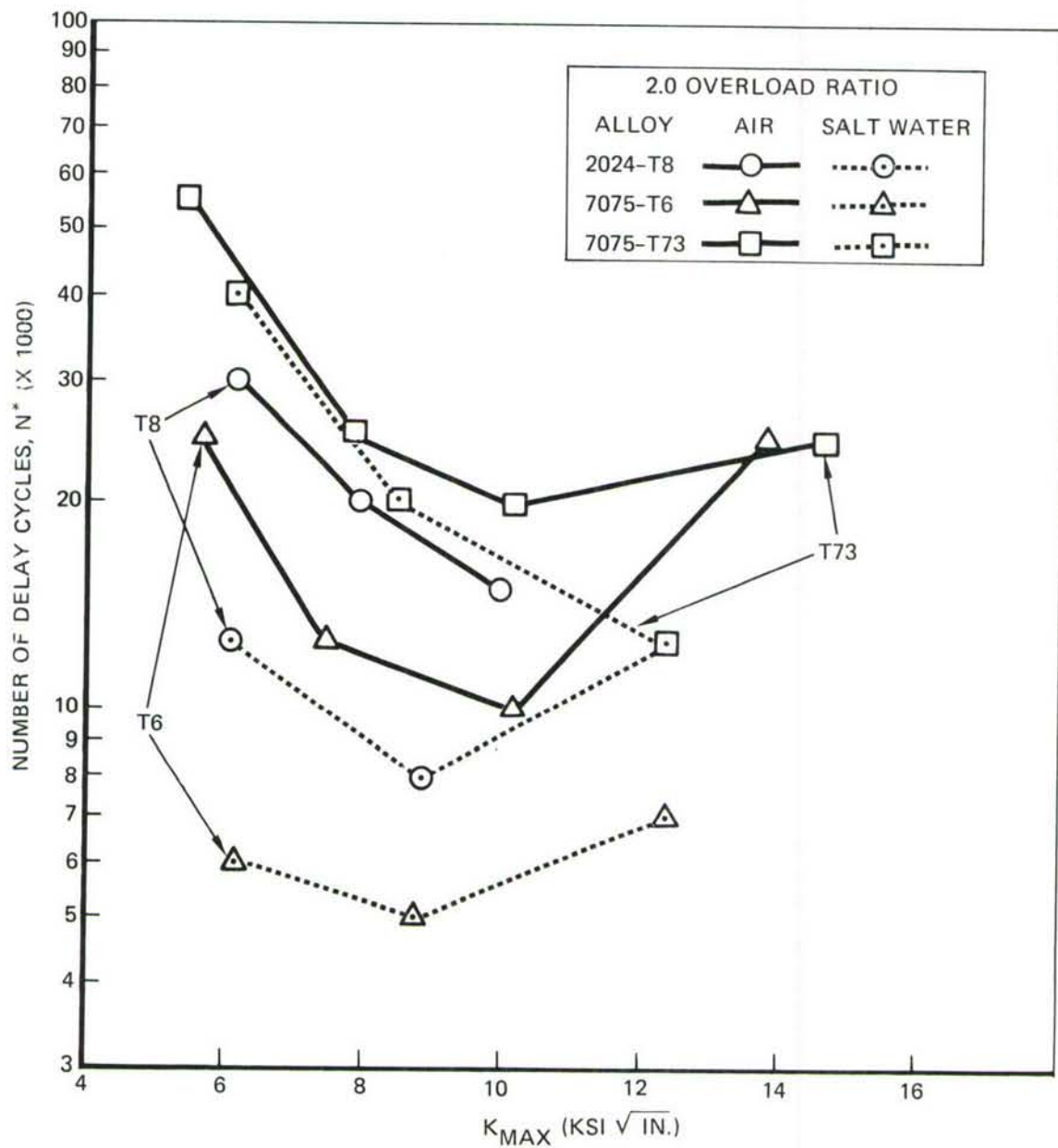
FIGURE C-6. NUMBER OF DELAY CYCLES AS FUNCTION OF BASELINE
STRESS-INTENSITY FACTOR IN AIR AND 3.5% SALT WATER
AFTER AN OVERLOAD RATIO OF 2.0
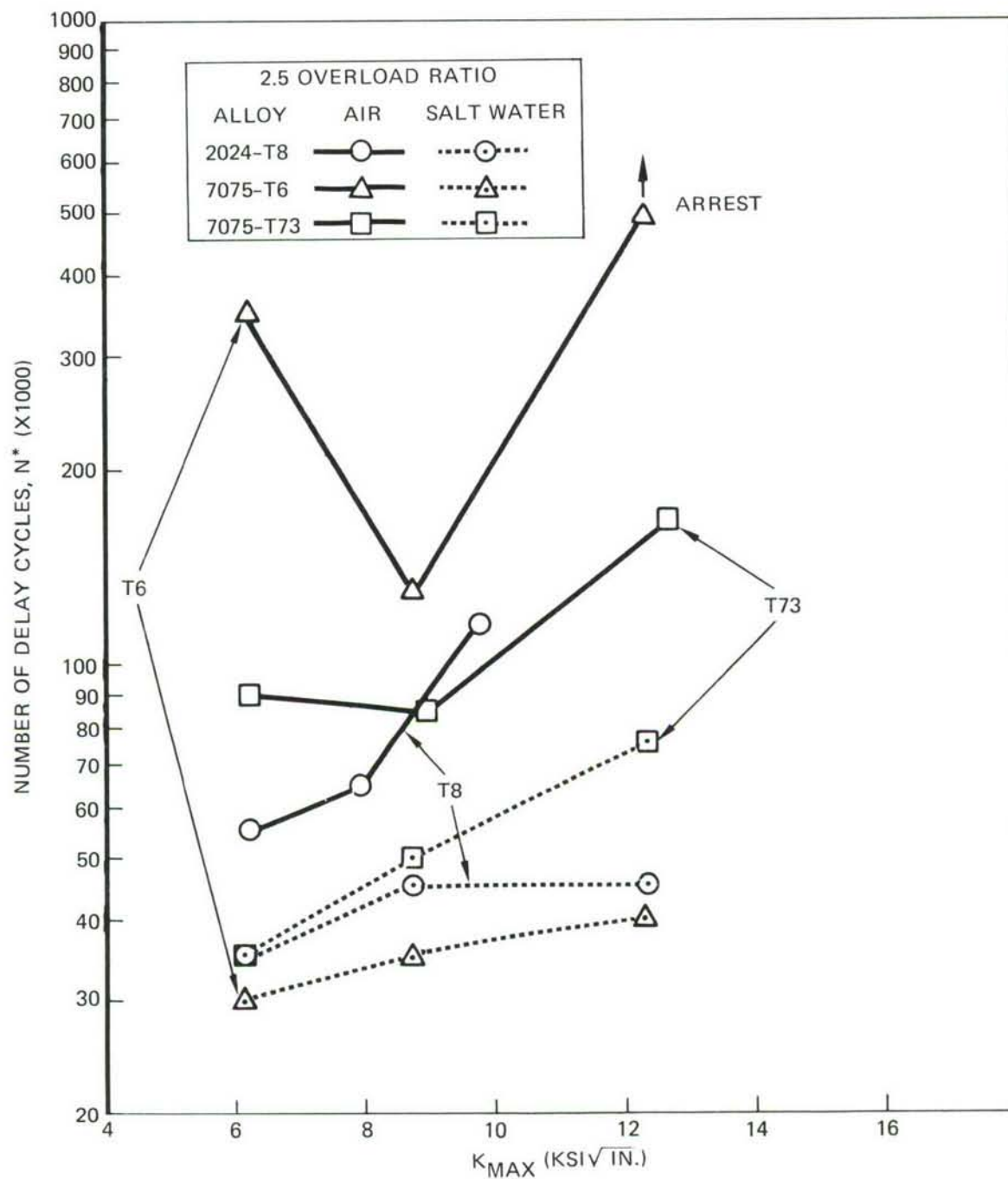
FIGURE C-7. NUMBER OF DELAY CYCLES AS A FUNCTION OF BASELINE
STRESS-INTENSITY FACTOR IN AIR AND 3.5% SALT WATER
AFTER AN OVERLOAD RATIO OF 2.5
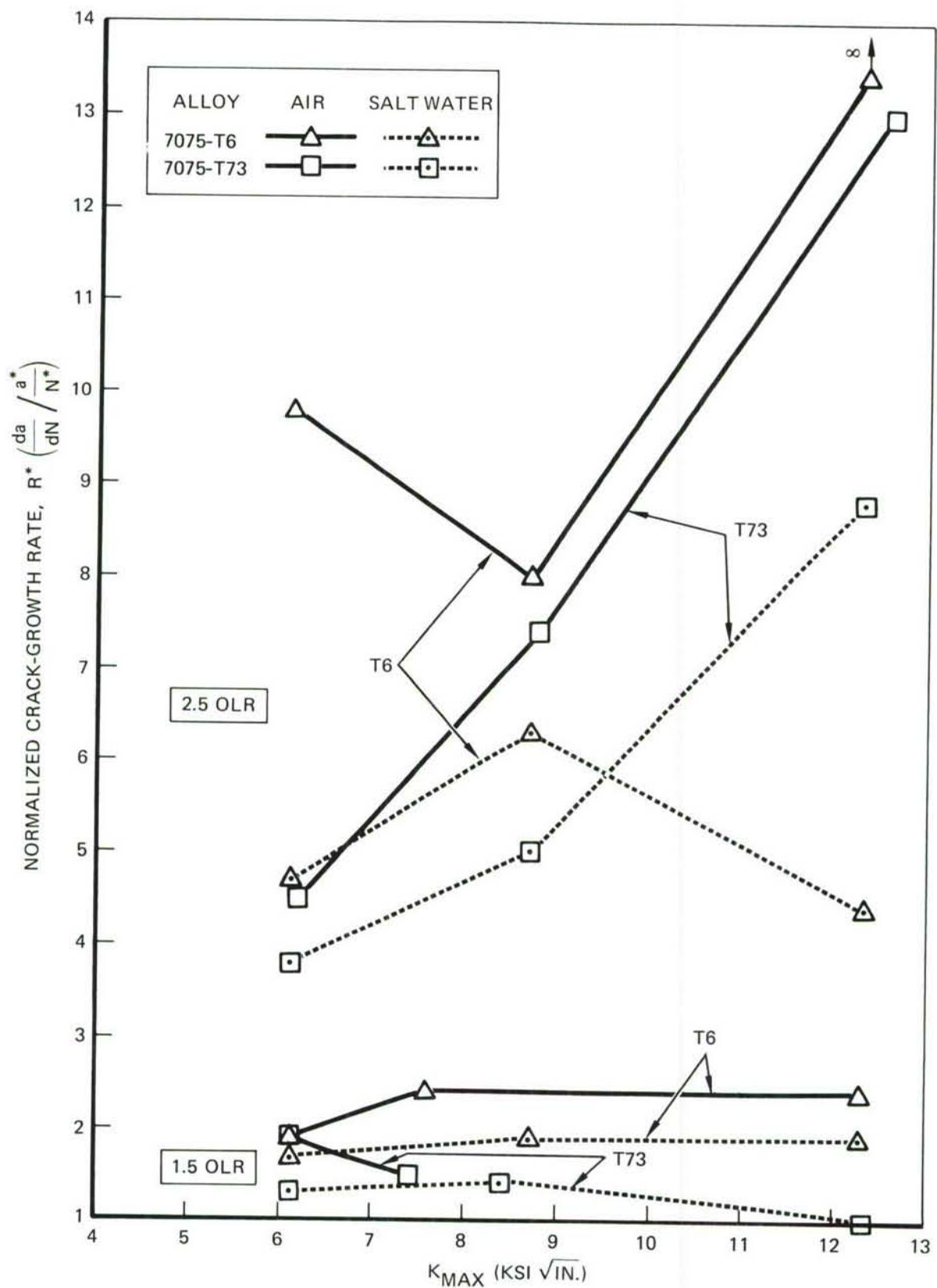
FIGURE C-8. THE EFFECT OF OVERLOAD RATIO (OLR) ON NORMALIZED
AVERAGE CRACK-GROWTH RATE IN AIR AND SALT WATER
FOR THE 7075 ALLOY

177

(a) K_{MAX} = 6.1 KSI $\sqrt{IN.}$ CRACK LENGTH AT OVERLOAD = 0.57 IN.

CRACK-GROWTH
DIRECTION

(b) K_{MAX} = 8.7 KSI $\sqrt{IN.}$ CRACK LENGTH AT OVERLOAD = 0.80 IN.

(c) K_{MAX} = 12.3 KSI $\sqrt{IN.}$ CRACK LENGTH AT OVERLOAD = 1.03 IN.

BASELINE P_{MAX} = 500 LBS

OVERLOAD RATIO = 2.5
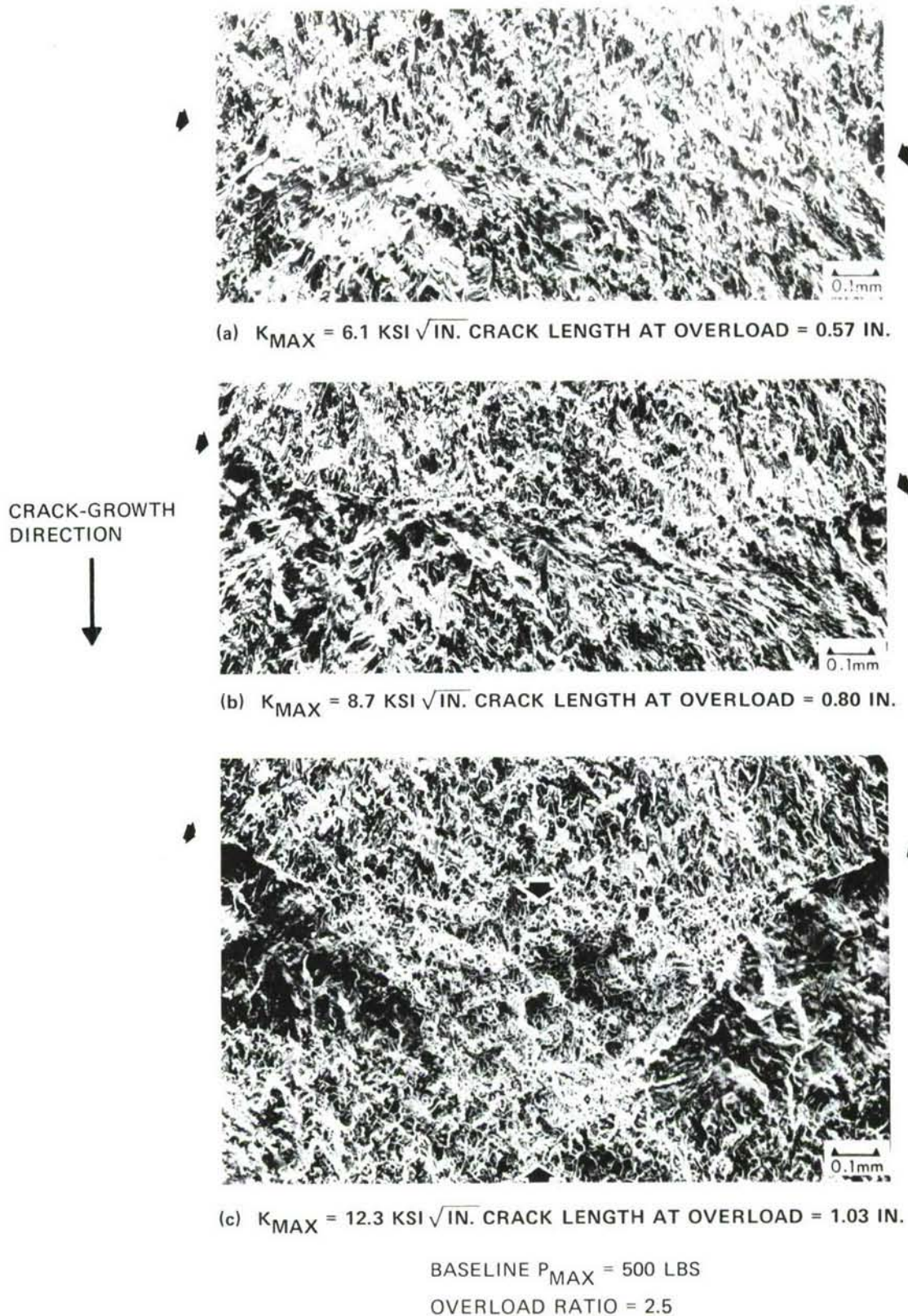
FIGURE C-9. FRACTOGRAPHS SHOWING EFFECT OF STRESS INTENSITY ON
OVERLOAD MARKING AFTER A 150% OVERLOAD CYCLE IN 7075-T6 IN AIR

(a) K_{MAX} = 6.1 KSI $\sqrt{IN.}$ CRACK LENGTH AT OVERLOAD = 0.57 IN.

CRACK-GROWTH
DIRECTION

(b) K_{MAX} = 8.7 KSI $\sqrt{IN.}$ CRACK LENGTH AT OVERLOAD = 0.80 IN.

(c) K_{MAX} = 12.3 KSI $\sqrt{IN.}$ CRACK LENGTH AT OVERLOAD = 1.03 IN.

BASELINE P_{MAX} = 500 LBS

OVERLOAD RATIO = 2.5
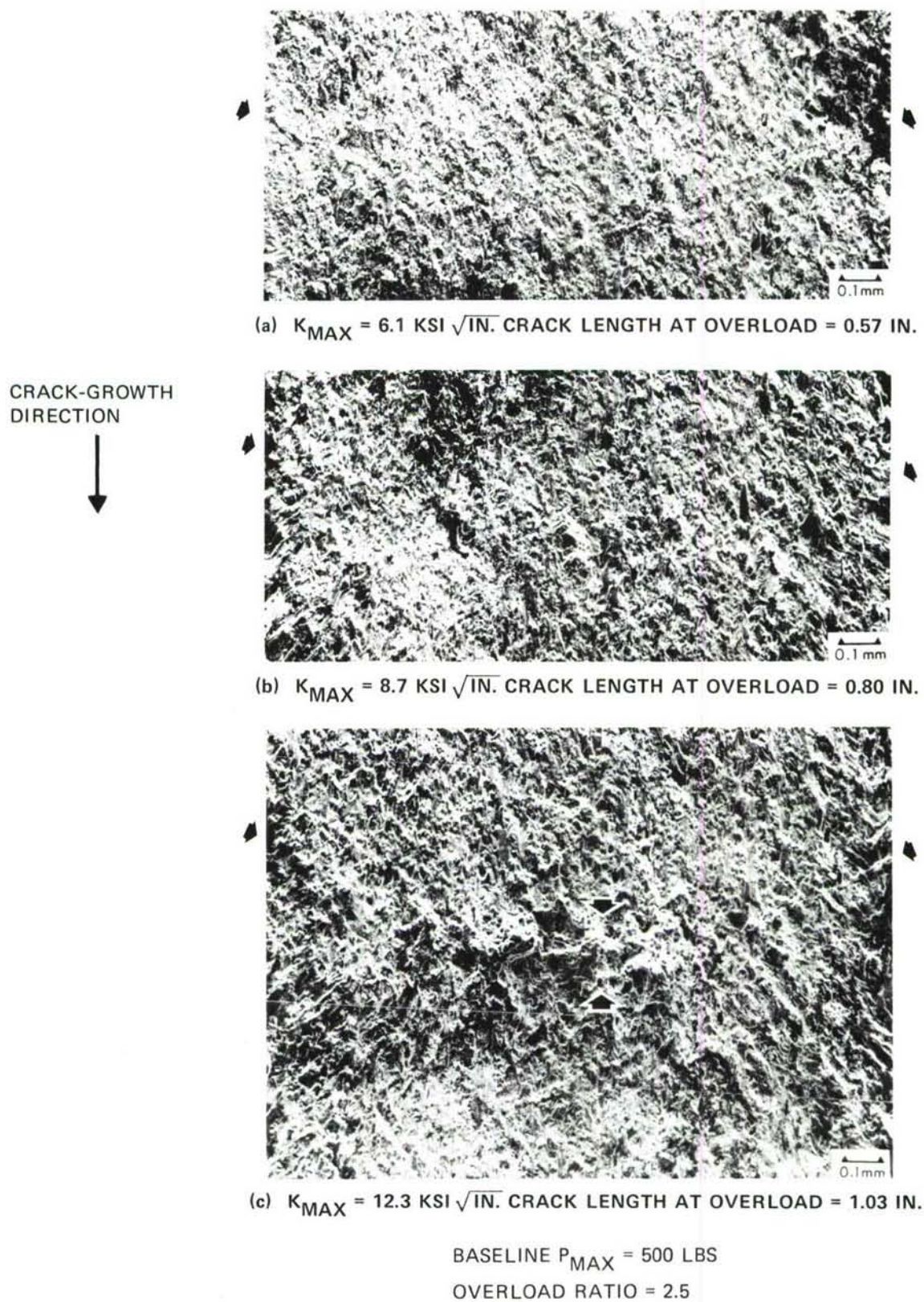
FIGURE C-10. FRACTOGRAPHS SHOWING EFFECT OF STRESS INTENSITY ON
OVERLOAD MARKING AFTER A 150% OVERLOAD CYCLE IN 7075-T6 IN
3.5% SALT WATER

179

(a) AIR

CRACK-GROWTH
DIRECTION
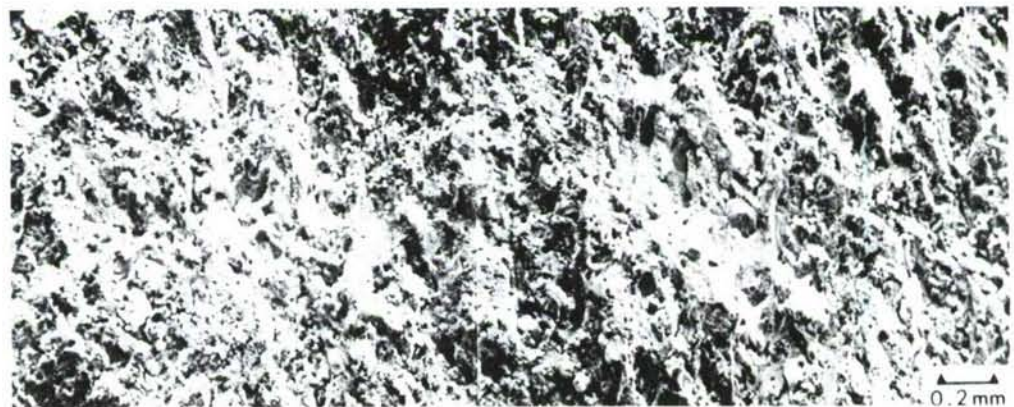
(b) 3.5% SALTWATER

BASELINE P_{MAX} (K_{MAX}): 500 LBS (6.1 KSI $\sqrt{IN.}$)

CRACK-LENGTH AT OVERLOAD: 0.57 IN.

OVERLOAD RATIO: 2.0

FIGURE C-11. FRACTOGRAPHIC FEATURES IN THE VICINITY OF A 100%
OVERLOAD CYCLE IN 2024-T8 IN AIR AND SALT WATER

CRACK-
GROWTH
DIRECTION

OVERLOAD
MARKINGS

(a) OVERLOAD RATIO = 2.0

0.2mm

OVERLOAD
MARKINGS

(b) OVERLOAD RATIO = 2.5

0.2mm
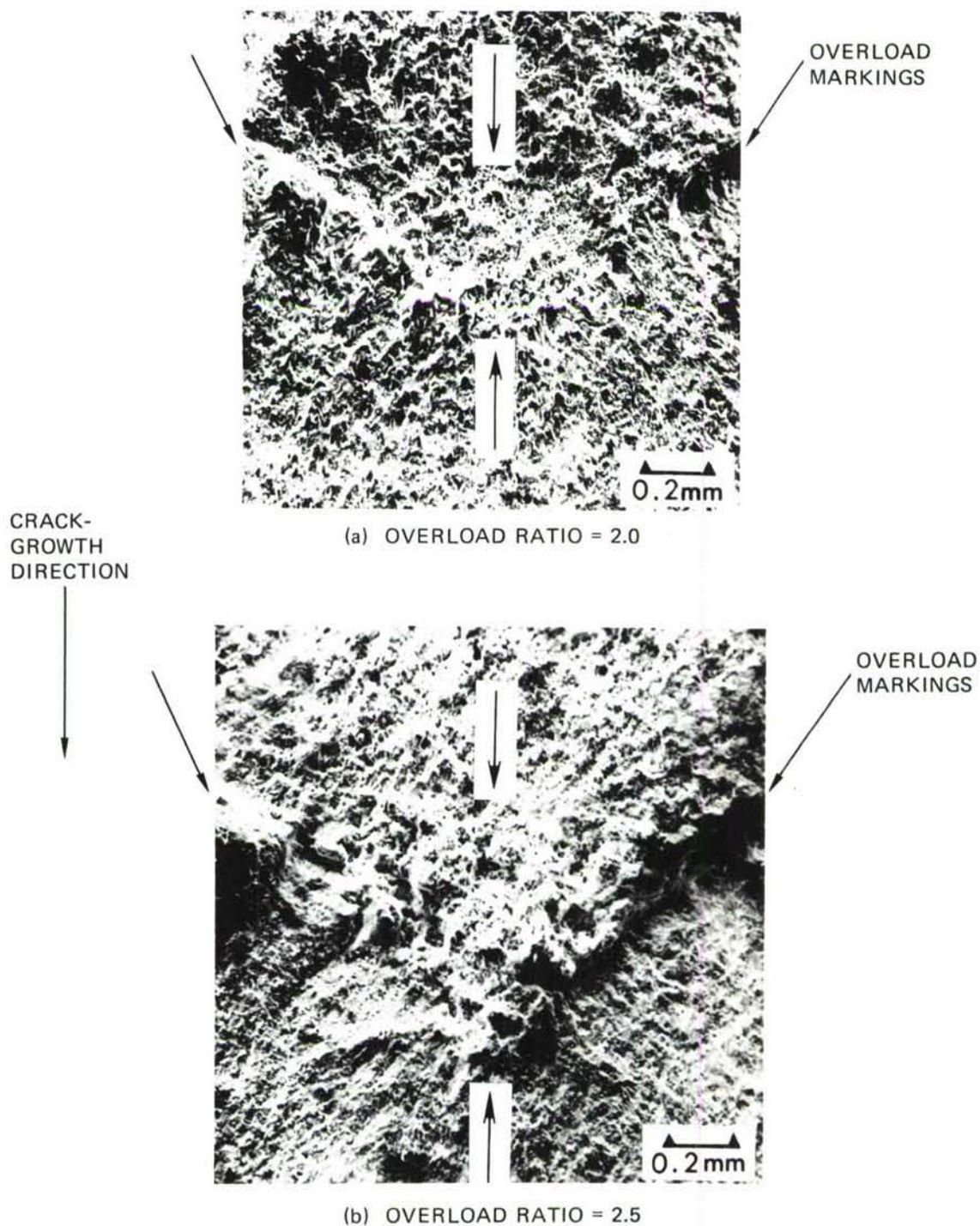
BASELINE P_{MAX} (K_{MAX}) = 500 LBS (12.3 KSI $\sqrt{IN.}$)

FIGURE C-12. FRACTOGRAPHIC FEATURES IN THE VICINITY OF AN
OVERLOAD CYCLE IN 2024-T8 AT OLR OF 2.0 AND
2.5 IN SALT WATER

CRACK-
GROWTH
DIRECTION

OVERLOAD
MARKINGS

0.2 mm

(a) OVERLOAD RATIO = 2.0

OVERLOAD
MARKINGS

0.2 mm
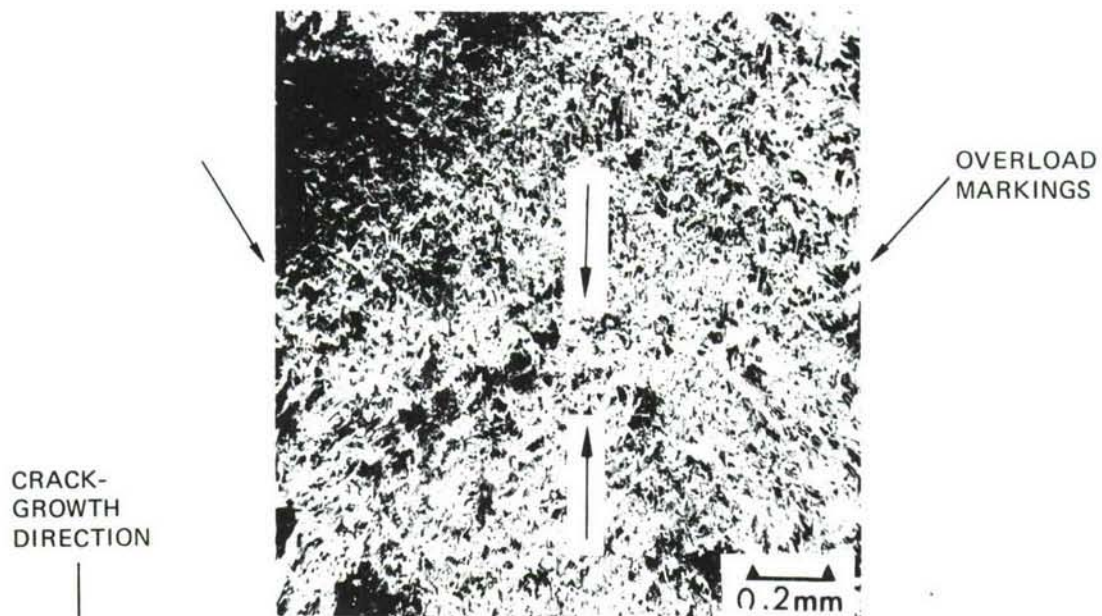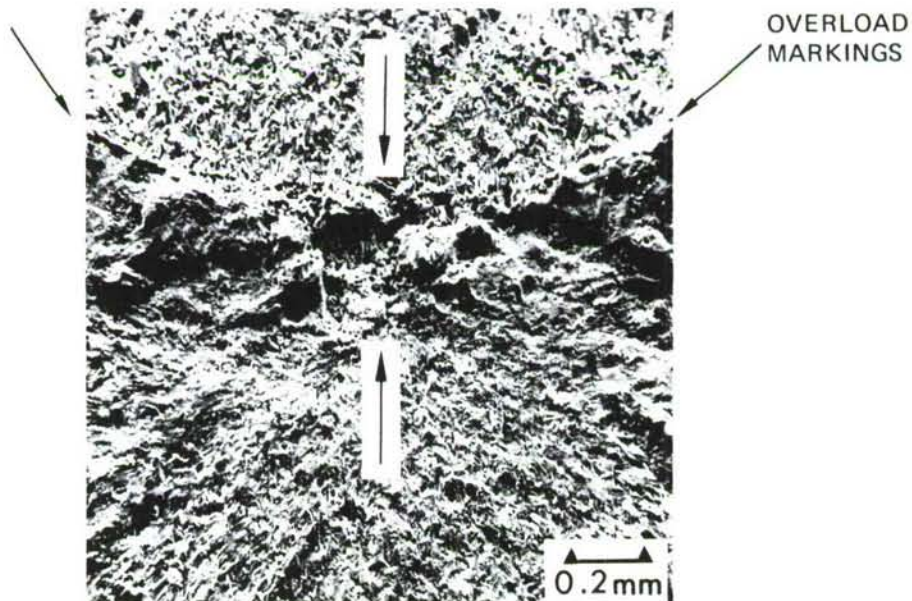
(b) OVERLOAD RATIO = 2.5

BASELINE P_{MAX} (K_{MAX}) = 500 LBS, (12.3 KSI $\sqrt{IN.}$)

**FIGURE C-13. FRACTOGRAPHIC FEATURES IN THE VICINITY OF AN
OVERLOAD CYCLE IN 7075-T6 AT OLR OF 2.0 AND
2.5 IN SALT WATER**

182

CRACK-GROWTH DIRECTION

OVERLOAD MARKINGS

(a) OVERLOAD RATIO = 2.0

OVERLOAD MARKINGS

(b) OVERLOAD RATIO = 2.5

BASELINE P_{MAX} (K_{MAX}) = 500 LBS (12.3 KSI $\sqrt{IN.}$)

FIGURE C-14. FRACTOGRAPHIC FEATURES IN THE VICINITY OF AN OVERLOAD CYCLE IN 7075-T73 AT OLR OF 2.0 AND 2.5 IN SALT WATER

APPENDIX D

EFFECT OF THICKNESS OF RETARDATION BEHAVIOR
OF 7075 AND 2024 ALUMINUM ALLOYS*

I. <u>INTRODUCTION</u>

Retardation of fatigue-crack growth due to tensile overloads is well estab-
lished[1-8]. However, the mechanisms of overload retardation have not been well
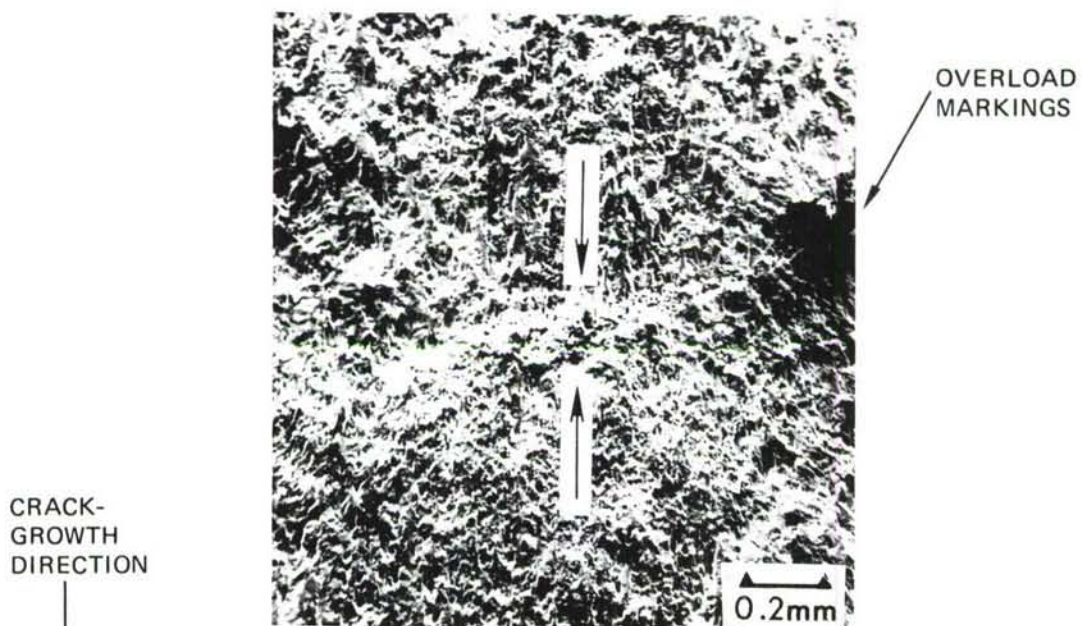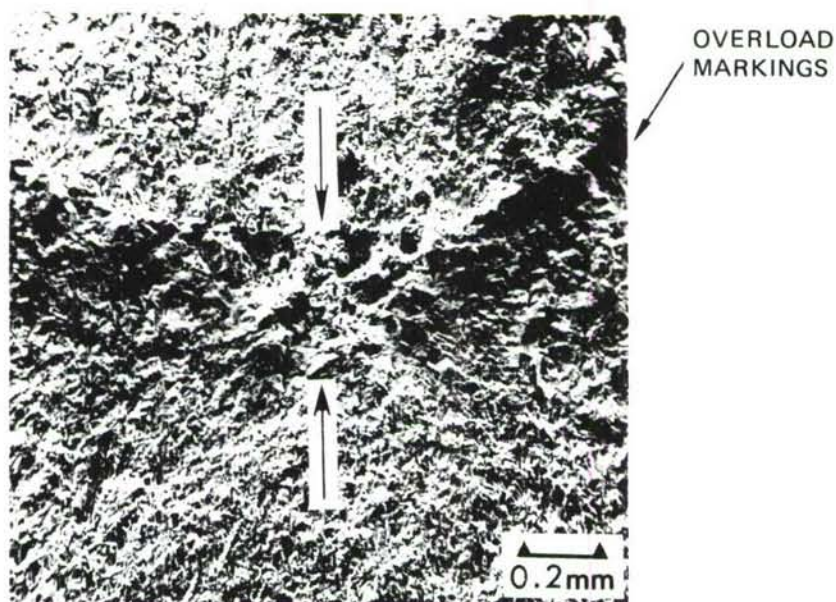understood. Several empirical models which take retardation into account have been
developed to predict the fatigue-crack growth under variable amplitude loading[9-13].
Most of these models are based on the changes in the plastic-zone size at the crack-
tip. Since thickness affects the plastic-zone size[14], it seems plausible to assume
that thickness may have an effect on retardation behavior. Some work has been re-
ported on this aspect of retardation behavior. Mills and Hertzberg[15] found that a
decrease in thickness increased the number of delay cycles in 2024-T3 alloy at an OLR
(overload ratio) of 2.0, while at an OLR of 1.5, the thickness effect was small.
Shih[16] also found a decrease in the number of delay cycles with an increase in thick-
ness in 7075-T6 alloy. However, Sharpe, et al[17], did not find any effect of thickness
on the number of delay cycles in the 2024-T851 alloy. Hence, it appears that there is
considerable uncertainty about the effect of thickness on retardation behavior, depend-
ing on the alloy and testing parameters used.

In the present investigation, 0.50-inch, 0.25-inch, and 0.063-inch thick single-
edge-notched specimens of two aluminum alloys in four heat treat conditions were used
with the 7075 alloy in the T6 and T73 conditions and the 2024 alloy in the T3 and T8
conditions. In this work, only single overload cycles were used. The changes in
strain distribution and the size of the surface plastic-zone at the crack-tip were de-
termined by optical interferometry. These interferometry results were correlated
with the retardation behavior. Fractography was also employed to understand the
micromechanisms of failure in different thicknesses and alloys.

---

*To be presented at the tenth National Symposium on Fracture Mechanics, August
23-26, 1976, Philadelphia, Pa.

II. EXPERIMENTAL PROCEDURE

Single-edge notched (SEN) specimens (Figure D-1) with three different thicknesses, 0.063-inch, 0.25-inch, and 0.50-inch, were used for this investigation. The 0.25-inch thick specimens were obtained from the center of the same stock as the 0.5-inch thick specimens.

The effects of single overloads on the fatigue-crack growth behavior were determined using a simple, 2-level spectrum of the type shown in Figure D-2. All of the constant-amplitude load cycles were conducted at an R ratio (P_{min}/P_{max}) of 0.1 and a frequency of 5 Hz, while the overload cycles were run at 0.1 Hz. The number of constant-amplitude cycles was sufficient for complete recovery of the unretarded crack-growth rate. The crack-lengths were measured using imprinted photogrids (intergrid spacings of 0.020-inch) to an accuracy of 0.0005-inch with a filar eyepiece in a high-magnification traveling microscope. Generally, crack-lengths were similar on both faces of each specimen. However, in some of the thick specimens, the crack-front did not grow uniformly on both faces; i.e., the crack-front on one face lagged behind the crack-front on the other face. In those tests where the crack on one face lagged the other by a small amount, an average of both the measurements was taken. If the difference in crack-length between the two faces was larger than 0.1-inch, the data was considered invalid and the test was repeated.

Thin foils of all four of the alloys were examined in a Hitachi HU-11A transmission electron microscope at 100 KV. These foils were prepared by a combination of mechanical sectioning, electropolishing, and ion-milling.

A Zeiss interference microscope with thallium spectrum lamp was used to observe the surface plastic-zone size and strain distribution at the crack-tip for all three thicknesses of the four alloys. With this procedure, one can measure surface thickness changes as small as 0.03 μ (300Å).

Changes in the morphology of the fracture surfaces due to overload cycles were determined using the scanning electron microscope (SEM) for each thickness. Fracture surfaces were cleaned by replication and then gold-shadowed before SEM observation.

III. RESULTS AND DISCUSSION

Table D-I lists the tensile properties of the four alloys obtained from both 0.063-inch thick sheets and 0.5-inch thick plates. Since the 0.25-inch thick specimens were obtained by machining the 0.5-inch thick plates, their tensile properties are essentially the same as those for the 0.5-inch thick specimens. The yield and tensile strengths of both the thick (0.25-inch and 0.5-inch) and thin (0.063-inch) material were generally within 5 percent of each other for three of the four alloys investigated. A significant difference in the yield strength, approximately 13 percent between the thick and thin conditions, was found only for the 2024-T8 alloy. The implications of this difference in determining the effect of thickness on the retardation behavior of the 2024-T8 alloy are discussed later on.

The retardation results are summarized in Tables D-II and D-III. The number of delay cycles, N^*, and affected crack-length, a^*, refer to the number of cycles and crack-length over which the retardation occurs, respectively. Figure D-3(a) schematically shows how the number of delay cycles and affected crack-length were determined, while Figure D-3(b) shows typical crack-length versus number of cycles for the three thicknesses of the 2024-T3 alloy after single overload cycles with an OLR of 2.0. These are typical of all the tests conducted. Due to the difficulty of obtaining a straight crack-front, particularly for the thicker specimens and the inherent scatter in the crack-growth rate after the overload cycle, a small difference in number of delay cycles between any two tests should not be considered significant.

The retardation, interferometry, and fractographic results are described and discussed below.

A. Retardation Test Results

7075-T73 Alloy

Figure D-4 shows the amount of delay for a given stress-intensity factor as a function of thickness for the 7075-T73 alloy. In this figure, the minimum recommended thickness[18] to obtain a plane-strain condition for each case is denoted by an X. The approximate minimum thickness for plane-strain was calculated from the formula:

$$B_O \geq 2.5 \left(\frac{K_O}{\sigma_{ys}} \right)^2 \tag{1}$$

where:

B_O = plane-strain thickness

σ_{ys} = yield strength of the alloy

K_o = overload stress intensity factor

In these and subsequent figures showing retardation behavior for other alloys, whenever the stress-intensity level for any particular data point was significantly different from those of other points, it was shown as a number in parenthesis next to that particular data point.

The number of delay cycles decreased with increasing thickness and decreasing OLR. Furthermore, at a given overload ratio, the number of delay cycles decreased as the baseline stress-intensity increased, even though the affected crack-length (Table D-II) increased. This was probably due to a higher baseline crack-growth rate and faster recovery of unretarded crack-growth rate which caused the crack to grow through the overload plastic zone in relatively fewer cycles.

Even though the K_{max} for two of the data points (A and B in Figure D-4b) are not completely consistent with other data points, the basic conclusions remain the same. This is so because, if we interpolate between A and B to obtain an approximate N^* at a K_{max} of 8.8 ksi $\sqrt{in.}$ for the 0.063-inch thick specimen, the value of N^* thus obtained will still be higher than that for the 0.25-inch thick specimen which corresponds to point C in the figure. This difference in K_{max} simply means that the drop in N^* as the thickness changes from 0.063-inch to 0.25-inch may not be as large as shown.

The observed thickness effect on the number of delay cycles at a given K level is probably due to an increase in the plastic-zone size associated with a decrease in thickness. The approximate plastic-zone size, R_p^*, under plane-stress conditions is:

$$R_p = \frac{1}{\pi} \left(\frac{K_o}{\sigma_{ys}} \right)^2 \tag{2}$$

while under plane-strain conditions, the plastic-zone size, R_p^*, is one third of the above value and given as:

$$R_p^* = \frac{1}{3\pi} \left(\frac{K_o}{\sigma_{ys}} \right)^2 \tag{3}$$

The crack-tips were under a plane-stress condition during the overload cycle in almost all of the 0.063-inch thick specimens, as confirmed by the interferometry measurements described in the next section. For mixed mode, the plastic-zone size is between the plane-stress and plane-strain values. The larger plastic-zone sizes under plane-stress conditions cause larger plastic-strains and residual-stresses at the crack-tip and also give rise to severly blunted cracks. For this reason, more retardation was observed in thin specimens of this alloy. However, other factors besides the state-of-stress play a role in determining the thickness effect. This is indicated by the fact that the 2024 alloy did not behave in the same manner as the 7075 alloy; in fact, as will be described later, the 2024-T8 alloy exhibited a completely different retardation behavior. This is also indicated by the observation that, even at thicknesses greater than those required for plane-strain conditions, the number of delay cycles decreases with an increase in thickness. The latter observation may have resulted because, in single overload retardation tests, plane-strain thickness is not always accurately described by equation (1) and, also, due to the fact that the metallurgical structure and hardening mechanisms of the 2024 alloys are different from those for the 7075 alloys.

7075-T6 Alloy

Figure D-5 illustrates the thickness effect on the retardation behavior of this alloy. Here too, with an increase in OLR and a decrease in K_{max} levels, the number of delay cycles increased. The effect of thickness was as expected. However, the results are not as obvious as those for the 7075-T73 alloy. The reason could be that here the plane-strain condition at the crack-tip is achieved at a much lower thickness because of the higher yield strength of the 7075-T6 alloy as compared to that for the 7075-T73 alloy, as illustrated by the equation (1), which shows that plane-strain thickness is inversely proportional to the square of yield strength. Also, since the number of delay cycles is fewer for this heat treatment, the experimental scatter may have masked some of the thickness effect in this alloy.

2024-T8 Alloy

Figure D-6 shows the effects of thickness on the number of delay cycles for this alloy. However, the thickness effect on the 2024-T8 alloy is less than that for the 7075 alloys, except for one point at OLR of 1.5, which is probably due to the difficulty of obtaining a straight crack-front in this thickness for the 2024-T8 alloy at low K

values. In this case, the thickness effect is even less when we consider that the 0.25-inch and 0.5-inch thick specimens had a higher yield strength (Table D-II) than the 0.063-inch thick specimens. Hence, the 0.25-inch and 0.5-inch thick 2024-T8 specimens have plastic-zone sizes even smaller than they would have had if the only change was in going from a plane-stress condition to a plane-strain condition. Therefore, the higher yield strength of 0.25-inch and 0.5-inch thick 2024-T8 alloy should enhance the thickness effects, if any, in this alloy. Furthermore, some of the observed differences in the number of delay cycles with changes in thickness in these tests become much less if the K_{max} differences in the corresponding tests are taken into account. Because of the difficulty of obtaining a straight crack-front, the tests on the 2024-T8 alloy could not be conducted at corresponding K_{max} levels for all the three thicknesses. When these K_{max} differences are taken into account, as discussed for the 7075-T73 alloy, the point A in Figure D-6(a) will probably become lower, while point C will move up, indicating practically no decrease in delay cycles with increase in thickness. Similarly, the difference between points D and E in Figure D-6(b) also becomes less. We should also note that N^* for the data under discussion is of the order of only 2000 to 4000 cycles. Thus, these results indicate that there is no thickness effect in the 2024-T8 alloy.

2024-T3 Alloy

The retardation behavior for the three thicknesses of this alloy is shown in Figure D-7. The trend here is essentially similar to that for the 7075-T6 and 7075-T73 alloys. The basic conclusions at OLR of 2.0 remain the same even though the K_{max} values are not exactly similar for all the data points because, here also, the trend is similar to that for the 7075-T73 alloy; i.e., the relationship between A, B, and C in Figure D-7(b) is similar to the corresponding points in Figure D-4(b). However, at an OLR of 1.5, a similar argument indicates relatively less effect of thickness at a K_{max} of 8.8 ksi $\sqrt{in.}$ and 12.6 ksi $\sqrt{in.}$

The anomalous behavior of one 0.5-inch point (L) in Figure D-7(b) could be due to either scatter or the difficulty of getting a straight crack-front across the 0.5-inch thick 2024 alloy at the lower K values or a combination of both. Also, these differences could be due to the hardening mechanism of 2024, which is different from the 7075 alloy. In all the other alloys, the 0.5-inch thickness was adequate for obtaining plane-strain at all the K values tested. However, in the 2024-T3 alloy, the plane-strain condition was not reached at the K_{max} of 12.4 ksi $\sqrt{in,}$ even for 0.5-inch thick

specimens. This is reflected by the fact that the number of delay cycles had not reached a minimum at 0.5-inch at a K_{max} of 12.4 ksi $\sqrt{in.}$ in the 2024-T3 alloy as had happened in all the other alloys.

Microstructural Differences and Summarization of Retardation Test Results

In general, a decrease in the number of delay cycles was observed with the increase in thickness. However, the results were not uniform or conclusive, particularly for the 2024-T8 alloy. With the 2024-T8 alloy, the thickness effect, if any, was minimal. This behavior apparently is due to cyclic hardening and microstructural differences. The transmission electron microscopic structures for all four alloys are shown in Figure D-8. Here, the 2024-T8 has S' precipitate, a platelet-type structure, along crystallographic planes. The 2024-T3 has essentially GP zones and dispersoids, while the 7075-T6 and T73 alloys have GP zones and η', which are spherical particles randomly distributed over the microstructure.

The cyclic hardening exponents for all four alloys are listed in Table D-I. They were determined by obtaining cyclic stress-strain curves. These curves were obtained by the incremental strain-cycling method described by Landgraf, et al[19], using 0.25-inch diameter cylindrical specimens obtained from the 0.5-inch thick stock. As seen in Table I, the 2024-T8 alloy does have a completely different cyclic hardening exponent. The cyclic hardening exponent apparently influences the plastic-zone size because, as shown in Table D-IV, the measured plane-stress plastic-zone for the 0.063-inch thick 2024-T8 specimen is smaller than that for the 0.063-inch thick 7075-T73, even though they both have the same yield strength. The reason for this difference in cyclic hardening exponent is probably due to the nature of the precipitates in the 2024-T8 alloy, which are essentially S' and not GP zones as in the 2024-T3 or η' as in the 7075-T6 alloy (Figure D-8). This difference in precipitate nature is probably responsible for the fact that, in this case, the number of delay cycles did not decrease with increase in thickness and, also, the number of delay cycles was generally lower for the 0.063-inch 2024-T8 alloy than that for the 0.063-inch 7075-T73 alloy, even though they both have a similar yield strength in this thickness. Hence, the microstructural differences are probably the key to the differences in observed retardation behavior. A more detailed metallurgical study should provide a definite answer.

It was thought that some of the difference in the number of delay cycles could be due to the basic difference in crack-growth rates of specimens of different thickness. For this purpose, the decrease in the average da/dN values in the affected crack-length

region was compared for each test. This was calculated by obtaining (1) da/dN from the retardation tests once crack-growth had stabilized and (2) a^*/N^* from Tables D-II and D-III. When these values (called degree of retardation, $R^* = (da/dN)/a^*/N^*$) were plotted as a function of thickness, no general trend was observed. Nevertheless, these results indicate that for improved prediction models, one has to take thickness and microstructural factors into consideration in addition to the yield strength and plastic-zone size.

B. Interferometry Results

As previously reported[1], the optical interference technique gives a reliable measurement of the plane-stress plastic-zone size for the SEN specimens. Here, interferometry patterns were obtained in each of the three thicknesses for all four alloys after 100% overload cycles. Table D-IV summarizes measured overload plastic-zone sizes from these observations. For comparison purposes, calculated plane-stress plastic-zone size (Equation 2) and plane-strain plastic-zone size (Equation 3) are also listed in this Table.

The agreement between measured and calculated plastic-zone size is very good for the 0.063-inch thick specimens, as shown in Table D-IV. Except for the 2024-T8 alloy, no alloy showed a consistent decrease in surface plastic-zone size with increase in thickness. However, the changes in plastic-zone size with change in thickness were manifested in fractographic observations described in the next section. This was so because the interferometry measures surface plastic-zone and, for specimens of any thickness, a pure plane-strain condition does not exist at the surface because of the lack of a three-dimensional constraint at the surface. The results confirm this. As an example, Figure D-9 shows interferometry patterns at the crack-tip for all three thicknesses of the 7075-T73 alloy immediately after an OLR of 2.0. Here, the decrease in plastic-zone size with thickness is not comparable to that required based on a change of stress-state from plane-stress to plane-strain, which indicates that even for the 0.5-inch thickness, the stress-state at the surface was not plane-strain. Hence, the changes in interferometry patterns as the crack passes through the plastic-zone can be correlated accurately with the retardation behavior only for the 0.063-inch thickness.

For this purpose, patterns were obtained (1) immediately after the overload cycle, (2) when the crack was halfway through the plastic-zone, and (3) when the crack was beyond the plastic-zone. The retardation behavior of these same specimens was

also measured. Figure D-10 shows such a correlation for the 7075-T6 alloy after a 100% overload cycle. The figure clearly shows an excellent correlation between the retardation behavior, affected crack-length, and the overload plastic-zone. However, when a similar figure was prepared for an 0.5-inch thick specimen, the correlation between affected crack-length and measured surface plastic-zone was not good for the aforementioned reasons.

Thus, the interferometry results clearly show the applicability of this technique for indicating how the crack-growth behavior changes as the crack progresses through the plastic-zone under plane-stress conditions, and they also confirm that the retardation occurs primarily in the overload plastic-zone.

C. Fractographic Results

The fracture surfaces of selected retardation specimens from each alloy and each thickness were examined to understand the micromechanisms of crack-growth due to the overload cycles with special attention to:

- The nature and size of the overload region, the occurrence of stretch-zones, dimples, abrasion, etc., and their relationship to the plastic-zone size for the three thicknesses tested.

- The effect of single overload cycles on the microscopic crack-growth rate as indicated by the changes in striation spacings.

For this purpose, fractographs were obtained (1) before overload, (2) in the overload stretch band, and (3) at several locations in the retardation zone. The overload cycle manifested itself as a stretch-band across the thickness of the failed specimens in almost all the cases. The width of the overload stretch zone and associated retardation region increased with decrease in thickness as well as increase in applied K level. It progresses from a barely visible thin line at low K levels and larger thicknesses to a wide band of overload zone exhibiting more dimpling and tunneling at lower thicknesses and higher K values. This increase in stretch band is a direct manifestation of the overload plastic-zone size which increases with decrease in thickness and increase in K.

Figure D-11 shows the results for a 0.063-inch thick 2024-T3 specimen. Here, as the stress intensity level went up, the width of the overload zone increased because the plastic-zone size is directly proportional to the square of applied K as shown in Equation (2).

The overload band or stretch zone associated with the incremental crack-growth during the rising-load portion of the overload cycle is marked by a dimpled region, Figure D-11(c). The tunneling effect in the stretch zone, particularly for 0.063-inch thick specimens, as shown in Figure D-11(b) and (c), is due to the relatively plane-strain condition along the midsection of the specimen. Immediately following the stretch marking is the retardation zone marked by a rather smooth topography, characteristic of a very low FCP rate. Evidence of abrasion and fatigue striations was also observed in these regions in some cases. As one proceeds further away from the overload region, the topography of the fracture surface becomes increasingly similar to that before the overload due to the recovery of constant-amplitude crack-growth rate.

Figure D-12 shows the change in stretch marking with a change in thickness. The baseline loads (which are the same when normalized for thickness), overload ratios, and baseline stress-intensity levels for the specimens are also shown in this Figure. As we can see, at 0.063-inch, the OL marking is clearly visible, while at the 0.25-inch, it is somewhat less marked, and at 0.5-inch, it is barely visible. This behavior was similar for all the alloys at both OLR. Only the degree of marking was different at OLR of 1.5. At the lowest K, there was no distinct marking for the 0.5-inch thick specimens. Instead, only a change in topography was seen. The change in marking is a direct result of the stress-state at the crack-tip, which gives rise to a much smaller plastic-zone. The 2024-T3 had the best marking and, hence, for clarity, only 2024-T3 fractographs are presented. This pronounced marking is expected based on the fact that the 2024-T3 has the lowest yield-strength of the four alloys. In the case of the aged alloys such as 2024-T8, cracking of intermetallic particles can be seen (Figure D-13), which indicates the brittleness of this alloy and the severe strain during the overload cycle.

The abrasion was generally higher in the thin specimens which could be due to higher compressive levels or crack-closure, as suggested by Mills[15]. The crack-closure does explain, qualitatively, the occurrence of abrasion. However, the degree of abrasion cannot be explained. Furthermore, there does exist controversy whether crack-closure can quantitatively explain the observed retardation behavior[17, 21, 22].

In comparing the overload regions and associated affected zones of the 2024 alloy with the 7075 alloy, the 7075-T6 and T73 fall in between those for the 2024-T3 and T8. This behavior is in agreement with the delay behavior observed during testing.

The 2024-T8 alloy shows the least amount of delay, while the 2024-T3 alloy shows maximum delay with the 7075-T6 and T73 alloys falling somewhere in between.

Changes in striation spacings across the overload stretch zone were noted, in some cases, depending on the baseline K. The striation spacings were correlated with measured da/dN. Figure D-14 shows typical results from 0.25-inch and 0.50-inch thick 7075-T73 specimens tested at an OLR of 2.0. Similar results were obtained for several more specimens. No striations were observed immediately after the overload cycle and at crack-growth rates below 3×10^{-6} inch/cycle. This lack of discernible striations in many cases could be either due to abrasion or due to the difficulty in resolving striations associated with the relatively low crack-growth rates or due to a change in crack-propagation mode, or a combination of all these factors. Nevertheless, for the specimens in which striations were discernible, the agreement between measured da/dN and striation spacings was good.

IV. SUMMARY AND CONCLUSIONS

- The number of delay cycles was found to decrease with an increase in thickness. However, only a minor effect of thickness was seen on the retardation behavior of the 2024-T8 alloy.

- For a given overload ratio, the number of delay cycles decreased as the baseline stress-intensity factor was increased, even though the affected crack-length increased.

- A good agreement between plastic-zone size measured by interferometry and that calculated under plane-stress condition was found for the 0.063-inch thick specimens of all four alloys.

- The results showed the applicability of the optical interference technique for investigating the crack-growth behavior as the crack progresses through the plastic-zone under plane-stress conditions and also confirmed that retardation occurs primarily in the overload plastic-zone.

- The overload cycle manifests itself as a stretch-band across the thickness of the failed specimens. The width of the overload-stretch zone and associated retardation region increased with a decrease in thickness. An increase in applied stress-intensity level caused an increase in the OL stretch zone and retardation region, as anticipated.

- In many cases, striations were not observed in the retardation zone. For those specimens with discernible striations, the correlation between measured da/dN rates and changes in striation spacing was good.

V. ACKNOWLEDGMENT

REFERENCES

1. G. R. Chanani, Met. Engr. Quarterly, Vol, 15, p. 40, 1975.

2. J. Schijve, "Fatigue Crack Propagation in Light Alloy Sheet Materials and Structures," Report MP-195, National Luchtvaartlaboratorium (Amsterdam), 1960.

3. C. M. Hudson and K. N. Raju, "Investigation of Fatigue-Crack Growth Under Simple Variable-Amplitude Loading," NASA TN D-5702, March 1970.

4. H. F. Hardrath, "Cumulative Damage," Fatigue - Interdisciplinary Approach, Syracuse University Press, Syracuse, New York, 1964.

5. E. F. J. Von Euw, R. W. Hertzberg, and R. Roberts, ASTM-STP-513, p. 230, 1972.

6. D. M. Corbly and P. F. Packman, Engr. Fracture Mechanics, Vol. 5, p. 479, 1972.

7. R. C. Rice and R. I. Stephens, ASTM STP-536, p. 95, 1973.

8. J. Schijve, Engr. Frac. Mech., Vol. 5, p. 269, 1973.

9. O. E. Wheeler: Trans. ASME, J. of Basic Engineering, Paper No. 71-Met-X.

10. J. Willenborg, R. M. Engle, and H. A. Wood: A Crack Growth Retardation Model Using An Effective Stress Concept, TM-71-1 FBR, WPAFB, Ohio, 1971.

11. T. R. Porter: Engr. Fract. Mech., Vol. 4, p. 717, 1972.

12. P. D. Bell and M. Creager, "Crack-Growth Analysis for Arbitrary Spectrum Loading," AFFDL-TR-74-129, Oct. 1974.

13. S. D. Antolovich, A. Saxena, and G. R. Chanani, Engr. Fract. Mech., p. 649, 1975.

14. H. W. Liu, Discussion to a paper of W. Weibull, Proceedings of the Crack Propagation Symposium, Cranfield, Vol. II, p. 514, 1961.

15. W. J. Mills and R. W. Hertzberg, Eng. Fract. Mech., Vol. 7, p. 705, 1975.

16. T. T. Shih, PhD Thesis, "Fatigue-Crack Growth Under Variable Amplitude Loading," Lehigh University, 1974.

17. W.N. Sharpe, D.M. Corbly, and A.F. Grandt, "The Effects of Rest-Time On Fatigue Crack Retardation and Observations of Crack Closure," presented at the ASTM Symposium on Fatigue Crack Growth Under Spectrum Loads, Montreal, June 1975.

18. Annual ASTM Standards, Part 10, E399-74, 1974.

19. R.W. Landraf, JoDean Morrow, and T. Endo, J. of Materials, JMLSA, Vol. 4, No. 1, p. 176, 1969.

20. G.R. Chanani, "Fundamental Investigation of Fatigue-Crack Growth Retardation in Aluminum Alloys," AF Contract F33615-74-C-5126, Northrop Corporation, Report No. NOR 75-199, December 1975.

21. G.R. Chanani and B.J. Mays, "Observation of Crack-Closure Behavior After Single Overload Cycles in 7075-T6 Single-Edge-Notched Specimens," accepted for publication in Engr. Fract. Mech.

22. T.T. Shih and R.P. Wei, Engr. Fract. Mech., Vol. 6, p. 19, 1974.

TABLE D-I. TENSILE PROPERTIES OF THE ALUMINUM ALLOYS

ALLOY AND HEAT TREATMENT	THICKNESS (IN.)	0.2% Y.S. KSI	U.T.S. KSI	% ELONGA- TION	MONOTONIC STRAIN HARDENING EXPONENT	CYCLIC HARDENING EXPONENT
7075-T6	0.063	73.1	80.2	12.5	0.071	- -
7075-T651	0.50	72.8	78.5	12.6	- - -	0.07
7075-T73	0.063	60.8	71.2	12.3	0.133	- -
7075-T7351	0.50	64.6	74.3	15.0	- - -	0.09
2024-T3	0.063	51.7	68.3	18.6	0.163	- -
2024-T351	0.50	52.4	66.3	18.8	- - -	0.06
2024-T8	0.063	61.2	68.3	10.0	0.083	- -
2024-T851	0.50	70.4	75.3	10.3	- - -	0.13

Note 1: For 0.063-inch thick sheet, flat specimens of 2-inch gage-length were used, while for 0.50-inch thick plate, cylindrical specimens of 1-inch gage-length were used.

Note 2: The reported values are average of three tests.

TABLE D-II. SUMMARY OF RETARDATION RESULTS IN AIR FOR DIFFERENT THICKNESSES OF 7075-T73 AND T6 ALLOYS

$$\frac{P_{max} \text{ (Baseline Max Load)}}{B \text{ (Thickness)}} = 8000 \text{ lbs/in.}$$

B (IN)	SPECIMEN NO.	OLR	K_{MAX} (KSI $\sqrt{IN}$)	a_i (IN)	a* (IN)	N* (1000)	ACCL[1]
			7075-T73				
0.5	HT73THK1	1.5	6.1	0.5696	0.003	12.5	a
			8.8	0.7976	0.0060	4	a
			12.4	1.0256	0.0180	3	c
	HT73THK2	2.0	6.1	0.5696	0.001	20	a
			8.8	0.7976	0.020	12.5	c
			12.4	1.0256	0.0348	8	c
0.25	HT73THK3	1.5	6.1	0.5696	0.009	15	a
			8.8	0.7976	0.012	5	b
			12.4	1.0256	0.0248	3	a
	HT73THK4	2.0	6.4	0.5924	0.005	20	a
			9.1	0.8224	0.0358	15	a
			12.9	1.0484	0.0536	10	b
0.063	DT73OLC1	1.5	6.1	0.5696	0.0122	17.5	a
			7.7	0.7132	0.0091	6	a
	DT73OLC2	2.0	5.4	0.5012	0.0190	55	a
			7.7	0.7170	0.0251	25	a
			10.2	0.9055	0.0433	20	b
			7075-T6				
0.5	HT6THK1	1.5	6.4	0.5924	0.0023	8	a
			7.9	0.7292	0.0061	5	a
			9.8	0.8660	0.0030	1.5	a
	HT6THK2	2.0	6.4[2]	0.5924	–	–	a
			7.9	0.7292	0.0270	9	a
			9.8	0.8660	0.0129	3	a
0.25	HT6THK3	1.5	6.4	0.5924	0.0058	8	c
			7.9	0.7292	0.0057	4	a
			9.8	0.8660	0.0228	1	b
	HT6THK4	2.0	6.1[2]	0.5696	–	–	a
			7.6	0.6988	0.0084	12.5	b
			9.3	0.8394	0.0144	8	b
0.063	DT6OLC1	1.5	6.1	0.5696	0.0110	17.5	a
			7.6	0.7074	0.0100	6	b
			9.3	0.8472	0.0120	4	a
	DT6OLC2	2.0	5.6	0.5112	0.0038	25	a
			7.4	0.6983	0.0106	12.5	b
			10.1	0.8989	0.0213	10	a

1 — a = No crack growth during overload cycle and no initial acceleration.
b = Crack growth during overload cycle.
c = Initial acceleration after the overload cycle.
2 — Crack grew only on one surface — making data invalid.

TABLE D-III. SUMMARY OF RETARDATION RESULTS IN AIR FOR DIFFERENT THICKNESSES OF 2024-T8 AND T3 ALLOYS

$$\frac{P_{max} \text{ (Baseline Max Load)}}{B \text{ (Thickness)}} = 8000 \text{ lbs/in.}$$

B (IN)	SPECIMEN NO.	OLR	K_{MAX} (KSI $\sqrt{IN}$)	a_i (IN)	a* (IN)	N* (1000)	ACCL[1]
			2024-T8				
0.50	HT8THK1	1.5	6.1[2]	0.57	–	–	a
			10.2	0.90	0.030	4	b
			13.0	1.06	0.012	2	b
	HT8THK2	2.0	6.1	0.57	0.016	25	a
			8.7	0.79	0.010	10	b
			12.4	1.02	0.066	8	b and c
0.25	HT8THK3	1.5	6.1	0.5696	0.0020	8	a
			8.8	0.7976	0.0023	1.5	a
			12.4	1.02636	0.0144	2	b
	HT8THK4	2.0	6.1	0.5696	0.0046	35	a
			8.8	0.7976	0.0114	15	a
			12.4	1.0256	0.076	15	b
0.063	DT80LC1	1.5	6.1	0.5696	0.0104	12.5	a
			7.9	0.7292	0.0028	5	a
			11.1	0.9587	0.0043	2	a
	DT80LC2	2.0	6.1	0.5696	0.0327	30	b
			7.9	0.7307	0.015	20	b
			9.8	0.8789	0.0421	15	b
			2024-T3				
0.50	HT3THK1	1.5	6.3	0.58	0.003	40	a
			8.8	0.80	0.009	15	a
			12.6	1.04	0.021	4	a
	HT3THK2	2.0	6.1	0.5696	0.0050	175	a
			8.8	0.7976	0.0258	60	b and c
			12.4	1.0256	0.0456	17.5	b
0.25	HT3THK3	1.5	6.1	0.57	0.003	50	a
			8.7	0.793	0.017	15	b
			12.6	1.03	0.028	5	a
	HT3THK4	2.0	6.1	0.57	0.026	185	a
			8.7	0.793	0.033	50	b
			12.6	1.03	0.076	80	a
0.063	DT30LC1	1.5	6.1	0.5696	0.0114	55	a
			7.6	0.7064	0.0152	20	a
			9.7	0.8660	0.0236	12.5	c
	DT30LC2	2.0	6.1	0.5696	0.0314	240	a
			7.7	0.711	0.0440	145	b
			9.4	0.848	0.0400	130	a

1 — a = No crack growth during overload cycle and no initial acceleration.
b = Crack growth during overload cycle.
c = Initial acceleration after the overload cycle.
2 — Crack grew only on one surface — making data invalid.

TABLE D-IV. COMPARISON OF CALCULATED AND MEASURED PLASTIC-ZONE SIZES IN THE FOUR ALLOYS

ALLOY	B_o, MIN. PLANE-STRAIN THICKNESS EQ. 1, IN.	CALCULATED R_p PLANE-STRESS EQ. 2 APPROX IN.	SPECIMEN THICKNESS / ORIENTATION	APPROX. MEASURED OVERLOAD PLASTIC-ZONE, INCHES			CALCULATED R_p* PLANE-STRAIN EQ. 3 APPROX IN.
				0.063 In.	0.25 In.	0.50 In.	
2024-T3	0.286	0.0365	X	0.030 ± 0.013	0.0342 ± 0.026	0.0282 ± 0.021	0.0118
			Y	0.0389 ± 0.0032	0.0484 ± 0.0016	0.0447 ± 0.004	
2024-T8	0.204	0.0260	X	0.0195 ± 0.0021	0.0111 ± 0.0008	0.0085 ± 0.0008	0.0066
			Y	0.0247 ± 0.0016	0.0161 ± 0.0013	0.0116 ± 0.001	
7075-T73	0.207	0.0263	X	0.022 ± 0.0016	0.0166 ± 0.0008	0.0163 ± 0.0074	0.0078
			Y	0.0313 ± 0.0068	0.0211 ± 0.0022	0.0211 ± 0.0034	
7075-T6	0.143	0.0182	X	0.0171 ± 0.0011	0.0253 ± 0.0031	0.0203 ± 0.0016	0.0061
			Y	0.025 ± 0.0016	0.0239 ± 0.0012	0.0237 ± 0.003	

*NOTE 1: ORIENTATION: CRACK ━━Ⱶ⟨X⟩━━

NOTE 2: All the measurements were made after an OLR of 2.0 and at a baseline K_{max} of 8.7 ksi$\sqrt{in.}$

202
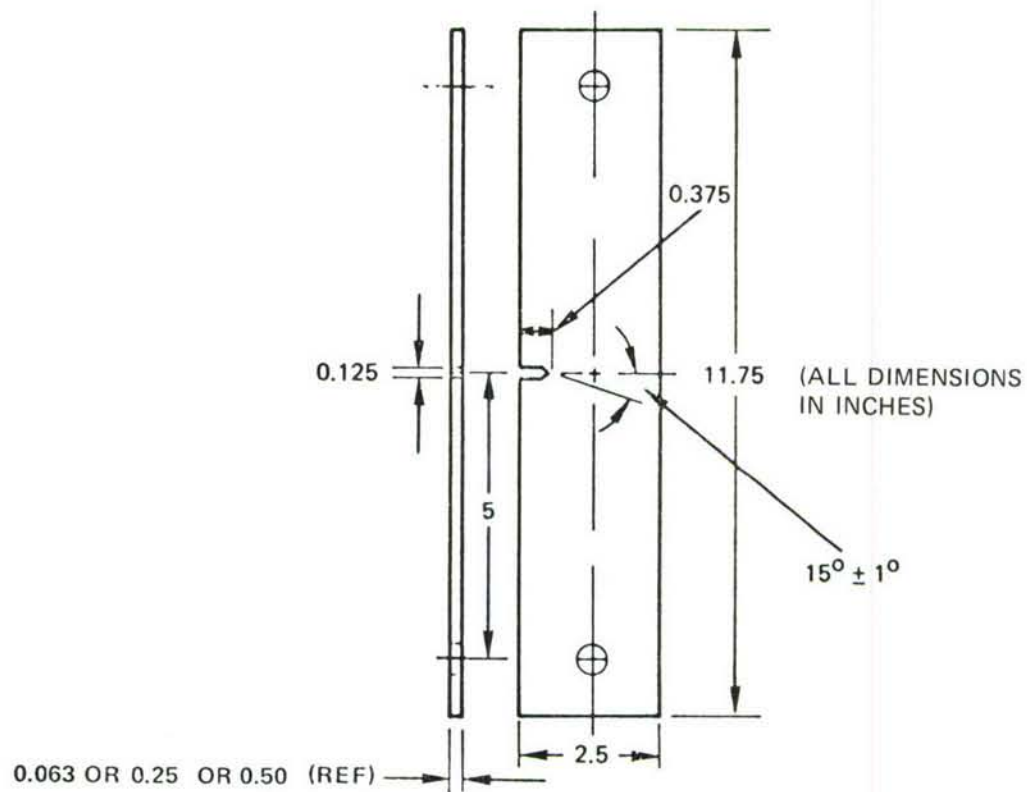
FIGURE D-1. SEN ALUMINUM SPECIMEN, LT (RW) ORIENTATION
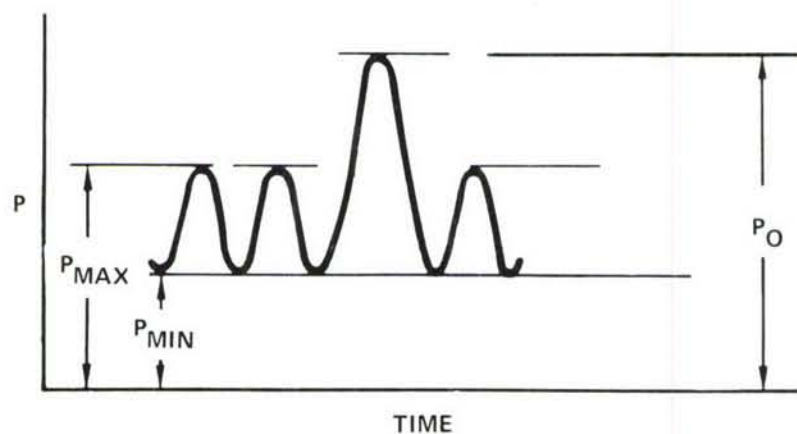
$$\text{OVERLOAD RATIO} = \frac{P_O}{P_{MAX}}$$

$$\% \text{ OVERLOAD} = \left(\frac{P_O - P_{MAX}}{P_{MAX}}\right) \times 100$$

FIGURE D-2. SCHEMATIC REPRESENTATION OF THE TEST SPECTRUM
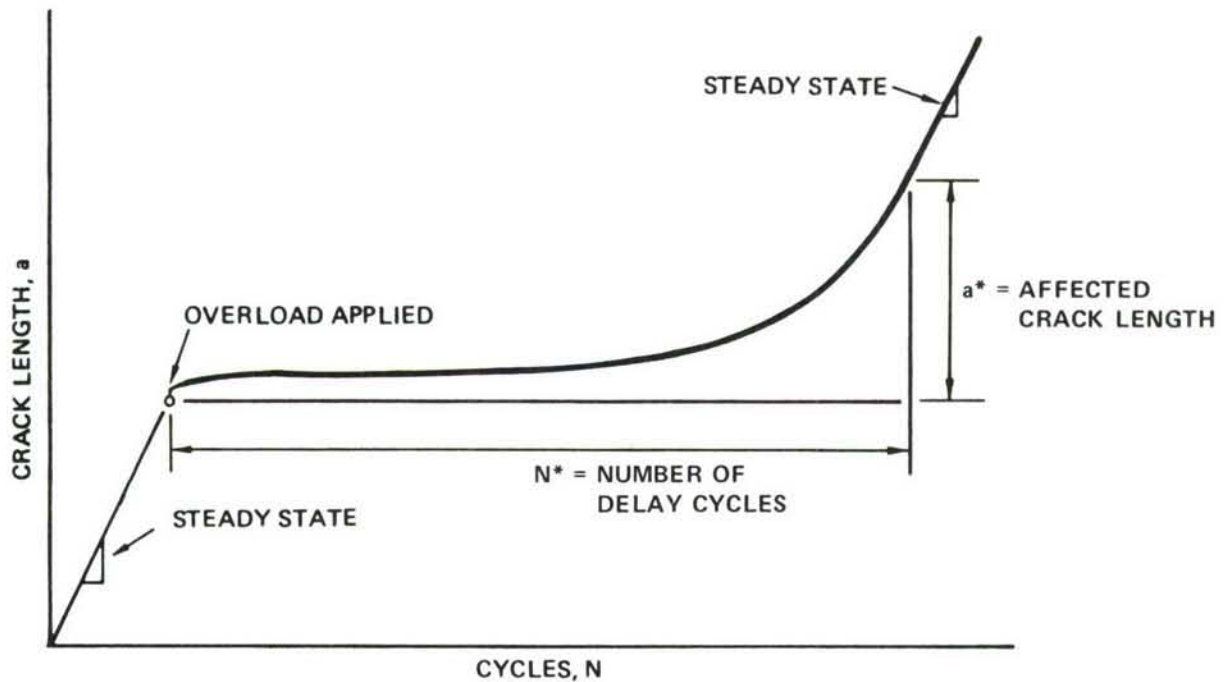
FIGURE D-3(a). CRACK-GROWTH RATE CURVE RESULTING FROM
APPLICATION OF A SINGLE OVERLOAD
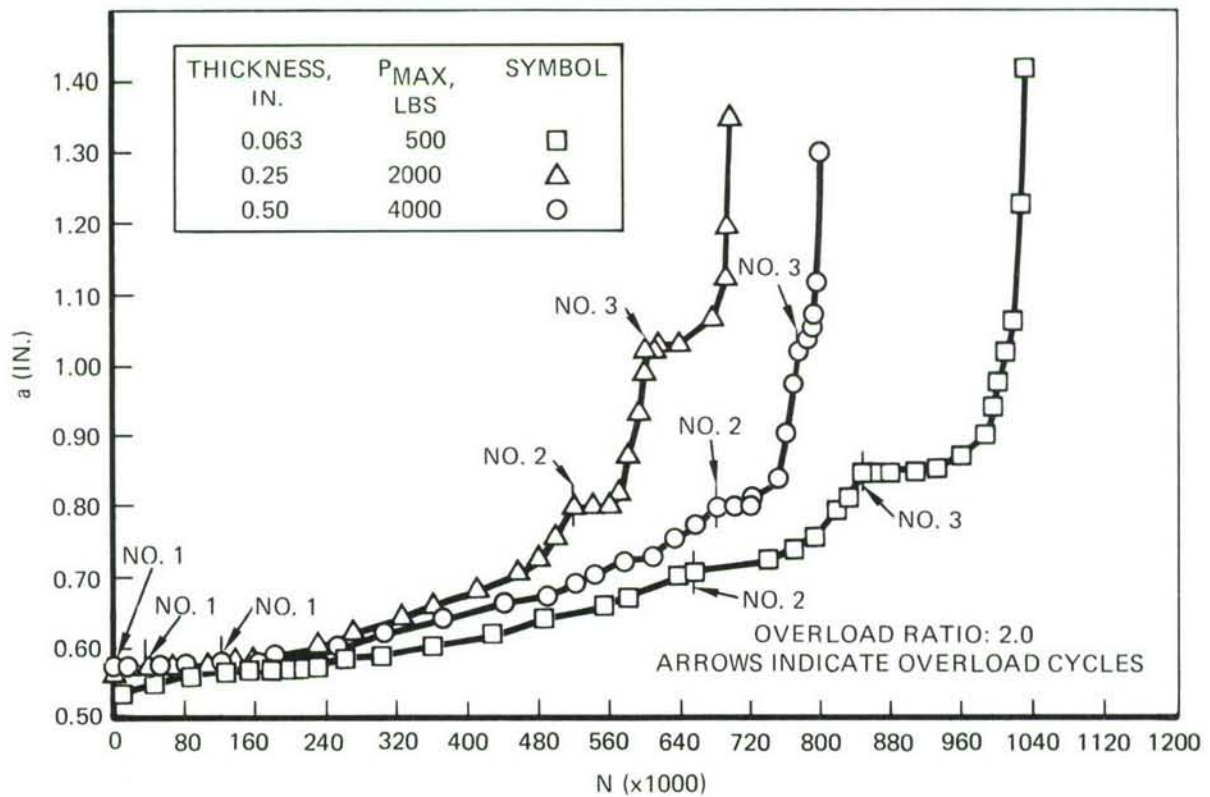
FIGURE D-3(b). CRACK-LENGTH VS NUMBER OF CYCLES FOR THREE
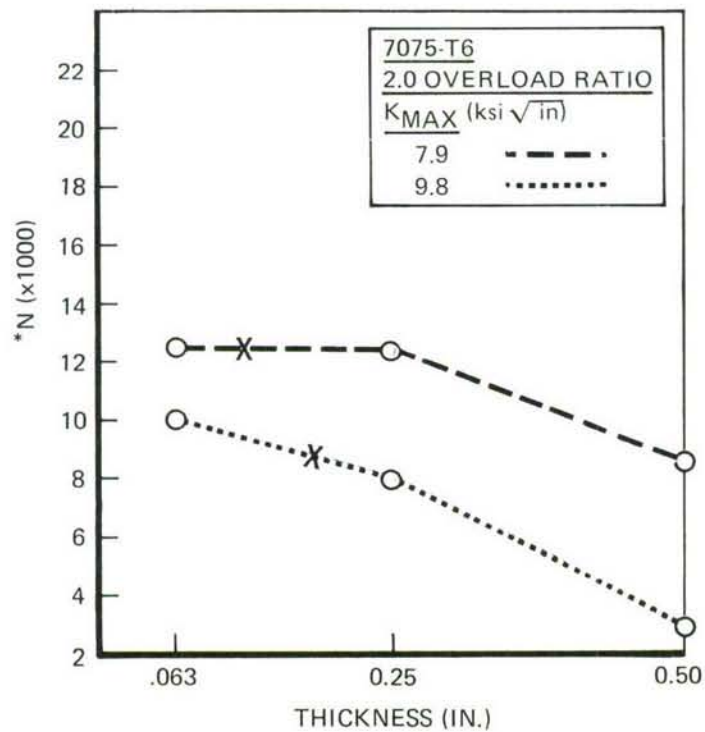THICKNESSES OF 2024-T3 ALLOY AT AN OVERLOAD RATIO OF 2.0

204
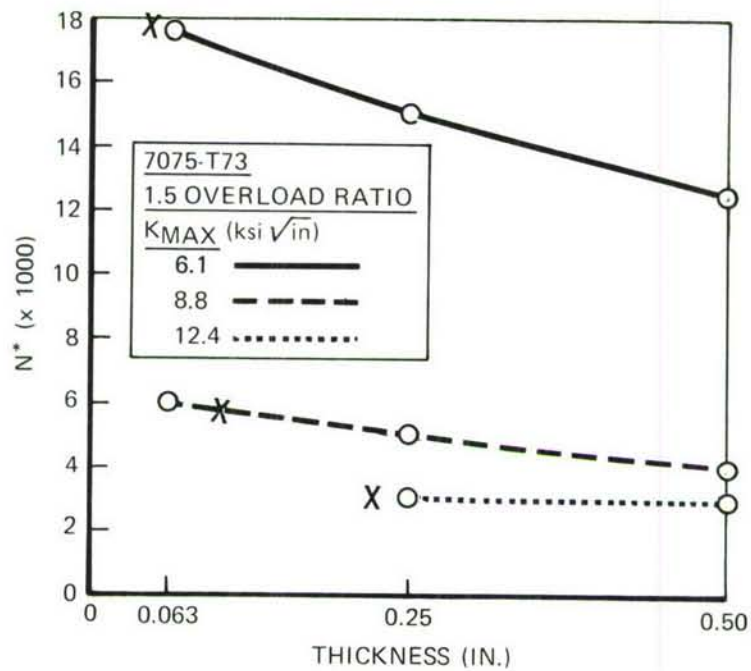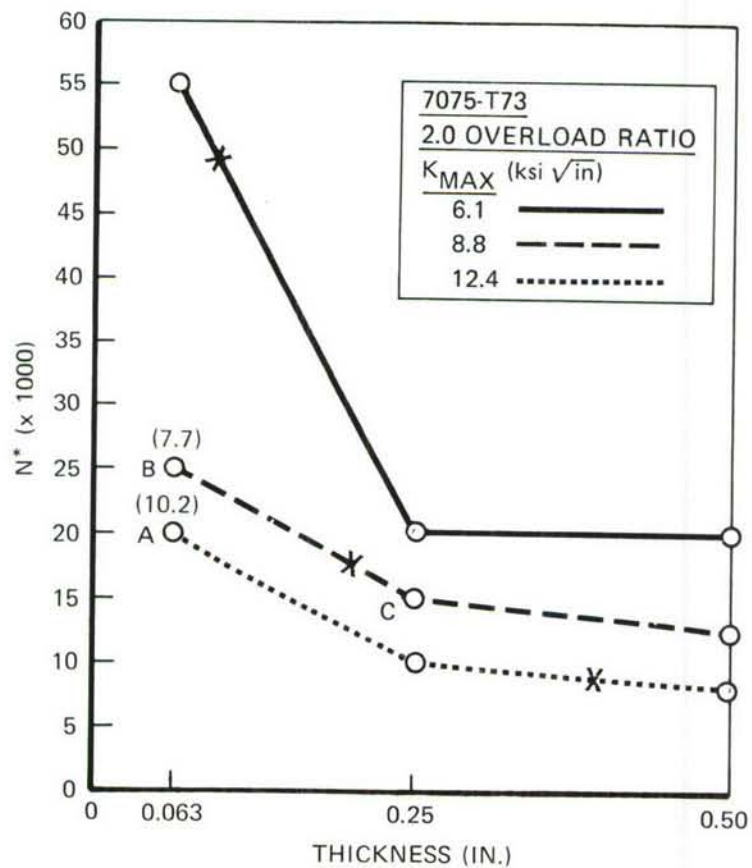
(a) 50% OVERLOAD CYCLE

(b) 100% OVERLOAD CYCLE

FIGURE D-4. EFFECT OF THICKNESS ON DELAY FOR 7075-T73 ALLOY.
THE X's DENOTE PLANE-STRAIN THICKNESS
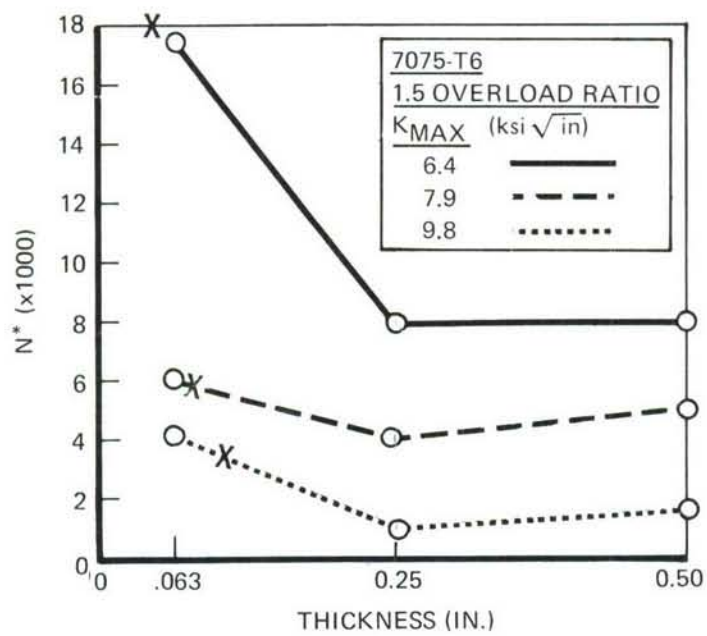
(a) 50% OVERLOAD CYCLE

(b) 100% OVERLOAD CYCLE

FIGURE D-5. EFFECT OF THICKNESS ON DELAY FOR 7075-T6 ALLOY.
THE X's DENOTE PLANE-STRAIN THICKNESS
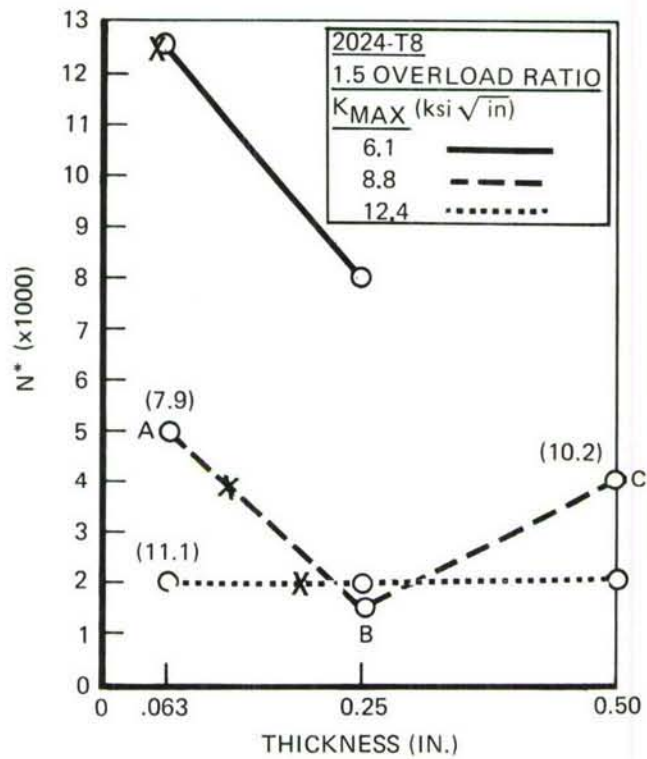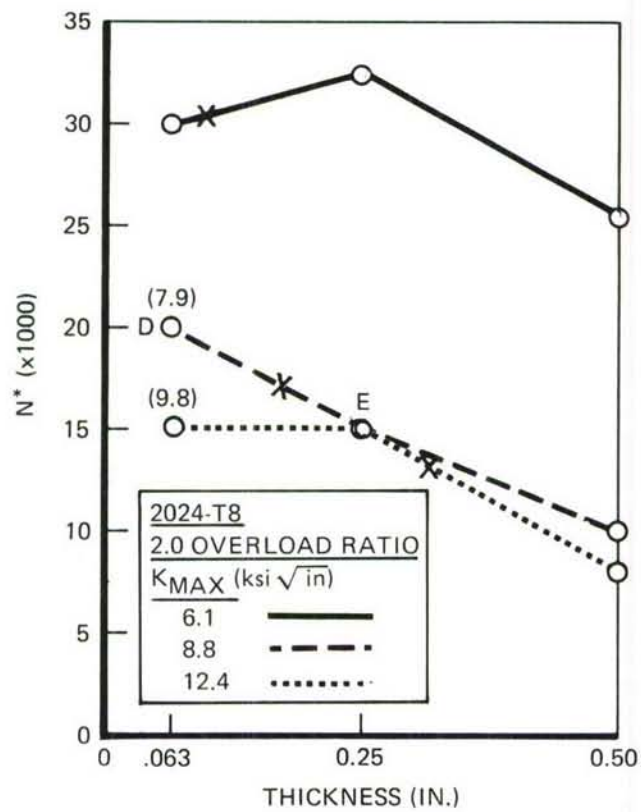
(a) 50% OVERLOAD CYCLE
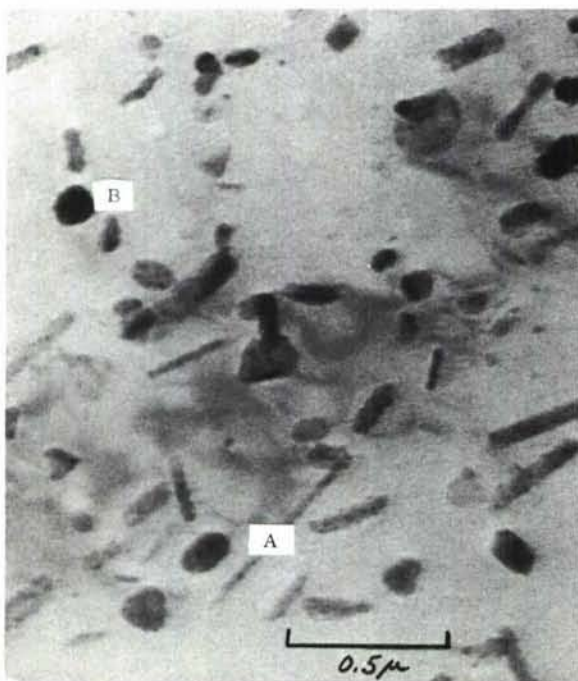

(b) 100% OVERLOAD CYCLE

FIGURE D-6. EFFECT OF THICKNESS ON DELAY FOR 2024-T8 ALLOY.
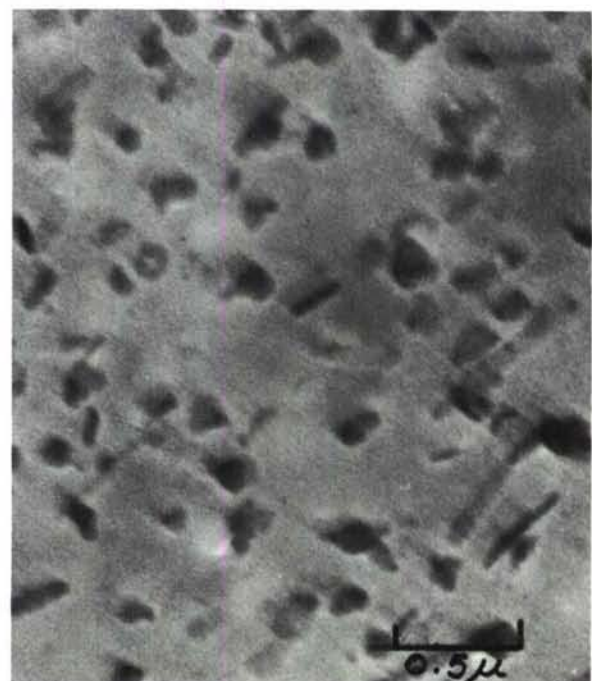THE X's DENOTE PLANE-STRAIN THICKNESS
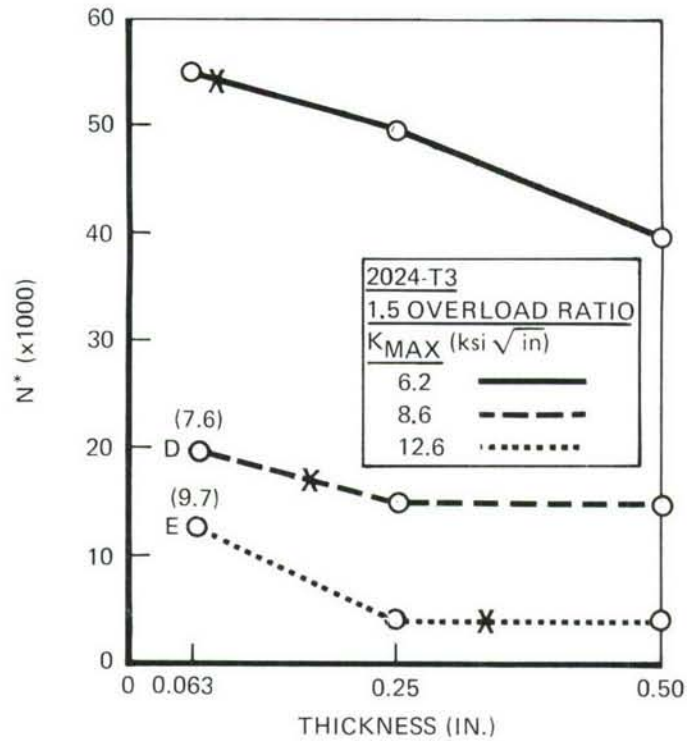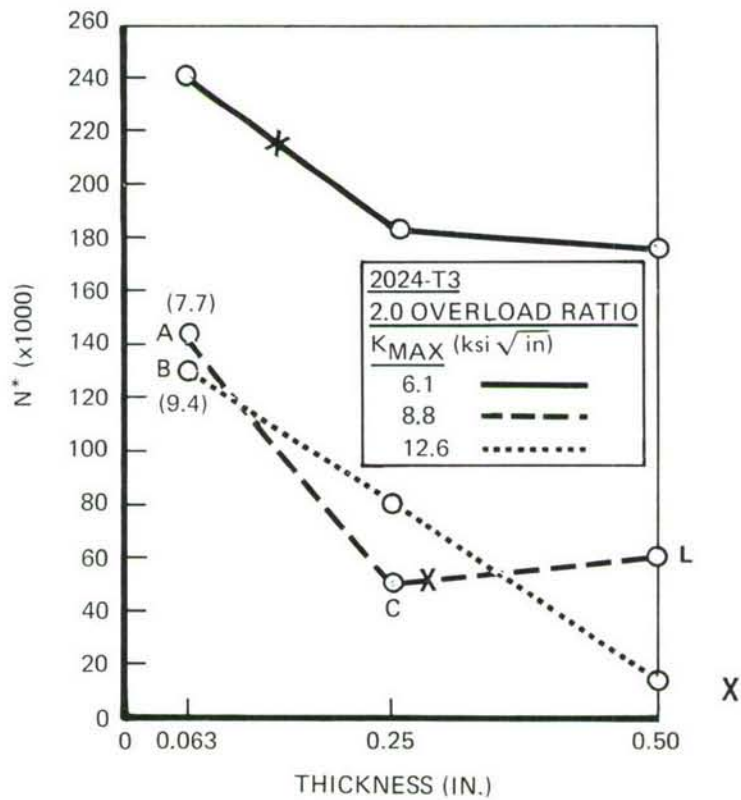
FIGURE D-7. EFFECT OF THICKNESS ON DELAY FOR 2024-T3 ALLOY.
THE X's DENOTE PLANE-STRAIN THICKNESS
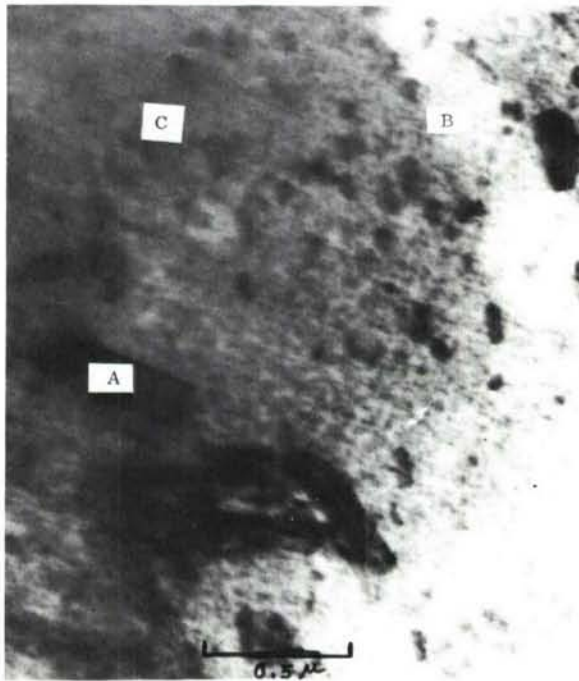
(a) 2024-T3 SHOWING Al_2O_3(A), GP ZONES (B), AND S'(C)
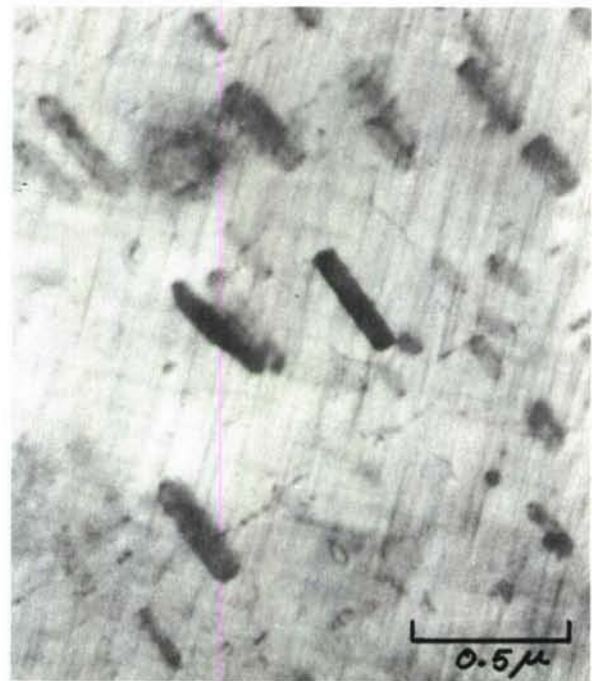
(b) 2024-T8 SHOWING S' PRECIPITATES AND DISPERSOIDS

(c) 7075-T6 SHOWING η'(A) AND DISPERSOID (B)

(d) 7075-T73 SHOWING η' AND DISPERSOID
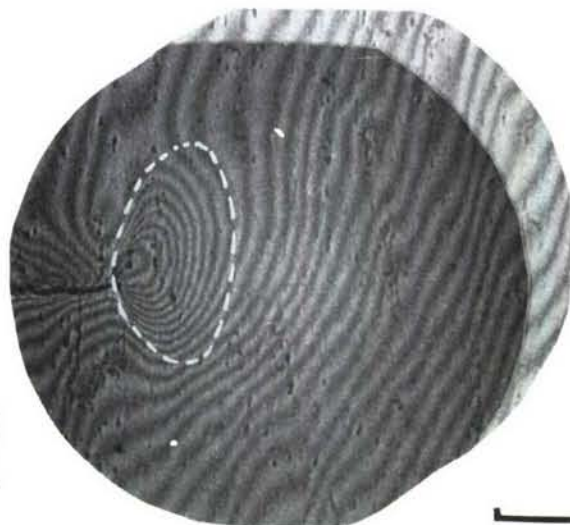
FIGURE D-8. SUBSTRUCTURE OF THE FOUR ALLOYS USED

THICKNESS: 0.063 IN.
P_{MAX} = 500 LBS

THICKNESS: 0.25 IN.
P_{MAX} = 2000 LBS

THICKNESS: 0.50 IN.
P_{MAX} = 4000 LBS

CRACK-LENGTH AT OVERLOAD = 0.80 IN.
K_{MAX} =8.7 KSI$\sqrt{IN.}$

0.3MM

FIGURE D-9. OPTICAL INTERFERENCE PATTERNS AT THE CRACK TIP OF 7075-T73
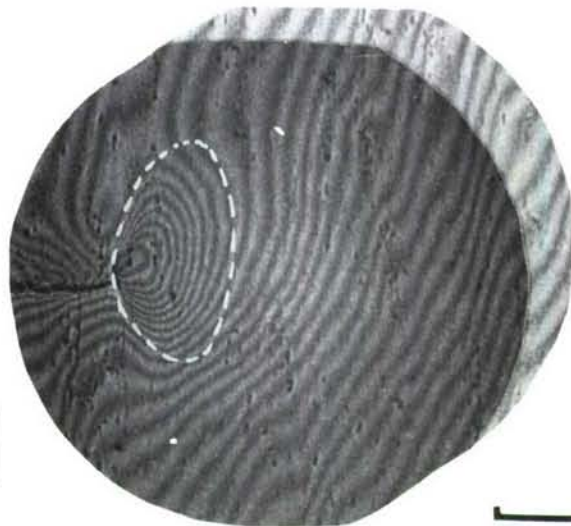SEN SPECIMENS OF THREE DIFFERENT THICKNESSES AFTER 100%
OVERLOAD CYCLE

THICKNESS : 0.063 IN.
P_{MAX} = 500 LBS

THICKNESS: 0.25 IN.
P_{MAX} = 2000 LBS

THICKNESS: 0.50 IN.
P_{MAX} = 4000 LBS

CRACK-LENGTH AT OVERLOAD = 0.80 IN.
K_{MAX} = 8.7 KSI√IN.

0.3MM

FIGURE D-9. OPTICAL INTERFERENCE PATTERNS AT THE CRACK TIP OF 7075-T73 SEN SPECIMENS OF THREE DIFFERENT THICKNESSES AFTER 100% OVERLOAD CYCLE
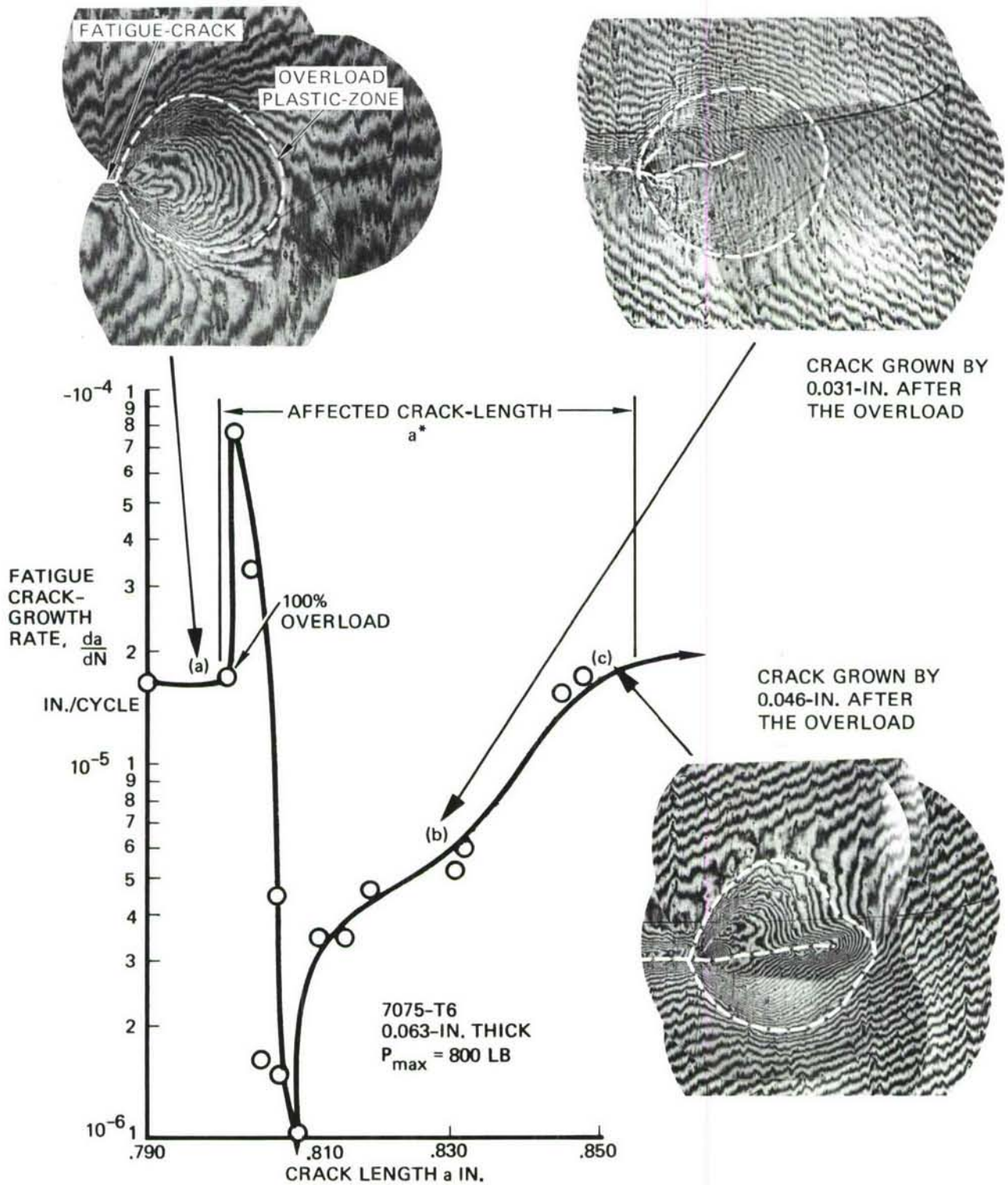
FIGURE D-10. INTERFERENCE PATTERNS AT DIFFERENT STAGES OF
CRACK-GROWTH AFTER A 100% OVERLOAD CYCLE

(a) K_{MAX} = 6.1 KSI $\sqrt{IN.}$ CRACK LENGTH AT OVERLOAD = 0.57 IN.

CRACK-GROWTH
DIRECTION

(b) K_{MAX} = 7.7 KSI $\sqrt{IN.}$ CRACK LENGTH AT OVERLOAD = 0.71 IN.

(c) K_{MAX} = 9.4 KSI $\sqrt{IN.}$ CRACK LENGTH AT OVERLOAD = 0.85 IN.

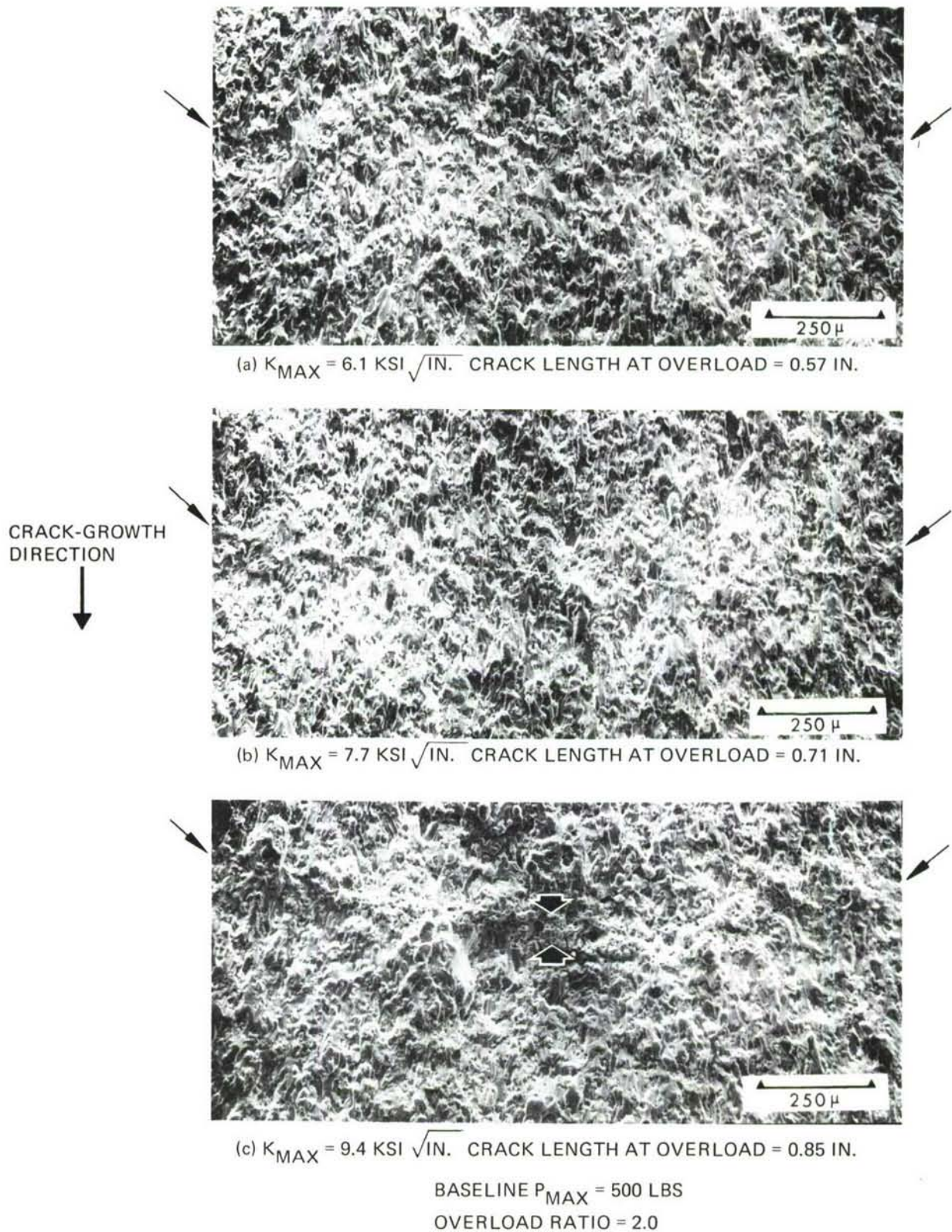BASELINE P_{MAX} = 500 LBS

OVERLOAD RATIO = 2.0

FIGURE D-11. FRACTOGRAPHS SHOWING EFFECT OF STRESS INTENSITY ON
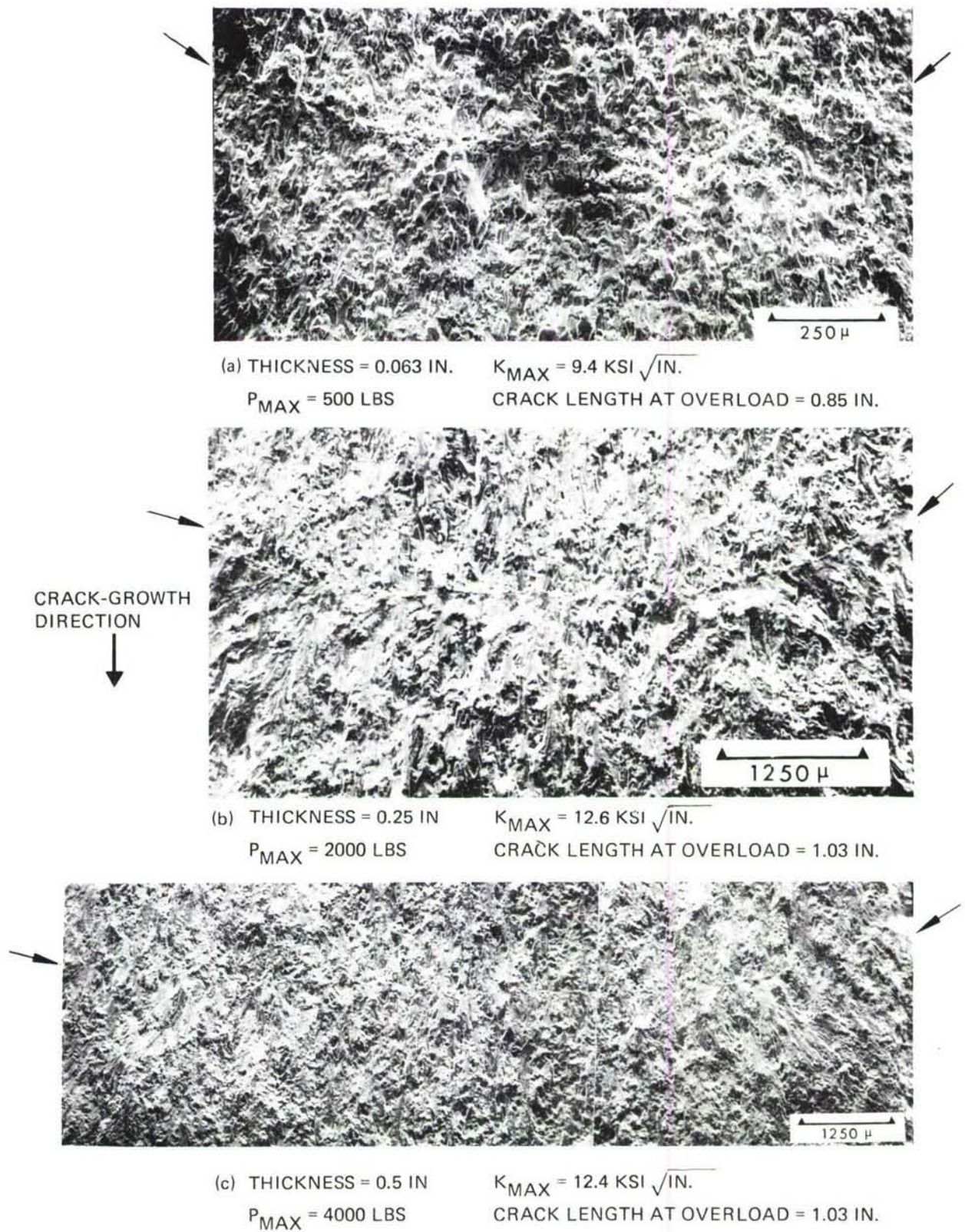OVERLOAD MARKING AFTER A 100% SINGLE OVERLOAD CYCLE IN A
0.063-INCH 2024-T3 SPECIMEN

(a) THICKNESS = 0.063 IN. K_{MAX} = 9.4 KSI $\sqrt{IN.}$

      P_{MAX} = 500 LBS   CRACK LENGTH AT OVERLOAD = 0.85 IN.

CRACK-GROWTH
DIRECTION

(b)   THICKNESS = 0.25 IN K_{MAX} = 12.6 KSI $\sqrt{IN.}$

      P_{MAX} = 2000 LBS   CRACK LENGTH AT OVERLOAD = 1.03 IN.

(c)   THICKNESS = 0.5 IN K_{MAX} = 12.4 KSI $\sqrt{IN.}$

      P_{MAX} = 4000 LBS   CRACK LENGTH AT OVERLOAD = 1.03 IN.

FIGURE D-12. FRACTOGRAPHS SHOWING EFFECT OF THICKNESS ON OVERLOAD
MARKING AFTER A 100% OVERLOAD CYCLE IN 2024-T3

213

CRACK-GROWTH
DIRECTION

THICKNESS = 0.25 IN. K_{MAX} = 12.4 KSI $\sqrt{IN.}$
P_{MAX} = 2000 LBS   CRACK LENGTH AT OVERLOAD = 1.03 IN.

FIGURE D-13. CRACKED INTERMETALLIC PARTICLES AND RUPTURED MATRIX
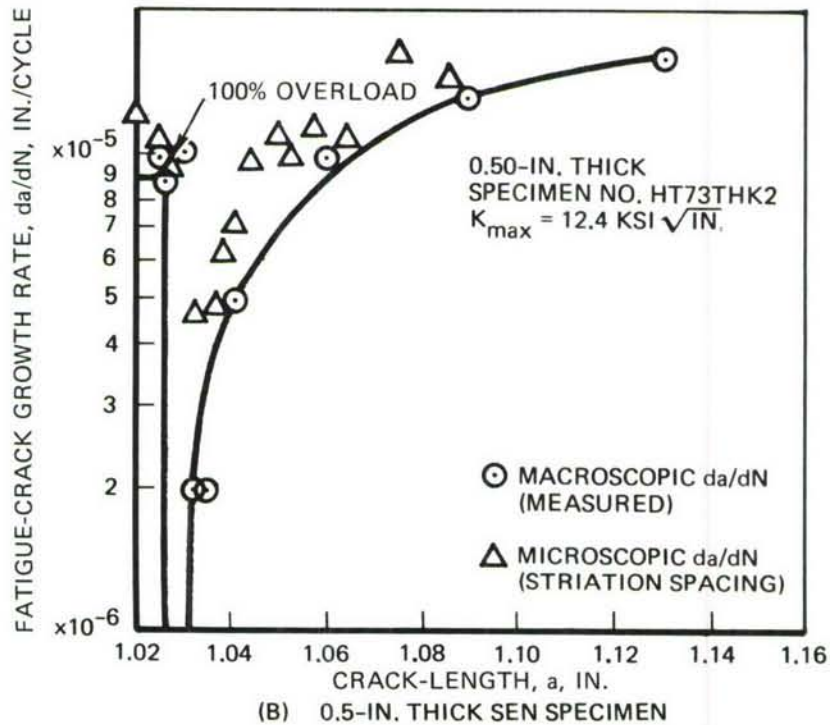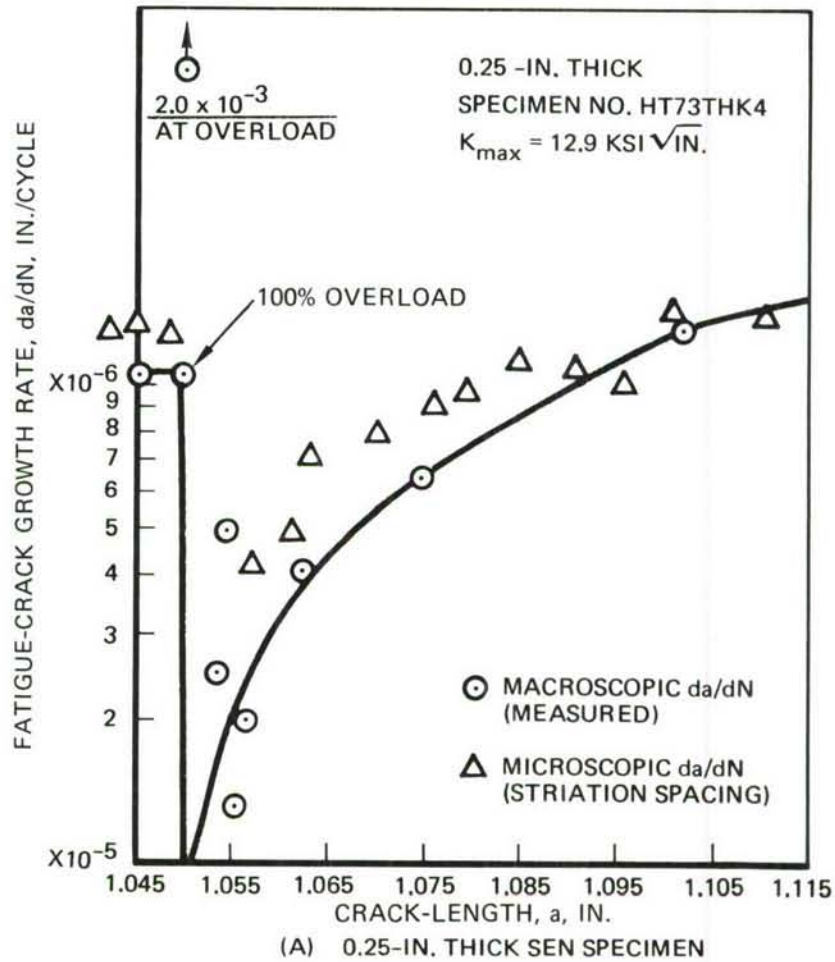(FINE DIMPLES) IN THE 100% OVERLOAD REGION OF A 2024-T8 SPECIMEN

FIGURE D-14. MICROSCOPIC AND MACROSCOPIC CRACK-GROWTH BEHAVIOR
AFTER 100% OVERLOAD CYCLE IN 7075-T73 ALLOY

215